ESTIMATION OF THE RADIOACTIVE AEROSOLS CAPTURE IN ACCIDENTAL SEQUENCES OF NUCLEAR POWER PLANTS

DOCTORAL THESIS

Author:
César Berna Escriche

Supervisors:
Dr. José Luis Muñoz-Cobo González
Dr. Facundo Alberto Escrivá Castells

Valencia, September 2017

ESTIMATION OF THE RADIOACTIVE AEROSOLS CAPTURE IN ACCIDENTAL SEQUENCES OF NUCLEAR POWER PLANTS

by
César Berna Escriche
Licenciado en Ciencias Físicas
at the Universitat de València
Ingeniero Industrial
at the Universitat Politècnica de València

Submitted to the Instituto Universitario de Ingeniería Energética
in partial fulfilment of the requirements for the degree of

DOCTOR of PHILOSOPHY

at the

Universitat Politècnica de València

September 2017

Certified by Dr. José Luis Muñoz-Cobo González. Thesis supervisor
Certified by Dr. Facundo Alberto Escrivá Castells. Thesis supervisor

I dedicate this work to
my parents Pedro and Pascuala,
to my Wife Reme
and to everyone
who awakened in me
the curiosity to learn

To my parents & wife:
Sir Isaac Newton once said 'If I have seen further,
it is by standing upon the shoulders of giants',
Thank you for being my giants.

ACKNOWLEDGEMENTS

The present document summarizes my research endeavors at the Group of Thermal-hydraulic and Nuclear Engineering of the Institute of Energy Engineering of the Universitat Politècnica de València (UPV). It does not fully capture, however, the wealth of experiences provided by many outstanding and brilliant people I had the privilege of meeting over these years. This work could not have come to fruition without the wonderful atmosphere existing in the Group of Thermal-hydraulic and Nuclear Engineering.

I owe my full and sincere gratitude to my two thesis supervisors Dr. Jose Luis Muñoz-Cobo González and Dr. Alberto Escrivá Castells. They devised this thesis and gave me the chance to carry it out. For their full confidence in me, for their contribution to this work through many hours of useful scientific discussions, for their advice, for their enthusiasm developing my interest and for many more reasons I will be eternally grateful.

I want to express my gratitude to Dr. Luis Enrique Herranz Puebla and Dr. Claudia Lopéz del Prá for their contribution to this PhD work. Without the collaboration between CIEMAT-UPV to carry out the works of the ARTIST-España Project, that began 10 years ago, this thesis would not have been possible.

I want to express my thankfulness to Dr. José Enrique Juliá Bolivar for his contribution to this PhD work. Without his free collaboration to carry out the experiments of pool discharge this thesis will not has had the circle closed.

I also want to thank my colleagues and friends of the Instituto de Ingeniería Energética of the UPV, José Luis, David, Yago and Enrique for all our technical and not-technical talks over these last years. The not technical ones had made the hard work days more enjoyable. I do not want to forget all colleagues and friends who worked here through the recent years: Arturo, Cris, Laura, Rafa, David and Tania.

Last, but not least, I would like to say that my words would not be enough to express how I am feeling inside. My parents, without you and your full support I would never have come so far, thank you for all your encouragement and support during all this time. I would also like to express my gratefulness to my wife Reme for your tolerance and support through these years, to support me and put up with my bad moments. I also want to thank all who have crossed my path and helped to found the right track, or posed me facing new challenges. However, it also helped me remember what is really important in life.

ABSTRACT

The turbulent submerged jets can be found fairly frequently in a great variety of processes, their study is essential in many industrial processes and engineering applications, such as in underwater propulsion, in metallurgical processes, in chemical processes or in the nuclear industry, among others. Within the nuclear world the submerged jets can occur in light water reactors (LWR), in both pressurized water reactors (PWRs) and boiling water reactors (BWR). These submerged jets are usually associated with complex multiphase flows, so that all processes occurring after such injection will be essentially unstable and turbulent.

A hypothetical severe accident in a reactor can cause deterioration of the core, so that the fission products can escape from the core and be transported through the primary system and, finally, can be released to the surrounding environment. But if there is a volume of water in the escape pathway of aerosols, a discharge in the shape of submerged jet can occur, whether in a suppression pool (during an accident with loss of power, SBO, in a water reactor boiling BWR) or in the secondary of a steam generator (in an accidental breakage sequence tube / s in U in a steam generator, SGTR, in a pressurized water reactor, PWR). So that there is a capture of aerosols in those volumes, being reduced the amount of them that escape outside. Usually these sequences have been considered only for BWRs and for low discharge velocities, but these may also take place at higher velocities and, as mentioned previously, in PWRs.

Throughout this thesis there is a contribution to a better understanding and quantification of natural mitigation processes that occur when a jet is discharged into a volume of water, so that it can be applied to discharges in suppression pools in a SBO sequence (BWRs), and inside of a steam generator during a SGTR event (PWRs). Being the central activity the expansion of SPARC90 code capabilities, so as to be able to quantify the aerosol capture that occurs when the discharge takes place at high velocity (originally the code only was developed to study discharges under globular regime, i.e., injection at low velocity).

So the process followed to carry out this work can be divided into several stages. The first one focuses on the literature search for available information, in a specific way on submerged jets and, given the scarce specific information, this has been extended to the literature search of processes with phenomenologies that present analogies with submerged jets. Within this part, it has on the one hand, finding aspects of jet hydrodynamics and on the other, those related to aerosol capture processes. In a second stage, there are aspects of the implementation into the new code subroutines of the expressions found and / or developed in the previous stage. While for the third stage, remains the assessment of the capabilities and behavior of the new models implemented in the code. For this last stage, first, it has been proceeded to conduct a verification process which has been tested the code robustness. And secondly, it has been proceeded to perform a validation process, which has been carried out through the comparison of the results predicted by the code against the limited experimental data that are available under similar conditions to those of the model.

Being the comparison against the experimental data satisfactory, showing a marked improvement in the code capabilities.

SINOPSIS

Los chorros sumergidos turbulentos se pueden encontrar con bastante asiduidad en muy diversos procesos, siendo esencial su estudio en gran cantidad de procesos industriales y aplicaciones ingenieriles, como por ejemplo, en la propulsión submarina, en procesos metalúrgicos, en procesos químicos o en la industria nuclear, entre otros. Dentro del mundo nuclear los chorros sumergidos pueden presentarse en los reactores de agua ligera (LWR), tanto en reactores de agua a presión (PWR), como en reactores de agua en ebullición (BWR). Estos chorros sumergidos llevan asociados complejos flujos multifásicos, de forma que los procesos que tienen lugar tras dicha inyección serán esencialmente inestables y turbulentos.

Un hipotético accidente grave en un reactor puede causar el deterioro del núcleo, de forma que los productos de fisión pueden escapar del núcleo y ser transportados a través del sistema primario y, finalmente, pueden ser liberados al medio ambiente circundante. Pero si existe un volumen de agua en la vía de escape de los aerosoles puede tener lugar la descarga en forma de chorro sumergido, ya sea una piscina de supresión (durante un accidente con pérdida del suministro eléctrico, SBO, en un reactor BWR) o el secundario de un generador de vapor (en una secuencia accidental con rotura de tubo/s en U en un generador de vapor, SGTR, en un reactor PWR). De forma que se tiene una captura de los aerosoles en dichos volúmenes, viéndose reducida la cantidad que escapan al exterior. Habitualmente estas secuencias se han considerado solamente para reactores BWR y para descargas a bajas velocidades, pero estas podrían tener lugar también a velocidades mayores y, como se ha dicho con anterioridad, en reactores PWR.

A lo largo de esta tesis se ha contribuido a una mejor compresión y cuantificación de los procesos naturales de mitigación que se producen cuando se descarga un chorro en un volumen de agua, de forma que puede ser aplicado para descargas en piscinas de supresión en una secuencia SBO (reactores del tipo BWR), como en el interior de un generador de vapor durante una secuencia SGTR (reactores del tipo PWR). Siendo la actividad central la ampliación de las capacidades del código SPARC90, de forma que sea capaz de cuantificar la captura de aerosoles que tiene lugar cuando la descarga se produce a alta velocidad (originalmente el código solamente fue desarrollado para el estudio de descarga en régimen globular, es decir, inyección a baja velocidad).

De modo que el proceso seguido para llevar a cabo el presente trabajo se puede dividir en varias etapas. La primera se centra en la búsqueda bibliográfica de la información disponible, de una forma específica relativa a chorros sumergidos y, dada la escasa información específica existente, esta se ha extendido a la búsqueda bibliográfica de procesos con fenomenologías que presentan analogías con los chorros sumergidos. Dentro de esta parte, se tiene por un lado, la búsqueda de los aspectos relativos a la hidrodinámica del chorro y, por otro, los relativos a los procesos de captura de aerosoles. En una segunda etapa se tienen los aspectos relativos a la implementación dentro de las nuevas subrutinas del código de las expresiones halladas y/o desarrolladas en la anterior etapa. Mientras que para la tercera etapa resta la evaluación de las capacidades y el comportamiento de los nuevos modelos implementados en el código. Para esta última etapa, en primer lugar, se ha

procedido a llevar a cabo un proceso de verificación con el que se ha comprobado la robustez del código. Y en segundo lugar, se ha procedido a realizar un proceso de validación, el cual ha sido llevado a cabo a través de la confrontación de los resultados predichos por el código frente a los limitados datos experimentales disponibles en condiciones similares a las introducidas en el modelo. Siendo la comparación frente a los datos experimentales satisfactoria, mostrando una mejora sostenible en las capacidades del código.

SINOPSI

Els dolls submergits turbulents es poden trobar amb prou assiduïtat en molt diversos processos, sent essencial el seu estudi en gran quantitat de processos industrials i aplicacions enginyerils, com per exemple, en la propulsió submarina, en processos metal·lúrgics, en processos químics o en la indústria nuclear, entre altres. Dins del món nuclear els dolls submergits poden presentar-se en els reactors d'aigua lleugera (LWR), tant en reactors d'aigua a pressió (PWR), com en reactors d'aigua en ebullició (BWR). Estos dolls submergits solen portar associats complexos fluxos multifàsics, de manera que els processos que tenen lloc després de la dita injecció seran essencialment inestables i turbulents.

Un hipotètic accident greu en un reactor pot causar el deteriorament del nucli, de manera que els productes de fissió poden escapar del nucli i ser transportats a través del sistema primari i, finalment, poden ser alliberats al medi ambient circumdant. Però si existeix un volum d'aigua en la via de fuita dels aerosols pot tenir lloc la descàrrega en forma de doll submergit, ja siga una piscina de supressió (durant un accident amb perduda del subministrament elèctric, SBO, en un reactor d'aigua en ebullició, BWR) o el secundari d'un generador de vapor (en una seqüència accidental amb trencament de tub/s en U en un generador de vapor, SGTR, en un reactor d'aigua a pressió, PWR). De manera que es té una captura dels aerosols en els anteriorment dits volums, veient-se reduïda la quantitat d'ells que escapen a l'exterior. Habitualment aquestes seqüències s'han considerat solament per a reactors BWR i per a baixes velocitats de descàrrega, però aquestes podrien tenir lloc també a velocitats majors i, com s'ha dit amb anterioritat, en reactors PWR.

Al llarg d'aquesta tesi s'ha contribuït a una millor compressió i quantificació dels processos naturals de mitigació que es produeixen quan es descarrega un doll en un volum d'aigua, de manera que pot ser aplicat per a descàrregues en piscines de supressió en una seqüència SBO (reactors del tipus BWR), com a l'interior d'un generador de vapor durant una seqüència SGTR (reactors del tipus PWR). Sent l'activitat central l'ampliació de les capacitats del codi SPARC90, de manera que siga capaç de quantificar la captura d'aerosols que té lloc quan la descàrrega es produeix a alta velocitat (originalment el codi solament va ser desenvolupat per a l'estudi de descàrrega en règim globular, és a dir, injecció a baixa velocitat).

De manera que el procés seguit per dur a terme el present treball es pot dividir en diverses etapes. La primera d'elles se centra en la cerca bibliogràfica de la informació disponible, d'una forma específica relativa a dolls submergits i, donada l'escassa informació específica existent, esta s'ha estés a la cerca bibliogràfica de processos amb fenomenologies que presenten analogies amb els dolls submergits. Dins d'aquesta part, es té d'una banda, la cerca dels aspectes relatius a la hidrodinàmica del doll i, per un altre, els relatius als processos de captura d'aerosols. En una segona etapa es tenen els aspectes relatius a la implementació dins de les noves subrutines del codi de les expressions trobades i/o desenvolupades en l'anterior etapa. Mentre que per a la tercera etapa resta l'avaluació de les capacitats i el comportament dels nous models implementats en el codi. Per a aquesta última etapa, en primer lloc, s'ha procedit a dur a terme un procés de verificació amb el qual

s'ha comprovat la robustesa del codi. I en segon lloc, s'ha procedit a realitzar un procés de validació, el qual ha estat dut a terme a través de la confrontació dels resultats predits pel codi enfront de les limitades dades experimentals disponibles en condicions similars a les introduïdes en el model. Sent la comparació enfront de les dades experimentals satisfactòria, mostrant una millora ostensible en les capacitats del codi.

NOMENCLATURE

AR	Aspect Ratio, degree of droplet deformation
c	Wave celerity
c_0	Speed of sound
C_c	Cunningham Slip-Correction Factor
C_α	Energy flow correction coefficient
C_β	Pulsating motions correction coefficient
C_D	Drag Coefficient
C_W	Surface Tension Factor
D	Gas jet diameter
D_{diff}	Diffusion Coefficient
D_N	Nozzle Diameter
DF	Decontamination Factor
DW	Disturbance Wave
E	Entrained Droplet Fraction
Eo	Eötvös number
Fr	Froude Number
f	Friction Factor
f_{gi}	Gas interfacial friction factor
f_s	Smooth Interface Friction Factor
g	Gravity acceleration
G	Mass Flux
Gr	Grashoff number
J	Superficial Velocity
J*	Dimensionless Superficial Velocity
k	Stephan Boltzmann Constant
K_b	Boltzmann constant
k_d	Deposition Coefficient
Kn	Knudsen number
Ku	Kutateladze number
L_B	Buoyant Jet Penetration
l_c	Droplet Length Scale
L_M	Momentum Jet Penetration
L_{Tot}	Total Jet Penetration Length
L_w	Wave Spacing
m	Mass
$\dot{m}$	Mass Flow Rate
MWe	Electric Power of a Reactor
MWt	Thermal Power of a Reactor
N	Number of particle size bins
N_d	Droplet concentration
N_μ	Viscosity number
OE	Onset of Entrainment

Oh	Ohnesorge Number
P	Pressure
Pe	Peclet Number
Pr	Prandtl number
Q	Volumetric Flow Rate
r	Radius
R	Gas jet radius
R_d	Deposition Rate
Re	Reynolds number
RW	Ripple Waves
S	Submergence
S_{impact}	Correction factor for the inertial impact collection efficiency
Sc	Schimdt number
St	Strouhal number
Stk	Stokes number
S_R	Slip Ratio
T	Temperature
u	Fluid velocity
U*	Friction Velocity
V	Volume
v_{incp}	Entrainment inception velocity
W	Mass Flow Rate
We	Weber Number
x	Dynamic quality
X	Lockhart-Martinelli number
X_s	Steam Volume Fraction
z	Axial direction
Z	Entrance Length

Greek Symbols

α	Void Fraction
δ	Liquid film thickness
δ^*	Dimensionless Liquid Film Thickness
δ_b	Base liquid film thickness
δ_{max}	Maximum liquid film thickness
Δh_w	Wave Amplitude
ϕ_d	Droplet diameter
ϕ_p	Particle diameter
γ	Isentropic expansion coefficient
$\gamma(k,z)$	Decontamination Factor Coefficient for aerosol class k at axial position z
Γ	Mass Flow Rate per Unit Length
Γ^*	Dimensionless Mass Flow Rate per Unit Length
λ	Mean Free Path

λ_A	Length Scale, from Azzopardi
$\lambda_{c,K\text{-}H}$	Wavelength of Kelvin-Helmholtz Instability
λ_W	Wave Lenght or Wave Width
η	Collection Efficiency
μ	Dynamic viscosity
θ	Jet expansion angle
υ	Wave Frequency
ρ	Density
σ	Surface tension
τ	Time Scale
τ_i	Interfacial shear stress
ζ, ξ	Dimensionless Distances

Subscripts

0	Reference or Initial Point
1	Final, after the expansion
32	Sauter Mean Diameter
crit	Critical
c	Characteristics
d	Droplet
D	Drag
ffOE	Liquid film values at the onset of entrainment
g	Gas
i	Interface
j	droplet class size
k	aerosol class size
in	Inlet
K-H	Kelvin-Helmholtz Instability
l	Liquid
le	Entrained Liquid
lf	Liquid film
lfc	Critical Liquid Film
max	Maximum
min	Minimum
p	Particle
out	Outlet
Rel	Relative
ref	Reference
ret	Retained
vm	Volume Mean
w	Wall
z	Axial Direction

Superscripts

+,*	Dimensionless Variable
—	Mean Value
·	Variation per Unit of Time
→	Vector

Acronyms & Abbreviations

ACE	Advanced Containment Experiments
AMMD	Aerodynamic Mass Median Diameter
ARTIST	Aerosol Trapping in a Steam Generator
ASTEC	Accident Source Term Evaluation Code
ATWS	Anticipated Transient Without Scram
AVB	AntiVibration Bars
BUSCA	Bubble Scrubbing Algorithm
BW	Wave Break-up
BWR	Boiling Water Reactors
CATHARE	Code for Analysis of THermalhydraulics during Accident Reactor and safety Evaluation
CIEMAT	Centro de Investigaciones Energéticas, Medioambientales y Tecnológicas
CN	Convergent Nozzle
DBA	Design Basis Accidents
DE	Droplet Entrainment
DF	Decontamination Factor
DW	Disturbance Waves
ECCS	Emergency Core cooling System
EPICUR	Experimental Program on Iodine Chemistry under Radiation
FCVS	Filtered Containment Venting Systems
FF	Free Fall experiments
FP	Fission Products
GDE	General Dynamic Equation
GWd/tU	Gigawatt-day per metric ton of Uranium, unit of burnup of nuclear fuel
HST	Horizontal Shock Tube
HWT	Horizontal Wind Tunnel
IGA	Inter-Granular Attack
IGSCC	Inter-Granular Stress Corrosion Cracking
INCONEL	Family of Austenitic Nickel-Chromium Based Superalloys
INES	International Nuclear and radiological Event Scale
INSAG	International Nuclear Safety Group
K-H	Kelvin Helmholtz Instability
LACE	Light Water Reactor Advanced Containment Experiments
LOCA	Loss Of Coolant Accident
LOSP	Loss of Off-Site Power
LWR	Light Water Reactor

MCCI	Molten Core – Concrete Interaction
MELCOR	Methods for Estimation of Leakages and Consequences Of Releases, US NRC code
MOX	Mixed Oxide Fuel (composed by a mixture of UO_2 and PuO_2)
MWe	Electric Mega Watts
MWt	Thermal Mega Watts
NPP	Nuclear Power Plant
NRC	Nuclear Regulatory Commission of the United States
NSSS	Nuclear Steam Supply System
ODW	Onset of Disturbance Waves
OE	Onset of Entrainment
ODE	Ordinary Differential Equation
ODSCC	Outside Diameter Stress Corrosion Cracking
PHÉBUS	International fission product programme
PIRT	Phenomena Identification Ranking Technique
PNL	Pacific Northwest Laboratory
POSEIDON	Pool Scrubbing Effect on Iodine Decontamination (experimental series)
PRA	Probabilistic Risk Assessments
PSA	Probabilistic Safety Assessment
PWR	Pressurized Water Reactor
PWSCC	Primary Water Stress Corrosion Cracking
RBMK	Graphite-Moderated Boiling Water Reactor (Soviet Union design)
RCA	Reinforced Concerted Action (experimental series)
RCS	Reactor Coolant System
RIA	Reactivity Induced Accident
RPV	Reactor Pressure Vessel
RW	Ripple Waves
SBO	Station Black-Out
SCC	Stress Corrosion Cracking
SD	Shut-Down
SG	Steam Generator
SGTR	Steam Generator Tube Rupture
SLB	Secondary Line Break
SMD	Sauter Mean Diameter
SO	Suction Orifices
SPARC	Suppression Pool Aerosol Removal Code
SUPRA	Suppression Pool Retention Analysis
TMI-2	Reactor 2 of the Three Mile Island NPP (in which a Level 5 accident took place in 1979)
ULLN	Upper Limit Log-Normal
UPV	Universitat Politècnica de València
US NRC	United States Nuclear Regulatory Commission
VERCORS	French acronym for “Realistic verification of the behavior of reactor containment”
VOF	Volume of Fluid Model

VWT	Vertical Wind Tunnel
WS	Venturi Scrubber
WC	Wave Coalescence
WD	Wave Development

Dimensionless Numbers

Eo Eötvös number, $Eo = \dfrac{gD^2(\rho_l - \rho_g)}{\sigma}$

Fr Froude number, $Fr = \dfrac{\rho_g u_0^2}{(\rho_l - \rho_g) g d_0}$ (submerged jets)

Fr_g Gas Froude number, $Fr_g = \dfrac{J_g}{\sqrt{gD}}$

Fr_l Liquid Froude number, $Fr_l = \dfrac{J_l}{\sqrt{gD}}$

Gr_l Grashoff number, $Gr_l = \dfrac{gD^3 \rho_l (\rho_l - \rho_\alpha)}{\mu_l^2}$

Kn Knudsen number, $Kn = \dfrac{2\lambda}{\phi_p}$

Ku Kutateladze number, $Ku^2 = \dfrac{\rho_g u_g^2}{\sqrt{\sigma g \rho_l}}$

N_μ Viscosity number, $N_\mu = \dfrac{\mu_l}{\left(\rho_l \sigma \sqrt{\dfrac{\sigma}{g \Delta\rho}}\right)^{1/2}}$

Oh Ohnesorge number, $Oh = \dfrac{\mu}{\sqrt{\rho \phi \sigma}}$

Pe Mass diffusion Peclet number, $Pe = \dfrac{\phi_d u_d}{D_{diff}}$

Pr Prandtl number, $\mathrm{Pr} = \dfrac{c_p \mu}{k}$

Re_α Gas Core Reynolds number, $\mathrm{Re}_\alpha = \dfrac{J_g \rho_\alpha D}{\mu_g}$

Re_d Droplet Reynolds number, $\mathrm{Re}_d = \dfrac{\rho_g (u_g - u_d)\phi_d}{\mu_g}$

Re_{ffOE} Onset of Entrainment Reynolds number,

$$\mathrm{Re}_{ffOE} = 160$$

$$\mathrm{Re}_{ffOE} = \exp\left(5.8504 + 0.429 \frac{\mu_g}{\mu_l}\left(\frac{\rho_l}{\rho_g}\right)^{0.5}\right)$$

$$\mathrm{Re}_{ffOE} = 13 N_\mu^{-0.5}$$

$$\mathrm{Re}_{ffOE} = 7.3(\log_{10}\omega)^3 + 44.2(\log_{10}\omega)^2 - 263(\log_{10}\omega) + 439$$

Re_g Gas Reynolds number, $\mathrm{Re}_g = \dfrac{\rho_g J_g D}{\mu_g}$

Re_l Liquid Reynolds number, $\mathrm{Re}_l = \dfrac{\rho_l J_l D}{\mu_l}$

Re_l Liquid Film Reynolds number, $\mathrm{Re}_{lf} = \dfrac{4W_{lf}}{\mu_l P} = \dfrac{4\Gamma_{lf}}{\mu_l} = \dfrac{4\rho_l u_{lf}\delta}{\mu_l} = \mathrm{Re}_l(1-E)$

Re_p Particle Reynolds number, $\mathrm{Re}_p = \dfrac{\rho_g (u_g - u_p)\phi_p}{\mu_g}$

Re_τ Friction velocity Reynolds number, $\mathrm{Re}_\tau = \dfrac{\rho_g U^* D}{\mu_g}$

Sc_k Schimdt number (component k), $Sc_k = \dfrac{\mu_g}{\rho_g D_{diff,k}}$

St_l Liquid Strouhal number, $St_l = \dfrac{\upsilon D}{J_l}$

St_l Gas Strouhal number, $St_g = \frac{\upsilon D}{J_g}$

St_{gl} Gas-Liquid Strouhal number, $St_{gl} = \frac{\upsilon D}{\sqrt{J_g \cdot J_l}}$

Stk Stokes number (particle vs. system responses time), $Stk = \frac{\tau_p}{\tau_d}$

Stk_p Stokes number (impactability of an aerosol particle with a droplet),

$$Stk_p = \frac{C_c \rho_p \phi_p^2 (u_g - u_d)}{9 \mu \phi_d}$$

We_{crit} Critical Weber number of entrained droplets, $We_{crit} \approx \frac{8}{C_D}$

We_d Droplet Weber number, $We_d = \frac{\rho_g (u_g - u_d)^2 \phi_d}{\sigma}$

We_g Gas Weber number, $We_g = \frac{\rho_g J_g^2 D}{\sigma}$

Modified Weber numbers $We_g = \frac{\rho_g J_g^2 D}{\sigma}\left(\frac{\Delta\rho}{\rho_g}\right)^{1/4}$ or $We_g = \frac{\rho_g J_g^2 D}{\sigma}\left(\frac{\Delta\rho}{\rho_g}\right)^{1/3}$

We_l Liquid Weber number, $We_l = \frac{\rho_l U_l^2 \delta_l}{\sigma}$

x* Gas Quality, $x^* = \frac{J_g \rho_g}{J_g \rho_g + J_l \rho_l}$

X Lockhart-Martinelli number, $X = \sqrt{\frac{\rho_l J_l^2}{\rho_g J_g^2}}$

LIST OF CONTENTS

LIST OF FIGURES

LIST OF TABLES

Chapter 1

INTRODUCTION

1. INTRODUCTION

Multiphase flows are present in many industrial processes and engineering applications. Particularly, submerged jets are crucial in metallurgical processes, underwater propulsion, chemical and energy industries, and so on.

As far a Nuclear Power Plants (NPP) is concerned multiphase flow is of great interests, not only in regard to efficiency, but also in regard to safety. Consequently, a growing interest in accident management to ensure defence in depth strategies of NPP has taken place over the last decades. Within this framework, an important aspect to public health and safety are the accidents in Pressurized Water Reactors (PWR) and Boiling Water Reactors (BWR), particularly, the ones involving Steam Generator Tube Rupture events (SGTR) for PWR's or pool discharges during station Black-Out (SBO) events in BWR's.

In most of the LWR's severe accident scenarios the paths followed by aerosols include discharges in stagnant water pools. Such as in BWR's when the mixture of gases, steam and fission products are directed towards the suppression pool, in which the steam is condensed to prevent the over-pressurization of the wet well. In the case of PWR's, the mixture might pass through the pressurizer, or under SGTR events could leak into the secondary side of a SG via a hypothetical tube rupture. Even though these pool scrubbing events in stagnant pools have been traditionally associated with low injection velocities, there are a number of potential scenarios in which fission product trapping in aqueous ponds might also occur under jet injection regime. And as for discharges into the SG's, these processes usually take place at high gas velocities, therefore under jet injection regimes. Consequently is very important to design an accurate model and carry out experiments to simulate the aerosol removal processes which are taking place in stagnant water pools and in pools filled with obstacles (which simulate de rod bundles of a SG).

Summarizing, this introduction section is devoted to the contextualization of the problem, the description of the studied scenario, added to the presentation of the thesis objectives and motivations.

1.1. Brief Description of Boiling and Pressurized Water Reactors

Nuclear reactor systems consist in sustained nuclear chain reactions. Nuclear reactors are mainly used for electricity generation, being also used for ship and submarine moving. There are mainly two varieties of light water reactors (LWR): the pressurized water reactor (PWR) and the boiling water reactor (BWR).

1.1.1. Boiling Water Reactor

Inside the vessel of a BWR, a steam water mixture is produced when very pure water (reactor coolant fluid) moves upward through the core (BWRs contain between 370-800

fuel assemblies), on this way up the water absorbs heat. The major difference in the operation of a BWR compared to a PWR is the steam formation into the core. This steam-water mixture leaves the top of the core and enters the two stages of moisture separation, where water droplets are removed before the steam is allowed to enter the steam line (since the presence of water will damage the turbine). The steam line directs the steam to the main turbine, this steam causes it to turn and, the attached electrical generator, produce the electricity. The unused steam is exhausted towards the condenser where it is condensed into water. This condensed water is pumped out of the condenser with a series of pumps and back to the reactor vessel and a new cycle starts. The recirculation pumps and jet pumps, which work in closed loops around the core, allow the operator to vary the coolant flow which cross through the core and change the reactor power. These pumps and other operating systems in the plant receive their power from the electrical grid. If offsite power is lost, emergency cooling water is supplied by other pumps, which can be powered by onsite diesel generators. Other safety systems, such as the containment cooling system, also need electric power.

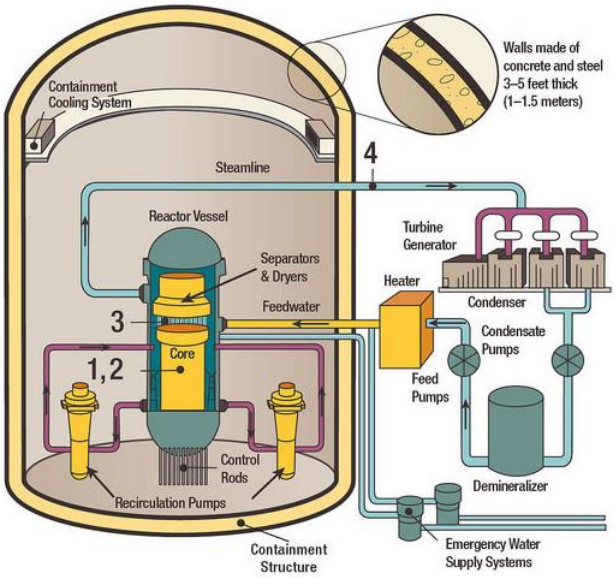

Figure 1.1. Schematic view of a BWR nuclear reactor [NRC].

In a typical design of a commercial BWR, the following process occurs, Figure 1.1. [Website of the Nuclear Regulatory Commission, NRC]:

1. The core inside the reactor vessel creates heat.

2. A steam-water mixture is produced when very pure water (reactor coolant fluid) moves upward through the core, absorbing heat.

3. The steam-water mixture leaves the top of the core and enters the two stages of moisture separation where water droplets are removed before the steam is allowed to enter the steam line.

4. The steam line directs the steam to the main turbine, causing it to turn the turbine generator, which produces electricity.

1.1.2. Pressurized Water Reactor

A PWR is a nuclear reactor that uses light water, in liquid phase at high pressure and temperature, as a coolant and moderator. PWR consists of two separated circuits, primary and secondary. In the primary circuit, the heat is created in the core which is inside the reactor vessel, the pressurized water carries the heat to the steam generator. Inside the SG, heat from the primary coolant loop vaporizes the water in a secondary loop, producing steam. The steam-lines direct the steam to the main turbine, causing it to turn the turbine generator, which produces electricity.

A typical design concept of a commercial PWR is shown in Figure 1.2. His operation is as follows [website AREVA]:

-The fission of the nucleus of uranium atoms to produce steam in the reactor is caused by bombarding atoms of nuclear fuel contained in the reactor core (1) with free neutrons. Every time that an atomic nucleus fissions takes place a new emission occurs, which turn new neutrons that keep the chain reaction going.

- The rate of this reaction is reduced or increased by lowering or raising the control rods (2) which are inside the core, due to free neutrons absorption. Dropping simultaneously all the control rods into the core, the chain reaction extinguishes instantaneously.

- In the primary circuit (in red, Figure 1.2), the water is heated inside the reactor vessel (3) in contact with hot fuel assemblies forming the reactor core (1), then passes through thousands of tubes that constitutes the SG (5) and driven by the reactor coolant pumps (6), returns to the reactor vessel.

- A pressurizer (4) maintains the primary system under high pressure conditions, generally between about 14 to 17 MPa, to force the water to remain in the liquid phase and thus ensure the most efficient heat transfer.

- Water in the secondary circuit (in blue and green, Figure 1.2) is heated by the primary water system outside the SG tubes and then is transformed into steam at a pressure of around 6-7.5 MPa.

- A set of tubes, collectors, carry this steam outside the reactor containment (7) to the turbine (8), so that it is set in motion, transforming part of the heat energy of the pressurized steam into mechanical energy.

Table 1.1. Vandellòs II, PWR NPP main features.

Reactor thermal power (MWt)	2940.6
Electrical power (MWe)	1087
Fuel	UO_2
Number of fuel bundles	157
Number of cooling loops	3
Reactor operating pressure (MPa)	15.4
Mean coolant temperature (K): Hot zero power Full power	 564.2 582.3
Coolant Recirculation Pumps	Westinghouse D 100
Volume of the primary (m^3)	106.19
Volume of pressurizer (PZR) (m^3)	39.65
PRZ heaters power (kW)	1400

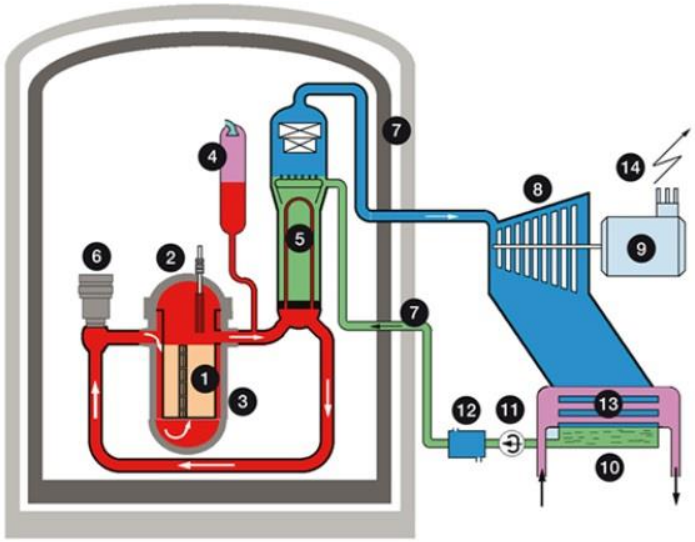

Figure 1.2. Schematic view of a PWR nuclear reactor [AREVA].

- At the turbine outlet, the steam is "sucked in" by the condenser (10), where it finishes cooling down sufficiently to be transformed back into liquid water. This water is then carried back to the SGs by the condensate extraction pumps (11), whereby the secondary circuit is closed.

- The turbine's mechanical energy drives the electric generator (9), which generates medium-voltage electrical energy.

- The electric current is fed to a transformer (14), where the voltage is raised for long-distance transport over the grid's high-voltage power lines.

- The cooling system (13) ensures the cooling of the secondary water in the condenser, with cool water taken from a nearby river or ocean. When the river's flow is not sufficient, cooling towers are added. The turbine's mechanical energy drives the generator (9), which generates medium-voltage electrical energy.

As a reference, in Table 1.1 are shown the design conditions of Vandellòs II NPP [Lozano, 2011]. It is a three looped PWR NPP of Westinghouse design, with has a nominal power of 1087 MWe (2940.6 MWt).

1.1.2.1. Steam Generators

PWRs of NPPs use indirect cycles to generate electricity. The thermal energy, generated by fission processes in the nuclear rector of the primary circuit, is transferred to the steam power cycle through Steam Generators (SGs).

Table 1.2. Steam Generator main features [Jimenez, 2012].

	Westinghouse F	Siemens/KWU Konvoi	Babcok & Wilcox 177	Mitsubishi 52FA
Heat Transfer Area (m^2)	4647	5427	12309.65	4870
Tube Pattern	Square w/T Slot	Triangular	Triangular	Square
Number of U-Tubes	4864	4118	15531	3382
Tube spacing (mm)	27.5	30.0	22.225	32.54
Tube Dimensions (mm)	19x1.1	22x1.23	15.875x0.863	22.23x1.27
Tube Material	Alloy 600	Alloy 800M	Alloy 600	Alloy 600
Tube Heat Treatment	Mill-Anneaded or Thermal Treated	ASTM SB 163	Mill-Anneaded	Thermally Treated
Tubesheet Expansion Method	Full Depth Rolled or Hydraulic	Full Depth Hydraulic Plus Parth Depth Rolled (both ends)	Partial Depth Rolled	Full Depth Hydraulic and One Step Rolled
Tubesheet Crevice Depth (mm)	None	None	558.8	None
Tube Support Type	Drilled	Eggerate	Broached Trefoil	Broached Eggerate
Tube Support Material	Carbon or Stainless Steel	Stainless Steel	Carbon or MnMo Steel	404 Stainless Steel
Preheater Type	Counterflow Expanded Preheater Tubes	None	None	None

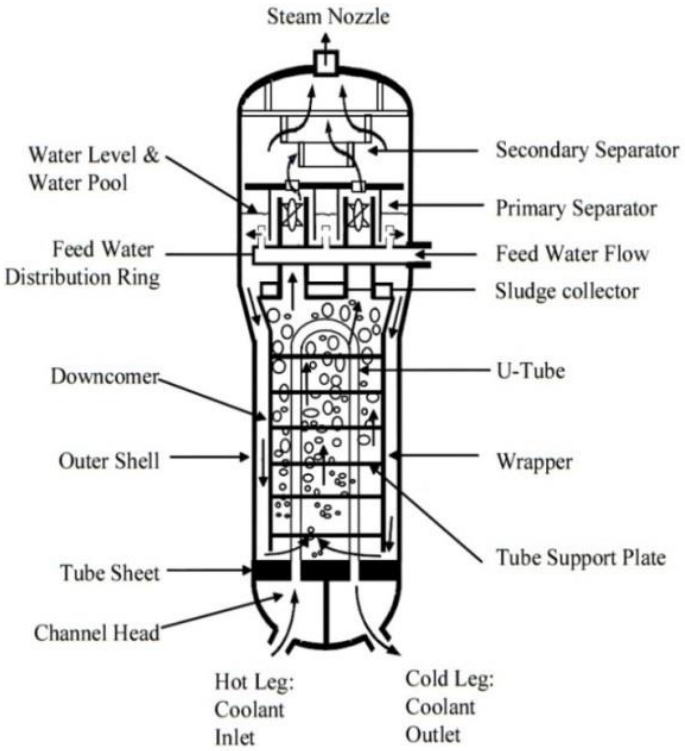

Figure 1.3. Schematic view of a typical Steam Generator.

The SGs of a PWR are boiling heat exchangers that use the reactor coolant water of the primary circuit, water at approximately 150 bars, as heat source to bring water of the secondary side into steam, water at a 70 bars approximately. These components perform the heat transfer from primary to secondary circuits and produce the steam needed in the turbine. The dimensions of SG's can reach more than 20 m high and 800 tons. Each SG has a great amount of cylindrical tubes, reaching to be above of 5000, they are usually made of INCONEL and are inverted U-shaped tubes with diameters around 1.5-2 cm. The U-shaped tubes are welded to a thick plate, tube sheet, in both ends (entrance of the hot water, exit of the cold water), place near the SG bottom. Figure 1.3 shows an outline views of a SG, while Table 1.2 show the general characteristics of two typical SG's.

A rough description of the operation of a SG is shown in the following lines. First, the primary coolant inventory enters the SG at the primary inlet nozzle, enters in the hot leg of the rod bundle, pass through the U-tubes and leave the SG through the cold leg. Regarding the secondary side of the SG's, the feedwater enters the side of the shell. The water flows down through the downcomer (annulus just inside the shell); in this area the feedwater mixes with the water coming from the separator. Then, the water enters the outside of the

U-tube bundle (heating surface). The water temperature raises, increasing the steam quality as ascends through the SG. Finally the steam-water mixture reaches the separators, so that the pure steam passes through the driers and then to the steam nozzle. While the rest of water is recirculated through the downcomer to the bottom of the SG.

1.2. Accidental Events in a Nuclear Power Plant

A nuclear accident can be defined as any unintended event, including operating errors, equipment failures or other mishaps, the consequences or potential consequences of which are not negligible from the point of view of protection or safety, these consequences can be significant to people, the environment and/or the facility [website IAEA]. While, severe accidents refer to events which causes damage to the reactor fuel, resulting in partial or total meltdown of the core.

1.2.1. Seriousness Scale of Nuclear and Radiological Events

The accidental events which can take place in a NPP are categorized in 8 levels according to the INES scale (International Nuclear and radiological Event Scale), Figure 1.4. This ranking is based on the degree of importance of the accidental event consequences [website IAEA; IAEA-INES, 2013]:

- Level 0, this level corresponds to a deviation from normal plant operation, without safety significance.

- Levels 1-3, these levels are qualified as nuclear incidents, with limited consequences. Level 1 refers only to degradation of the defence in depth. While levels 2 and 3 refer to a more serious degradation of the defence in depth or to low consequences to people or facilities.

- Levels 4-7, qualified as nuclear accidents. Refer to increasing levels of consequences to people, the environment or facilities. Only accidents of level 4 have not significant seriousness outside of the facility in which took place.

The INES scale is a tool for communicating to the general public in a consistent and organized way the importance of a nuclear or radiological event. The ranking is made in terms of the impact effects in three different areas: impact on people and the environment (for instance, the degree of exposure to radiation of workers or rest of people, release of radioactive materials to the environment, etc.); impact on radiological barriers and controls of facilities (for instance, the degree of melting or damage to the reactor core, fuel rods, containment, etc.); and impact on defence in depth (for instance, the degree of failures in the safety measures, inadequately packaging of highly radioactive sealed sources, etc.). A brief description of the impact in each in the three areas which considers the INES scale for each accident severity level is shown in Table 1.3. Further information is available in the report of the IAEA [IAEA-INES, 2013].

Table 1.3. Brief description of an accident impact in each of the INES levels.

INES Level	People & Environment	Radiological Barriers & Control	Defence-In-Depth
Major Accident Level 7	• Major release of radioactive material with widespread health and environmental effects requiring implementation of planned and extended countermeasures.		
Serious Accident Level 6	• Significant release of radioactive material likely to require implementation of planned countermeasures.		
Accident with Wider Consequences Level 5	• Limited release of radioactive material likely to require implementation of some planned countermeasures. • Several deaths from radiation.	• Severe damage to reactor core. • Release of large quantities of radioactive material within an installation with a high probability of significant public exposure. This could arise from a major criticality accident or fire.	
Accident with Local Consequences Level 4	• Minor release of radioactive material unlikely to result in implementation of planned countermeasures other than local food controls. • At least one death from radiation.	• Fuel melt or damage to fuel resulting in more than 0.1% release of core inventory. • Release of significant quantities of radioactive material within an installation with a high probability of significant public exposure.	
Serious Incident Level 3	• Exposure in excess of ten times the statutory annual limit for workers. • Non-lethal deterministic health effect (e.g., burns) from radiation.	• Exposure rates of more than 1 Sv/h in an operating area. • Severe contamination in an area not expected by design, with a low probability of significant public exposure.	• Near accident at a nuclear power plant with no safety provisions remaining. • Lost or stolen highly radioactive sealed source. • Misdelivered highly radioactive sealed source without adequate procedures in place to handle it.
Incident Level 2	• Exposure of a member of the public in excess of 10 mSv. • Exposure of a worker in excess of the statutory annual limits.	• Radiation levels in an operating area of more than 50 mSv/h. • Significant contamination within the facility into an area not expected by design.	• Significant failures in safety provisions but with no actual consequences. • Found highly radioactive sealed orphan source, device or transport package with safety provisions intact. • Inadequate packaging of a highly radioactive sealed source.
Anomaly Level 1			• Overexposure of a member of the public in excess of statutory annual limits. • Minor problems with safety components with significant defence-in-depth remaining. • Low activity lost or stolen radioactive source, device or transport package.
Deviation Level 0	**No Safety Significance**		

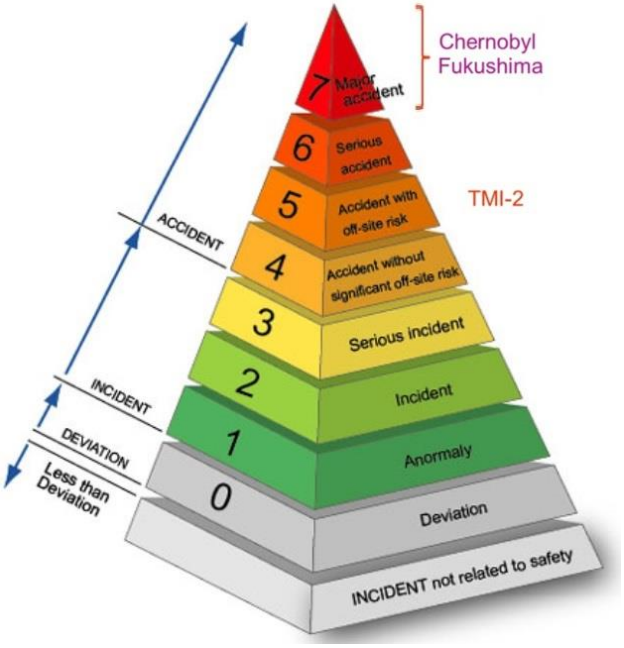

Figure 1.4. International Nuclear and radiological Event Scale (INES).

1.2.2. Severe Nuclear Accidents

As far as severe accidents or core melt accidents are concerned, say that in these kinds of accidents the fuel of the core reactor can be significantly damaged, having a more or less melting region in the reactor core. Usually, these accidents start with partial or total loss of the primary circuit cooling. Most of the times the accidental scenario is triggered by the combination of several factors, such as, natural disasters, human errors, equipment malfunction, etc. The loss of the primary cooling for a long period of time leads to the heat up of the core, followed by the uncovering of the fuel rods, caused by the boiling of the remaining coolant. Is common to divide the accident in three phases: early in-vessel (the main events that occur in this phase are: core uncover, metals oxidation, cladding deformation and failure, release of fission Products (FPs), melting of the core, reflooding of the damaged core), late in-vessel (the main events are: formation of the molten corium pool, discharge to of the corium to the lower head, potentially failure of the lower head) and ex-vessel (erosion of the reactor pit walls and basemat, which can lead to the loose of the containment integrity, release to the environment). The sequence of events that occurs in an accident does not take place in an ordinate way but in a simultaneous form and in several parts of the reactor vessel. Over the history several incidents or accidents took place in LWRs around the world, even though only three of them have had off-site consequences:

- The accident in the reactor 2 of the Three Mile Island plant (TMI-2), which occurred in USA in 1979 and was classified as level 5 in the INES scale. The facility consisted of two PWRs of 2568 MWth (786 MWe) and 2772 MWth (900 MWe) respectively. This accident started as a simple operation incident caused by a failure in the water supply of the secondary side of the Steam Generators (SGs), but due to operator mistakes and malfunction of safety devices led to a LOCA. FPs were maintained into the containment with reduced effect to the surrounding environment, but 45% of the reactor core was melted.

- The Chernobyl accident, which occurred in Ukraine in 1986 and was classified as level 7 in the INES scale. The plant consisted of four RBMK-1000 (Graphite-Moderated Boiling Water Reactor) with 3200 MWth (1000 MWe) each one of them. The accident occurred in the unit 4 during a test aimed to verifying the response of the reactor under an accident scenario. The test was performed without following the procedure, situation which leads to made wrong decisions. Because of the specific characteristics of RBMK reactors design, a RIA (Reactivity Induced Accident) accident took place, so that the reactor power rose to 100 times its nominal value, which leads to the disintegration of the fuel, the subsequent steam explosion which blow up the top of the reactor, ending with the instantaneous release of huge amounts of radioactive materials to the environment. The most severe accident which has took place in the history in terms of damage to the environment.

- The Fukushima Daiichi accident, which occurred in Japan in 2011 and was classified as level 7 in the INES scale too. The plant consisted of 6 BWR with a total capacity of 14.2 GWth (4.7 GWe distributed between Unit 1 with 460 MWe, Units 2 to 5 with 784 MWe each and Unit 6 with 1100 MWe), being one of the largest NPPs in the world. The cause was a natural disaster, a magnitude 9 earthquake in the Richter scale, which stopped the off-site power, triggering the shutdown of the reactors (only reactors 1 to 3 where in operation) and turned on the emergency power systems. But almost one hour later, a fifteen meters tsunami, which reached more than twice the predicted level, caused by the earthquake destroyed almost all the emergency energy generators, leading to a SBO (Station Black-Out). The environment consequences of the Fukushima Daiichi accident were very important, but not as important as the Chernobyl's.

1.2.3. Defence-In-Depth in Nuclear Power Plants

The concept of defence-in-depth was introduced in the early 70s and has been evolving from this moment on up to the present days; it refers to the protection of both public and workers in a nuclear installation. As far as NPP safety concerns, all technical and organizational measures taken in a NPP during all its lifetime phases (design, construction - commissioning, operation, decommissioning and dismantling) are aimed to ensure normal operation, to prevent incidents and accidents and to limit the consequences of possible incidents or accidents. All safety activities are constituted by several layers with overlapping provisions, so that if any failure occurs, there are other safety measures which

can compensate or correct the plant failure, without causing harm to individuals or to the public. This idea of the existence of multiple levels of protection is the key feature of the defence-in-depth concept.

The defence–in-depth consists of several protection levels, which includes successive barriers (first barrier: the fuel matrix; second barrier: the fuel cladding; third barrier the boundaries of the reactor coolant system; and fourth barrier: the reactor containment building) to prevent the release of radioactive materials to the surrounding environment. Nowadays the defence-in-depth concept comprises five levels, which might vary from one country to another or by the NPP design. Its major objective is to avoid the occurrence of any possible failure or malfunction in the NPP and, in case of occurring, to limit its consequences. In Figure 1.5 a schematic view of the defence-in-depth concepts, methods and means is shown, this comes from the INSAG-10 document [IAEA-INSAG-10, 1996]. The INSAG (International Nuclear Safety Group) is auspiced by the IAEA and is constituted by a group of experts with a high professional competence in the safety field working in regulatory, technical support, research, academic and nuclear industry organizations. Figure 1.5 shows the objectives and the means needed to achieve an effective implementation of the defence-in-depth in a NPP. The protection levels of the defence-in-depth, from 1 to 5, correspond to each of the concentric rectangles shown in the figure, i.e., from inside for level 1 to outside for level 5. In the upper part of each rectangle are represented the objectives, while in the lower part the essential means are presented.

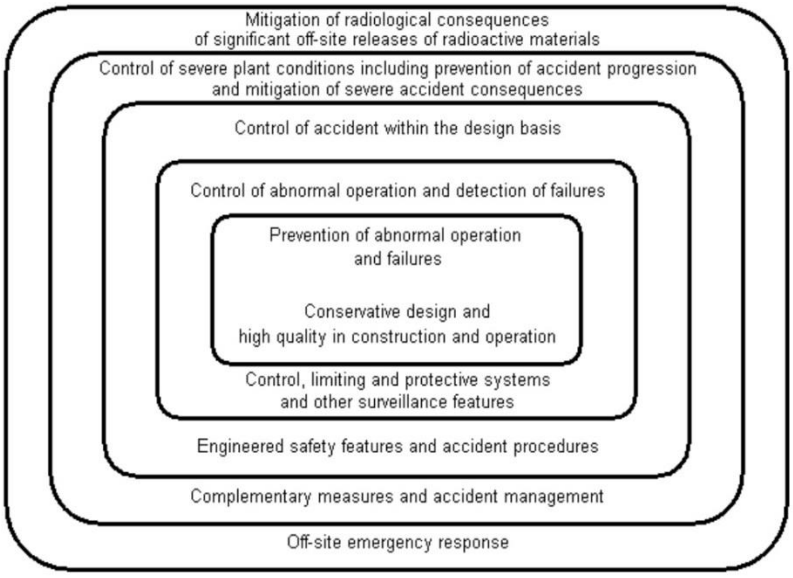

Figure 1.5. Schematic view of the five defence-in-depth implementation consistent with the INSAG-10 report.

To put into practice the concepts of the defence-in-depth a wide variety of specific measures have to be fulfilled in both the design and the operation phases of a NPP. In particular, the major measures that must be fulfilled are [IAEA-INSAG-10, 1996]:

- a deterministic design, which provides effective means to perform safety functions under normal-abnormal operating conditions and under accidental events.

- to carry out probabilistic studies, probabilistic safety assessment (PSA) is an effective mean to understand plant vulnerabilities, which includes complex situations caused by several equipment and/or human failures.

- several means to achieve operational safety. Such as: implementation of technical specifications and operating procedures (usually derived from the deterministic design, the probabilistic studies and the operating experience); training of plant personnel (human error is potentially one important factor in safety, human actions are crucial to safe operation, then safety culture of the plant staff is a key factor to ensure a reliable operation of the plant and to detect and prevent any anomaly at an initial stage); maintenance and surveillance (to prevent the degradation of the plant equipment is a basic objective, while an appropriate surveillance of the ancillary and support systems is another basic objective that must be fulfilled); management and safety culture (management of accident conditions and emergencies has to be periodically exercised, whereas safety culture is crucial in all areas related with the defence-in-depth and particularly in operational safety).

- the enhancement of safety, through operation experience (feedback helps to ensure and enhance safety under operational conditions and to prevent accidents) and analysis of the safety impact of plant modifications (any design changes have to be carefully reviewed and their implementation carefully planned in order to not have detrimental to safety).

- implementation of accident control, which includes specific procedures and staff training.

- management of severe accidents, the development of means to control severe accidents and/or to mitigate their consequences.

- emergency response, in both on-site and off-site emergency responses, has to be integrated with each other and with accident management.

- safety assessment and verification of the defence-in-depth. A systematic assessment of the implementation of the defence-in-depth throughout the lifetime of the plant has to be performed. This verification process uses two complementary methods, the deterministic and the probabilistic. In the deterministic approach some postulated events that can lead to challenges in safety of the plant are studied, during this study conservative assumptions are made during all the calculations steps in order to show that the response of the plant meet safety targets. While in the probabilistic approach,

some assumptions and data, as realistic as possible, are used as a tool to assess the completeness and balance of the efforts undertaken within defence-in-depth.

- the regulatory body, the major aim of the regulatory body is to check the observance of the safety objectives by its own independent review and technical assessment of the safety.

- international peer review processes, the defence-in-depth can be improved by the contribution of international experts under Conventions on Nuclear Safety.

The studies and development of the new subroutine into the SPARC90 code, carried out in the scope of this PhD work, are framed within the deterministic and probabilistic approaches focused on the assessment of NPPs Nuclear Safety when facing accidental scenarios.

1.3. Aerosol Transport-Capture in Reactor Accidents

The study of the key parameters of a hypothetical severe accident in a nuclear power plant includes the behavior of aerosols that may be released from the melted reactor core. These aerosols can be described as small airborne particles and, when released from a reactor core, they are highly radioactive. Initially they are enclosed in the primary circuit or in the containment and they will deposit within a time scale which depends on their size distribution and on the geometry of the compartment. Other important parameters are the thermal-hydraulic and chemical conditions. Aerosol particles are produced in the molten core as long as the core debris has a sufficiently high temperature and/or if mechanical effects cause their resuspension and/or if the deposited particles are re-evaporated due to a high surface temperature. The aerosols which do not deposit can eventually leak into the environment and cause radioactive contamination.

Aerosols are mainly produced in the primary circuit, as this region has the highest temperature. Radioactive aerosols are not only produced in the reactor vessel, but also in the cooling system. Their production starts at much lower temperatures than the melting point of the fuel. The melting fuel will vaporize, producing fission products among other constituents.

The size distributions of these radioactive particles are strongly dependent on their concentration and thermal-hydraulic conditions. The average size can range from submicron to several tens of micrometers or even more. The smaller the aerosol size the greater the chance to agglomerate, quickly reaching the micron sizes.

The aerosols are transported from the melting core to other regions in the primary circuit or to the containment. If the gas velocities are high, deposition is enhanced by impaction, particularly in bends and on rough surfaces. The most important cause for deposition processes is the gravitational force, which causes settling on horizontal surfaces, these deposited particles stick to each other and to the surface by molecular forces. If

resuspension processes take place, the average particle size will be larger than for the original particles and, consequently, the deposition rate is improved. Other mechanisms to remove aerosols can also be the use of water sprays and by driving the aerosols through a water pool, for example the suppression pool in a BWR, or the wet secondary side in a Steam Generator Tube Rupture (SGTR) event in a PWR. These systems are the most efficient ones to eliminate radioactive aerosols.

The probability and importance of accident consequences are strongly dependent on plant design. There are several accident sequences in both, BWRs and PWRs plants that might produce with a release of fission products to the environment. Aerosols escaped from the reactor core can be carried by a gas stream through the primary circuit in several accident scenarios. In the case of PWRs, since the pressure in the primary circuit is higher than that of the secondary circuit, any leakage or rupture of the SG U-tubing can result in the release of radioactive aerosols to the environment. Whereas for BWRs, any accidental sequence with loss of coolant from the primary circuit and leakage or opening of the safety relief valve in the containment may result in aerosol release to the surrounding environment. These aerosols released from the core can be removed, as explained in the previous section, by the discharge into a liquid volume, this process is usually called scrubbing. In a hypothetical severe accident in a LWR, particle fission products may escape from the core and be transported through the primary system and finally may be released to the surrounding environment. If a water pool exists in the aerosol pathway, either a suppression pool or secondary side of a SG, the aerosol retention will be enhanced. Although pool scrubbing has been traditionally associated with fission product retention, mainly in suppression pools of BWR during SBO's events, Figure 1.6 (a). There also exits a number of potential scenarios in PWR, in which fission product trapping in aqueous ponds may play a key role in the attenuation of source term. This is the case of SGTR core meltdown sequences Figure 1.6 (b).

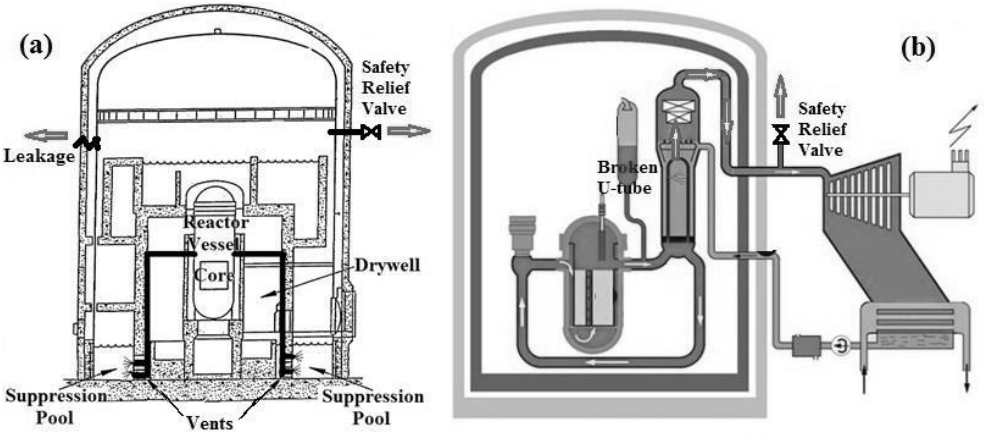

Figure 1.6. Pathway of the fission products from the core to the environment: (a) BWR; (b) PWR.

1.3.1. Pool Scrubbing

Pool scrubbing or wet scrubbing is the removal process of aerosol particles, usually when they are carried by the rising gas bubbles in a quiescent liquid pool. In these situations, the pool thus acts as a filter. Pool scrubbing has its fundamental applications in the chemical industry (gas cleaning) and in the nuclear industry.

In the case of nuclear industry, pool scrubbing is important during the so-called severe accidents, which are likely to result in the release of fission product aerosols from the damaged core into the containment atmosphere or into the secondary piping system. These discharge events can take place in quench tanks of a PWR or in the suppression pool of a BWR, under such circumstances large quantities of radioactive materials released from the fuel rods are discharged through safety relief valves. These fission products transport paths usually include passage through stagnant pools of water. In most cases, pools are the last barrier before radioactivity release into the environment. The gas emerging from the pool is cleaner than that entering it.

Various fundamental processes, of highly complexity, take place during aerosol pool scrubbing: inertial impaction and interception in the vicinity of gas injection, Brownian diffusion, thermophoresis, diffusiophoresis, gravity settling, centrifugal deposition and diffusion during bubbles rise, etcetera [Allelein, 2009]. To study this aerosol capture mechanisms particular attention has to be given to aerosol characteristics and gas hydrodynamics. Aerosol characteristics (i.e., composition, size distribution, hygroscopicity, etcetera.) are key factors for the effectiveness of these removal processes. Gas hydrodynamics plays an essential role determining key variables for pool scrubbing such as injection mode (jet or globule) and his evolution downstream. In addition, there are other parameters that can heavily influence individual pool scrubbing processes, like pool depth and water sub-cooling, carrier gas composition, temperature and velocity, etcetera. Therefore, in order to determine this decontamination capacity, an accurate knowledge of the pool scrubbing phenomenon is of vital importance.

1.3.2. Steam Generators Tube Rupture Accident Scenarios

Steam generator tube rupture events (SGTRs) are considered to be one of the design basis accidents (DBA) of PWRs. Consequently, NPPs are designed to cope with this kind of accidents with no major consequences, i.e. assuring public health and safety.

SGTRs can be divided in two groups, the spontaneous and the induced U-tube ruptures. First group is the rupture of a SG U-tube or more caused by any intrinsic problem of the component, i.e. damage is not caused by an external event or alteration of the expected operational plant parameters. Whereas the induced rupture is caused by an external event or accidental sequence in the rest of the NPP.

The triggering element for SGTR accidents can be a major leak or the rupture of one or several SG tubes, or a break in the secondary line, either in the feed water or steam lines. These secondary line break events lead to the quasi-immediate rupture of one or several SG tubes.

As it has been presented in previous sections SGs are key elements for the overall performance of a NPP, they play an important role in safety because of their boundary function between primary and secondary circuits. Their reliability and performance are in serious concern in the operation of PWRs. The integrity of the U-tubes of a SG may be challenged because of the high temperature and pressure conditions of the primary circuit. Consequently the U-tubes are subjected to a great variety of degradation processes (primary water stress corrosion cracking, outside diameter stress corrosion cracking, fretting, pitting, denting, high-cycle fatigue, wastage, etcetera) that can lead to tubes fissure, wall thinning, and potential leakage or finally rupture [MacDonald, 1996]. During the last years considerable efforts have been spent to understand and predict these degradation processes; however SGs steam leakage incidents have continued taken place. When a SGTR event occurs during a severe accident, radionuclides may leak from primary to secondary circuit and eventually bypass the containment. According to several Probabilistic Safety Assessment (PSA) studies, a relevant fraction of fission products are assumed to flow through a not-isolated broken tube of a SG. This assumption is based on an expert elicitation panel, since no experimental data of this phenomenon is available to verify it.

The SGTR events are not always the cause of the incident-accident, on other occasions SG tubes rupture will be the consequence of a severe accident [US NRC, 1990; Liao, 2009]. Regarding to SGTR, this scenario is a concern because the increase in the secondary circuit pressure can lead to relief valves to fail. Due to the fact that SG tubes are part of the PWR reactor coolant pressure boundaries, this situation may cause to fission products bypassing the containment, resulting in an open pathway to the surrounding environment.

The aerosol phenomenology involved during SGTR sequences is wide and complex due to the wide range of components and boundary conditions existent. The main processes governing aerosol removal when the secondary side is empty are slightly simpler than in the case of wet conditions (i.e., submerged tube breaches). Although for accident management purposes, water injection in dry SGs secondary side may be an option in order to re-establish heat removal and provide a pool where the incoming aerosols can be scrubbed. Consequently, in all cases retention processes in wet condition would take place. Modeling of aerosol retention in wet scenarios has resulted to be extremely complex. On one side, particle-laden gas is anticipated to reach the SG at very high velocities resulting in the formation of a submerged jet when entering the secondary side. On the other, all the tubes in the secondary side will presumably affect gas hydrodynamics. These two effects on gas behavior will strongly influence in-pool particle trapping.

As a result of the previously SGTR events explanations, the potential retention capability within the secondary side of a broken SG is an important aspect that has to be taken into consideration. This retention capability is seen as one of the largest uncertainties in the analyses reported in several SG failure reports, for instance NUREG-1150 [US NRC, 1990]. In this document little retention of radionuclides is considered to occur in both, the reactor coolant piping and the failed steam generator, being the overall transmission factor to the environment higher than 75% for all radionuclides considered. Consistently with

these affirmations, and given the lack of complete databases or specific models for the determination of retention capability in the secondary side of a broken SG, Probabilistic Risk Assessments (PRA) usually give no contribution to particle decontamination within the secondary side of a SG [Güntay, 2001; US NRC, 1990]. However, the geometry of SGs (adjacent tube bundle, support plates, separators, dryers, etcetera) provide large surface areas on which fission products may be trapped, added to these surfaces, the presence of water probably will produce a further augment in the radionuclide retention. In this sense, during the last decade EU-SGTR, ARTIST and ARTIST II investigation projects (Aerosol Trapping in a Steam Generator) have experimentally demonstrated that some retention should be expected within the SG [Güntay, 2004; Dehbi, 2008; Lind 2010a; Lind, 2011].

Under such circumstances, the major concerns for SGTR events are a possible release of contaminated aerosols to the atmosphere. In this sense, a direct pathway from the reactor vessel to the surrounding environment can be opened, so that radioactive aerosols are able to bypass the reactor containment and the safety systems of the NPP. Consequently, if these safety systems measures fail, only natural aerosol capture processes can mitigate the effects of such accidents. Therefore it is very important to have a thorough knowledge of all these capture phenomena and, additionally, the ones associated with the way in which discharge processes occur when a SGTR occurs. In this sense, this thesis is a theoretical contribution to the technical knowledge, understanding and quantification of these natural processes of mitigation of the consequences produced by SGTR accidents. This work is focused on the study of discharge processes from the primary to the secondary side of a Steam Generator (SG) and in his aerosol retention capabilities.

1.3.2.1. Degradation problems in the U-tubes

As explained in detail in NUREG/CR-6365 [MacDonald, 1996], in the 90s about one-half of the PWR NPP in the world had to plug or sleeve SG tubes in any given year. This means that about one-half of these plants were operating with tubing defects near or beyond the national limits boundaries. Only 7-10% of the plants did not reported problems leading to plug or sleeve of SG tubes after 5 years of operation. In Table 1.4 are listed the NPP that reported problems in the U-tubes of the SG's in 1977, 1982 and 1994. Up to ten SG tubing rupture events and other seven in an incipient rupture phase are discussed by MacDonald, all of them took place in US. Although it is true that in all cases the NPP were able to deal with the accident without major consequences, it is nonetheless true that the possibility of a severe accident has been present. Despite being highly unlikely a SGTR accident carries a significant risk, due to the potential for radionuclides to escape from the reactor containment, although this tube breaking event must be coupled with a broken in the barriers of the secondary circuit.

The major problems that took place in the life time of SGs are listed in Table 1.4, a schematic view is displayed in Figure 1.7 and a short description of each one of them is explained in the following lines [MacDonald, 1996; Newberry, 2000]:

- Denting is a mechanical deformation or a constriction of a carbon steel tube, it can takes place at a support plate intersection or within the tubular plate, and it can be

caused by the accumulation of deposits and the growth of bulky corrosion products in the annulus between the tube and its tube sheet or plate. This kind of problems has also been observed in the sludge pile region of certain plants where iron particles were embedded in the sludge pile.

- Wastage, this term refers to a relatively uniform corrosion and thinning of the surface of SG U-tubes. Wastage degradation usually takes place in regions with the fluid under fairly stagnant conditions and with relatively high concentrations of phosphate.

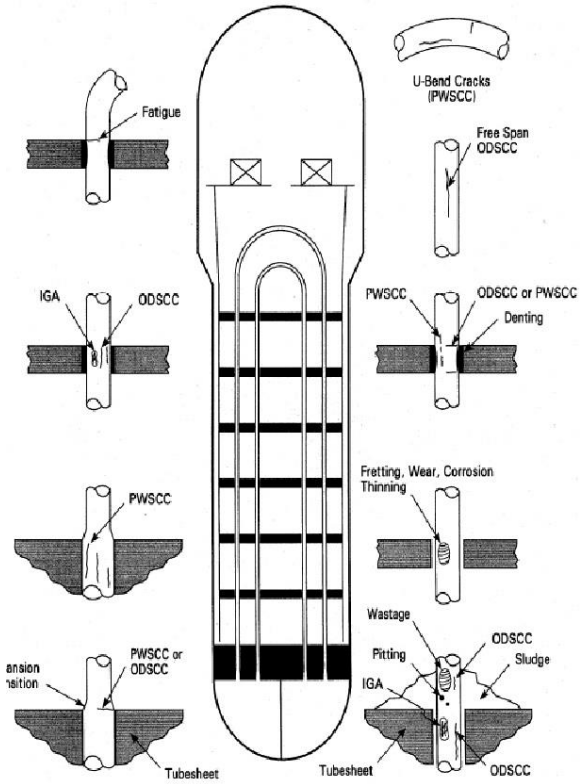

Figure 1.7. Major degradation mechanisms of a SG in a PWR [Newberry, 2000].

- Pitting, this degradation process consists of groups of small diameter wall penetrations, which are caused probably by the presence of sulfate or chloride acids. These acidic impurities come from condenser leaks, leakage of beads, resin fines, or regeneration chemicals from ion exchangers.

- Primary Water Stress Corrosion Cracking (PWSCC), this type of corrosion of austenitic alloys is an inter-granular cracking mechanism. The PWSCC mechanism

needs three conditions: high applied or residual tensile stress; a corrosive environment (high temperature water); and susceptible material, i.e. is strongly dependent on nickel and chromium content of the material. The corrosion is favored by the presence of chloride ions, but only in certain alloys. For instance, Alloy 600 is susceptible of PWSCC, but Alloy 690 and 800M are not so susceptible to PWSCC.

- Outside Diameter Stress Corrosion Cracking (ODSCC), this corrosion mechanism includes Inter-Granular Stress corrosion Cracking (IGSCC) and Inter-Granular Attack (IGA). IGSCC requires of the same three conditions of the PWSCC mechanism, but in this case, the corrosive environment has to consist not only of water but aggressive chemicals too. IGSCC is strongly dependent on the corrosive impurity concentrations, these impurities come from the feed water (corrosion of heat exchanger piping and/or equipment, condensate polisher leakage, condenser in-leakage, etc.). The impurities concentrate over the time mainly in the tube sheet and tube support plate crevices, or in the sludge pile. IGA is similar to IGSCC but can occur with smaller tensile stresses.

Table 1.4. PWR and CANDU units reporting SG's degradation problems [MacDonald, 1996].

Date	3/77	8/82	12/94
NO. Units	52	99	240
Reported Problems			
Denting			
- Tube Support Corrosion	15	30	37
- Tube sheet Corrosion	6	12	49
Tubing Corrosion			
- Wastage	19	28	30
- Pitting	0	3	21
- Inner Diameter Cracking	1	22	103
- Outside Diameter SCC/IGA	6	22	87
Mechanical Damage			
- Fretting	9	15	131
- Fatigue Cracking	3	4	16
- Impingement	0	2	8
No Problems	26	32	56
No Problem after ≥ 5 years of operation	1/14	4/57	28/217

- Fretting, Wear and Thinning, these corrosion mechanisms are mainly caused by the flow induced vibration, from both cross and parallel flows. Initiation, growth and stability of these damage mechanisms are influenced by a large number of variables, for instance, position of the tube support, gap size between supports and tubes, stiffness of the supports and tubes, oxide layer characteristics, secondary flow velocities and directions, etc. Regarding the differences among the three corrosion mechanisms: The term fretting is used to designate the degradation caused by the oscillatory motion of small amplitude between surfaces in continuous friction; Sliding wear or simply wear is a relatively large amplitude vibrational movement which leads to an intermittent sliding contact between tubes and support; and Thinning refers to the concurrent effects of vibration and corrosion.

- High-Cycle Fatigue, this damage mechanism takes place in SGs with high recirculation factors and with inappropriate design of the AntiVibrations Bars (AVBs) supports. This mechanism conducts to flow induced vibrations in the U-bend region.

1.4. Submerged Gaseous Jets

During the above described SGTR sequences, the radionuclides are discharged at very high velocities into the SG secondary side, consequently, submerged gaseous jets must be studied in depth. But submerged gaseous jets not only has a relevant importance in SGTR events, it may have an outstanding relevance in many industrial processes, even though are particularly relevant in severe nuclear accident scenarios, like the one happened at the Fukushima Daiichi NPP several years ago, which is a Boiling Water Reactor (BWR) type. Although pool scrubbing has been traditionally associated with fission product retention in suppression pools of BWRs, in which lower injection velocities exist. Then, there are a number of potential scenarios in BWR and even in PWR reactors, in which fission product trapping in aqueous ponds may play a key role in the attenuation of source term [Allelein, 2009]. This is the case of SGTR core meltdown sequences, these accidents lead in that a direct pathway from the reactor vessel to the environment might be set through the broken tubes, so that radioactive material bypass reactor containment and other engineering safety features. However, when fission products escaping the damaged fuel reach the steam generator, the secondary side might contain water. Whether water level is over the tubes break, a fraction of the incoming material might be absorbed by her.

The submerged gaseous jet forms a complex multiphase system which is important in several industrial areas not only nuclear sector. Therefore, the understanding of the mechanisms of the entrainment of the surrounding water into the gaseous jet and the generation of droplets, in addition to the prediction of the droplet size distributions, are prerequisite in order to accurately model and predict the capture capabilities of the secondary side of a SG. Several works have been carried out in the last decades concerning some aspects related to submerged gaseous jets. For void fraction measurements of the entrained water droplets into submerged gas jets, Loth and Faeth [Loth, 1989; Loth 1990] measured the local void fraction distribution and static pressure distribution of

underexpanded jets submerged in water. Someya et al. [Someya, 2011] investigated the spread angle and entrained droplet velocities of submerged gaseous jets and the velocity distribution of ambient water using their own visualization method. For diameter determination of entrained water droplets, several authors proposed empirical expressions which correlate droplets sizes with dimensionless numbers, even though all these correlations has been developed under aerodynamic break-up conditions ("free" droplets suddenly exposed to a high speed gas stream) or in annular flow (thin liquid film flowing on the pipe wall and a high velocity gas core flowing in its center, which carries the entrained liquid droplets). Following this path of annular flow correlations, many of the variables that concern submerged gaseous jets can be estimated, for instance, the ones related with gas-liquid interface (wave celerity and frequency, onset of entrainment and inception velocity, etcetera), the entrained droplets key parameters (entrained fraction, size distribution, velocity, etcetera). All these issues will be developed in detail throughout the next sections.

1.5. The SPARC90 code

For all these reasons, over the last decades several international projects have investigated different aspects of source term under anticipated SGTR core melt condition [Güntay, 2004]. In addition, to set up a sound database on aerosol retention, deep insights into aerosol behavior have been gained and, as a result, semi-empiric models have been developed. Several specific codes for pool scrubbing were developed in the late 80s and early 90s, such are SPARC90 [Owczarski, 1991], BUSCA [Ramsdale, 1991] and SUPRA [Wassel, 1985]. All of them modeled gas injection under the "globule regime", so that gas-liquid interactions under jet injection regime are missing. More recently, studies concentrated under jet injection regime, but under dry conditions (i.e., no water in the secondary side of the SG) [Herranz, 2012; Lopez, 2012] have been developed.

The SPARC90 code was developed to determine the aerosol pool trapping during vent discharge processes, but only for low gas velocities. However, there are accident sequences, like SGTR core meltdown sequences, at which particle laden gases reach the aqueous ponds at very high velocities and new particle removal mechanisms become effective right at the nozzle or break inlet. This work outlines the fundamentals, major hypotheses and changes introduced into the code in order to estimate particle removal during gas injection in pools under jet regime. To do so, a simplified and reliable approach to submerged jet hydrodynamics has been intended to describe both the gas-liquid and the drop-particles interactions. This paper summarizes this update process of the SPARC90 code to capture the phenomena which take place under high velocity injection conditions (SPARC-Jet), it is based on the state-of-the–art equations for jet hydrodynamics and aerosol removal (remind that the old version of the SPARC90 code was only developed for the study of discharges with low velocity injection regimes).

1.6. Thesis Motivation and Objectives

The motivation of the present PhD work arose from lacks of knowledge when the radioactive aerosol filtering capabilities of aqueous ponds of NPPs under accidental sequences are estimated. This aerosol source term attenuation has to be taken into account either in the safety studies of probabilistic risk assessment and/or when developing severe accident management guidelines. In particular this work comes from the need of determination of the potential radioactive aerosol retention capability of aqueous ponds during accidental sequences in NPPs, i.e., mainly a SGTR sequence in PWRs and in the suppression pool discharges in a SBO event in BWRs. Consequently, the main motivation of this thesis is to provide a predictive tool capable to determinate the retention capacity of radioactive materials by stagnant water with a good accuracy.

As mentioned in the previous paragraph, this scenario can takes place mainly under two accidental events, i.e., SGTR in PWRs and SBO in BWRs. SGTR events, in which the high speed jet discharges from the primary to the secondary circuit, take place through the broken tubes of SGs, i.e., the radioactive materials escape through one or several breaks in the inverted U-tubes. The second possible scenarios are steam discharges generated by the core of a BWR in suppression pools during a SBO sequence. To fulfill this major objective, an enhancement of the SPARC90 code has been carried out, which originally only was able to estimate events with globular discharges. This thesis summarizes the SPARC90 code extension to jet injection regime (SPARC90-Jet code).

In order to achieve this primary and major objective, i.e., estimation of the retention capacity of radioactive materials when discharged in stagnant water pools, a sequence of specific objectives has been fulfilled:

- Jet hydrodynamics characterization. All major phenomena and key variables that affect the submerged discharges have to be studied and taken into account. The in depth description of the jet hydrodynamics has been accomplish through an in extensively search in the open literature of the phenomena involved in pool discharge processes. In several aspects of jet hydrodynamics, due to the lack of information specifically developed for submerged jets, a study of alternative approaches has been carried out. In particular, the available information, which originally was developed for annular flows, has been used for the study of several phenomena involved in the jet discharges processes.

- Aerosols capture mechanisms. The retention phenomena associated with aerosol particles carried by gaseous streams has to be studied. Accomplish through an in depth search of aerosol retention mechanisms in the open literature. As in the previous point, due to the lack of information specifically developed for submerged jets, a study of alternative approaches has been carried out, in particular, wet scrubber studies have been used.

- Adaptation/development of expressions/correlations for submerged jets. As a consequence of the two previous points, several expressions of annular flows and wet scrubbers have been adapted to the particular conditions of submerged jets. Additionally, in some particular cases of special importance, as in the characterization of the entrained

droplet velocities in submerged jets, experimental work have been carried out in the frame of this PhD.

- Build up a platform capable of determine/estimate the aerosol retention capability under high velocity discharges scenarios. Through the implementation of new subroutines into the original SPARC90 code, i.e., the original code is only able to study discharges at low velocities and the new code preserve this capability, while the SPARC90-Jet code is also able to carry out with the calculations of high velocity discharges.

- Validation of the robustness of the new SPARC90-Jet code. The capability to provide results and that they are reasonable has been assessed with a process of verification. This verification process has demonstrated its robustness and stable behavior under lots of different discharge conditions, providing reasonable results.

- Validation of the SPARC90-Jet performance, which has been carried out through modeling conditions of pool scrubbing experimental scenarios. After having a robust code, the next step is to assess its capabilities against experimental data, to do so, the experimental cases found in the open literature that meet the jet discharge conditions have been used. This tests have been reproduced with the code and, finally, they have been compared with the experimental data.

In summary, the most important objective is to estimate the retention capabilities of aqueous ponds when high speed gaseous discharges, carrying aerosols, take place. To fulfill this final objective two major previous objectives must be achieved, on the one hand, the determination of the jet hydrodynamics and, on the other hand, the estimation of the aerosol capture processes which take place inside the jet.

With the ultimate aim to manage with the all these previously presented objectives the PhD report has been arranged in the following main parts:

Chapter 1: along current lines a contextualization of the PhD thesis is shown.

Chapter 2: the study of the key variables of annular flows related with the gas-liquid interface properties has been accomplished. An extensive review of the available gas-liquid interface information together with collection and analysis of experimental data found in the open literature for key variables has been made. Giving, as a result, the development of new correlations for these key variables carried out throughout this thesis. The entrainment process has been also studied in this chapter, analyzing the onset of entrainment and the entrainment inception velocity, point under which no entrainment can takes place.

Chapter 3: description of the most important variables with the aim of characterize the entrained droplets, in particular their sizes, velocities and total amount. Together with this variable description, the collection and analysis of experimental data found in the open literature for key variables defining the entrained droplets has been carried out. Giving, as a result, the development of new correlations for these key variables conducted throughout this thesis.

Chapter 4: aspects related to hydrodynamics of submerged jets are shown. Due to the lack of knowledge related to many of those aspects, the way as these key concepts have been adapted is displayed.

Chapter 5: the fission products and heavy nucleus inventory and characteristics in a LWR, for both normal operation and under an accidental sequence, are studied. Those particles are the precursors of radioactive aerosols. Followed by the description of aerosol formation and growth mechanisms during a nuclear accident have been studied. Finally the aerosol size distribution function is shown.

Chapter 6: the aerosol collection mechanisms have been studied. Due to the lack of aerosol collection expressions specifically developed to submerged jets the majority come from wet scrubbers. The calculation of the aerosols capture efficiency, which is determined from the Decontamination Factor (DF), is also shown.

Chapter 7: focuses on the SPARC90 code. A short description of the code, originally designed to discharge processes at low velocities, is shown. Next, the organization and development of the new subroutines, to study injections at high velocities, is displayed.

Chapter 8: concentrates on the code results related with the jet hydrodynamics.

Chapter 9: concentrates on the code results related with the capture processes. The theoretical results offered by the SPARC90-Jet code have been compared with four experimental programs (ACE, LACE, POSEIDON and RCA).

Chapter 10: the final remarks and further works related with this PhD thesis are shown.

Chapter 2

INTERFACIAL WAVES AND ONSET OF ENTRAINMENT IN ANNULAR FLOW

2. APPROACH TO THE CHARACTERIZATION OF SUBMERGED GASEOUS JETS I: INTERFACIAL WAVES AND ONSET OF ENTRAINMENT IN ANNULAR FLOW

Due to the complexity of submerged gaseous jets there are a limited number of expressions to characterize this type of injections. For this reason, a preliminary study has been carried out, trying to find those types of flows with similar characteristics to those found in a submerged gaseous jet. Leading to the conclusion that the annular flow is the one that most approximates the desired conditions. The fruit of this literature search are presented below, focusing on what concerning the characterization of interface waves and in the determination of the inception point on which entrainment begins.

This chapter has been published in Progress in Nuclear Energy, Vol. 74, pp. 14-43, 2014 [Berna, 2014].

Abstract

Annular two-phase flow has been vastly investigated because of its large and deep involvement in industrial processes, particularly in nuclear engineering. This paper reviews most of the recent literature on the matter, with emphasis in all those variables and processes occurring in the liquid-gas interface that cause droplet entrainment. Further than presenting correlations, the paper shows the existing scattering found when expressions are compared to each other and it highlights the gaps of knowledge still existing. Additionally, based on some of the open data, alternate equations are derived for key variables in the annular flow descriptions, like liquid film thickness and wave celerity and frequency.

2.1. Introduction

Two-phase gas-liquid flows are widely encountered in many different industrial applications: petroleum, chemical, civil and nuclear industries, and particularly in boiling and condensing heat transfer equipment. Nuclear power plants involve two-phase flow. In pressurized water reactors (PWRs) two-phase flow is especially encountered in the steam generators and in the upper-core components during normal operation and in the reactor itself during off-normal conditions, including accident sequences. In boiling water reactors (BWRs) the two-phase flow occurs in the core during normal operation. In all these processes two-phase flows play an important role in their operation, safety and cost, that is why, a proper understanding of their behavior is particularly interesting. Consequently, a large number of publications have been performed focusing on the study of multiphase flow research, in particular its investigation began in the 40s and continues until present time.

Two-phase flows in pipes can be grouped into classes, commonly called flow regimes or flow patterns. The wide variety of classifications that exist in the literature are mainly

due to the subjective nature of the characterization method, and as a general reference maps for vertical and horizontal flow are presented in Figure 2.1.

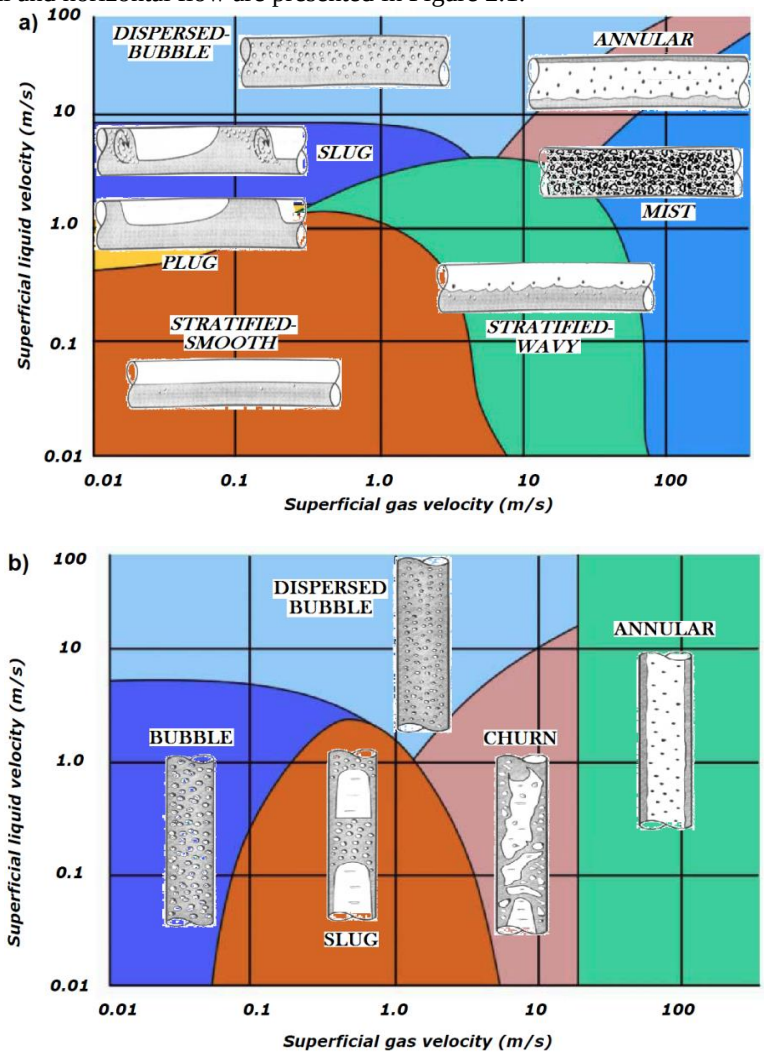

Figure 2.1. Flow maps for two-phase gas–liquid flow: a) horizontal pipes; b) vertical pipes.

In particular, the annular flow pattern can be found in many important industrial applications. For instance, in the evaporators and condensers of conventional power generating plants; in pressurized water reactors of nuclear power plants during a LOCA (Loss Of Coolant Accident) and in boiling water reactors during normal operation; in geothermal and gas-oil wells, etcetera. As a result, the ability to understand and model

annular two-phase flow is a subject of central importance to achieve a reliable design of this equipment.

Annular flow is normally characterized by: a gas core flowing through the center of the tube; a part of the liquid, as a thin film, flowing on the tube wall; while the other part flows as entrained liquid droplets in the gas core. For horizontal pipes, at the beginning of the transition from stratified wavy to annular flow, only the gas core (without entrained droplets) and the thin liquid film exist. As the difference in velocity between gas and liquid phases increases, a series of waves begin to appear on the gas-liquid interface. When this difference is high enough, a flow rate of droplets is entrained from the liquid film surface into the core of the gas stream. The point in which this entrainment phenomenon starts is called "onset of entrainment" and its associated velocity is the entrainment inception velocity. These entrained droplets contribute significantly to heat and mass transfer, and the modeling of the gas-liquid interface properties, droplets extraction mechanisms and droplets itself are of high practical interest. The contact area between the liquid film and the gas, gas-liquid interface, is covered with waves, and the water droplets are extracted from the crest of these waves and are then transported into the gas core by the high velocity gas stream.

This review presents and analyzes most of the extensive literature that exists on annular two-phase flow. In particular, the paper focuses on the study of the liquid film layer and the gas-liquid interface, presenting its main characteristics and analyzing the process of droplet extraction from this liquid phase to the gas phase (the entrainment process). The aim of this article is, firstly, to reveal the dispersion in the abundant information available, collecting them insofar as possible and, moreover, presenting the lacks of knowledge that still exist in annular flow. Secondly, its interest is to have on hand in the same document a summary of the various expressions found in the literature. And finally, several analysis of the different experimental values found in the open literature have been made, presenting a new set of correlations for its adjustment.

In this work, we will focus on the study of the liquid film properties, gas-liquid interface and the mechanisms governing these water droplets extraction processes. To do so, this paper is organized as follows:

- First, in section 2.2, we present a summary of the main characteristics of the waves that are present on the gas-liquid interface.

- Section 2.3 is devoted to present the onset of entrainment process.

- Section 2.4 focuses on the entrainment inception velocity.

- Section 2.5, in which the comparison of the experimental measurements, the results obtained with the different expressions available in the literature and the developed in the present work are presented.

- Finally, section 2.6 settles the main conclusions from this study.

2.2. Waves on the Annular Flow

2.2.1. General Description

It is generally assumed that two different types of waves can exist on the liquid film surface: long-length disturbance waves (DW), with amplitude several times higher than the average liquid film thickness, and small-scaled ripple waves (RW), Figure 2.2. Then, for the physical modeling of the entrainment phenomenon, detailed information on the origin of these two types of waves is needed. Respect to RW, they are considered to be omnipresent on the film surface in the presence of a turbulent gas stream, even for very low liquid film Reynolds numbers. Regarding the DW, they appear when the liquid flow rate grows, and, consequently, the entrainment occurs.

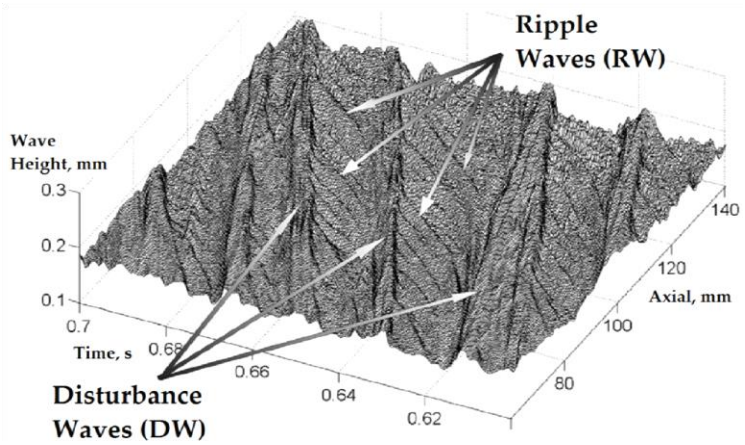

Figure 2.2. Three-dimensional representation of wave height, axial component and time evolution in the entrainment regime.

Hundreds of interfacial wave behavior studies have been carried out by different authors in both vertical and horizontal flows. All of them refer to the existence of two types of waves, the first one have small amplitudes compared with the liquid film thickness, move at low velocities, their lifetime is short, they usually do not occupy the whole tube circumference and do not appear to carry mass [Hewitt and Govan, 1990; Schubring, 2008; Alekseenko 2008 & 2009]. The second type of waves have a longer lifespan, their amplitudes are usually several times the liquid film thickness and carry mass along the tube [Hanratty and Hershman, 1961; Asali and Hanratty, 1993; Schubring, 2008; Alekseenko 2008 & 2009]. For vertical tubes, in the order of 6 cm or smaller, the liquid film is uniformly distributed around the tube circumference [Asali, 1985], and the disturbance waves appear circumferentially coherent [Hall-Taylor, 1963; Hewitt and Lovegrove, 1969; Asali and Hanratty, 1993] and symmetrical [Hewitt and Hall-Taylor, 1970; Ohba and Nagae, 1993]. The work made by Martin [Martin, 1983] shows that waves are highly

regular in tubes with an inner diameter of 1 cm. The disturbance waves present a long region of relatively quiet fluid between crests [Wallis, 1969]. Sekoguchi et al. [Sekoguchi, 1985] presented images of disturbance waves, which were directly based on their measurements in vertical annular flow in a 25.8-mm tube. Zhu's physical wave model [Zhu, 2004] provides similar wave profiles based on the measurement data of MacGillivray [MacGillivray, 2004] in vertical annular flow in a 9.525 mm tube. An important aspect to emphasize is the fact that, in vertical annular flow, all its properties tend to be distributed uniformly around the pipe circumference. But in the case of horizontal annular flow, there is a highly asymmetric distribution of all its properties due to the gravity force. For instance, as it is shown by the work in horizontal flow conditions of Paras and Karabelas [Paras, 1991] for low gas flow rates (gas velocities lower than 40-50 m/s approximately) and for all liquid rates tested, all the film properties are highly asymmetric; but as the gas flow rate increases, all its properties tend to be distributed uniformly around the pipe circumference. This implies that the role of gravity is almost negligible at high velocities, the values of film properties at the top of the pipe are almost 80% of the ones at the bottom for gas velocities of 50 m/s.

At very low liquid flow rates the ripple waves dominate the two-phase interface. Above a critical liquid flow rate, disturbance waves appear in the flow [Andreussi, 1985; Schadel, 1988], where they exert a strong influence due to their significant dimensions and dynamic properties. Although both types of waves exist over the full range of annular flow, due to the minor role of the last ones, only the disturbance waves are studied here.

As it has been explained earlier, when the liquid mass flow rate is above its critical value the disturbance waves are the ones prevailing, in this case, several transitions can take place depending on the gas velocity [Hewitt and Hall-Taylor, 1970; Wallis, 1969; Brodkey, 1967; Van Rossum, 1959; Lamb, 1975; Levich, 1962]. When the gas velocity is very small, the interface presents a relative stability. However, with the increase in the gas velocity, it can be said that the interface becomes wavy due to the well-known Kelvin-Helmholtz instability [Lamb, 1975; Levich, 1962]. In horizontal and inclined pipes or channels, the gravity and surface tension force has a stabilizing effect, whereas the relative velocity between the phases destabilizes the film by variation in pressure distribution over the wave. At the wave crest, the gas velocity is higher, corresponding to a lower pressure, according to the Bernoulli theorem, and through the wave trough there is a lower gas velocity which results in a higher gas pressure. When the relative velocity between the gas and the liquid film is further increased, the waves become irregular and three-dimensional [Van Rossum, 1959; Hanratty and Hershman, 1961]. These are the roll waves studied by Hanratty and Engen [Hanratty, 1957], Hanratty and Hershman [Hanratty, 1961], Chung and Murgatroyd [Chung, 1965], Brodkey [Brodley, 1967], Wallis [Wallis, 1969], etcetera. Detailed experimental works using various liquids were carried out by Van Rossum [Van Rossum, 1959], whose data indicate that there exist several different mechanisms of entrainment, not only the above mentioned roll wave mechanism. As a consequence, the next step will be to describe these waves.

2.2.2. Wave Characteristics

An adequate characterization of the waves in the gas-liquid interface is important for entrainment modeling, because wave modeling deals with the prediction of the conditions at which waves are formed and become unstable. A complete description of their characteristics involves obtaining: celerity, wavelength, amplitude and shape, etcetera, see Figure 2.3.

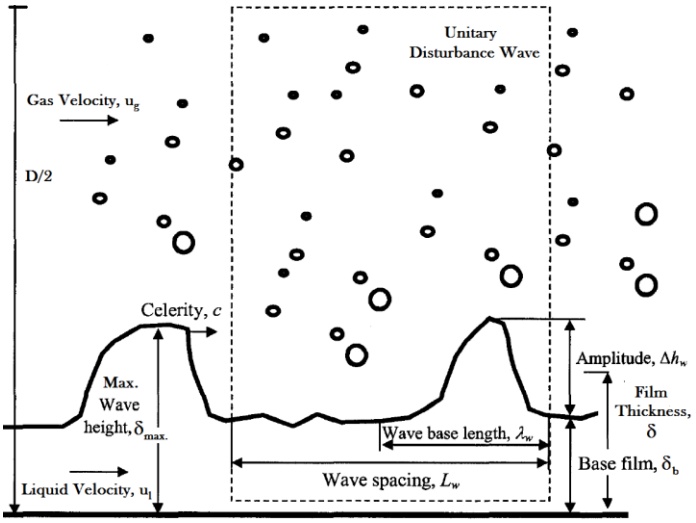

Figure 2.3. Schematic view of an Unit Disturbance Wave.

Concerning Figure 2.3, the following terms are of significance in the characterization of the disturbance wave shape. The wave spacing, L_W, is equal to the total measured length of the film time trace divided by the number of peaks that appear in this entire time trace. The wave peak height or maximum wave height, δ_{max}, is obtained as the average of the observed peaks in the film time trace. The base film thickness or wave base height, δ_b, is defined as the average value of the film thickness between the ending point of a wave and the starting point of the next one. The wave amplitude or wave roughness height, Δh_w, is defined as the difference between the wave peak height and the wave base height. Celerity, c, is the wave displacement velocity. The wave base length or wave width, λ_w, is the distance between the starting point and ending point of a single wave. Another definition, which is not shown in the Figure 2.3, is the wave separation, which is defined as the distance between the starting point of one wave and the ending point of the previous one, it also corresponds to the wave spacing minus wave base length.

2.2.2.1. Liquid Film Thickness

Liquid film thickness is the distance from the pipe wall to a mean height of the waves produced into the gas-liquid interface, see Figure 2.3.

1. Ambrosini's correlation *[Fukano 1998; Rodriguez, 2009]*

Kosky was one of the first authors to develop a model to obtain the liquid film thickness for vertical upward flows. He performed a balance force for the liquid film assuming the velocity profile to be that for single phase turbulent flow. Since the turbulent profile used depended on the height of the film, Kosky derived the following two equations for the dimensionless film thickness

$$\delta_l^+ = \sqrt{2}\,\mathrm{Re}_{lf}^{0.5} \qquad \textbf{Eqn. (2.1)}$$

for $\delta_l^+ < 25$ (low Re_{lf}), whereas for $\delta_l^+ > 25$ (high Re_{lf}) recommends the next relationship

$$\delta_l^+ = 0.0512\mathrm{Re}_{lf}^{0.875} \qquad \textbf{Eqn. (2.2)}$$

being Re_{lf} the liquid film Reynolds number defines as

$$\mathrm{Re}_{lf} = \frac{4W_{lf}}{\mu_l P} = \frac{4\Gamma_{lf}}{\mu_l} = \frac{4\rho_l u_{lf}\delta}{\mu_l} \qquad \textbf{Eqn. (2.3)}$$

where W_{lf} is the mass flow rate of the liquid in the wall layer; P is the wetted perimeter of the pipe or channel; Γ_{lf} is the mass flow rate of the liquid film per circumferential length unit.

The dimensionless thickness is defined as

$$\delta_l^+ = \frac{\rho_l \delta u_l^*}{\mu_l} \qquad \textbf{Eqn. (2.4)}$$

where u_l^* is the friction velocity, which is expressed as

$$u_l^* = \sqrt{\frac{\tau_c}{\rho_l}} \qquad \textbf{Eqn. (2.5)}$$

where τ_c is a characteristic shear stress, and approximately equal to the interfacial shear stress, τ_i, being defined as

$$\tau_i = \frac{1}{2} f_{gi}\rho_g \left(u_g - u_{lf}\right)^2 \qquad \textbf{Eqn. (2.6)}$$

where f_{gi} is the interfacial friction factor, one of the most popular expresions to calculate this friction factor is the Wallis correlation,

$$f_{gi} = 0.005\left(1 + 300\frac{\delta}{D}\right) \qquad \textbf{Eqn. (2.7)}$$

This correlation has been modified over the years, and lots of different correlations are available in the open literature, but the most widely used is

$$f_{gi} = f_g\left(1+300\frac{\delta}{D}\right) \qquad \textbf{Eqn. (2.8)}$$

where f_g is the single-phase gas friction factor, usually defined as

$$f_g = \frac{0.079}{\mathrm{Re}_g^{0.25}} \qquad \textbf{Eqn. (2.9)}$$

Regarding the gas and liquid superficial velocities, say that they are related with the expressions of the gas and liquid velocities, since the liquid film is thin and almost all the pipe is occupied by the gas phase, then

$$\begin{aligned} u_g &\approx J_g \\ u_{lf} &\approx \frac{D}{4\delta}J_{lf} \end{aligned} \qquad \textbf{Eqn. (2.10)}$$

Asali, from his data for low Re_{lf} ($Re_{lf} \cong$ 20-300), proposed a modification of the Kosky expression to low Re_{lf}. He recommended the following expression

$$\delta_l^+ = 0.34\mathrm{Re}_{lf}^{0.6} \qquad \textbf{Eqn. (2.11)}$$

Several years later, Ambrosini re-correlated the previously developed expressions with a wide range of data, in which pipe diameters and working fluids had been varied. They found that the data were best fitted using the mean film thickness correlation of Asali for $Re_{lf} < 1000$, Eqn. (2.11), and the high Re_{lf} model of Kosky for $Re_{lf} > 1000$, Eqn. (2.2)

$$\delta_l^+ = \frac{\rho_l \delta u_l^*}{\mu_l} = \begin{cases} 0.34\mathrm{Re}_{lf}^{0.6} & \mathrm{Re}_{lf} \le 1000 \\ 0.0512\mathrm{Re}_{lf}^{0.875} & \mathrm{Re}_{lf} > 1000 \end{cases} \qquad \textbf{Eqn. (2.12)}$$

2. Fukano's correlation *[Fukano, 1998]*

Another expression to estimate the liquid film thickness for vertical upward flows proposed by Fukano is

$$\frac{\delta}{D} = 0.0594\exp\left(-0.34Fr_g^{0.25}\,\mathrm{Re}_l^{0.19}\,x^{*0.6}\right) \qquad \textbf{Eqn. (2.13)}$$

where Fr_g is the gas Froude number defined by the superficial velocity of the gas phase, Re_l is the liquid film Reynolds number defined by the superficial velocity of the liquid phase and x* is the gas quality. These magnitudes are defined as follows

$$Fr_g = \frac{J_g}{\sqrt{gD}} \qquad \textbf{Eqn. (2.14)}$$

$$\mathrm{Re}_l = \frac{\rho_l J_l D}{\mu_l} \qquad \textbf{Eqn. (2.15)}$$

$$x^* = \frac{J_g \rho_g}{J_g \rho_g + J_l \rho_l} \qquad \textbf{Eqn. (2.16)}$$

Since part of the total mass flow of liquid introduced into the pipe is dragged by the gas, there will be a relationship between the liquid superficial velocity and the liquid film superficial velocity

$$J_{lf} = (1-E) J_l \qquad \textbf{Eqn. (2.17)}$$

where E is the entrained fraction, which is defined as the mass flow of liquid dragged by the gas divided by the total mass flow of liquid. Consequently

$$\mathrm{Re}_l = \frac{\rho_l J_l D}{\mu_l} = \frac{\rho_l \dfrac{J_{lf}}{1-E} D}{\mu_l} = \frac{\mathrm{Re}_{lf}}{1-E} \qquad \textbf{Eqn. (2.18)}$$

and the gas Reynolds number is almost equal in both cases, at the inlet of the pipe and in the region of the developed flow (in both cases almost all the pipe diameter is occupied by the gas), then the only definition of the gas Reynolds number is

$$\mathrm{Re}_g = \frac{\rho_g J_g D}{\mu_g} \qquad \textbf{Eqn. (2.19)}$$

Fukano experimental conditions were vertical upward annular flow, inner pipe diameter 26 mm, tube length 4.5 m, superficial gas velocity 10-50 m/s, superficial liquid velocity 0.04-0.3 m/s, system pressure 0.103-0.117 MPa, air and liquid temperature 27-29ºC.

An expression proposed by Hori et al., which also appears in Fukano's work, is

$$\frac{\delta}{D} = 0.905 \mathrm{Re}_g^{-1.45} \mathrm{Re}_l^{0.90} Fr_g^{0.93} Fr_l^{-0.68} \left(\frac{\mu_l}{\mu_{l,ref}} \right)^{1.06} \qquad \textbf{Eqn. (2.20)}$$

where Re_l, Re_g, Fr_l, Fr_g are the Reynolds and Froude numbers of liquid and gas phases, respectively, which are defined from the superficial velocities of gas and liquid phases; μ_l and $\mu_{l,ref}$ are the liquid viscosity of the used liquid at the experimental conditions and a

liquid dynamic viscosity reference value of water at a temperature of 20ºC, respectively. Re_l, Re_g and Fr_g have been defined in Eqn. (2.14), Eqn. (2.15) and Eqn. (2.19) respectively, and Fr_l is defined, in the same way as in the previous case, as follows

$$Fr_l = \frac{J_l}{\sqrt{gD}} \qquad \textbf{Eqn. (2.21)}$$

3. Henstock's and Tatterson's correlations *[Henstock, 1976; Tatterson, 1977]*

Other researchers correlated data against additional terms to include effects other than film Reynolds number. Henstock and Hanratty [Henstock, 1976] correlated the film thickness against a limited set of horizontal and vertical air-water data. They found that the vertical data (Re_{lf} ~ 10-10000) were best fitted using

$$\frac{\delta}{D} = \frac{6.59F}{(1+1400F)^{0.5}} \qquad \textbf{Eqn. (2.22)}$$

while their horizontal data (Re_{lf} ~ 1000-10000) were best fitted using

$$\frac{\delta}{D} = \frac{6.59F}{(1+850F)^{0.5}} \qquad \textbf{Eqn. (2.23)}$$

the parameter F can be defined in two ways, one proposed by the own Henstock and a subsequent amendment from Tatterson. These are expressed respectively by

$$F = \frac{1}{\sqrt{2}\,\mathrm{Re}_g^{0.4}} \frac{\mathrm{Re}_l^{0.5}}{\mathrm{Re}_g^{0.9}} \frac{\mu_l}{\mu_g} \frac{\rho_g^{0.5}}{\rho_l^{0.5}} \; ; \; F = \frac{\gamma(\mathrm{Re}_{lf})}{\mathrm{Re}_g^{0.9}} \frac{\mu_l}{\mu_g} \frac{\rho_g^{0.5}}{\rho_l^{0.5}} \qquad \textbf{Eqn. (2.24)}$$

where

$$\gamma(\mathrm{Re}_{lf}) = \left[\left(0.707\mathrm{Re}_{lf}^{0.5}\right)^{2.5} + \left(0.0379\mathrm{Re}_{lf}^{0.9}\right)^{2.5} \right]^{0.4} \qquad \textbf{Eqn. (2.25)}$$

being Re_{lf} the Reynolds number of the liquid film flowing in the wall layer, defined as in Eqn. (2.3).

4. Roberts' correlation *[Roberts, 1997]*

Next expression is a correlation proposed by Spurrett to calculate the film thickness at the bottom of a horizontal pipe. This expression correlates the data of Sekoguchi taken in pipes of diameter 0.026 m

$$\delta = 846 \frac{\mathrm{Re}_{lf}^{0.44}}{\mathrm{Re}_g^{0.59}} \qquad \textbf{Eqn. (2.26)}$$

where Re_{lf} and Re_g are the Reynolds numbers based on the film velocity, determined using the entrained fraction correlation of Asali [Azzopardi, 1999], and the superficial gas velocity, respectively.

Then Roberts, following Jepson's reasoning [Roberts, 1997], assumed that the value of δ/D is the same for all the pipes with the same superficial velocities, which allows the calculation of the film thickness at the bottom of a pipe of diameter D, in meters, given by the expression

$$\delta = 846 \frac{D}{D_{ref}} \frac{\mathrm{Re}_{lf}^{0.44}}{\mathrm{Re}_g^{0.59}} \qquad \textbf{Eqn. (2.27)}$$

where D_{ref} is a reference diameter equal to 0.026 m.

5. Okawa's correlation *[Okawa, 2002]*

The authors propose to estimate the liquid film thickness from a balance between the interfacial shear force and the wall friction force acting on the liquid film

$$\delta = \frac{1}{4} \sqrt{\frac{f_w \rho_l}{f_{gi} \rho_g}} \frac{J_{lf}}{J_g} D \qquad \textbf{Eqn. (2.28)}$$

being f_w the wall friction factor, evaluated with $\max\left(\frac{16}{\mathrm{Re}_{lf}}, 0.005\right)$; f_{gi} is the interfacial friction factor, and the authors recommended to calculate it by using Wallis correlation, Eqn. (2.7) and Eqn.(2.8); J_{lf} and J_g are the liquid film and gas superficial velocities.

6. Ishii and Grolmes' correlation *[Ishii, 1975]*

The authors propose to estimate the liquid film thickness by the following correlation

$$\delta = 0.347 \mathrm{Re}_{lf}^{2/3} \sqrt{\frac{\rho_l}{\tau_i}} \frac{\mu_l}{\rho_l} \qquad \textbf{Eqn. (2.29)}$$

being Re_{lf} the Reynolds number of the liquid flowing in the wall layer, defined as in Eqn. (2.3).

They derived this criterion for the roll-wave mechanism by considering a force balance between the drag force, F_D, from the gas acting on a wave crest on the film, and the retaining force of the surface tension, F_σ.

2.2.2.2. Base Liquid Film Thickness

Observations made by several researchers indicate that liquid film can be divided into two layers [Levy, 1999], a continuous layer and a disturbed wavy layer. Base film thickness

is the liquid layer from wall to wave trough, see base film, δ_b, in Figure 2.3. A correlation proposed by Dobran [Levy, 1999; Mantilla, 2008] and tested for upward and downward vertical flows is

$$\delta_b = D\left(140 Gr_l^{-0.2165} \mathrm{Re}_\alpha^{-1.35}\right) \quad \textbf{Eqn. (2.30)}$$

where Gr_l is a two-phase Grashoff number and Re_α is the gas core Reynolds number, defined as

$$Gr_l = \frac{gD^3 \rho_l (\rho_l - \rho_\alpha)}{\mu_l^2} \quad \textbf{Eqn. (2.31)}$$

and

$$\mathrm{Re}_\alpha = \frac{J_g \rho_\alpha D}{\mu_g} \quad \textbf{Eqn. (2.32)}$$

being J_g the superficial gas velocity and ρ_α the core density, given by

$$\rho_\alpha = \alpha \rho_g + (1-\alpha)\rho_l \quad \textbf{Eqn. (2.33)}$$

being α the void fraction. The Dobran's expression has been obtained from correlating data of vertical upward and downward flows, and for different tube diameters.

From Eqn. (2.30) it can be observed that all parameters are almost constant when carrying out an experiment under certain conditions. Then, the major source of variation in the above expression is the gas velocity, being the thickness of the base liquid layer an inverse function of this variable. As it is confirmed from several experimental works, it can be said that the wave base height decreases with the gas mass flux. For instance, Han [Han, 2006] shows that, when the gas mass flux is doubled, the wave base height decreases about 18%.

A first approximation to the base liquid film thickness correlation is presented in the PhD work of Schubring [Schubring, 2009b]. The correlation is shown below

$$\delta_b = 4.8 D \mathrm{Re}_g^{-0.6} \quad \textbf{Eqn. (2.34)}$$

2.2.2.3. Wave Amplitude

The wave roughness height or wave amplitude can be defined as the distance between the wave base height or base film thickness and the wave peak height. In order to estimate the wave amplitude, the Kelvin-Helmholtz instability has been taken into account. Under this kind of instability, the wave is caused by the relative motion of two continuous phases [Chandrasekhar, 1981]. For that instability, the most unstable wave amplitude is (for gas as a continuous phase)

$$\Delta h_{w,K-H} = 3\pi \frac{\left(1+\frac{\rho_g}{\rho_d}\right)\sigma_l}{\rho_g\left(u_g - u_l\right)^2} \qquad \textbf{Eqn. (2.35)}$$

Holowach [Holowach, 2002] proposes an expression for the wave amplitude that is dependent on fluid properties and interfacial shear. This methodology comes from Ishii and Grolmes [Ishii, 1975], which assumes that the motion of the wave crest with respect to the liquid film can be expressed by a shear flow model. The model is an approximation for the case of wave formation in vertical annular flow, given that gravitational forces are neglected since this analysis calculates the wave height in the radial direction. Then, the proposed expression is

$$\Delta h_w = \frac{\sqrt{2}C_W \mu_l}{\left(\rho_l \tau_i f_{li}\right)^{1/2}} \qquad \textbf{Eqn. (2.36)}$$

being τ_i the interfacial shear stress, whose expression is presented later on; C_W is a factor that accounts for the effect of the surface tension on the circulation/dissipation flow in the wave, and it was defined by Ishii and Grolmes [Ishii, 1975] as follows

$$C_W = 0.028 N_\mu^{-4/5} \quad for \quad N_\mu \le 1/15$$
$$C_W = 0.25 \quad for \quad N_\mu > 1/15 \qquad \textbf{Eqn. (2.37)}$$

where N_μ (originally used by Hinze [Hinze, 1955]) is the viscosity number, which compares the viscous force induced by an internal flow to the surface tension force, defined as

$$N_\mu = \frac{\mu_l}{\left(\rho_l \sigma \sqrt{\frac{\sigma}{g\,\Delta\rho}}\right)^{1/2}} \qquad \textbf{Eqn. (2.38)}$$

The interfacial liquid friction factor, f_{li}, is calculated using the correlation developed by Hughmark [Hughmark, 1973]. Thus

$$\sqrt{f_{li}} = K\,\mathrm{Re}_{lf}^{m} \qquad \textbf{Eqn. (2.39)}$$

where K and m are given by

K = 3.73 , m = -0.47 for $2 < \mathrm{Re}_{lf} < 100$

K = 1.962, m = -1/3 for $100 < \mathrm{Re}_{lf} < 1000$

K = 0.735, m = -0.19 for 1000 < Re_{lf}

For the wave amplitude calculation the author proposes the liquid interfacial friction factor presented above for Re_{lf} > 1000, and for the interfacial shear stress, an expression defined by the gas core mixture properties

$$\tau_i = \frac{f_{gi}\rho_\alpha J_\alpha^2}{2} \qquad \textbf{Eqn. (2.40)}$$

where all magnitudes are based on the superficial gas core mixture properties, and their expression is

$$J_\alpha = \frac{G_g}{\rho_g} + \frac{G_e}{\rho_l} \qquad \textbf{Eqn. (2.41)}$$

being G_g and G_e the gas and entrained mass fluxes, respectively. On the other hand, the interfacial gas friction factor is defined as

$$f_{gi} = 0.079\mathrm{Re}_\alpha^{-1/4}\left[1 + 24\left(\frac{\rho_l}{\rho_g}\right)^{1/3}\frac{\delta}{D}\right] \qquad \textbf{Eqn. (2.42)}$$

In this case Re_α is the gas core Reynolds number, defined as

$$\mathrm{Re}_\alpha = \frac{(G_g + G_e)D}{\mu_g} \qquad \textbf{Eqn. (2.43)}$$

Han et al. [Han, 2006] performed an experimental work in a vertical pipe of 9.525 mm, in which liquid mass fluxes were ranging from 126 to 198 kg/m^{2}s and gas mass fluxes were ranging from 18 to 47 kg/m^{2}s. The correlation proposed by the authors can be approximated as follows

$$\Delta h_w = 4000 D\,\mathrm{Re}_g^{-1.12} \qquad \textbf{Eqn. (2.44)}$$

Han's experimental measurements confirm that the peak height (sum of the base liquid film thickness and the wave amplitude) decreases when the gas mass flux increases, but to a greater extent than in the previous case of the base thickness. In fact, he shows that when the gas mass flux is doubled, the wave peak height decreases by about 43%.

2.2.2.4. Wave Celerity

The next parameter that will be presented is the wave celerity, Several expressions are presented, such as the ones proposed by Kumar, Pearce, Swanson and Marmottant.

Kumar [Mantilla, 2008] proposed a model where the wave velocity or celerity is obtained by calculating the interfacial friction factors based on the gas velocity and liquid velocity. Equating the two interfacial friction factors, the interfacial velocity (wave celerity) is determined as follows

$$c = \frac{\psi \cdot J_g + J_l}{1+\psi} \qquad \textbf{Eqn. (2.45)}$$

where ψ is obtained from the next expression

$$\psi = \sqrt{\frac{\rho_g}{\rho_l}\frac{f_{gi}}{f_{li}}} \qquad \textbf{Eqn. (2.46)}$$

being f_{li} and f_{gi} the liquid and gas interfacial friction factors. However, they proposed the following empirical correlation to estimate this parameter

$$\psi = 5.5\sqrt{\frac{\rho_g}{\rho_l}}\left(\frac{\mathrm{Re}_l}{\mathrm{Re}_g}\right)^{0.25} \qquad \textbf{Eqn. (2.47)}$$

Pearce's correlation is given by the following expression [Alamu, 2010]

$$c = \frac{KV_l + J_g\sqrt{\frac{\rho_g}{\rho_l}}}{K + \sqrt{\frac{\rho_g}{\rho_l}}} \qquad \textbf{Eqn. (2.48)}$$

being

$$V_l = \frac{DG_l(1-E)}{4\rho_l\delta} \qquad \textbf{Eqn. (2.49)}$$

G_l is the total liquid mass flux, E is the entrained fraction and δ is the liquid film thickness. The Pearce coefficient, K, is function of pipe diameter and inlet conditions. The value used by Alamu for the K factor varies between 0.3 and 0.65, depending on the correlated data.

Omebere-Iyari and Azzopardi [Omebere-Iyari, 2007; Sawant, 2008b] correlated, using the Pearce's correlation, a database of disturbance wave velocity, and they also evaluated the diameter dependence of Pearce coefficient. The authors found that K increases from 0.51 to 0.9 when the pipe diameter increases from 0.5 to 2.5 cm. Between 2.5 and 4.2 cm, the value of K remains constant in 0.9.

Swanson [Schubring, 2008] found that the gas friction velocity was equal to the wave celerity for his databank. The gas friction velocity is defined as follows

$$u_g^* = \sqrt{\frac{\tau_w}{\rho_g}} \qquad \textbf{Eqn. (2.50)}$$

being τ_w the wall shear stress.

Marmottant and Villermaux [Belt, 2010] performed a theoretical study on co-axial jets, whose configuration was in fact very similar to that of annular flow. They showed that a shear instability governs the large waves on the jet. The linear shear instability analysis provides an equation for the wave velocity

$$c = \frac{\sqrt{\rho_g} J_g + \sqrt{\rho_l} J_l}{\sqrt{\rho_g} + \sqrt{\rho_l}} \qquad \textbf{Eqn. (2.51)}$$

This equation is obtained whit the assumption $J_g >> J_l$.

Schubring [Schubring, 2009a] proposes a correlation to determine the wave velocity in horizontal annular flow

$$c = 0.41 \frac{J_g}{\sqrt{x}} \mathrm{Re}_g^{-0.25} \qquad \textbf{Eqn. (2.52)}$$

being x the gas dynamic quality, quotient between gas mass flow rate and the total mass flow rate, given by

$$x = \frac{\dot{m}_g}{\dot{m}_g + \dot{m}_l} \qquad \textbf{Eqn. (2.53)}$$

The author says that the performance of this correlation is good enough for all diameters studied. Even though, he says that the effect of gas flow is not entirely grasped, as the measured wave velocities vary over a somewhat narrower range than the correlated values do.

Al-Sarkhi et al. [Al-Sarkhi, 2012a] explains that wave celerity is a strong function of the superficial liquid and gas velocities, being also dependent on the inclination angle. They propose three different correlations for the horizontal: the inclination angles from 10º to 20º, the inclination angles of 45º and up to 90º cases. These expressions are, respectively

$$\frac{c}{J_l} = 2.379 \cdot X^{-0.9} \qquad \textbf{Eqn. (2.54)}$$

$$\frac{c}{J_l} = 2.323 \cdot X^{-0.94}$$ **Eqn. (2.55)**

$$\frac{c}{J_l} = 1.942 \cdot X^{-0.91}$$ **Eqn. (2.56)**

being X the Lockhart-Martinelli number, defined as

$$X = \sqrt{\frac{\rho_l J_l^2}{\rho_g J_g^2}}$$ **Eqn. (2.57)**

2.2.2.5. Wave Frequency

A wave frequency correlation for disturbance waves has been proposed by Azzopardi [Azzopardi, 2006; Mantilla, 2008]. This expression is a relationship between the Strouhal number (dimensionless wave frequency) and the Lockhart-Martinelli number

$$St_l = 0.25 X^{-1.2}$$ **Eqn. (2.58)**

where St_l and X are the liquid Strouhal number and the Lockhart-Martinelli number, respectively. The Strouhal number is defined as

$$St_l = \frac{\upsilon D}{J_l}$$ **Eqn. (2.59)**

being υ the wave frequency.

Another empirical correlation for wave frequency in terms of Strouhal number has been obtained by Alamu [Alamu, 2010]. He used a curve-fitting method based on his own data. This correlation is very similar to the one presented above, and is given by

$$St_l = 0.4292 X^{-0.908}$$ **Eqn. (2.60)**

Alamu's experimental data have been obtained in a vertical pipe in upward flow conditions and with a water-glycerin mixture as working liquid.

Azzopardi [Al-Sarkhi, 2012a] proposes a quite similar expression for the wave frequency

$$St_l = 1.1 X^{-0.93}$$ **Eqn. (2.61)**

Hazuku et al. [Sawant, 2008b] measured the frequency of disturbance waves in vertical annular flow experiments performed at atmospheric pressure condition in 1.1 cm diameter pipe and using as working fluids water and air. They were able to correlate their

disturbance wave frequency data with Sekoguchi's expression, and the values were within ±25% of deviation. The Sekoguchi's correlation is as follows

$$St_g = \frac{\upsilon D}{J_g} = f_1(Eo) f_2\left(\mathrm{Re}_l, Fr_g\right) \qquad \textbf{Eqn. (2.62)}$$

where Eo and Fr_g are the Eötvös and the Froude numbers, respectively, which are defined as

$$Eo = \frac{gD^2\left(\rho_l - \rho_g\right)}{\sigma} \qquad \textbf{Eqn. (2.63)}$$

and the Froude number which has been defined in Eqn. (2.14). Being f_1 and f_2 given by

$$f_1(Eo) = Eo^{-0.5}\left[0.5Ln(Eo) - 0.47\right]$$
$$f_2\left(\mathrm{Re}_l, Fr_g\right) = 0.0076\, Ln\left(\frac{\mathrm{Re}_l^{2.5}}{Fr_g}\right) - 0.051 \qquad \textbf{Eqn. (2.64)}$$

Although, as it has been said by Sawant, the presented correlation successfully predicts the low-pressure data, it failed to predict the high-pressure data. Therefore, the following new correlation was proposed

$$St_g = 0.086\mathrm{Re}_l^{0.27}\left(\frac{\rho_l}{\rho_g}\right)^{-0.64} \qquad \textbf{Eqn. (2.65)}$$

where the adjustment constants are obtained based on the Sawant's experimental data, using regression analysis. This correlation predicts their experimental data for all pressure conditions within ±25% deviation. They also correlated Schadel's (carried out with air–water) and Willetts's (carried out with air–water and helium–water at 1.5 bar) experimental data and they were predicted satisfactorily.

In Alamu's PhD thesis [Alamu, 2010] an expression quite similar to Sawant's correlation is also presented

$$St_g = 0.009 J_g\left(\frac{\rho_l}{\rho_g}\right)^{0.5} \qquad \textbf{Eqn. (2.66)}$$

This expression has been obtained by fitting his experimental data points.

2.3. The Onset Of Entrainment Process

For low relative velocities between liquid and gas phases, there is a smooth interface. As this difference in velocity increases, the interface covers with waves and, from a certain point, part of the liquid is dragged by the gas phase, this is called the "onset of entrainment". The processes that take place on the gas-liquid interface are at dynamic equilibrium with continuous exchange of mass, momentum and energy between the liquid film and the gas stream. The liquid in the film continuously enters the gas core in the form of droplets, in a process called liquid entrainment, and the droplets in the gas core continuously deposit on the film, in a process called droplet deposition. When the mass flow rate of entrained and deposited droplets equals, that is to say the mass of liquid droplets remains constant in the gas core, the fully developed annular flow is achieved. The ratio of the mass flow rate of the liquid phase, in the form of droplets in the gas core, to the total mass flow rate of the liquid phase is defined as the liquid entrainment fraction.

The deformation mechanisms in the gas-liquid interface are caused by a force balance. The hydrodynamic and the surface tension forces govern the motion and deformation of the disturbance waves. Under certain conditions, this force balance leads to an extreme deformation of the interface, which results in break-up of a portion of a wave into several liquid droplets; this point is the onset of entrainment. These droplets can be entrained into the gas core in several different ways. There are five basic types of entrainment mechanisms [Ishii, 1975] and all of them can occur in concurrent flow except the last one. These mechanisms are: roll wave, wave undercut, bubble bursting, liquid impingement and liquid bulge disintegration; all of them are shown in Figure 2.4.

It is important to remark that for low viscous fluids, as water, the dominant mechanism of liquid entrainment into the gas core flow is the roll wave, but wave undercut mechanism is also possible for low liquid Reynolds numbers. This statement is supported by the findings of Van Rossum [Van Rossum, 1959], Hall-Taylor et al. [Hall-Taylor, 1963], Woodmansee and Hanratty [Woodmansee, 1969] and Schadel [Schadel, 1988]; consequently only the roll wave mechanism is analyzed in the present document. In this mechanism, the drag force acting on the wave tops deforms the gas-liquid interface, shearing off the tops of large amplitude roll waves by the turbulent gas flow. The relation between the disturbance waves and droplet entrainment processes has been established since the 60s by several methods and authors [Cooper et al., 1964; Jacowitz and Brodkey, 1964; Arnold and Hewitt, 1967; Woodmansee and Hanratty, 1969]. However, the exact mechanism for how the liquid droplets are generated out of a disturbance wave is still controversial.

In the entrainment mechanisms, when a gas phase is flowing over a liquid film, the gas-liquid interface may become unstable depending on the magnitude of the gas and liquid velocities. For a very small gas velocity, the interface is relatively stable. However, as the gas velocity increases, the interfacial wave appears as result of the Kelvin-Helmholtz instability. The amplitude and irregularity of the waves become more and more pronounced as the gas velocity is further increased. At a sufficiently high gas flow, the interfacial waves

transform into large amplitude roll waves. Beyond this point, the interfacial shear forces become greater than the surface tension forces and the onset of entrainment occurs. The critical condition for entrainment to take place depends on the liquid film Reynolds number and on the gas stream velocity, as shown in Figure 2.5.

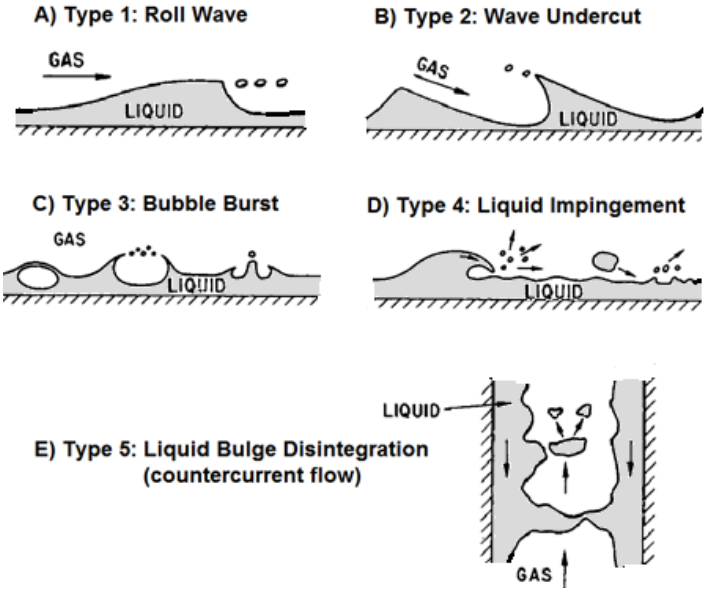

Figure 2.4. Entrainment mechanisms in concurrent two-phase flow.

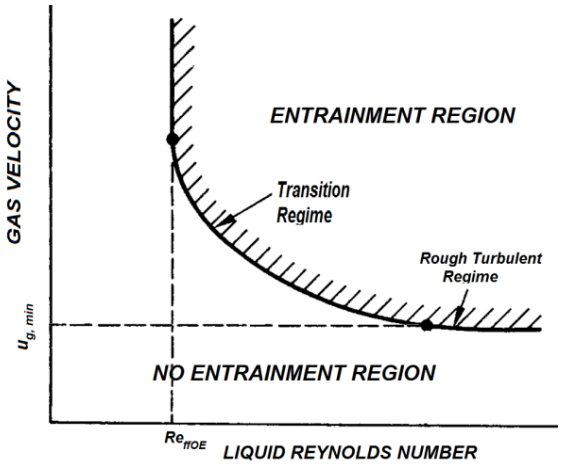

Figure 2.5. Schematic entrainment inception velocity boundary for each particular combination of liquid and gas conditions.

In the fifties and sixties, considerable theoretical and experimental works were carried out on the study of the onset of entrainment (OE) and on the onset of disturbance waves (ODW) [Hanratty & Engen, 1957; Van Rossum, 1959; Hanratty & Hershman, 1961; Zhivaikin, 1962; Cousins, 1965], and all of them point out that the large amplitude DW disappear at the OE. The conclusion made by these researchers is that the OE and ODW conditions are always similar. This assumption has been confirmed subsequently by other researchers, for instance Ishii [Ishii, 1975], Azzopardi [Azzopardi, 1997] and Hills [Hills, 1997].

The value of the liquid film Reynolds number corresponding to that DW transition, the onset of entrainment Reynolds number, Re_{ffOE}, is not firmly established. However, the results of the various investigations for low viscous liquids suggest that the onset of entrainment Reynolds number is in the range of 2 for vertical downward flows. For horizontal and vertical upward flows, which are the most widely studied due to its industrial importance, the onset of entrainment Reynolds number is between 100 and 400 approximately, depending on the author. For instance, Ishii and Grolmes [Ishii, 1975] suggest a value of 160; Abolfadl [Azzopardi, 1997] linked the start of entrainment with the onset of turbulence in the film, then he specified a value to the onset of entrainment Reynolds number of 268 based on its available experimental data; Okawa [Okawa, 2003] takes a critical value of 320 from experimental data. Lower values are proposed by other authors, for instance, Nigmatulin [Alipchenkov, 2004] proposes a value for the onset of entrainment Reynolds number of 180, Andreussi et al. [Andreussi, 1985] suggest a value of 94 approximately, Azzopardi [Azzopardi, 1983; Lopez de Bertodano 1998] gave a value of 80 based on wave inception results for both Freon and water.

The transition also depends on the gas flow. Under high gas velocity condition, the ODW correspond to the values at which OE is produced, that condition corresponds to a limiting value of the liquid Reynolds number, the so called onset of entrainment Reynolds number. As it has been explained previously, for low viscous fluids, this transition occurs at approximately Reynolds numbers of 160 [Ishii, 1975]; but it has been also proposed that, for $Re_{ffOE} < 160$, suppression of entrainment takes place due to the suppression of DW [Azzopardi, 1983; Alipchenkov, 2004; Andreussi, 1985]. Although the works of other researchers suggest higher values for this Re_{ffOE} [Owen, 1987; Azzopardi, 1997; Pan, 2002b; Sawant, 2009], they explain that the asymptotic liquid velocity or the critical liquid velocity at ODW is higher than the prediction of Ishii and Grolmes criterion. Otherwise, a careful examination of the limited experimental data on the inception of entrainment indicates that there exists a deviation from the criterion based on the DW mechanism when the gas velocity is not high enough, see Figure 2.6. So, at lower gas velocity, the trends presented by ODW and OE conditions are opposite. The ODW boundary shows that the liquid velocity at ODW decreases with the decreasing gas velocity and the OE boundary shows the liquid velocity at the OE increases with the decreasing gas velocity. Thus, it appears that, only under high gas velocity, the conditions for OE and ODW are similar, and only under these conditions the Re_{ffOE} can be employed.

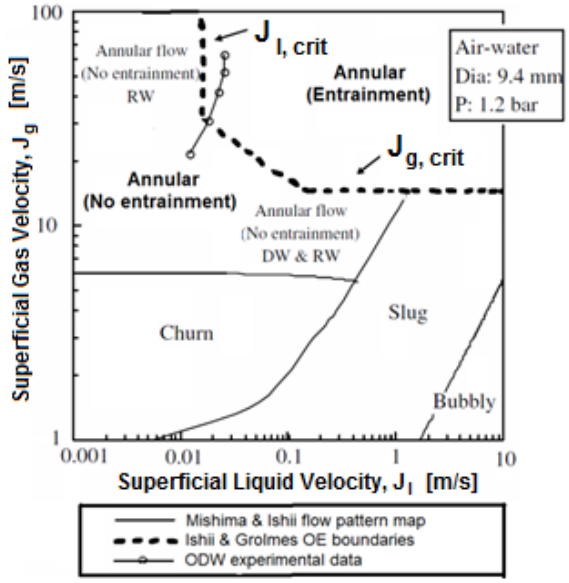

Figure 2.6. Flow Pattern Map of two-phase gas-liquid for vertical upward annular [Sawant 2009].

As it has been presented in the previous paragraph, the Re_{ffOE} corresponds to the critical liquid film flow rate at which OE takes place under high gas velocity condition. For horizontal and vertical upward annular flows, a value of 160 for the Re_{ffOE} can be chosen as a first approximation for this transition, even though several expressions to obtain this value are presented in the next paragraphs.

Pan and Hanratty [Pan, 2002a,b] developed an entrainment correlation for liquids with viscosities close to that of water, based on a balance between the rates of atomization and deposition. Both the gravity and droplet size effects are considered in the correlation. This correlation for horizontal flow, as well as the one for vertical flows, is the only correlation that considers explicitly the concept of critical liquid film rate. This liquid critical flow is the liquid flow above which the initiation of atomization occurs, that is, when disturbance waves appear on the liquid layer, the so called onset of entrainment condition. Measurements of Andreussi et al. [Andreussi, 1985] of the liquid flow needed to initiate disturbance waves in vertical flows can be used to calculate the critical flow per unit length, $\Gamma_{lfc} = \dot{m}_{lfc} / \pi D$, where W_{lfc} is the critical film flow rate below which atomization does not occur. The calculation of that critical flow rate employs the onset of entrainment Reynolds number. These two magnitudes are represented by the following equations

$$Re_{ffOE} = 7.3(\log_{10}\omega)^3 + 44.2(\log_{10}\omega)^2 - 263(\log_{10}\omega) + 439 \qquad \textbf{Eqn. (2.67)}$$

where the onset of entrainment Reynolds number can be written as

$$Re_{ffOE} = \frac{4\Gamma_{lfc}}{\mu_l} \qquad \textbf{Eqn. (2.68)}$$

and

$$\omega = \frac{\mu_L}{\mu_g}\sqrt{\frac{\rho_g}{\rho_l}} \qquad \textbf{Eqn. (2.69)}$$

For air and water at standard conditions, ω=1.861 and Re_{ffOE}=370. Measurements in horizontal flows, by Dallman [Dallman, 1978] and by Laurinat [Laurinat, 1982], suggest larger values of Γ_{lfc} by a factor of about 1.3, probably because of the asymmetry of the liquid layer. Eqn. (2.67) was derived from measurements for ω=1.8 to 28, and it should not be used outside this range.

Another expression to calculate the critical Reynolds number, Re_{ffOE}, is the one proposed by Owen [Owen, 1987; Jiao, 2009]. In that equation, the Reynolds number above which entrainment happens is obtained as follows

$$Re_{ffOE} = \exp\left(5.8504 + 0.4249\frac{\mu_g}{\mu_l}\left(\frac{\rho_l}{\rho_g}\right)^{0.5}\right) \qquad \textbf{Eqn. (2.70)}$$

Azzopardi [Azzopardi, 1997] presented a review of experimental data on measurement of ODW and OE conditions, and correlations available for the prediction of these conditions (Table 2.1). In the existing experimental data there is a reasonable range of liquid viscosity, surface tension and pipe diameter covered, but all the experiments were carried out at or near atmospheric pressure. The database covered a range of pipe diameter from $16 \cdot 10^{-3}$ to 0.125 m and a range of viscosity from 1.0 to $24.4 \cdot 10^{-3}$ Pa·s. He found that the existing correlations for ODW failed to predict the diameter and viscosity effects.

Table 2.1. Critical Liquid Reynolds numbers for wave inception at high gas velocity conditions [Azzopardi, 1997].

Author	Experimental	Asali	Owen&Hewitt	Ishii&Grolmes
Azzopardi et el. (1983)	211	290	429	58
Martin (1983)	245	272	412	43
Whalley et al. (1977)	330/360	272/284	412/423	43/53
Azzopardi et el. (1979)	255	284	423	53
Shearer (1964)	282/300	231/272	383/411	22/46
Asali (1984)	205-240	225	261/345	7/40
Hall-Taylor & Nedderman (1968)	105/298	225/284	351/423	1.8/53

Later on, experiments of Sawant et al. [Sawant 2008a & 2009] covered higher pressure conditions, 1.2, 4.0 and 6.0 bar, a range of diameters from 0.94 to 12.5 cm, and a range of liquid viscosities from 1 to 24 x 10^{-3} Pa·s. They concluded that previous non-dimensional numbers failed to predict the pressure effects or density ratio changes observed in their data. Using the Viscosity number (N_μ, originally used by Hinze [Hinze, 1955], defined in Eqn. (2.38), which compares the viscous force induced by an internal flow to the surface tension force), they were able to collapse their data and a database of experimental measurements, all of them with D ≤ 3.2 cm. And under high gas velocity conditions, the non-dimensional group $\mathrm{Re}_{lf} N_\mu^{0.5}$ asymptotically approaches a value of 13. Since the conditions of OE or ODW under high gas velocity are similar, a new correlation for Re_{ffOE} can be given as follows

$$\mathrm{Re}_{ffOE} = 13 N_\mu^{-0.5} \qquad \textbf{Eqn. (2.71)}$$

Observations of Andreussi et al. [Andreussi, 1985] of the conditions for the initiation of roll waves are shown in Figure 2.7. These results also clearly show that, at large gas velocities, the transition is approximately independent of gas flow. As can be observed from the figure, the results for the critical condition at large gas velocities are given by $\mathrm{Re}_{ffOE} \approx 95$, instead of the previously higher values presented above. However, the authors explain that good agreement between this calculation and experiment is obtained at high liquid Reynolds numbers, but the film is more stable than the calculated for low liquid Reynolds numbers.

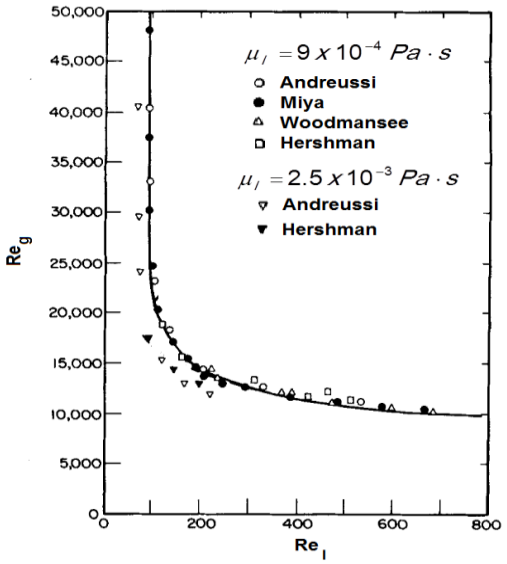

Figure 2.7. Effect of gas and liquid Reynolds numbers on roll wave transition [Andreussi, 1985].

The entrainment process occurs, under high gas velocity condition, when the liquid film Reynolds number, defined by Eqn. (2.18), is bigger than the onset of entrainment Reynolds number

$$\mathrm{Re}_l > \mathrm{Re}_{ffOE} \qquad \textbf{Eqn. (2.72)}$$

Then, finally, the critical liquid film velocity above which entrainment occurs can be expressed as

$$J_l = \mathrm{Re}_{ffOE}\,\frac{\mu_l}{\rho_l D} \quad ; \quad u_l = \mathrm{Re}_{ffOE}\,\frac{\mu_l}{\rho_l 4\delta} \qquad \textbf{Eqn. (2.73)}$$

being u_l and J_l the liquid film and superficial liquid film velocities, respectively.

2.4. The Entrainment Inception Velocity

The onset of entrainment Reynolds number, presented in the previous section, only shows the limiting value of the liquid film velocity under which no entrainment is possible. This value is regardless of the gas flow conditions, but does not indicates the critical gas velocity above which entrainment takes place when liquid film number is above its critical value. This critical gas velocity is the entrainment inception velocity.

The entrainment inception velocity is the gas critical velocity above which the entrainment process can take place. Different models have been developed in the course of time, the most widely used are the Kutateladze criterion and the Ishii and Grolmes model, but many others are available in the literature. Next sections are devoted to the description of many of these entrainment inception expressions.

2.4.1. Kutateladze Number Criterion

Abundant work on the inception velocity can be found in the two-phase flow domain. However, in most cases, evaluation sustained by theoretical considerations is provided for a gas flowing over a pool or a liquid film. In the Epstein paper [Epstein, 1990], it is obtained from the Kutateladze number criterion (Ku > 3.1). This model gives as a result a constant velocity value above which entrainment takes place

$$Ku^2 = \frac{\rho_g u_g^2}{\sqrt{\sigma g \rho_l}} \geq 9.61 \qquad \textbf{Eqn. (2.74)}$$

Then, working out the values of the velocity, the limiting gas velocity is given by

$$u_g \geq \sqrt{\frac{9.61\sqrt{\sigma g \rho_l}}{\rho_g}} \qquad \textbf{Eqn. (2.75)}$$

Note that the Kutateladze number may be written as a Weber number:

$$Ku^2 = \frac{\rho_g u_g^2}{\sigma}\sqrt{\frac{\sigma}{g\rho_l}} = \frac{\rho_g u_g^2}{\sigma} l_{interf} = We_{interf} \qquad \textbf{Eqn. (2.76)}$$

where $l_{interf} = \sqrt{\frac{\sigma}{g\,\rho_l}}$ is a characteristic length in the interface stability theory. In this approach, only the interfacial tension and gravity acceleration are considered, and not the liquid viscosity.

The above criterion gives a constant entrainment inception velocity value depending only on gas and liquid properties. An improvement of the previous model is the one proposed by Crowe [Crowe, 2006]. In that model, three regions are considered:

1.- No entrainment zone. Reynolds numbers under Re_{ffOE}, where entrainment is not possible.

2.- Rough turbulent zone. Liquid film Reynolds number exceeds a value of about 1500-1750, the liquid film flow becomes completely rough-turbulent and the entrainment inception velocity has a constant value.

3.- Transition zone. Reynolds number between these two values, the entrainment inception velocity has not a constant value.

First region, below the Re_{ffOE}, see section 2.3, "The Onset of Entrainment Process", where different values of this parameter have been presented. In that region, the critical Kutateladze number has a high value and liquid entrainment is difficult or impossible to achieve.

Second region is the rough turbulent regime (the typical critical value proposed for this region is Re_{lf} = 1635); according with Crowe's suggestions, liquid entrainment is expected to exist in this region for Kutateladze numbers bigger than 3.2 (slightly different Ku number that the one proposed by Epstein)

$$Ku^2 = \frac{\rho_g u_g^2}{\sqrt{\sigma g \rho_l}} \geq 10.24 \qquad \textbf{Eqn. (2.77)}$$

Then, using the same procedure of the Epstein model, gives as a result the following limiting gas velocity expression

$$u_g \geq \sqrt{\frac{10.24\sqrt{\sigma g \rho_l}}{\rho_g}} \qquad \textbf{Eqn. (2.78)}$$

Third region is the transition regime, where the critical Kutateladze number increases with decreasing Reynolds number. Using as a first approximation the value of 160 for the onset of entrainment Reynolds number, and the value of 1635 for the beginning of the rough turbulent region; then the transition regime covers the liquid film Reynolds numbers $160 < Re_{lf} < 1635$. At the lower Reynolds side of the regime, the critical Kutateladze number is $Ku \approx 7.5$. So, considering as linear the variation in that transition region

$$Ku^2 = \frac{\rho_g u_g^2}{\sqrt{\sigma g \rho_l}} \geq 61.241 - 0.0312 Re_{fl} \qquad \textbf{Eqn. (2.79)}$$

being Re_{lf} the liquid film Reynolds number, defined in Eqn. (2.15).

Then, the entrainment inception velocity is

$$u_g \geq \sqrt{\frac{(61.241 - 0.0312 Re_{lf})\sqrt{\sigma g \rho_l}}{\rho_g}} \qquad \textbf{Eqn. (2.80)}$$

2.4.2. Ishii and Grolmes Model

In annular flow, the surface of the liquid film is not smooth but covered with waves, see Ishii and Grolmes [Ishii, 1975]. The shape of waves depends on the velocities of liquid and gas phases. The paper of Ishii and Grolmes states that there exists a lower limit of Re_{lf}, under which roll-wave entrainment will not take place no matter how high is the gas velocity over the film, the previously presented Re_{ffOE}. In the other extreme, at high Re_{lf} (rough turbulent regime), the gas velocity necessary for the inception of the entrainment process becomes independent of the liquid film Reynolds number; this regime starts at $Re_{lf} \approx 1635$.

Ishii and Grolmes derived a criterion for the onset of roll-wave entrainment by considering a force balance between the drag force F_D, from the gas acting on a wave crest on the film, and the retaining force of the surface tension F_σ (Figure 2.8). They assumed that roll wave entrainment was possible when the drag forces exceeded the retaining force of the surface tension.

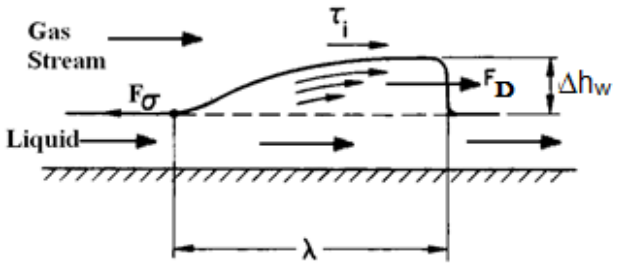

Figure 2.8. Side view of entrainment model based on roll-wave break-up.

An entrainment inception criterion velocity can be found depending on the viscosity number, Eqn. (2.38), and the liquid film Reynolds number, Eqn. (2.15). For horizontal flow and $Re_{lf}>Re_{ffOE}$ (remember that the authors used for Re_{ffOE} a value of 160 for horizontal and vertical upward flow and 2 for vertical downward flow), the inception criterion is

$$\begin{aligned} \frac{\mu_l J_g}{\sigma}\sqrt{\frac{\rho_g}{\rho_l}} &\geq 11.78 N_\mu^{0.8} \mathrm{Re}_{lf}^{-1/3} \quad for \quad N_\mu \leq \frac{1}{15}; \mathrm{Re}_{ffOE} \leq \mathrm{Re}_{lf} \leq 1635 \\ \frac{\mu_l J_g}{\sigma}\sqrt{\frac{\rho_g}{\rho_l}} &\geq 1.35 \mathrm{Re}_{lf}^{-1/3} \quad for \quad N_\mu > \frac{1}{15}; \mathrm{Re}_{ffOE} \leq \mathrm{Re}_{lf} \leq 1635 \end{aligned} \qquad \textbf{Eqn. (2.81)}$$

where J_g is the volumetric flux of gas (superficial gas velocity).

For the rough turbulent regime ($Re_{lf}>1635$) the inception criterion is

$$\begin{aligned} \left|J_g\right| &> \frac{\sigma}{\mu_l}\sqrt{\frac{\rho_l}{\rho_g}} \times N_\mu^{0.8} \quad for \quad N_\mu \leq \frac{1}{15}; \mathrm{Re}_{lf} > 1635 \\ \left|J_g\right| &> \frac{\sigma}{\mu_l}\sqrt{\frac{\rho_l}{\rho_g}} \times 0.1146 \quad for \quad N_\mu > \frac{1}{15}; \mathrm{Re}_{lf} > 1635 \end{aligned} \qquad \textbf{Eqn. (2.82)}$$

2.4.3. Other Entrainment Inception Velocity Models

Large discrepancies exist among the different correlations and also between the different experimental data. Hence, the agreement of the simulation results with Ishii and Grolmes correlation is satisfactory. Other correlations are available in the literature, for instance the ones of Kulov, Sawant, etc.

The correlation obtained by Kulov [Yun, 2010] is quite simple and it only shows the relation between the gas and liquid velocities. That relation is shown via the gas and fluid Reynolds numbers

$$\mathrm{Re}_g = \frac{5.32 \times 10^4}{\mathrm{Re}_{lf}^{0.19}} \qquad \textbf{Eqn. (2.83)}$$

In Figure 2.9, the comparison of Yun's numerical simulation versus the Kulov's correlation for the onset of entrainment is shown. The results of the numerical simulation data of Yun et al. [Yun, 2010] are smaller than the ones of this equation. Most of the data are located between 50 and 100% of the Kulov's correlation values.

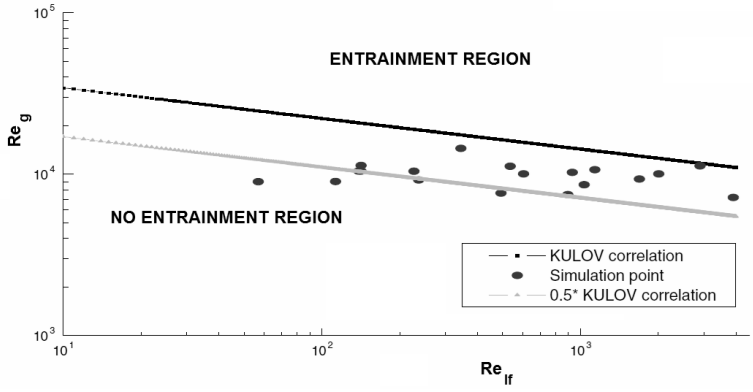

Figure 2.9. Comparison of the onset criteria for entrainment based on the Kulov relation and the numerical simulation data of Yun et al. [Yun, 2010].

In the articles of Sawant et al. [Sawant, 2008a] and Pan et al. [Pan, 2002a] the following expression to obtain the critical gas velocity at the onset of entrainment is proposed

$$\frac{D^{0.5} J_g \left(\rho_l \rho_g\right)^{0.25}}{\sigma^{0.5}} \cong 40 \qquad \textbf{Eqn. (2.84)}$$

This correlation is empirical and dimensional, so it is necessary to check its applicability range.

A summary of critical gas velocities obtained by different authors is shown in the Table 2.2 and it summarizes the measurements by Willetts, Wallis, Lopez de Bertodano and Andreussi [Pan, 2002a].

As was explained by Pan, all the studies, with the exception of one, used ρ_l= 1000 kg/m^3 and σ=0.073 N/m. His analysis suggest that in Eqn. (2.84) should be used $\rho_g^{0.5}$ rather than $(\rho_g \rho_l)^{0.25}$. However, the opposite conclusion would be reached by examining the results of Willetts for air–water and helium–water.

Another expression to obtain the onset of entrainment gas velocity in annular flow has been correlated over a wide database by Hewitt and Hall-Taylor [Flores, 1995]

$$u_g = 1.5x10^{-4} \sqrt{\frac{\rho_l}{\rho_g}} \frac{\sigma}{\mu_g} \qquad \textbf{Eqn. (2.85)}$$

Table 2.2. Summary of critical gas velocities for different authors [Pan, 2002a].

Author	Fluids	D (cm)	ρ_g (kg/m^3)	V_g (m/s)	X_E [a]
Willets (1987)	Air-water	1.026	1.83	22	53
	He-water	1.026	0.27	35	53
	Air-Genklene	1.026	2.41	8	39
Wallis (1968)	Air-water (1atm)	1.588	1.5(assumed)	18	53
	Air-water (2atm)	1.588	3.0(assumed)	12	42
	Air-water (3atm)	1.588	4.5(assumed)	11	41
	Air-water (4atm)	1.588	6.0(assumed)	10	41
Lopez de Bertodano & Jan (1998)	Air-water	0.953	1.6	24	54
Lopez de Bertodano et al. (1997,1998)	Air-water	0.953	2.8	15	40
	Air-water	0.953	4.4	13	39
Andreussi & Zanelli (1976,1979) (downflow)	Air-water	2.4	1.38	11	39

[a] $X_E = \dfrac{D^{0.5} J_g \left(\rho_l \rho_g\right)^{0.25}}{\sigma^{0.5}}$

2.5. Study of Experimental Data and Adjustment Correlations

This section is dedicated to present all the studies conducted to determine the most important characteristics of the liquid film layer in annular two-phase flow. In particular, we have concentrated on the determination of the film thickness of this liquid layer, wave celerity and wave frequency. Thus, we have made a division into three subsections. The first one is devoted to the liquid layer thickness, the second to wave velocity (usually called celerity or wave celerity) and the third, and last, to the frequency of these waves. Each subsection is organized as follows: the first part is devoted to present some conclusions drawn directly from the experimental data; the next part presents the empirical correlations found in the literature and the work made to improve them from the available experimental data; and finally, we will present the comparison of all these correlations with the experimental data.

2.5.1. Thickness of the Liquid Film Layer

A lot experiments have been carried out in the last decades in order to determine the thickness of the liquid film existent in annular flow. In particular, in the present work, we have analyzed the following experimental data series: Tatterson's [Tatterson, 1977], Cousins and Hewitt [Tatterson, 1977], Paras and Karabelas [Paras, 1991], Schubring's [Schubring, 2009b] and Alamu's [Alamu, 2010]; the experimental conditions of each of them will be described below. For Tatterson's data, the measurements were taken with the electrical probe technique in a horizontal channel of 0.305 m high and 0.025 m width. Paras and Karabelas data were obtained in a horizontal pipe of 5.068 cm of inner diameter; liquid film thickness along the pipe was measured using parallel-wire conductance probes. Schubring's data were taken with an optical technique; this non-intrusive technique uses the

pattern of diffuse light reflected from the liquid surface to determine the liquid film thickness; these experimental series covered measurements mainly in horizontal conditions[1] (3 series with inner diameters of 0.88, 1.51 and 2.63 cm, respectively), but also in vertical upward conditions (pipe of 2.34 cm of inner diameter). Finally, Alamu's data were taken on a vertical pipe with an inner diameter of 1.9 cm, the working fluids were air and a mixture of water and glycerin (dynamic viscosity of 3.6 mPa s and density of 1097 kg), at a pressure of 1.5 bars and ambient temperature.

This section is organized as follows: first, an initial analysis of the available experimental measurements, followed by the presentation of the new proposed correlation and, finally, the comparison of the experimental data with the correlations found in the open literature and with the new developed correlation.

2.5.1.1. Initial Analysis of Liquid Film Thickness from the Experimental Data

First, we present a previous analysis of the experimental data in order to have a general view of the liquid film thickness behavior in each experimental series. Figure 2.10 and Figure 2.11 display the liquid film thickness versus the gas superficial velocity with constant liquid velocity for Schubring's vertical data series, and the liquid film thickness versus the liquid superficial velocity with constant gas velocity for Schubring's horizontal data, respectively.

From both figures, it can be seen that, as gas velocity increases, a decrease in the liquid film thickness is produced and vice versa. Whereas for liquid superficial velocity, there is the opposite trend, as liquid superficial velocity increases (increase in total liquid mass flow) liquid film thickness increases too; although this tendency becomes less noticeable as the gas velocity increases, until it becomes practically constant for high gas velocities. This trend can be seen very clearly in Figure 2.11, which shows that, for low superficial gas velocities, the trend lines are ranked in a decreasing thickness order. While with the increase of gas velocity this trend breaks, being liquid film thicknesses greater for higher gas velocities. For example, the lowest thicknesses are measured experimentally for gas velocities of 60-52 m/s, whereas for higher gas velocities (89-79, 79-70 and 70-58 m/s) the liquid film thicknesses are greater. The same trends that have been explained previously are observed for Alamu's experimental data, in this case for a mixture of water and glycerin, as can be seen in Figure 2.12.

[1] The horizontal Schubring's experimental data of the liquid film thickness were measured in bottom (δ_{bottom}), side (δ_{side}) and top (δ_{top}) of the test section, consequently a mean film thickness has been used to correlate these data. This magnitude is defined as $\delta_{experimental} = \frac{\delta_{bottom} + 2\delta_{side} + \delta_{top}}{4}$.

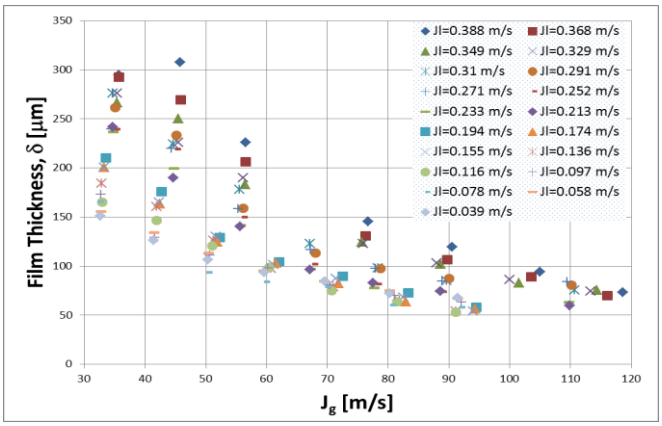

Figure 2.10. Schubring's experimental Liquid Film Thickness data vs. Superficial Gas Velocity (Vertical Upward Flow, D=0.0234 m, P & T ambient, Working fluids: Air-Water) with constant liquid velocity.

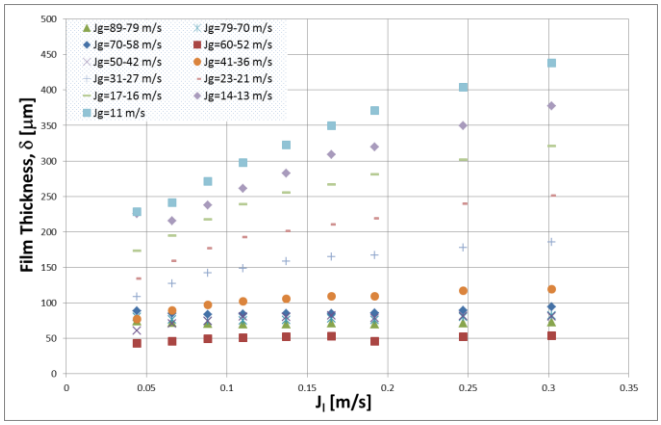

Figure 2.11. Schubring's experimental Liquid Film Thickness data vs. Superficial Liquid Velocity (Horizontal Flow, D=0.0088 m, P & T ambient, Working fluids: Air-Water) with "constant" gas velocity (actually the gas velocity was somewhat higher for higher liquid mass flows, the range is indicated in the Figure legend).

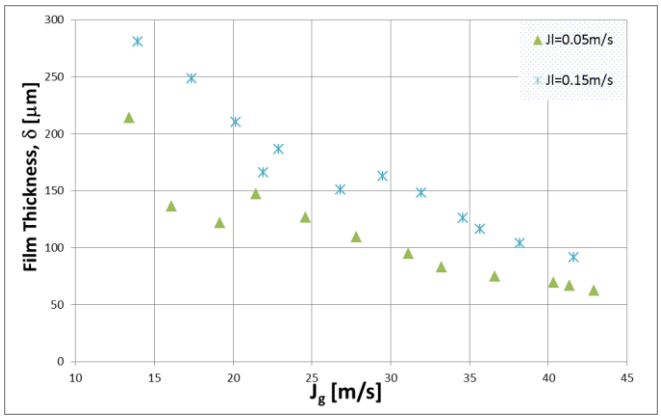

Figure 2.12. Alamu's experimental Liquid Film Thickness data vs. Superficial Gas Velocity (Vertical Upward Flow, D=0.019 m, P=1.4 bars, T ambient, Working fluids: Air-Water-Glycerin) with constant liquid velocity.

2.5.1.2. New Correlation of Liquid Film Thickness

From the experimental data discussed above, a large number of adjustments have been made in order to correlate the liquid layer film thickness with the physical properties and conditions under which the experiments have been carried out. In particular, we have taken as variables for the adjustment the corresponding dimensionless numbers, in order to obtain more general relationships. For the determination of these dimensionless numbers have been needed, as mentioned above, the physical properties of the working fluids and the conditions of the experiments, namely gas and liquid superficial velocities, densities and dynamic viscosities for both fluids, and surface tension of the liquid phase (obtained from the experimental pressure and temperature conditions and from the working fluids composition). Thus, finally, the new correlation obtained is

$$\frac{\delta}{D} = 7.165 \cdot \mathrm{Re}_g^{-1.07}\, \mathrm{Re}_l^{0.48} \left(\frac{Fr_g}{Fr_l} \right)^{0.24} \qquad \textbf{Eqn. (2.86)}$$

where, for the gas and liquid phases, the Reynolds and Froude numbers are defined by Eqn. (2.19), Eqn. (2.18), Eqn. (2.14) and Eqn. (2.21), respectively, in which these dimensionless numbers are defined in terms of superficial velocities.

The fitting of the new correlation with the experimental data shown in the previous section is presented in Figure 2.13. As can be seen in the figure, the new correlation produces a reasonable fitting for all experimental data, as they almost collapse to the correlation's line. In fact, almost all of them are located between the error lines of ±25%, with a value for the Pearson product-moment correlation coefficient of R^2=0.902.

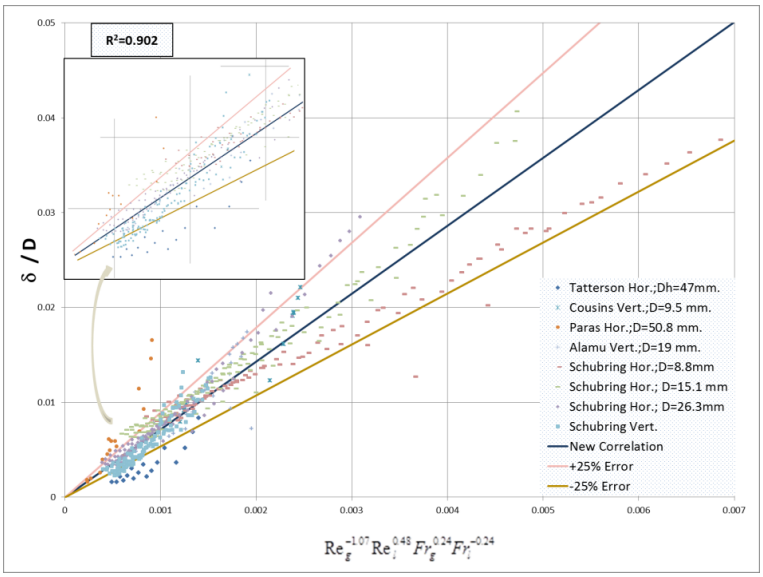

Figure 2.13. Comparison of liquid film thickness experimental data with the new correlation developed in the present study.

2.5.1.3. Comparison of Liquid Film Thickness Correlations with Experimental Data

This section is devoted to compare the results obtained with the available correlations, including the new correlation presented earlier, Eqn. (2.86), with the experimental data (for more details see Section 2.2.1 and Table 2.3). The next figures, from Figure 2.14 to Figure 2.17, show the variation of the liquid film thickness with the superficial liquid velocity, maintaining constant the gas superficial velocity and vice versa. In all figures, in order to calculate the liquid film thickness, the liquid Reynolds number has been employed in terms of the superficial liquid velocity. This has been done this way to have more simple equations, due to the fact that the entrained fraction, E, is not usually available in the experimental measurements. But to see the difference between the two possibilities, the Okawa's expression has been presented in both forms. For the estimation of E, the article of Cioncolini and Thome [Cioncolini, 2010] and the Mantilla's Thesis [Mantilla, 2008] can be consulted.

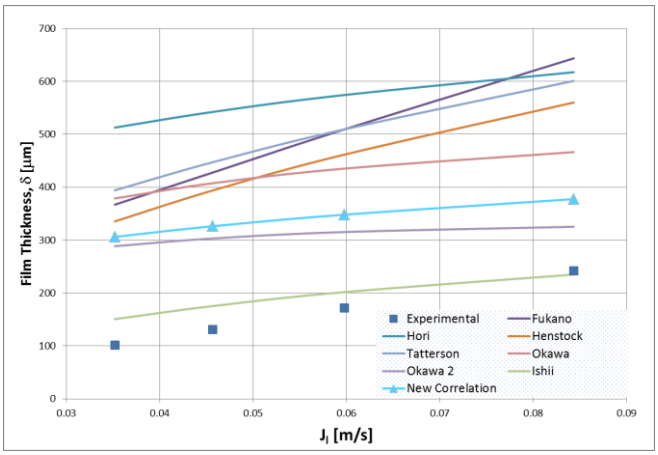

Figure 2.14. Comparison of Liquid Film Thickness vs. Superficial Liquid Velocity of Tatterson's data (Horizontal Flow, Channel 0.305x0.025 m, P & T ambient, $J_g \cong 35$ m/s) for the available correlations.

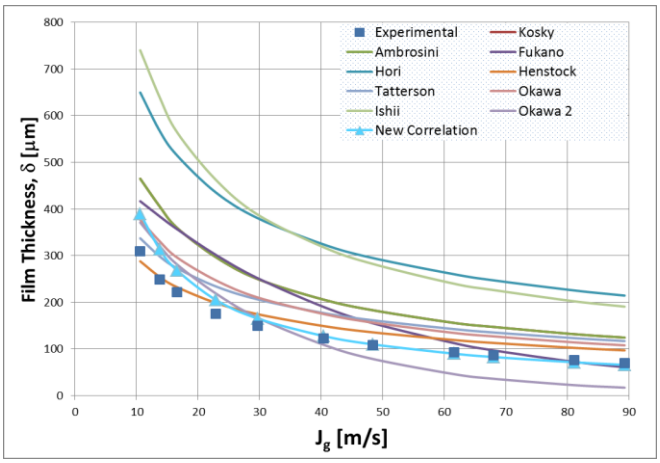

Figure 2.15. Comparison of Liquid Film Thickness vs. Superficial Gas Velocity of Schubring's horizontal data (Horizontal Flow, D=0.0088 m, P & T ambient, $J_l = 0.192$ m/s) for the available correlations.

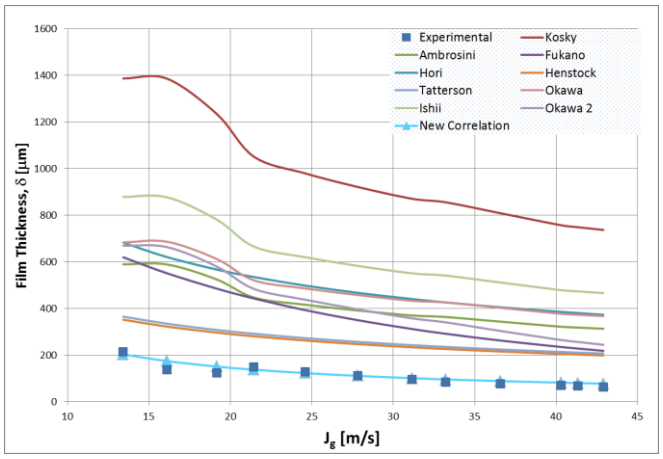

Figure 2.16. Comparison of Liquid Film Thickness vs. Superficial Gas Velocity of Alamu's data (Vertical Flow, D=0.019 m, P=1.4 bar & T ambient, J_l = 0.05 m/s, Air-Water-Glycerin) for the available correlations.

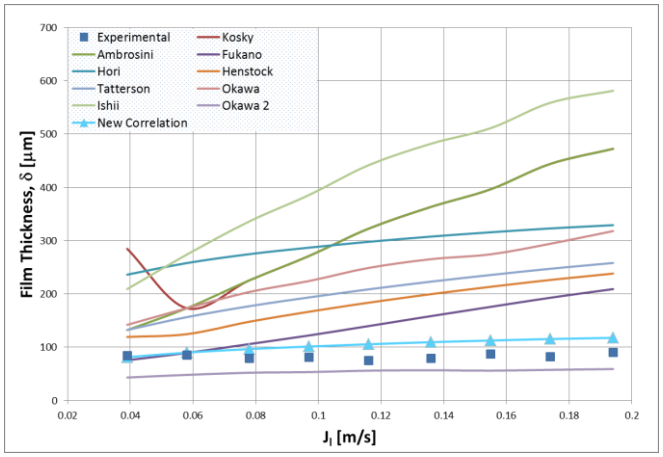

Figure 2.17. Comparison of Liquid Film Thickness vs. Superficial Liquid Velocity of Schubring's vertical data (Vertical Upward Flow, D=0.0234 m, P & T ambient, $J_g \cong 71$ m/s) for the available correlations.

Table 2.3. Summary of correlations for the liquid film thickness.

Reference	Correlation
Ambrosini [Rodriguez, 2009]	$\delta_l^+ = \frac{\rho_l \delta u_l^*}{\mu_l} = \begin{cases} 0.34\mathrm{Re}_{lf}^{0.6} & \mathrm{Re}_{lf} \le 1000 \\ 0.0512\mathrm{Re}_{lf}^{0.875} & \mathrm{Re}_{lf} > 1000 \end{cases}$ Eqn. (2.12) $u_l^* = \sqrt{\frac{\tau_i}{\rho_l}}$ $\tau_i = \frac{1}{2} f_{gi} \rho_g \left(u_g - u_{lf}\right)^2$
Fukano [Fukano, 1998]	$\frac{\delta}{D} = 0.0594\exp(-0.34 Fr_g^{0.25} \mathrm{Re}_l^{0.19} x^{*0.6})$ Eqn. (2.13) $x^* = \frac{J_g \rho_g}{J_g \rho_g + J_l \rho_l}$
Hori [Fukano, 1998]	$\frac{\delta}{D} = 0.905 \mathrm{Re}_g^{-1.45} \mathrm{Re}_l^{0.90} Fr_g^{0.93} Fr_l^{-0.68} \left(\frac{\mu_l}{\mu_{l,ref}}\right)^{1.06}$ Eqn. (2.20)
Henstock [Henstock, 1976]	Vertical Flows $\frac{\delta}{D} = \frac{6.59F}{(1+1400F)^{0.5}}$ Eqn. (2.22) Horizontal Flows $\frac{\delta}{D} = \frac{6.59F}{(1+850F)^{0.5}}$ Eqn. (2.23) $F = \frac{1}{\sqrt{2}\mathrm{Re}_g^{0.4}} \frac{\mathrm{Re}_l^{0.5}}{\mathrm{Re}_g^{0.9}} \frac{\mu_l}{\mu_g} \frac{\rho_g^{0.5}}{\rho_l^{0.5}}$
Tatterson [Tatterson, 1977]	Vertical Flows $\frac{\delta}{D} = \frac{6.59F}{(1+1400F)^{0.5}}$ Eqn. (2.22) Horizontal Flows $\frac{\delta}{D} = \frac{6.59F}{(1+850F)^{0.5}}$ Eqn. (2.23) $F = \frac{\gamma(\mathrm{Re}_{lf})}{\mathrm{Re}_g^{0.9}} \frac{\mu_l}{\mu_g} \frac{\rho_g^{0.5}}{\rho_l^{0.5}}$ $\gamma(\mathrm{Re}_{lf}) = \left[\left(0.707\mathrm{Re}_{lf}^{0.5}\right)^{2.5} + \left(0.0379\mathrm{Re}_{lf}^{0.9}\right)^{2.5}\right]^{0.4}$

Roberts [Roberts, 1997]	$\delta = 846 \frac{D}{D_{ref}} \frac{\mathrm{Re}_{lf}^{0.44}}{\mathrm{Re}_g^{0.59}}$	Eqn. (2.27)
Okawa [Okawa, 2002]	$\delta = \frac{1}{4} \sqrt{\frac{f_w \rho_l}{f_{gi} \rho_g}} \frac{J_{lf}}{J_g} D$	Eqn. (2.28)
Ishii [Ishii, 1976]	$\delta = 0.347 \mathrm{Re}_{lf}^{2/3} \sqrt{\frac{\rho_l}{\tau_i}} \frac{\mu_l}{\rho_l}$	Eqn. (2.29)
New Correlation [Berna, 2014]	$\frac{\delta}{D} = 7.165 \cdot \mathrm{Re}_g^{-1.07} \mathrm{Re}_l^{0.48} \left(\frac{Fr_g}{Fr_l} \right)^{0.24}$	Eqn. (2.86)

Figure 2.14 displays the comparison of Tatterson's experimental measurements with the values predicted by several correlations studied, and by the new one proposed correlation. As can be seen, Ishii's correlation gives the best results, followed by Okawa's[2], and the new proposed correlation, being the remaining correlations further from the experimental measurements. We have presented this figure first to indicate that the new correlation is not the best fit for this experimental series, as well as some cases of Paras's series. But for the newest experimental measurements of Alamu (made with a mixture of water and glycerin in standpipe) and for all Schubring's series (made for both horizontal and vertical flow in the latter case for 3 different sizes of pipe with about 500 experimental values), the adjustments are really good, as can be seen in Figure 2.15, Figure 2.16 and Figure 2.17. In these last cases, the Kosky's and Ambrosini's correlations presented earlier, which are the ones that best fitted Tatterson's series, present significant deviations. We must conclude by saying that the new correlation provides better results than the other ones studied, although in certain specific cases some of the other correlations provide more accurate results.

2.5.2. Wave Celerity

In the present section, we have analyzed the following experimental data series: Mantilla's[3] [Mantilla, 2008], Schubring's [Schubring, 2009b] and Alamu's [Alamu, 2010]. The experimental conditions of Schubring's and Alamu's measurements have been introduced in the previous section. Whereas Mantilla's experimental conditions were the following: all measurements were conducted in horizontal pipes, the air-water series were

[2] The difference between the called Okawa and Okawa 2 correlations during all the present section is that Okawa's correlation is obtained from Eqn. (2.28), but without taking into consideration the entrained fraction, that is E=0; whereas Okawa 2 has been obtained using directly Eqn. (2.28), in which E must be estimated from a correlation.

[3] Mantilla's experimental data include measurements of wave celerity below the onset of entrainment, which have not been used for the realization of the settings, since this point marks the beginning of droplet entrainment processes.

made in pipes of 4.86 and 15.3 cm of inner diameters, while the air-water-butanol and air-water-glycerin-salt were made only for the 4.86 cm pipe. The temperature in all cases was ambient conditions, whereas pressure was ambient for air-water series in the 15.3 cm pipe, and 2 bars for the rest of measurements.

This section is organized in the same way as the previous one. First, an initial analysis of the available experimental measurements, followed by the presentation of the new proposed correlation and, finally, the comparison of the experimental data with the correlations found in the open literature, and with the new developed correlation.

2.5.2.1. Initial Analysis of Wave Celerity from the Experimental Data

In order to have a general view of the wave celerity behavior in each experimental series, a previous analysis has been done. In Figure 2.18 it is shown the wave celerity versus the gas superficial velocity with constant liquid velocity for a 1.51 cm diameter pipe under horizontal flow conditions (Schubring's experimental measurements). From the figure, it can be seen that, as gas velocity increases, an increase in the wave celerity is produced, and the wave celerity increases when the liquid superficial velocity increases too. But only is applicable for low gas velocities, because this increase with liquid velocity becomes smaller, until it disappears for higher gas velocities. Whereas for vertical upward data (Schubring's experimental measurements presented in Figure 2.19), it can be seen that, in general, there is an increasing trend of wave celerity for both gas and liquid superficial velocities. While, for intermediate values of liquid velocity, in some cases the mentioned increase does not occur, but stabilizes. For mixtures of water with glycerin and water with butanol, being for vertical and horizontal flows, respectively, it is noted that wave celerity increases with gas and liquid superficial velocities, see Figure 2.20 and Figure 2.21. The same trend is observed for all the analyzed experimental series. Therefore, it can be said that this is the general trend of wave celerity with gas and liquid superficial velocities.

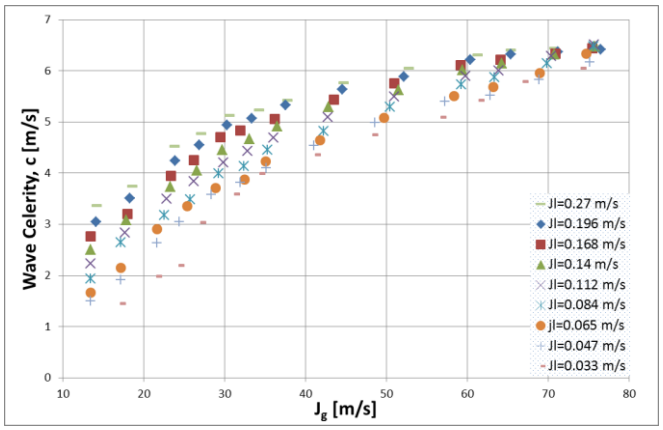

Figure 2.18. Schubring's experimental Wave Celerity data vs. Superficial Gas Velocity (Horizontal Flow, D=0.0151 m, P & T ambient, Working fluids: Air-Water) with constant liquid velocity.

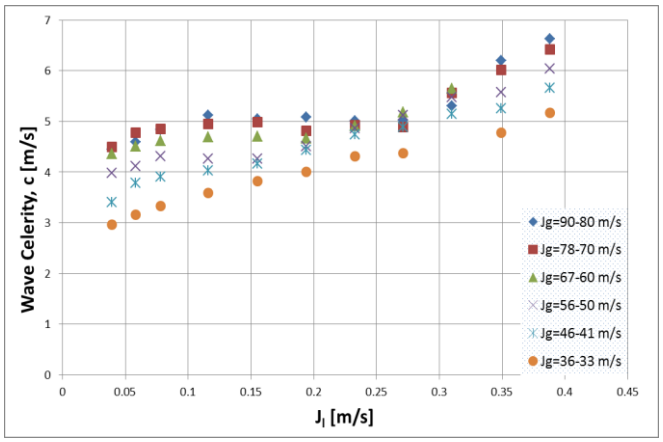

Figure 2.19. Schubring's experimental Wave Celerity data vs. Superficial Liquid Velocity (Vertical Upward Flow, D=0.0234 m, P & T ambient, Working fluids: Air-Water) with constant gas velocity.

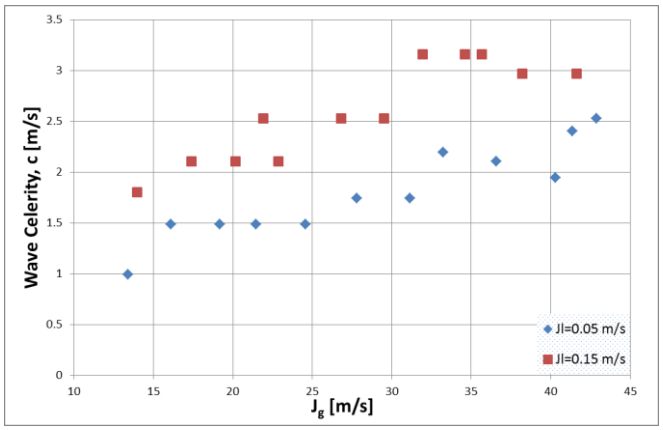

Figure 2.20. Alamu's experimental Wave Celerity data vs. Superficial Gas Velocity (Vertical Upward Flow, D=0.019 m, P=1.4 bars, T ambient, Working fluids: Air-Water-Glycerin) with constant liquid velocity.

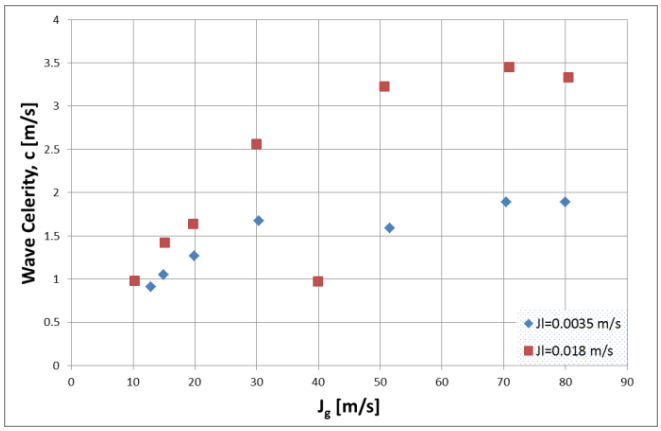

Figure 2.21. Mantilla's experimental Wave Celerity data vs. Gas Superficial Velocity (Horizontal Flow, D=0.0486 m, P=2 bars, T ambient, Working fluids: Air-Water-Butanol), effect of liquid velocity with constant liquid velocity.

2.5.2.2. New Correlation of Wave Celerity

From the experimental data discussed above, a large number of adjustments have been made in order to correlate wave celerity with physical properties and conditions at which the experiments have been carried out. In particular, we have taken as variables for the adjustment the corresponding dimensionless numbers, in order to obtain more general relationships. For the determination of these dimensionless numbers, it have been needed, as mentioned above, the physical properties of the working fluids and the conditions of the experiments, namely gas and liquid superficial velocities, densities and dynamic viscosities

for both fluids, and surface tension of the liquid phase (obtained from the experimental pressure and temperature conditions and composition of the working fluids). Regarding to wave celerity normalization, various possibilities have been studied, such as: dividing by gas superficial velocity, the square root of gas and liquid velocities product, etc., but the final choice is the one shown below. Then, the new correlation is

$$\frac{c}{\frac{\sqrt{\rho_g}J_g+\sqrt{\rho_l}J_l}{\sqrt{\rho_g}+\sqrt{\rho_l}}} = 50\cdot \mathrm{Re}_g^{-0.38}\,\mathrm{Re}_l^{0.16}\,C_W^{-0.13} \qquad \textbf{Eqn. (2.87)}$$

where the gas and liquid Reynolds numbers are defined in terms of the gas and liquid superficial velocities, respectively, Eqn. (2.19) and Eqn. (2.18). The expression for the surface tension factor is the one defined originally by Ishii, Eqn. (2.38).

The fitting of the proposed new correlation with the experimental data shown in the previous section is presented in Figure 2.22. As can be seen in the figure, the new correlation produces a reasonable fitting of all experimental data, as they collapse almost all data to the correlation's line. In fact, almost all of them are located between the error lines of ±25%, with a value for the Pearson product-moment correlation coefficient of R^2=0.885.

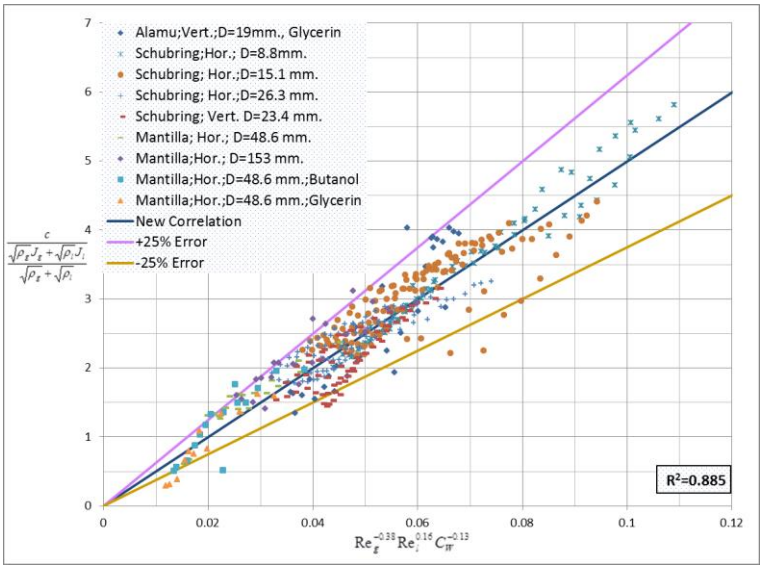

Figure 2.22. Comparison of experimental data of wave celerity with the new correlation developed in the present study.

2.5.2.3. Comparison of Wave Celerity Correlations with Experimental Data

This section is devoted to compare the results for wave celerity obtained with the available correlations, including the new correlation presented earlier Eqn. (2.87), with the experimental data (for more details see section 2.2.2.4 and Table 2.4). The next figures, from Figure 2.23 to Figure 2.26, show the variation of the wave celerity with the superficial liquid velocity, maintaining constant the gas superficial velocity and vice versa.

Table 2.4. Summary of correlations for the wave celerity.

Reference	Correlation	
Kumar [Mantilla, 2008]	$c = \frac{\psi \cdot J_g + J_l}{1+\psi}$ $\psi = 5.5\sqrt{\frac{\rho_g}{\rho_l}}\left(\frac{\mathrm{Re}_l}{\mathrm{Re}_g}\right)^{0.25}$	Eqn. (2.45)
Marmottant [Belt, 2010]	$c = \frac{\sqrt{\rho_g}J_g + \sqrt{\rho_l}J_l}{\sqrt{\rho_g}+\sqrt{\rho_l}}$	Eqn. (2.51)
Schubring [Schubring, 2009a]	$c = 0.41\frac{J_g}{\sqrt{x}}\mathrm{Re}_g^{-0.25}$ $x = \frac{\dot{m}_g}{\dot{m}_g + \dot{m}_l}$	Eqn. (2.52)
Al-Sarkhi [Al-Sarkhi, 2012a]	Horizontal $\frac{c}{J_l} = 2.379 \cdot X^{-0.9}$ Inclination 10-20º $\frac{c}{J_l} = 2.323 \cdot X^{-0.94}$ Inclination 45-90º $\frac{c}{J_l} = 1.942 \cdot X^{-0.91}$ $X = \sqrt{\frac{\rho_l J_l^2}{\rho_g J_g^2}}$	Eqn. (2.54) Eqn. (2.55) Eqn. (2.56)
New Correlation [Berna, 2014]	$\frac{c}{\frac{\sqrt{\rho_g}J_g + \sqrt{\rho_l}J_l}{\sqrt{\rho_g}+\sqrt{\rho_l}}} = 50 \cdot \mathrm{Re}_g^{-0.38}\mathrm{Re}_l^{0.16}C_W^{-0.13}$	Eqn. (2.87)

Figure 2.23 displays the comparison of Schubring's experimental measurements in a horizontal pipe with inner diameter of 1.51 cm, compared with the predictions done by several correlations. As can be seen, the correlation proposed in this work give the best results; only for low superficial gas velocities the Kumar's correlation is closer to the experimental data. The results obtained for Schubring's vertical upward data are displayed in Figure 2.24, but in this case, the figure shows the variation of wave celerity as function of superficial liquid velocity. As in the previous figure, the correlation proposed in the present article gives quite good results, especially for low superficial liquid velocities, while for higher values the correlation of Kumar gives the best results. For Alamu's measurements, Figure 2.25, with vertical upward conditions and a mixture of water and glycerin, the situation is quite similar to the previous figure. In this case, the new correlation proposed here gives somewhat higher values than the experimental ones, whereas the expression of Kumar gives slightly lower values, although the predictions of the equation developed here is slightly closer. Finally, Figure 2.26 displays the results for Mantilla's data of a water-butanol mixture. In this case the correlations that are closer to the experimental measurements are also the Kumar and the one developed in this paper. We must conclude by saying that the new correlation provides better results than other correlations studied, although Kumar's expression presents good results too, being closer to the experimental measurements.

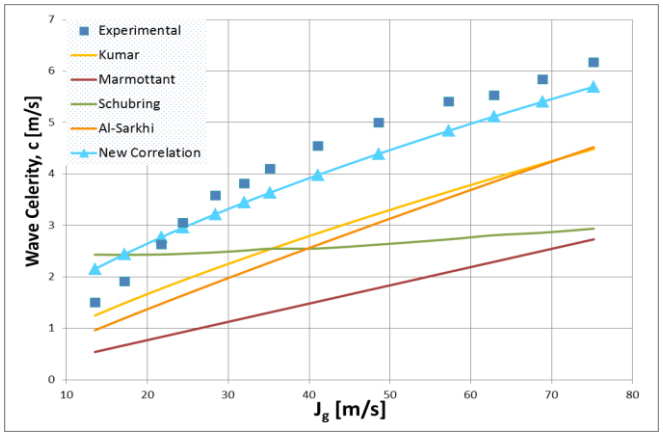

Figure 2.23. Comparison of Wave Celerity vs. Superficial Gas Velocity of Schubring's horizontal data (Horizontal Flow, D=0.0151 m, P & T ambient, J_l = 0.065 m/s) for the available correlations.

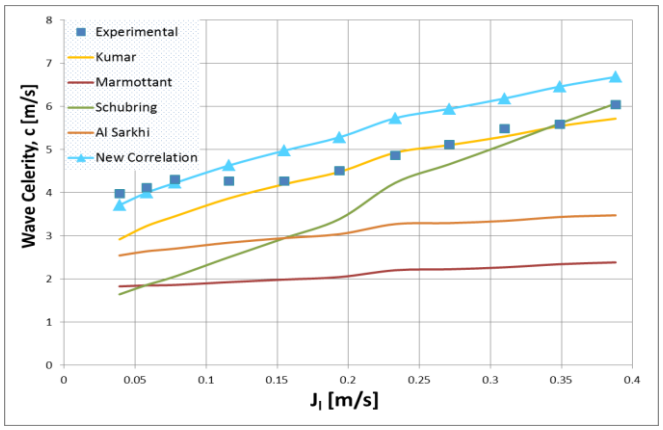

Figure 2.24. Comparison of Wave Celerity vs. Superficial Liquid Velocity of Schubring's data (Vertical Upward Flow, D=0.0234 m, P & T ambient, Working fluids: Air-Water, $J_g \cong$ 56-60 m/s) for the available correlations.

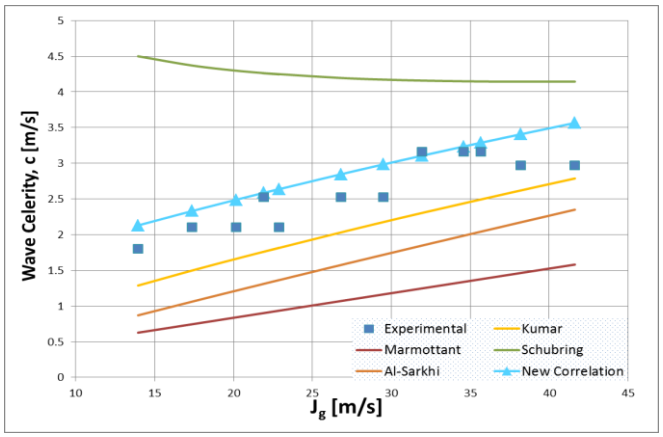

Figure 2.25. Comparison of Wave Celerity vs. Superficial Gas Velocity of Alamu's data (Vertical Upward Flow, D=0.019 m, P=1.4 bars, T ambient, Working fluids: Air-Water-Glycerin, J_l = 0.15 m/s) for the available correlations.

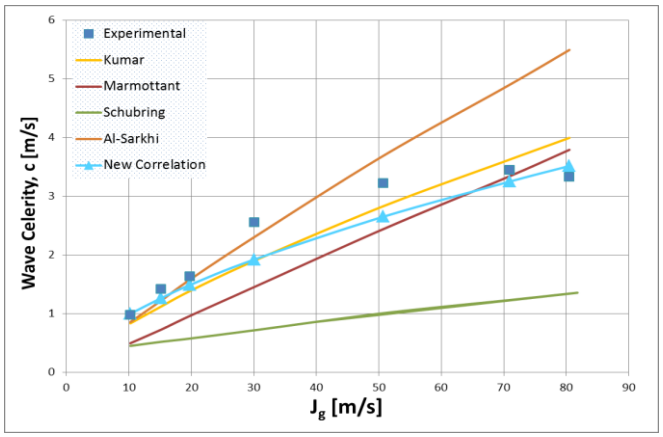

Figure 2.26. Comparison of Wave Celerity vs. Superficial Gas Velocity of Mantilla's data (Horizontal Flow, D=0.0486 m, P=2 bars, T ambient, Working fluids: Air-Water-Butanol, J_l = 0.018 m/s) for the available correlations.

2.5.3. Wave Frequency

The experimental series analyzed in order to study the frequency of the waves that appear on the gas-liquid surface are the same ones that have been used to correlate the wave celerity in the previous section, that is to say: Mantilla's[4] [Mantilla, 2008], Schubring's [Schubring, 2009b] and Alamu's [Alamu, 2010] measurement series.

This section is organized in the same way as the two previous sections. First, an initial analysis of the available experimental measurements, followed by the presentation of the new proposed correlation and, finally, the comparison of the experimental data with the correlations found in the open literature, and with the new developed correlation.

2.5.3.1. Initial Analysis of Wave Frequency from the Experimental Data

In order to have a general view of the wave frequency behavior in each experimental series, a previous analysis has been done. In Figure 2.27 it is plotted the wave frequency versus the liquid superficial velocity with constant gas velocity for horizontal flow conditions with the 2.63 cm diameter pipe of Schubring's data. From the figure, it can be deduced that, for higher values of gas superficial velocity; as liquid velocity increases, an increase in the wave frequency is produced. However, the slope of this increase reduces progressively until, at about 30 m/s, is almost flat, and below this value, the wave frequency decreases with the increase of liquid superficial velocity. As can be seen in the figure, the wave frequency also increases with gas superficial velocity at constant liquid superficial velocities. Whereas for vertical upward data (Schubring's experimental measurements

[4] As in the wave celerity, Mantilla's experimental data include measurements of wave frequency below the onset of entrainment, which have not been used for the realization of the settings.

presented in Figure 2.28), it can be seen that, in general, there is an increasing trend of wave frequency with gas superficial velocity, but the slope of this increase is smaller for bigger superficial liquid velocities. However, at low values of gas and liquid superficial velocities there are lower frequencies, whereas higher gas superficial velocities and lower liquid superficial velocities produce higher waves frequencies. For mixtures of water with butanol in horizontal flow conditions (Mantilla's series), there is the opposite tendency, as explained in the previous lines, see Figure 2.29. While Alamu's measurements, Figure 2.30, which used as working liquid a mixture of water-glycerin in vertical flow conditions, there is a lower wave frequency with lower gas and liquid superficial velocities, having a steeper slope for the higher value of the liquid superficial velocity. These last two statements must be made with appropriate caution, as only two different liquid rates are available.

The same trend is observed for all the analyzed experimental series. Therefore, it can be said that there is a general increasing trend of wave frequency with gas and liquid superficial velocities, except for low gas superficial velocities in Schubring's measurements, made in horizontal flow conditions, in which the tendency is in the opposite direction.

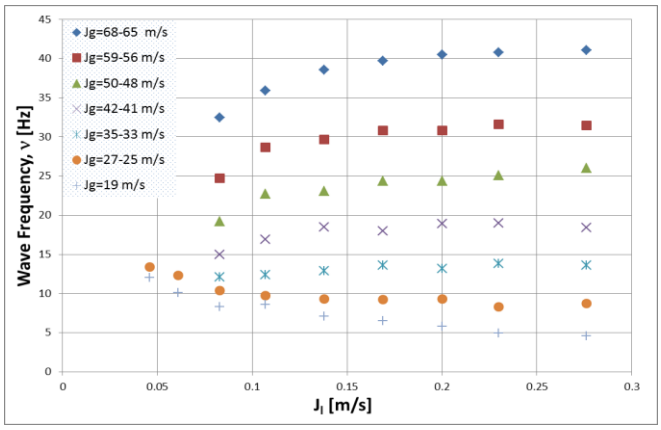

Figure 2.27. Schubring's experimental Wave Frequency data vs. Superficial Liquid Velocity (Horizontal Flow, D=0.0263 m, P & T ambient, Working fluids: Air-Water) with "constant" gas velocity.

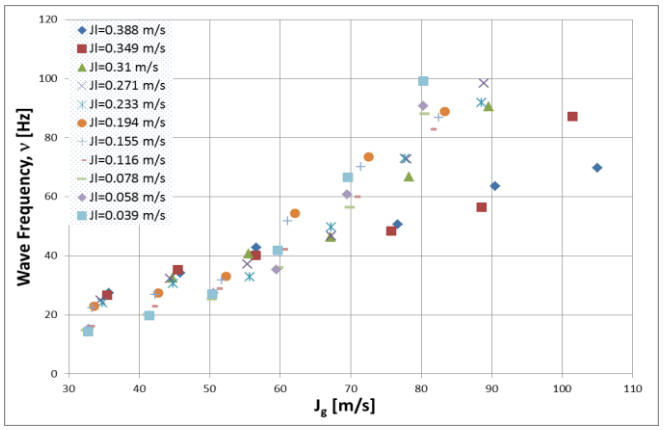

Figure 2.28. Schubring's experimental Wave Celerity data vs. Superficial Gas Velocity (Vertical Upward Flow, D=0.0234 m, P & T ambient, Working fluids: Air-Water) with constant liquid velocity.

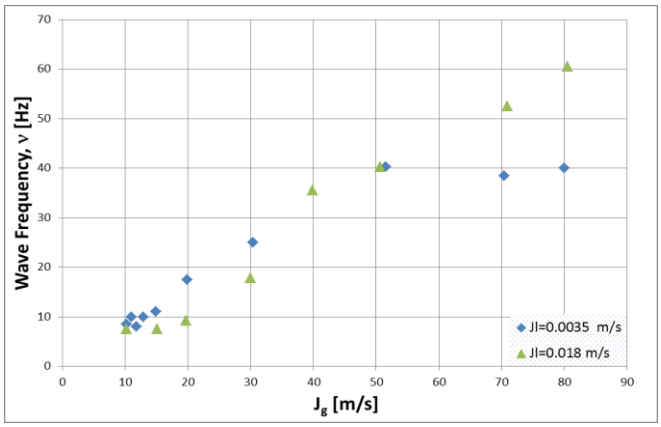

Figure 2.29. Mantilla's experimental Wave Celerity data vs. Gas Superficial Velocity (Horizontal Flow, D=0.0486 m, P=2 bars, T ambient, Working fluids: Air-Water-Butanol), effect of liquid velocity with constant liquid velocity.

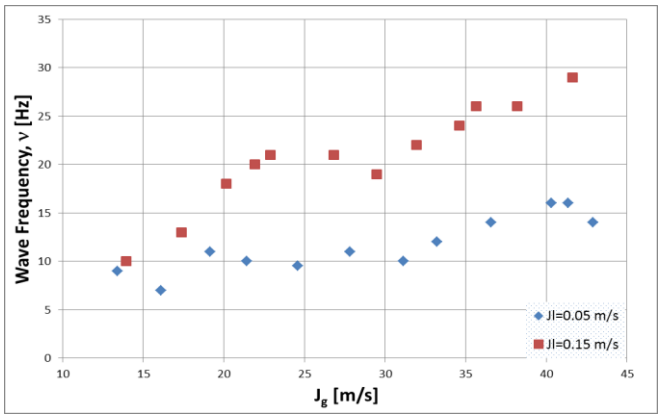

Figure 2.30. Alamu's experimental Wave Celerity data vs. Superficial Gas Velocity (Vertical Upward Flow, D=0.019 m, P=1.4 bars, T ambient, Working fluids: Air-Water-Glycerin) with constant liquid velocity.

2.5.3.2. New Correlation for the Wave Frequency

From the experimental data discussed above, a large number of adjustments have been made in order to correlate wave frequency with physical properties and conditions in which the experiments have been carried out. In particular, we have taken as variables for the adjustment the corresponding dimensionless numbers, in order to obtain more general relationships. For the determination of these dimensionless numbers, has been needed, as mentioned above, the physical properties of the working fluids and the conditions of the experiments, namely gas and liquid superficial velocities, densities and dynamic viscosities for both fluids, and surface tension of the liquid phase (obtained from the experimental pressure and temperature conditions, and from the working fluids composition). Then, the new correlation proposed is

$$St_{gl} = 1.38 \cdot 10^{-2}\, \mathrm{Re}_g^{0.53}\, \mathrm{Re}_l^{-0.48}\, Eo^{0.27} \left(\frac{\rho_g}{\rho_l}\right)^{0.14} C_W^{0.68} \qquad \textbf{Eqn. (2.88)}$$

where St_{gl} is the gas-liquid Strouhal number, which has been defined in the same way that liquid Strouhal number, Eqn. (2.59), and gas Strouhal number, Eqn. (2.62), St_{gl} is defined as

$$St_{gl} = \frac{\upsilon D}{\sqrt{J_g \cdot J_l}} \qquad \textbf{Eqn. (2.89)}$$

where the gas and liquid Reynolds numbers are defined in terms of the gas and liquid superficial velocities, respectively, Eqn. (2.19) and Eqn. (2.18). The Eötvös number is

defined by Eqn. (2.63). The expression of the surface tension factor is the same one as originally defined by Ishii, Eqn. (2.38).

The fitting of the proposed new correlation with the experimental data shown in the previous section is presented in Figure 2.31. As can be seen in the figure, the new correlation does not produce a quite good fitting of the experimental data, but it collapses almost all data between the error lines of ±50%, with a value for the Pearson product-moment correlation coefficient of R^2=0.683.

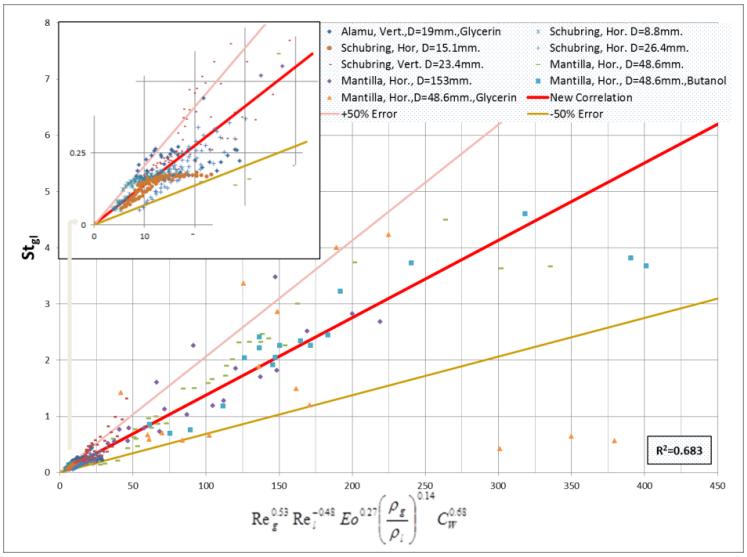

Figure 2.31. Comparison of experimental data of wave frequency with the new correlation developed in the present study.

2.5.3.3. Comparison of Wave Frequency Correlations with Experimental Data

This section is devoted to compare the experimental results for the wave frequency with the results obtained with the available correlations, including the new correlation presented earlier Eqn. (2.88), (for more details see section 2.2.2.5 and Table 2.5).

As it is shown from Figure 2.32 to Figure 2.36, which display the experimental measurements and results of the correlations studied, the expression which gives better predictions of the experimental data is the correlation proposed in the present PhD report.

Generally speaking, we must say that there is an upward trend in wave frequency with both liquid and gas superficial velocities, which is well reproduced by the proposed correlation. This increase takes place for all working fluids and in all conditions studied, only in some specific cases of Schubring's measures for low gas velocities there is a decrease in wave frequency with increasing superficial liquid velocity, as noted above, see Figure 2.27. We must highlight the wide range of variation that presents this magnitude,

from low values in the range of 3-5 m/s for pipe 15.3 cm in diameter, Figure 2.34, to values hovering around 100 m/s for some Schubring's series at high gas velocities, Figure 2.33. Also we must mention the good agreement obtained with the proposed correlation for working liquids different to water, concretely mixtures of water with butanol, and water with glycerin, Figure 2.35 and Figure 2.36. In all cases, the correlation proposed here provides a suitable outcome, note that Azzopardi's correlation also gives good estimations for most cases, except for the measurements performed in the larger diameter pipes (Mantilla's measurements series in a pipe diameter of 15.3 cm). Finally, we must conclude that the correlation proposed here shows a better performance than the other expressions found in the literature.

Table 2.5. Summary of correlations for the wave frequency.

Reference	Correlation	
Azzopardi [Azzopardi, 2006]	$St_l = 0.25X^{-1.2}$ $St_l = \frac{\upsilon D}{J_l}$	Eqn. (2.58)
Sekoguchi [Sawant, 2008b]	$St_g = \frac{\upsilon D}{J_g} = f_1(Eo) f_2\left(\mathrm{Re}_l, Fr_g\right)$ $Eo = \frac{gD^2\left(\rho_l - \rho_g\right)}{\sigma}$ $f_1(Eo) = Eo^{-0.5}[0.5Ln(Eo) - 0.47]$ $f_2\left(\mathrm{Re}_l, Fr_g\right) = 0.0076Ln\left(\frac{\mathrm{Re}_l^{2.5}}{Fr_g}\right) - 0.051$	Eqn. (2.62)
Sawant [Sawant, 2008b]	$St_g = 0.086\mathrm{Re}_l^{0.27}\left(\frac{\rho_l}{\rho_g}\right)^{-0.64}$	Eqn. (2.65)
New Correlation [Berna, 2014]	$St_{gl} = 1.38\cdot 10^{-2}\,\mathrm{Re}_g^{0.53}\,\mathrm{Re}_l^{-0.48}\,Eo^{0.27}\left(\frac{\rho_g}{\rho_l}\right)^{0.14} C_W^{0.68}$ $St_{gl} = \frac{\upsilon D}{\sqrt{J_g \cdot J_l}}$ $C_W = \begin{cases} 0.028N_\mu^{-4/5} & for \quad N_\mu \le 1/15 \\ 0.25 & for \quad N_\mu > 1/15 \end{cases}$ $N_\mu = \frac{\mu_l}{\left(\rho_l \sigma \sqrt{\frac{\sigma}{g\,\Delta\rho}}\right)^{1/2}}$	Eqn. (2.88)

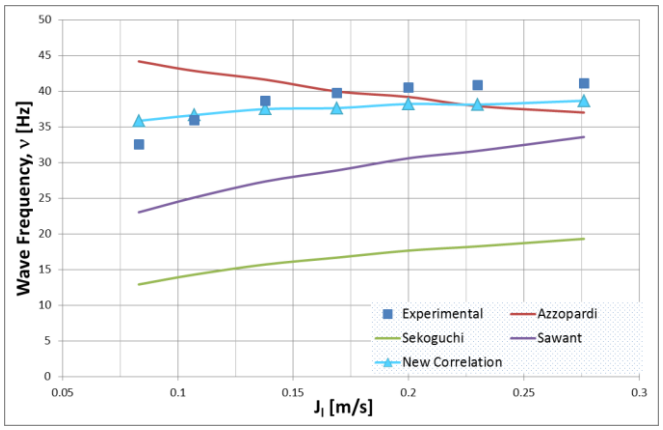

Figure 2.32. Comparison of Wave Frequency vs. Superficial Liquid Velocity of Schubring's horizontal data (Horizontal Flow, D=0.0263 m, P & T ambient, $J_g \cong$ 66 m/s) for the available correlations.

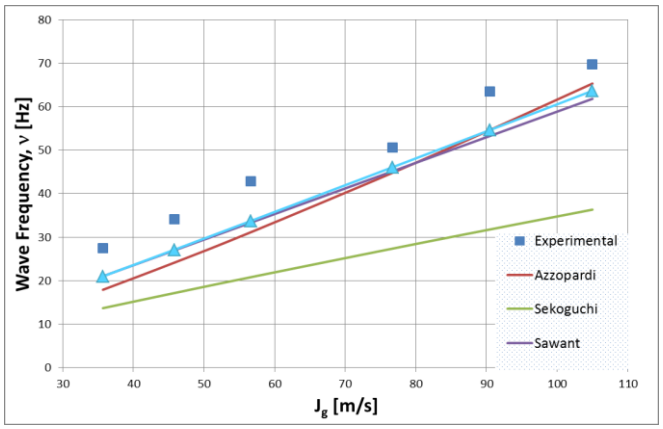

Figure 2.33. Comparison of Wave Frequency vs. Superficial Gas Velocity of Schubring's data (Vertical Upward Flow, D=0.0234 m, P & T ambient, Working fluids: Air-Water, J_l = 0.388 m/s) for the available correlations.

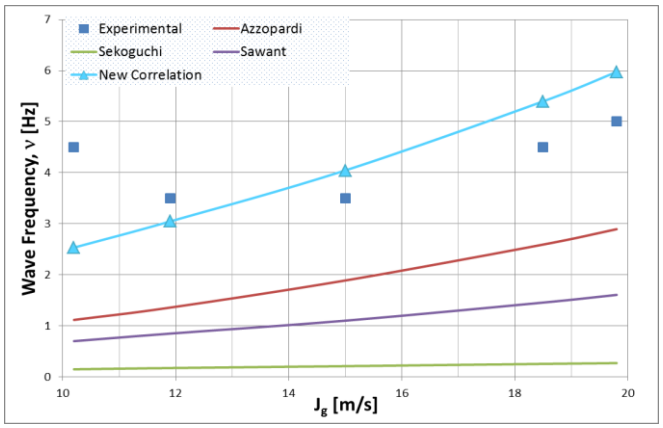

Figure 2.34. Comparison of Wave Frequency vs. Superficial Gas Velocity of Mantilla's horizontal data (Horizontal Flow, D=0.153 m, P & T ambient, J_l = 0.018 m/s) for the available correlations.

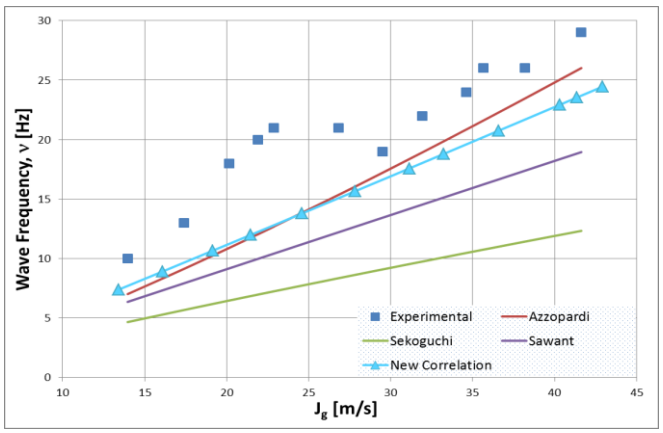

Figure 2.35. Comparison of Wave Frequency vs. Superficial Gas Velocity of Alamu's data (Vertical Upward Flow, D=0.019 m, P=1.4 bars, T ambient, Working fluids: Air-Water-Glycerin, J_l = 0.15 m/s) for the available correlations.

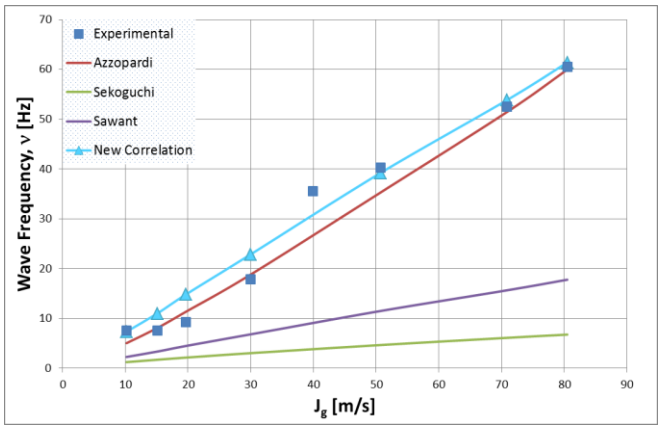

Figure 2.36. Comparison of Wave Frequency vs. Superficial Gas Velocity of Mantilla's data (Horizontal Flow, D=0.0486 m, P=2 bars, T ambient, Working fluids: Air-Water-Butanol, J_l = 0.018 m/s) for the available correlations.

2.6. Conclusions

An in-depth characterization of liquid and liquid-gas interface is mandatory for a thorough understanding of annular two-phase flow. An extensive review of phenomena, together with a collection and analysis of data found in the open literature for key variables defining the liquid-gas interface, have been described in the present paper.

Liquid-gas interface shows a wavy structure that very much depends on the liquid and gas flow rates magnitudes. A thorough review of their properties (i.e., amplitude and frequency) has been done in previous sections.

In the present work, a number of insights into key two-phase flow variables have been drawn, either from analyses reported in the literature or from new analysis that have yielded new correlations for those variables:

A) Liquid Film Thickness

Liquid film thickness decreases with increasing superficial gas velocity, although this decrease becomes smaller for higher gas velocities. Liquid film thickness increases with superficial liquid velocity.

A new correlation to obtain the liquid film thickness as function of dimensionless numbers has been developed. Liquid film thickness has been made non-dimensional with pipe diameter and correlated with the dimensionless numbers which better fit the experimental results. In this case, these dimensionless numbers have been Reynolds and Froude numbers of gas and liquid phases. This new correlation has been compared to the

available ones found in the open literature and an improvement in the estimations of this magnitude has been achieved.

B) Wave celerity

Wave celerity increases when increasing superficial gas velocity, although this increase becomes slightly smaller for higher gas velocities.

Wave celerity increases with the decrease of liquid superficial velocity, although this increase is not large.

A new correlation to obtain the wave celerity as a function of dimensionless numbers has been developed. Wave celerity has been made non-dimensional with gas and liquid velocities averaged with their densities and correlated with the dimensionless numbers which better fit the experimental results. In this case, the dimensionless numbers used have been gas and liquid Reynolds numbers and the viscosity number. This correlation has been compared to the available ones found in the open literature and an improvement in the estimations of this magnitude has been achieved.

C) Wave frequency

Wave frequency is strongly influenced by the gas superficial velocity. An increase in this magnitude is produced with the increase of gas superficial velocity, although this increase becomes smaller for higher gas velocities.

Wave frequency is strongly influenced by liquid superficial velocity. This magnitude increases with the liquid superficial velocity, although for high gas superficial velocities, wave frequency remains constant.

A new correlation to obtain the wave frequency as a function of dimensionless numbers has been developed. We have obtained the wave frequency from the Strouhal number, but defined in terms of the geometric mean of gas and liquid superficial velocities. The Strouhal number has been correlated with the dimensionless numbers which better fit the experimental results. In this case, the dimensionless numbers used have been gas and liquid Reynolds numbers, the viscosity number and the density ratio. This correlation has been compared to the available expression found in the open literature, and an improvement in the estimation of this magnitude has been achieved.

Regarding the entrainment processes, when a gas is flowing over a liquid film, the gas-liquid interface may become unstable depending on the magnitude of the gas and liquid velocities. On one hand, there is the onset of entrainment Reynolds number, Re_{ffOE}, below which no entrainment is possible. Nevertheless, when looking through literature one may find numbers ranging from 80 to 500 for air-water systems in horizontal or vertical orientations. The most usual is 160, as proposed by Ishii and Grolmes. On the other hand, even if $Re_l > Re_{ffOE}$ condition is met, gas velocity should be greater than a given threshold for entrainment to take place. Several expressions to estimate this entrainment inception velocity (i.e., Kutateladze criterion, Ishii and Grolmes model, Sawant model, etc.) have been found and collected in this document.

We must finalize this work by emphasizing the development of new correlations for the key variables of annular two-phase flow, which produces a noticeable improvement, compared with those found in the open literature.

Chapter 3

CHARACTERIZATION OF THE ENTRAINED DROPLETS IN ANNULAR FLOW

3. APPROACH TO THE CHARACTERIZATION OF SUBMERGED GASEOUS JETS II: CHARACTERIZATION OF THE ENTRAINED DROPLETS IN ANNULAR FLOW

As in the previous section, due to the limited number of expressions to characterize submerged gaseous jets, expressions developed for annular flow have been used. This second section devoted to annular flow is focused on the characterization of the entrained droplets.

This chapter has been published in Progress in Nuclear Energy, Vol. 79, pp. 64-86, 2015 [Berna, 2015a].

Abstract

Annular flow is characterized by a thin liquid film flowing on the pipe wall and a high velocity gas core flowing in its center, which normally carries liquid droplets. This review presents and analyzes most of the extensive literature existing on the annular two-phase flow, focusing specifically on the analysis of the main phenomena that are involved. In particular, the paper focuses on the study of the liquid droplets that are entrained by the gas stream from the gas-liquid interface, due to the strong influence that these droplets exert in many important parameters of both, flow and heat transfer processes. Consequently, it is important to be able to know the maximum amount of information about them, in order to characterize droplets' size and velocity, and to determine the amount of them that are entrained into the gas stream and, finally, apply this knowledge in all processes in which annular flow is involved.

This review analyzes most of the extensive literature on droplets, specifically analyzes its main characteristics once they have been formed, such as its sizes, speeds and total amount. A vast amount of data has been found in the open literature and collected here. Their analysis leads to two major observations: their huge scattering and the existence of remaining knowledge gaps. Some of the experimental data have been also used to derive new correlations on variables as important as amount and size of entrained droplets.

3.1. Introduction

The study of two phase flows, and annular flow in particular, is important due to its relevance in many industrial processes; for instance, channel flow during steam generation processes, nuclear reactors and other power plants, heating and refrigeration equipment, such as, heat exchangers and condensers, gas-liquid mixers and gas-liquid separators, transportation of natural gas and crude oil, etcetera.

The annular flow, in both horizontal and vertical pipes, has been the subject of many theoretical studies. When describing the annular flow, one may split the scenario in three major features: the existence of a series of waves at the gas-liquid interface; the droplet entrainment into the gas core from the interface; and the subsequent deposition of a fraction of entrained droplets onto the gas-liquid interface. Recently, a first part of this work, with the main emphasis on interfacial waves and onset of entrainment, was published [Berna, 2014]. To close-up the study of two-phase annular flow, this paper is focused on the key parameters associated with the entrained droplets i.e., size, velocity and total amount. These parameters are studied in steady state conditions, that is, when entrainment and deposition processes reach the equilibrium.

A huge number of papers have been published previously on the matter tackled with in this paper. Given the review nature of this one, those papers with a major impact on the area will be referenced properly in next sections.

The present paper is structured as follows: sections 3.2 and 3.3 deal with equations characterizing droplet sizes and velocities; section 3.4 reviews the existing expressions for estimating the total amount of droplets entrained; section 3.5 analyzes the data and sets comparisons with preceding equations and other new ones derived in this paper; section 3.6 wraps up the whole paper with a number of conclusions.

3.2. Droplet Sizes

The determination of droplets sizes is one of the key parameters in order to describe the entrained process in annular flow, for this purpose an open literature search was carried out. When estimating the droplet size distribution should be noted that the aerodynamic break-up is an important mechanism for the description of two-phase flows associated with droplets suddenly exposed to a high speed gas stream. Detailed developments of the droplets break-up phenomenon can be found in several works, for instance, accurate descriptions are shown in Crowe [Crowe, 2006], Kolev [Kolev, 2007] and Azzopardi [Azzopardi, 1997].

The initial droplet sizes are determined by the mechanism from which have been generated, such as shearing off of roll-wave crests in the case of annular flow, or primary atomization in the case of sprays formation from a liquid jet or sheet. But, in addition to the formation mechanisms, when these droplets are surrounded by a continuous phase which is moving at a high relative velocity, the aerodynamic forces will cause the deformation and fragmentation of these droplets. Then the droplets with a diameter larger than the maximum stable size begin to oscillate, which finally results in the rupture of the droplet. Consequently, a distribution of smaller droplets is produced by the generation mechanisms (Appendix I).

The droplet break-up mechanisms can be expressed as a balance of forces between external stress forces and surface forces. External stress forces, which attempt to disrupt the

droplet and surface tension forces, which try to avoid droplet deformation. Consequently, the Weber number, which is the ratio between these two forces, has to be considered. A larger value of Weber number indicates that there is a higher tendency toward break-up. In this sense, equations estimating droplet sizes may be classified in two groups: those that are based on a critical Weber number (the one corresponding to the maximum stable droplet diameter) and correlations depending directly on fluid properties and dimensionless numbers. The basic model of the We group is the critical Weber number criterion, which sets We_{crit} to 12 (although experimental values range from 5 to 20 in low viscosity fluids, like water); other models just add a correction factor usually based on the viscosity effect on shear stresses on droplets. The second group expressions are diverse as for the target variable, some give the maximum stable diameter, while others correlate the mean or the Sauter diameter.

3.2.1. The Critical Weber Number

Based on experimental data it has been observed that water droplets break-up whenever Weber dimensionless number (the ratio between inertia and surface tension forces) exceeds a certain value (We_{crit}). In low viscosity liquids, We_{crit} ranges from 5 to 20 [Kolev, 2007], a complete summary of the experiments carried out to determine the critical Weber number is shown in Wierzba's paper [Wierzba, 1990].

3.2.1.1. The Critical Weber Number Criterion

The most widely used criterion to estimate the size of the droplets is related to an empirical value of the Weber number:

$$We_{crit} = \frac{\rho_g \, u_g^2 \, \phi_{d,\max}}{\sigma} = CONSTANT \quad (6 \ or \ 12) \qquad \textbf{Eqn. (3.1)}$$

This equation implies that the droplets diameter varies as the inversed square of the gas velocity, $\phi_d \propto \frac{1}{u_g^2}$.

3.2.1.2. Droplet Break-up

Suspended particles undergoing significant local stresses may break-up into two or more particles. The instabilities caused may be driven by density differences (Rayleigh-Taylor) and/or velocity differences (Kelvin-Helmholtz) [Loth, 2010].

If a fluid particle submitted to high accelerations has a density quite different from that of the continuous-phase, the interface become unstable. These instabilities are likely to take place when the deformations due to dynamic pressure become so severe that surface tension is insufficient to maintain the particle's surface integrity. Under these conditions, the Rayleigh-Taylor instabilities are considered to be dominant. Then, the suggested value of the critical Weber number is:

$$We_{crit,R-T} = \frac{\rho_g u_g^2 \phi_{crit,R-T}}{\sigma} \approx 8 \qquad \textbf{Eqn. (3.2)}$$

The Kelvin-Helmholtz (K-H) instability is mainly associated with flows which have tangential variation in the velocity field, i.e. for high relative velocity between the gas and the droplet. This instability is caused by the hydrodynamic amplification of perturbations that arise at the gas-liquid interface with a discontinuity in the velocity field. A critical Weber number related to the fluid's densities can be defined, while experiments may be used to determine the proportionality constant, the final proposed expression is:

$$We_{crit,K-H} = \frac{\rho_g \left| u_g - u_d \right|^2 \phi_{crit,K-H}}{\sigma} \approx 12 \frac{\left(\rho_l + \rho_g\right)}{\rho_l} \qquad \textbf{Eqn. (3.3)}$$

for the condition of $\rho_d \gg \rho_g$ (droplets in a gas), this corresponds to $We_{crit,K\text{-}H} \approx 12$.

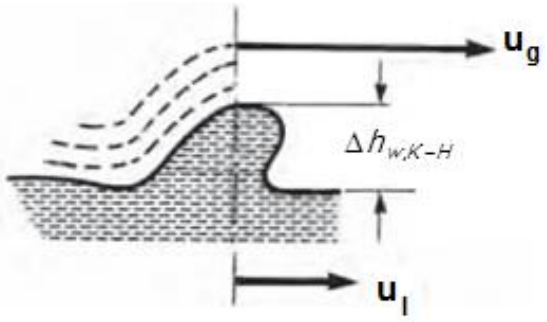

Figure 3.1. Unstable wavelength during relative motion of two continuos phases.

A similar expression applicable to the Kelvin-Helmholtz instability analysis is presented by Kolev [Kolev, 2007]. That expression is useful if the entrained particle in this process has a size approximately equal to the height of the most unstable wavelength, $\phi_d = \Delta h_{w,K-H}$, Figure 3.1. In order to estimate the wave amplitude, is taken into account the Kelvin-Helmholtz instability, which is caused by the relative motion of two continuous phases [Chandrasekhar, 1981]. For that instability, the most unstable wave amplitude is (for gas as a continuous phase):

$$\Delta h_{w,K-H} = 3\pi \frac{\left(1 + \frac{\rho_g}{\rho_l}\right)\sigma}{\rho_g \left(u_g - u_d\right)^2} \qquad \textbf{Eqn. (3.4)}$$

then, the critical Weber number would be

$$We_{crit} = \frac{\rho_g \left| u_g - u_d \right|^2 \phi_d}{\sigma} \approx 3\pi \left(1 + \frac{\rho_g}{\rho_l} \right) \qquad \textbf{Eqn. (3.5)}$$

Note that for water droplets in a gas stream $We_{crit} \approx 9.5$.

An attempt to obtain the droplet diameter from Kelvin-Helmholtz instability in the interface of a submerged gas jet was done by Chawla [Kolev, 2007]. He analyzed the instabilities of the interface of a gas jet entering into a liquid and found that, when the amplitude of the disturbance becomes large enough, the liquid at the wave crests (protruded into the gas jets) is torn off by the gas jet. The size of the resulting droplets is governed by the Kelvin-Helmholtz instabilities for Mach numbers less than one:

$$\phi_d \approx c_0 \Delta h_{w,K-H} \qquad \textbf{Eqn. (3.6)}$$

The constant c_0 is estimated by comparison with experimental data, $c_0 \approx 1.5$. Thus, for low Mach numbers, the stability criterion is $We_{crit} \approx 14$. However, there is a lack of reliable data for the development of a more accurate correlation for entrainment at high gas velocity.

3.2.1.3. Correction of We_{CRIT}: the Ohnesorge Number

The so called aerodynamic break-up is an important mechanism for the description of two-phase flows (Crowe [Crowe, 2006], Kolev [Kolev, 2007], Pilch and Erdman [Pilch, 1987]).

Several researchers have noted that viscous effects might stabilize a droplet, which would allow reaching higher values of We_{crit}. The Ohnesorge dimensionless number, a relation between viscosity and the product of inertia and surface tension forces,

$$Oh = \frac{\mu_l}{\sqrt{\rho_l \sigma \phi}} = \frac{\sqrt{We}}{\mathrm{Re}} \qquad \textbf{Eqn. (3.7)}$$

might properly encapsulate such a potential effect attributable to viscosity.

According to Hinze [Hinze, 1955], the critical Weber number may be modified using the following expression to account for the effect of liquid viscosity:

$$We_{crit} = We_{crit,0} \left(1 + f(Oh) \right) \qquad \textbf{Eqn. (3.8)}$$

where $We_{crit,0}$ is the critical Weber number without considering the viscous forces. A first empirical relationship has been proposed [Hinze, 1955]:

$$We_{crit} = We_{crit,0} + 14 Oh \qquad \textbf{Eqn. (3.9)}$$

Multiple equations along the years that have considered the viscosity effects on the critical Weber number are available on the literature. A first comprehensive study was

presented by Pilch and Erdman [Pilch, 1987]. The maximum stable droplet diameter when droplets are immersed in a high speed gas jet is calculated from correlations like

$$We_{crit} = We_{crit,0}\left(1 + 1.077Oh^{1.6}\right) \quad \textbf{Eqn. (3.10)}$$

where $We_{crit,0}$ is usually equal to 12, but some authors propose slightly different values (11, according to Guildenbecher [Guildenbecher, 2009]).Other expressions with a similar structure might be found in the literature; like Gelfand´s [Gelfand, 1996],

$$We_{crit} = We_{crit,0}\left(1 + 1.5Oh^{0.74}\right) \quad \textbf{Eqn. (3.11)}$$

being $We_{crit,0}$ 12 or Krzeczkowski's correlation [Krzeczkowski, 1980]:

$$We_{crit} = We_{crit,0}\left(1 + 1.2Oh^{0.89}\right) \quad \textbf{Eqn. (3.12)}$$

Schmehl, based on data from Hsiang and Faeth [Hsiang, 1995], derived the best fit for the size break-up threshold [Schmehl, 2003; Crowe, 2006]:

$$We_{crit} = We_{crit,0}\left(1 + 1.7Oh^{1.4}\right) \quad \textbf{Eqn. (3.13)}$$

where $We_{crit,0}$ is set to 13.

The above mentioned approaches did not consider any dependence on droplet Reynolds number that, in fact, might exist [Kolev, 2007]. Sarjeant summarized the data of Hinze, Lane and Hanson and found that Reynolds numbers between $3 \cdot 10^2$ and 10^5 produce a variation of the critical Weber number. From these the following expression was obtained by Kolev [Kolev, 2007]:

$$We_{crit,0} = \begin{cases} 55\left(\dfrac{24}{\mathrm{Re}_d} + \dfrac{20.1807}{\mathrm{Re}_d^{0.615}} - \dfrac{16}{\mathrm{Re}_d^{2/3}}\right) & for \quad 200 < \mathrm{Re}_d < 2000 \\ 5.48 & for \quad 2000 \le \mathrm{Re}_d \end{cases} \quad \textbf{Eqn. (3.14)}$$

being the droplet Reynolds number defined as

$$\mathrm{Re}_d = \frac{\rho_g (u_g - u_d)\phi_d}{\mu_g} \quad \textbf{Eqn. (3.15)}$$

The limiting value of $Re_d \approx 200$ is chosen to take into account the observations of Schröder and Kitner reporting that a droplet oscillates only in the presence of a vortex tail behind the droplet, which requires at least a Reynolds number of 200. That is to say, two conditions are needed for a droplet, under the influence of a high velocity gas stream, to become unstable; a droplet Reynolds number higher than 200 and a Weber number greater than a critical value, which depends on the droplet Reynolds number too, i.e. an iterative process is required to calculate We_{crit}.

Brodkey and Gelfand approximated the dependence of the critical Weber number on the viscosity based on experimental results obtained by several authors [Kolev, 2007]. Their final conclusion was that the critical Weber number for water had to be multiplied by a correction factor containing the Reynolds and Ohnesorge numbers calculated from the droplet properties. Finally, for suddenly applied relative velocity, the critical Weber number recommended by Kolev is:

$$We_{crit} = \begin{cases} 55\left(\frac{24}{\mathrm{Re}_d} + \frac{20.1807}{\mathrm{Re}_d^{0.615}} - \frac{16}{\mathrm{Re}_d^{2/3}}\right)\left[1 + 1.077Oh^{1.64}\right] & for \;\; 200 < \mathrm{Re}_d < 2000 \\ 5.48\left[1 + 1.077Oh^{1.64}\right] & for \;\; 2000 \le \mathrm{Re}_d \end{cases} \quad \textbf{Eqn. (3.16)}$$

Remind that for gradually applied relative velocity, the expression for the critical Weber number is expected to be larger than the expression presented in Eqn. (3.14), which is applicable for suddenly applied relative velocity. For gradually applied relative velocities, Taylor [Kolev, 2007] proposes the critical Weber number to be about $\sqrt{2}$ times greater than the one for suddenly applied relative velocities. This study is based on a theoretical analysis and is not definitely confirmed by experimental measurements.

Summarizing, almost all the previous expressions have a similar structure:

$$We_{crit} = We_{crit,0}\left(1 + aOh^b\right) \quad \textbf{Eqn. (3.17)}$$

where $We_{crit,0}$ is the critical Weber number when $Oh \to 0$ (viscosity effects not considered); all the above presented expressions use a constant value for this critical Weber number, $We_{crit,0} \approx 11$ - 12, except the proposed by Kolev, which has not a constant but an expression, Eqn. (3.14). For the adjustment coefficients, a and b, all the expressions presented above have values in close to unity, a between 1.0 - 1.8 and b between 0.74 - 1.64, see Table 3.1.

Table 3.1. Summary of coefficients for the critical Weber number.

Correlation	$We_{crit,0}$	a	b
Pilch and Erdman [Pilch, 1987]	12	1.077	1.6
Guildenbecher [Guildenbecher, 2009]	11		
Gelfand [Gelfand, 1996]	12	1.5	0.74
Krzeczkowski [Krzeczkowski, 1980]	12	1.2	0.89
Hsiang and Faeth [Hsiang, 1995]	13	1.7	1.4
Kolev [Kolev, 2007]	Eqn. (3.14)	1.077	1.64

3.2.2. Empirical Correlations for Annular Flow

An alternative approach to the We_{crit} one is the direct correlation of a specific droplet size (i.e., mean, median, maximum, etc) as a function of scenario characteristics (fluid

properties and flow conditions). One of the earliest works was carried out by Tatterson et al. [Tatterson, 1977], who based on their own data and others' (Wicks and Dukler [Wicks, 1966] and Cousins and Hewitt [Cousins, 1968]) derived a correlation for the volume median diameter valid of vertical and horizontal flows in pipes and channels:

$$\frac{\phi_{vm}}{D} = 1.6x10^{-2}\left(\frac{\rho_g J_g^2 f_s D}{2\sigma}\right)^{-\frac{1}{2}} \qquad \textbf{Eqn. (3.18)}$$

where ρ_g is the gas density; J_g is the superficial gas velocity; σ is the surface tension; f_s is the friction factor for a smooth interface.

Fore et al. [Fore, 2002] rearranged Tatterson's expression by using the definitions of the gas Reynolds number $\left(\mathrm{Re}_g = \frac{\rho_g J_g D}{\mu_g}\right)$, the gas Weber number $\left(We_g = \frac{\rho_g J_g^2 D}{\sigma}\right)$ and the friction factor for a smooth interface $\left(f_s = \frac{0.046}{\mathrm{Re}_g^{0.2}}\right)$:

$$\frac{\phi_{vm}}{D} = 0.106 \cdot We_g^{-1/2}\,\mathrm{Re}_g^{1/10} \qquad \textbf{Eqn. (3.19)}$$

These correlations are good enough to predict the Wicks and Cousins and Hewitt data, from which they were developed, but it under predicts Fore's data obtained at significantly higher pressures.

An expression proposed by Ishii and Kataoka [Ishii, 1983] is a semi-empirical correlation to predict the entrainment droplet size for roll-wave entrainment. This equation is based on the mechanism for the entrainment inception criterion developed by Ishii and Grolmes [Ishii, 1975]. The correlation obtained by Ishii in terms of the average maximum droplet size is

$$\phi_{\max} = 0.031\frac{\sigma}{\rho_g J_g^2}\mathrm{Re}_g^{2/3}\left(\frac{\rho_g}{\rho_l}\right)^{-\frac{1}{3}}\left(\frac{\mu_g}{\mu_l}\right)^{\frac{2}{3}} \qquad \textbf{Eqn. (3.20)}$$

And a similar expression, but in terms of the Sauter Mean Diameter, ϕ_{32}[5], is expressed as [Kim, 1993]

[5] Sauter mean diameter, ϕ_{32}, can be regarded as the ratio of the particle volume to surface area in a distribution.

$$\phi_{32} = 0.00796\frac{\sigma}{\rho_g J_g^2}\mathrm{Re}_g^{2/3}\left(\frac{\rho_g}{\rho_l}\right)^{-\frac{1}{3}}\left(\frac{\mu_g}{\mu_l}\right)^{\frac{2}{3}} \qquad \textbf{Eqn. (3.21)}$$

Assuming an Upper Limit Log-Normal (ULLN) distribution (Appendix I: "The Droplet Size Distribution Functions") and fixing their input parameters, the relation between the different diameters can be easily obtained, these are ϕ_{vm} =0.319 ϕ_{max} and ϕ_{32} =0.257 ϕ_{max}. The values of the ULLN parameters used are b = 2.13 and λ = 0.884, being $b = \frac{\phi_{\max} - \phi_{vm}}{\phi_{vm}}$ and λ the deviation about the mean.

Moreover, in Eqn. (3.20) and Eqn. (3.21), the Weber number can be easily introduced and the resulting expression of the mean diameter would be

$$\frac{\phi_{vm}}{D} = 0.0099 \cdot We_g^{-1}\mathrm{Re}_g^{2/3}\left(\frac{\rho_g}{\rho_l}\right)^{-\frac{1}{3}}\left(\frac{\mu_g}{\mu_l}\right)^{\frac{2}{3}} \qquad \textbf{Eqn. (3.22)}$$

Kataoka [Fore, 2002] proposes the following correlation, which relates the Weber number based on the volume median diameter with the gas and liquid Reynolds numbers, fluid densities and fluid viscosities,

$$\frac{\rho_g u_g^2 \phi_{vm}}{\sigma} = We_{vm} = 0.028 \cdot \mathrm{Re}_l^{-1/6}\,\mathrm{Re}_g^{2/3}\left(\frac{\rho_g}{\rho_l}\right)^{-\frac{1}{3}}\left(\frac{\mu_g}{\mu_l}\right)^{\frac{2}{3}} \qquad \textbf{Eqn. (3.23)}$$

where the liquid Reynolds number is defined as

$$\mathrm{Re}_l = \frac{\rho_l J_l D}{\mu_l} = \frac{4\rho_l u_l \delta}{\mu_l} \qquad \textbf{Eqn. (3.24)}$$

expression in which all terms are the liquid properties (density, velocity, film thickness and viscosity) and D is the pipe hydraulic diameter. Rearranging this correlation in terms of the gas Weber number yields to:

$$\frac{\phi_{vm}}{D} = 0.028 \cdot We_g^{-1}\mathrm{Re}_l^{-1/6}\,\mathrm{Re}_g^{2/3}\left(\frac{\rho_g}{\rho_l}\right)^{-\frac{1}{3}}\left(\frac{\mu_g}{\mu_l}\right)^{\frac{2}{3}} \qquad \textbf{Eqn. (3.25)}$$

Like the Tatterson et al. correlation, the Ishii and Kataoka's expression correlates the data from which it was developed. Similarly, the Fore et al. data [Fore, 2002] at a pressure of 3.5 atm are roughly correlated although with significant scatter but with the correct trend. However, the data obtained at a pressure of 17.5 atm, as well as the Fore and Dukler

data [Fore, 1995] obtained at a higher liquid viscosity, are significantly underpredicted. This difference indicates that the effects of gas density and liquid viscosity are not properly accounted for by the previously presented correlations. This poor correlation is not surprising since all of the data used to build these correlations were obtained using air and water at pressures between 1 and 2 atm.

Patruno et al. [Patruno, 2010] propose a new correlation to improve the previous expressions for the fitting of other author's experimental data and their recent experimental data. The authors correlated the experimental measures of Fore and Duckler [Fore, 1995], Fore et al. [Fore, 2002], Kataoka's measurements [Kataoka, 1983] and their experimental results, even though their experimental measurements were made using a mixture of Exxsol D60^{TM} (aliphatic hydrocarbon aromatized, his major components are normal paraffins, isoparaffins and cycloparaffins) as the liquid phase and nitrogen as the gas phase. The experiments were conducted in a pipe with an equivalent hydraulic diameter of 5 cm, the system's pressure varied from 900 to 1600 kPa, with surface tensions of 24.0–24.3 mN/m, the gas mean velocity ranged from 4 to 8 m/s and the liquid velocity from 0.05 to 0.15 m/s. The data set was found to be best represented by next expression:

$$\frac{\phi_{vm}}{D} = 0.007 \cdot We_g^{0.75}\,\mathrm{Re}_l^{0.2}\,\mathrm{Re}_g^{-1.97}\left(\frac{\rho_g}{\rho_l}\right)^{1.23}\left(\frac{\mu_g}{\mu_l}\right)^{-4.47} C_W^{5.18} \qquad \textbf{Eqn. (3.26)}$$

where C_W is a factor that accounts for the effect of the surface tension on the circulation/dissipation flow in the wave. It was defined by Ishii and Grolmes [Ishii, 1975] as follows

$$\begin{aligned} C_W &= 0.028 N_\mu^{-4/5} \quad for \quad N_\mu \le 1/15 \\ C_W &= 0.25 \qquad\quad for \quad N_\mu > 1/15 \end{aligned} \qquad \textbf{Eqn. (3.27)}$$

where N_μ (originally used by Hinze [Hinze, 1955]) is the viscosity number, which compares the viscous force induced by an internal flow to the surface tension force, and it is defined as

$$N_\mu = \frac{\mu_l}{\left(\rho_l \sigma \sqrt{\frac{\sigma}{g\,\Delta\rho}}\right)^{1/2}} \qquad \textbf{Eqn. (3.28)}$$

Kocamustafaogullari et al. [Kocamustafaogullari, 1994] developed a correlation for the maximum droplet diameters s in annular flow

$$\frac{\phi_{\max}}{D} = 2.609 \cdot C_W^{-4/15} We_g^{-3/5}\left(\mathrm{Re}_g^4 / \mathrm{Re}_l\right)^{1/15}\left(\frac{\rho_g}{\rho_l}\frac{\mu_g}{\mu_l}\right)^{4/15} \qquad \textbf{Eqn. (3.29)}$$

They supposed that the droplet size distribution function was an ULLN, analyzed the experimental data collected from various sources and determined the averaged values of the main parameters of this distribution. They obtained values of 1.93 and 0.75 for b and λ respectively. Consequently, the relations among the different droplet sizes are ϕ_{vm} =0.341 ϕ_{max} and ϕ_{32} =0.25 ϕ_{max}.

There are other expressions without the We_g embedded, one of the most remarkable ones developed on the Kelvin-Helmholtz theory for the flow of an inviscid fluid over a small amplitude wave by Tatterson [Pan, 2002b] is:

$$\left(\frac{\rho_g J_g^2 \phi_{32}}{\sigma}\right)\left(\frac{\phi_{32}}{D}\right) = 0.0091 \qquad \textbf{Eqn. (3.30)}$$

Or as a function of the length scale:

$$\left(\frac{\rho_g J_g^2 \phi_{32}}{\sigma}\right)\left(\frac{\phi_{32}}{\lambda_A}\right) = 0.14 \qquad \textbf{Eqn. (3.31)}$$

where λ_A is the length scale, defined by Azzopardi [Azzopardi, 1997] and based on the critical wave length of Taylor's instability,

$$\lambda_A = \left(\frac{\sigma}{\rho_l g}\right)^{0.5} \qquad \textbf{Eqn. (3.32)}$$

Eqn. (3.31) suggests that the droplet diameter varies with u_g^{-1}, which is in agreement with experiments.

Other simple correlations that only consider pipe diameter, gas liquid velocity and fluid properties are proposed by Al-Sarkhi et al. [Al-Sarkhi, 2002]:

$$\phi_{vm} = \left[0.196 D^{0.36}\left(\frac{\rho_g J_g^2}{\sigma}\right)^{-0.37}\right]^{1.3699} \qquad \textbf{Eqn. (3.33)}$$

$$\phi_{32} = \left[0.154 D^{0.36}\left(\frac{\rho_g J_g^2}{\sigma}\right)^{-0.55}\right]^{1.0989} \qquad \textbf{Eqn. (3.34)}$$

Another simple correlation was suggested by Azzopardi [Azzopardi, 2006] for vertical annular flow. It is expressed as follows:

$$\phi_{32} = \left[0.069 J_g + 0.0187 \left(\frac{\rho_l J_l}{\rho_g J_g} \right)^2 \right] \frac{\sigma}{\rho_g J_g^2} \qquad \textbf{Eqn. (3.35)}$$

Many other expressions have been found in the open literature, but are difficult to use because data on entrainment (G_e) are needed.

3.3. Droplet Velocity Profiles

Droplet velocity profiles are another key factor in the study of the hydrodynamics in all processes involving interactions between droplets and gaseous jets. We will start first with the application of the force balance equation to a droplet submerged in a fluid including all existing forces. And, after several approximations, the "constant lag" solution of the force balance equation will be found. In the next subsection, this "constant lag" solution is used together with the Stokes number, defined from droplet and gas characteristics times, to obtain the slip ratio, quotient between droplet and gas velocities. This section ends presenting the conclusions of several experimental measurements made in annular flow.

3.3.1. Force Balance Equation

The general particle translational motion equation simply specifies that the rate of change of the particle's linear momentum is equal to the net sum of forces acting on the particle [Loth, 2010]. This yields to a general Lagrangian equation of momentum, given by

$$m_d \frac{d\vec{u}_d}{dt} = \vec{F}_{body} + \vec{F}_{surf} + \vec{\vec{F}}_{coll} \qquad \textbf{Eqn. (3.36)}$$

The right hand side includes the forces associated with these temporal changes. It has three terms:

- Body forces $\left(\vec{F}_{body}\right)$, which are proportional to the droplet mass,
- Surface forces $\left(\vec{F}_{surf}\right)$, proportional to the droplet surface area and related with the surrounding fluid stress,
- Collision forces $\left(\vec{F}_{coll}\right)$, which includes the effects of other droplets or obstacles which may come in contact with the particle.

The body forces are assumed to be represented mainly by the gravitational force $\left(\vec{F}_g\right)$, which acts in the direction of the gravity acceleration vector $\left(\vec{g}\right)$. Assuming that other body forces (such as electromagnetic forces) are negligible, the body forces are given by

$$\vec{F}_{body} \approx \vec{F}_{gravity} = m_d \vec{g} \qquad \textbf{Eqn. (3.37)}$$

The surface forces can be decomposed into a linear sum of various fluid dynamic forces related to certain flow properties:

$$\vec{F}_{surf} = \vec{F}_D + \vec{F}_L + \vec{F}_\forall + \vec{F}_H + \vec{F}_S + \vec{F}_{Br} + \vec{F}_{\nabla T} + \vec{F}_{Diff} + \vec{F}_Q \quad \textbf{Eqn. (3.38)}$$

These individual components include forces due to: drag $\left(\vec{F}_D\right)$, which is opposite to the relative velocity; lift $\left(\vec{F}_L\right)$, which arise due to particle spin or fluid shear; virtual-mass $\left(\vec{F}_\forall\right)$, which is related to the surrounding fluid that accelerates with the particle; history $\left(\vec{F}_H\right)$, which takes into account unsteady stress over the particle; fluid-stress $\left(\vec{F}_S\right)$, which stems from the fluid dynamic stresses in the absence of the particle; Brownian motion $\left(\vec{F}_{Br}\right)$, random motion from discrete molecular interactions; thermophoresis $\left(\vec{F}_{\nabla T}\right)$, force due to molecular interactions along a temperature gradient; diffusiophoresis $\left(\vec{F}_{Diff}\right)$, moves particles towards diffusionally-growing hydrometeors due to water vapor concentration gradients; and the electric charge force $\left(\vec{F}_Q\right)$, interaction between droplets (Q_d) and gas particles (q_g), with opposite or equal electric charge. The drag force is usually the main contribution to the droplet momentum, so that the momentum equation may be largely simplified:

$$m\frac{du_d}{dt} = F_D \quad \textbf{Eqn. (3.39)}$$

The aerodynamic drag on a droplet can be written in the usual form:

$$F_D = \frac{1}{2}\rho_g A_d C_D \left|u_g - u_d\right|\left(u_g - u_d\right) \quad \textbf{Eqn. (3.40)}$$

where C_D is the drag coefficient. This parameter has been widely studied and many semi-empirical correlations are available in the literature. In Table 3.2 a number of those correlations have been gathered.

Integration of the simplified momentum equation can be expressed in terms of the droplet Reynolds number:

$$a_d = \frac{du_d}{dt} = \frac{3}{4}C_D\frac{\rho_g}{\rho_d}\frac{\mathrm{Re}_d\,\mu_g}{\phi_d^2}\left(u_g - u_d\right) \quad \textbf{Eqn. (3.41)}$$

which might be written as the usually called “constant lag solution”:

$$\frac{du_d}{dt} = \frac{1}{\tau_d}\left(u_g - u_d\right) \quad \textbf{Eqn. (3.42)}$$

where τ_d is the droplet characteristic time, presented by Pozorsky and Miniers [Pozorsky, 1998] and Shirolkar et al. [Shirolkar, 1996], which is defined as:

$$\tau_d = \frac{4\rho_p \phi_d^2}{3C_D \,\mathrm{Re}_d\, \mu_g} \qquad \textbf{Eqn. (3.43)}$$

Table 3.2. Summary of Drag Coefficient correlations.

Reference	Correlation	Validity Range
Schiller-Naumann [Kolev, 2007]	$C_D = \frac{24}{\mathrm{Re}_d}\left(1 + 0.15\mathrm{Re}_d^{0.687}\right)$	$\mathrm{Re_d} < 500$
Ishii and Chawla [Levy, 1999]	$C_D = \frac{24}{\mathrm{Re}_d}\left(1 + 0.1\mathrm{Re}_d^{0.75}\right)$	Up to $\mathrm{Re_d} \approx 1000$
White [Loth, 2010]:	$C_D = \frac{24}{\mathrm{Re}_d} + \frac{6}{1+\sqrt{\mathrm{Re}_d}} + 0.4$	Up to drag crisis ($\mathrm{Re_d} < 2*10^5$)
Kelbaliyev and Ceylan [Ashgriz, 2011]	$C_D = \frac{24}{\mathrm{Re}_d}\left[1 + 18.5\mathrm{Re}_d^{3.6} + \left(\frac{\mathrm{Re}_d}{2}\right)^{11}\right]^{1/30} + \frac{4}{9}\frac{\mathrm{Re}_d^{4/5}}{330 + \mathrm{Re}_d^{4/5}}$	Up to drag crisis ($\mathrm{Re_d} < 2*10^5$)
Cheng [Cheng, 2009]*	$C_D = \frac{24}{\mathrm{Re}_d}(1 + 0.27\mathrm{Re}_d)^{0.43} + 0.47\left[1 - \exp\left(-0.04\mathrm{Re}_d^{0.38}\right)\right]$	Up to drag crisis ($\mathrm{Re_d} < 2*10^5$)

*In Cheng's article [Cheng, 2009] several expressions of drag coefficient are shown and this new expression is also proposed

Integration of Eqn. (3.42) and after some manipulation we obtain:

$$u_d = u_g - \left(u_g - u_{d_0}\right)e^{-t/\tau_d} \qquad \textbf{Eqn. (3.44)}$$

If the initial value of the particle velocity is zero, $u_{d_0} = 0$, the previous equation reduces to:

$$u_d = u_g\left(1 - e^{-t/\tau_d}\right) \qquad \textbf{Eqn. (3.45)}$$

The objective of these calculations is to determine the time it would take to a single particle to reach the maximum velocity. So rearranging,

$$t = \tau_d \cdot Ln\left(\frac{1}{1 - u_d/u_g}\right) \qquad \textbf{Eqn. (3.46)}$$

Integration of Eqn. (3.45) yields the expression of the displacement

$$z_d = z_{d_0} + u_g t + u_g \tau_d \left(e^{-t/\tau_d} - 1\right) \quad \textbf{Eqn. (3.47)}$$

3.3.2. The Stokes Number

The Stokes number is defined as the ratio of the particle momentum response time (in our case the droplet response time, τ_d) over the flow system time (τ_g) [Crowe, 2006]:

$$Stk = \frac{\tau_d}{\tau_g} = \frac{\rho_d \phi_d^2 u_g}{18 \mu_g D} \quad \textbf{Eqn. (3.48)}$$

where D is the problem characteristic length. According the Stk ranges, the droplet behavior can be classified: if Stk << 1, droplets response time is instantaneous to any change in the gas hydrodynamics; if Stk>>1, droplets are hardly affected by fluid velocity changes. At Stk around 1, both phases have similar reaction time to any condition fluctuation.

By introducing the phases slip ratio, $S_R \left(S_R = \frac{u_d}{u_g} \right)$, the droplet motion equations can be eventually written in terms of S_R and Stk (carrier gas acceleration, du_g/dt, assumed to be approximated as u_g/τ_g), as noted by several authors [Rahman, 2009; Crowe, 2006]:

$$S_R = \frac{u_d}{u_g} \approx \frac{1}{1 + Stk} \quad \textbf{Eqn. (3.49)}$$

3.3.3. Annular Flow Expressions

Another way to estimate the droplet velocity is by studying the experimental measurements made in annular flow. In the article of Fore and Dukler [Fore, 1995], the probability density functions for the droplet axial velocity at the tube centerline are shown, Figure 3.2. It must be emphasized that there is an increasing dispersion of the droplet velocity distributions with the increasing of the gas velocity.

The slip ratio is used in order to estimate the droplet velocity. Local measurements of the gas velocity provide the slip ratio at the tube centerline, S_{R0}, defined with the mean centerline gas velocity and the mean centerline droplet velocity (Figure 3.3 illustrates this quantity). Under the present circumstances, the droplets at the centerline are traveling, on average, at 80% of the local mean gas velocity.

The article by Azzopardi [Azzopardi, 1997] provides similar results for droplet velocities, values are about 20% lower than those of the gas. But he mentions that there is a trend for smaller droplets to be travelling at higher velocities.

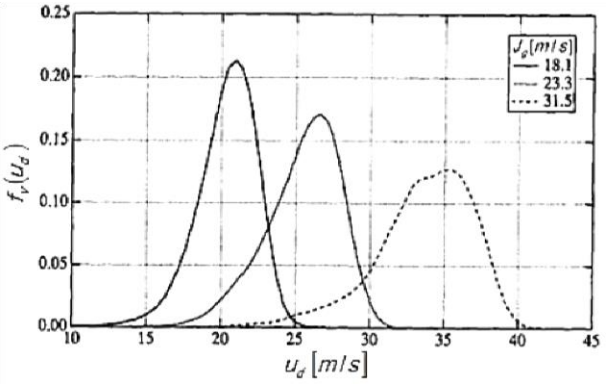

Figure 3.2. Droplet velocity probability density functions for water with Re_l=750 [Fore, 1995].

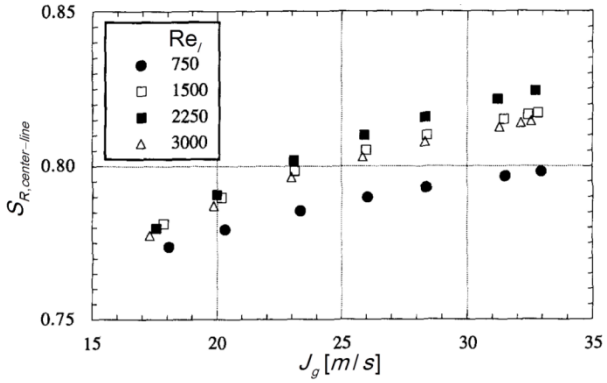

Figure 3.3. Slip ratio at the center-line for water [Fore, 1995].

3.4. The Amount of Entrained Droplets

The measurement or prediction of the total amount of entrained droplets in a gas stream is another hugely important parameter to model the annular flow. Mainly, two magnitudes appear in the literature to determine this quantity, these are the entrained fraction (E) and the total mass flux of entrained liquid (G_e). The experimental measurement of liquid entrained is a very challenging task, the most frequently used experimental techniques are quite invasive and can significantly perturb the annular two-phase flow that is being analyzed. As such, a part of the available experimental data might be affected by considerable uncertainties, and significant scatter can be expected when merging data from different studies. In the next subsections, many expressions found in the open literature will be presented to estimate these magnitudes. Other concepts that have to be taken into account are: the developing and fully developed entrainment region, and its transition point.

In the next paragraphs the following questions will be presented and clarified: the distance needed to reach the equilibrium conditions; several correlations available to obtain the entrainment in the developing entrainment region; and, several correlations to calculate the entrainment into the fully developed region.

3.4.1. The Developing and Fully Developed Entrainment Region

A particularly important concept that must be clarified before the presentation of the equations for the entrained fraction, is the fact that, there are two clearly differentiated areas. These are, as was proposed by Kataoka and Ishii [Kataoka, 1982]: the under-entrained or developing entrainment region and the over-entrained or fully developed entrainment region. Consequently, a point of separation between these two regions is necessary to find or define.

According to Ishii and Mishima [Kataoka, 2000], the entrainment reaches its equilibrium value at points far from the tube entrance. From this point on, the entrainment and the deposition processes reach the equilibrium, thus the entrainment remains constant. The distance necessary to reach this condition is given approximately by

$$Z = \frac{440 D We_g^{0.25}}{\mathrm{Re}_l^{0.5}} \qquad \textbf{Eqn. (3.50)}$$

where Re_l is the liquid Reynolds number and We_g is the gas Weber number (but in a slightly different form, the so called "modified Weber number"[6]):

$$We_g = \frac{\rho_g J_g^2 D}{\sigma}\left(\frac{\rho_l - \rho_g}{\rho_g}\right)^{1/3} \qquad \textbf{Eqn. (3.51)}$$

This necessary distance to reach the quasi-equilibrium, according to Ishii and Kataoka [Ishii, 1983], is

$$Z = 600 D \sqrt{\frac{J_g^*}{\mathrm{Re}_l}} \qquad \textbf{Eqn. (3.52)}$$

being J_g* a dimensionless superficial velocity, defined as

$$J_g^* = \frac{J_g}{\left[\frac{\sigma\, g(\rho_l - \rho_g)}{\rho_g^2}\left(\frac{\rho_g}{\rho_l - \rho_g}\right)^{2/3}\right]^{1/4}} \qquad \textbf{Eqn. (3.53)}$$

[6] The modified Weber number is defined with exponent 1/3 or 1/4 depending on the author.

In both expressions, Eqn. (3.50) and Eqn. (3.52), the entrance length, Z, has been defined as the distance from the entrance at which the entrainment measurements had changed less than 2% of its ultimate value, that is, difference in entrainment values less than 2% in successive measurement points.

It is important to highlight that, while not otherwise stated, the terms discussed concern the fully developed region. This region is the most studied and on which more available data and correlations can be found.

3.4.2. Entrained Fraction

As it has been said above, a crucial parameter in the analysis and modeling of annular flows is the fraction of liquid entrained as droplets in the gas core. The so called entrained droplet fraction (E) is defined as the ratio of the entrained droplets mass flow rate divided by the total liquid mass flow rate:

$$E = \frac{\dot{m}_{le}}{\dot{m}_{l}} \qquad \textbf{Eqn. (3.54)}$$

where ṁ is the mass flow rate, subscript le corresponds to the mass flow of droplets (mass flow rate of entrained droplets) and l to the total mass flow rate of liquid.

But, before presenting the expressions for the entrained fraction, we must underline the fact that all the entrainment fraction expressions presented are developed for the equilibrium region, that is, far from the entrance region, only a small note on this developing region will be done. Thus, in the entire document, until otherwise stated, we always refer to the fully developed entrained region, also when referring to the developing region the subscript z will be used.

3.4.2.1. The Developing Entrainment Region

Some experimental data indicate that the entrainment process is heavily affected by the so called "entrance effects", particularly due to gas expansion when entering a lower pressure region. The entrance region is comprised between the entrance point and Z, given by Eqn. (3.50) and Eqn. (3.52). From the entrance point, the expression of the entrained fraction takes a typical form of an exponential relaxation [Kataoka, 2000]. Thus, for the case of liquid being injected smoothly as a film at inlet, the entrainment develops according to

$$E_z = \left[1 - \exp\left(-1.87x10^{-5}\xi^2\right)\right] E \qquad \textbf{Eqn. (3.55)}$$

where E_z is the entrained fraction (dependency with the axial dimension), E is its value far from the entrance region (quasi-equilibrium entrained fraction) and ξ is a dimensionless distance given by

$$\xi = \frac{(z/D)\mathrm{Re}_l^{0.5}}{We_g^{0.25}} \qquad \textbf{Eqn. (3.56)}$$

Ishii and Kataoka [Ishii, 1983] proposed another exponential relaxation expression

$$E_z = \left[1 - \exp\left(-10^{-5}\zeta^2\right)\right] E \qquad \textbf{Eqn. (3.57)}$$

where ζ is a dimensionless distance defined similarly than Eqn. (3.56)

$$\zeta = \frac{z}{D}\sqrt{\frac{\mathrm{Re}_l}{J_g^*}} \qquad \textbf{Eqn. (3.58)}$$

3.4.2.2. The Fully Developed Entrainment Region

The fully developed entrainment region is the most widely studied one in the literature over the last decades, so consequently, many correlations of the entrainment fraction have been presented. Some of them are compiled here below and they are also summarized in Table 3.3 along with different expressions, for instance, the correlations of Paleev and Filippovich, Wallis, Oliemans, Ishii and Mishima, Nakazatomi and Sekoguchi, Utsuno and Kaminaga, Pan and Hanratty, Sawant, among others.

3.4.2.2.1. The Sawant's Expression and Al-Sarkhi's Modification

A new tendency to estimate the entrained fraction has been proposed in Sawant et al. works [Sawant, 2008a and 2009]. It consists in determining a "maximum entrained fraction" and, from this maximum value, to obtain the value in each particular case. In the following paragraphs it will be presented in a more detailed way the calculation method proposed by Sawant.

Two types of experiments have been carried out by Sawant: air–water experiments and organic fluid experiments. The air-water data were collected in a vertical upward pipe of 9.4 mm i.d., the regime was co-current annular two-phase flow, the range of pressures were: 1.2, 4, and 6 bar, the superficial gas velocities of 15–100 m/s, and the superficial liquid velocities of 0.05–0.75 m/s. The organic data were collected in a quite similar condition, but the vertical pipe had an inner diameter of 10.2 mm. It covered also three pressure conditions, in this case: 2.8, 5.0 and 8.5 bar, the superficial gas velocities of 6–24 m/s, and the superficial liquid velocities of 0.08–0.40 m/s.

From Sawant's experimental data it can be shown that for a given liquid flow rate, as gas velocity increases, entrainment fraction also increases and, eventually, under very high gas velocity it asymptotically approaches a limiting condition of maximum entrainment fraction (E_{max}). We must highlight that as liquid Reynolds number increases, the curve of entrainment fraction reaches a higher value of E_{max}. The methodology for the modeling of entrainment fraction proposed by Sawant et al. [Sawant, 2008a and 2009] is shown in Figure 3.4. The curve in this figure is a schematic representation of entrainment fraction variation with Weber number at a constant liquid phase Reynolds number. The entrainment curve 0-A-B-C is divided into three regions; a Weber number dependent region 0-A, a transition region A-B and a liquid phase Reynolds number dependent region B-C. But the authors propose to use a simplified correlation, which is presented in the following

paragraphs, until the methodology to determine the correlations for the first transition criteria (point A), the second transition criteria (point B) and the limiting entrainment fraction (E_{max}) have been developed.

Table 3.3. Summary of Entrainment Fraction correlations.

Reference	Correlation	Experimental Conditions
Sawant et al. [Sawant, 2008a and 2009]	$E = \left(1 - \frac{13N_\mu^{-0.5} + 0.3\left(\mathrm{Re}_l - 13N_\mu^{-0.5}\right)^{0.95}}{\mathrm{Re}_l}\right) \cdot \tanh\left[2.31\times10^{-4}\,\mathrm{Re}_l^{-0.35}\left(We - We_{crit}\right)^{1.25}\right]$ $\mathrm{Re}_{ffOE} = 13N_\mu^{-0.5}$; $N_\mu = \frac{\mu_l}{\left(\rho_l\sigma\sqrt{\frac{\sigma}{g\,\Delta\rho}}\right)^{1/2}}$	Air–water Vertical upward flow D = 0.94 cm P = 1.2., 4.0 and 6.0 bar 15 m/s < J_g < 100 m/s 0.05 m/s < J_l < 0.75 m/s Organic fluid Vertical upward flow D = 1.02 cm P = 2.8, 5.0 and 8.5 bar 6 m/s < J_g < 24 m/s 0.08 m/s < J_l < 0.4 m/s
Oliemans [Mantilla, 2008]	$\frac{E}{1-E} = 10^{-2.52}\rho_l^{1.08}\rho_g^{0.18}\mu_l^{0.27}\mu_g^{0.28} \cdot \sigma^{-1.80}D^{1.72}J_l^{0.70}J_g^{1.44}g^{0.46}$	Developed in vertical upward annular flows ρ_g < 56 kg/m^3; 0.012 < σ < 0.073 N/m (air-water, air-ethanol, air-trichloroethane and water-steam) 0.06 < D < 3.2 cm 1 < Fr_g < 10
Ishii and Mishima [Mantilla 2008, Cioncolini 2010]	$E = \tanh\left(7.25\cdot10^{-7}\,We_g^{1.25}\,\mathrm{Re}_l^{0.25}\right)$	Re_l > 2 (Vertical downward flow) Re_l > 160 (Vertical upward and horizontal flows) Low viscosity liquids (air-water) 1 < p < 4 atm 0.95 < D < 3.2 cm 370 < Re_l < 64000 J_g < 100 m/s
Paleev and Filippovich [Mantilla, 2008]	$E = 0.015 + 0.44\,Log_{10}\left[\frac{\rho^*}{\rho_l}\left(\frac{\mu_l J_g}{\sigma}\right)^2\cdot10^4\right]$ $\rho^* = \rho_g\left[1+\frac{\rho_l J_l}{\rho_g J_g}\right]$	Developed in horizontal channel Not sensitive to the pipe diameter. Not valid near the maximum entrainment

Wallis [Mantilla, 2008]	$E = 1 - \exp\left\{-\left[0.125\left(\frac{10^4 J_g \mu_g}{\sigma}\left(\frac{\rho_g}{\rho_l}\right)^{1/2} - 1.5\right)\right]\right\}$	Large error for entrainment fractions greater than 0.5 Not valid for low liquid Reynolds numbers
Nakazatomi and Sekoguchi [Nakazatomi, 1996]	From 0.12 to 5.0 MPa $E = \tanh\left(10^{-4}\, C\, We_l^a\, Fr_g^{1.5}\, n^{-b}\right)$ $C = N^{1.75} + 10\sqrt{\frac{N}{0.8 + N^{1.75}}};\quad N = 100\frac{\rho_g}{\rho_l}$ $a = \frac{0.68\,m - 1}{m^2};\quad b = 2.5\exp(-m)$ $m = \ln(n)\ ;\quad n = \frac{\rho_l}{\rho_g}$ From 7.0 to 20.0 MPa $E = \exp\left(\frac{-0.35\,m}{We_l^{0.14m}\, Fr_g^{1.5}\, N^{-2} + 0.2}\right)$	Developed in vertical upward annular flows 0.12 MPa < P < 20 MPa but not applicable from 5.0 to 7.0 MPa Air-Water D = 1.92 cm.
Utsuno and Kaminaga [Utsuno, 1998]	$E = \tanh\left(0.16 We_g^{0.08}\, \mathrm{Re}_l^{0.16} - 1.20\right)$	3 MPa < P < 9 MPa $260 < We_g < 8.3\cdot10^4$ $5.4\cdot10^3 < Re_l < 3.5\cdot10^5$ 1.0 < D < 2 cm Steam-water
Pan and Hanratty [Cioncolini 2010, Mantilla 2008]	$\frac{E/E_{\max}}{1 - E/E_{\max}} = 6\cdot10^{-5}\, We$ $E_{\max} = 1 - \frac{W_{lfc}}{W_l}$ $\mathrm{Re}_{lc} = \frac{4\,\dot{m}_{lfc}}{\pi\mu_l D} = 7.3(\log_{10}\omega)^3 +$ $+ 44.2(\log_{10}\omega)^2 - 263(\log_{10}\omega) + 439$ $\omega = \frac{\mu_L}{\mu_g}\sqrt{\frac{\rho_g}{\rho_L}}$ $We = \frac{\sqrt{\rho_l\,\rho_g}\,(J_g - J_{gc})^2\, D}{\sigma};\quad J_{gc} = 40\sqrt{\frac{\sigma}{D\sqrt{\rho_l\,\rho_g}}}$	Vertical upward flows 1.06 < D < 5.72 cm 20 m/s < J_g < 119 m/s 0.27 kg/m^3 < ρ_g < 35 kg/m^3 0.01 N/m < σ < 0.073 N/m

Zhang et al. [Zhang, 2011]	$\frac{E}{1-E} = 0.003 We_g^{1.8} Fr_g^{-0.92} \mathrm{Re}_l^{0.7} \mathrm{Re}_g^{-1.24} \left(\frac{\rho_l}{\rho_g}\right)^{0.38} \left(\frac{\mu_l}{\mu_g}\right)^{0.97}$	Large ranges of fluid properties and flow condition (Harwell's databank)
Petalas and Aziz [Zhao, 2005]	$\frac{E}{1-E} = 0.735 N_B^{0.074} \left(\frac{J_g}{J_l}\right)^{0.2}$ $N_B = \frac{\mu_l^2 J_g^2 \rho_g}{\sigma^2 \rho_l}$	
Dallman et al. [Rodriguez, 2009]	$E = E_{\max} \frac{3.6x10^{-8}\left[(D-2\delta)(\rho_g \rho_l)^{0.25} J_g^3\right]^{1.5}}{1+3.6x10^{-8}\left[(D-2\delta)(\rho_g \rho_l)^{0.25} J_g^3\right]^{1.5}}$ E_{max} as Pan and Hanratty's correlation	Air/water data 2.54 < D < 5.08 cm Different flow conditions

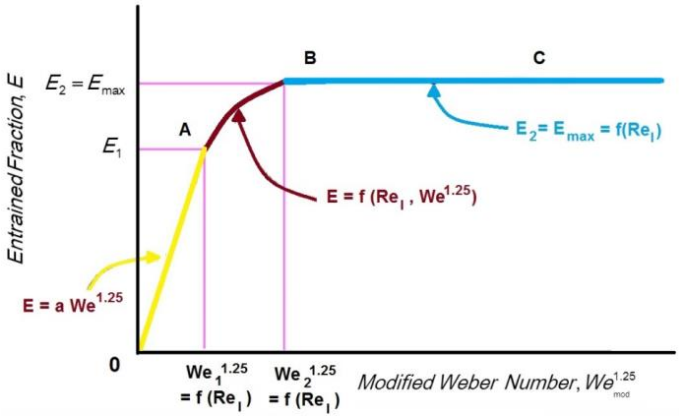

Figure 3.4. Sawant's methodology for the entrained fraction calculation.

Based on the trends observed in the experimental data, the following correlation has been proposed for the prediction of the entrainment fraction:

$$E = E_{\max} \tanh\left[a(We - We_{crit})^{1.25}\right] \qquad \textbf{Eqn. (3.59)}$$

where E_{max} (maximum entrainment fraction) is a function of liquid phase Reynolds number:

$$E_{\max} = 1 - \frac{\mathrm{Re}_{lf\_\min}}{\mathrm{Re}_l} \qquad \textbf{Eqn. (3.60)}$$

The coefficient '*a*' accounts for the dependence of the transition points A and B on liquid phase Reynolds number. Based on the experimental data of Sawant's study, the following correlation is obtained for the coefficient '*a*':

$$a = 2.31\times 10^{-4}\,\mathrm{Re}_l^{-0.35} \qquad \textbf{Eqn. (3.61)}$$

The value of the limiting liquid film Reynolds number (Re_{lf_min}, minimum liquid film Reynolds number at the maximum entrainment fraction condition) is obtained by:

$$\mathrm{Re}_{lf\_\min} = \mathrm{Re}_{ffOE} + 0.3\left(\mathrm{Re}_l - \mathrm{Re}_{ffOE}\right)^{0.95} \qquad \textbf{Eqn. (3.62)}$$

Sawant uses an expression for the liquid film Reynolds number as function of the superficial velocity, Eqn. (3.24), and for the Weber number it does not use the usual definition, but the so called "modified" expression, which is given by[2]:

$$We_{\mathrm{mod}} = \frac{\rho_g J_g^2 D}{\sigma}\left(\frac{\Delta\rho}{\rho_g}\right)^{1/4} \qquad \textbf{Eqn. (3.63)}$$

An expression for the onset of entrainment Reynolds number, useful under high gas velocity conditions, was also presented by the author, is

$$\mathrm{Re}_{ffOE} = 13 N_\mu^{-0.5} \qquad \textbf{Eqn. (3.64)}$$

where N_μ is the viscosity number defined in Eqn. (3.28). The onset of entrainment Reynolds number has been analyzed in depth in the article of Berna et al. [Berna, 2014], in which several expressions have been presented.

Sawant's correlation depends only on non-dimensional numbers Re_l, We, We_{crit} and N_μ. The critical Weber number, We_{crit}, is calculated from Eqn. (3.63), in which the entrainment inception velocity (velocity above which entrainment occurs) is calculated from the Ishii and Grolmes criteria [Ishii, 1975]. The expressions for the entrainment inception criterion are:

$$\begin{aligned} &\frac{\mu_l J_g}{\sigma}\sqrt{\frac{\rho_g}{\rho_l}} \geq 11.78 N_\mu^{0.8}\,\mathrm{Re}_l^{-1/3} \quad for \quad N_\mu \leq \frac{1}{15};\ \mathrm{Re}_{ffOE} \leq \mathrm{Re}_l \leq 1635 \\ &\frac{\mu_l J_g}{\sigma}\sqrt{\frac{\rho_g}{\rho_l}} \geq 1.35\,\mathrm{Re}_l^{-1/3} \quad for \quad N_\mu > \frac{1}{15};\ \mathrm{Re}_{ffOE} \leq \mathrm{Re}_l \leq 1635 \end{aligned} \qquad \textbf{Eqn. (3.65)}$$

The authors initially proposed a value of 160 for the Re_{ffOE}.

For the rough turbulent regime ($Re_l > 1635$) the inception criterion is:

$$\begin{aligned} &\left|J_g\right| > \frac{\sigma}{\mu_l}\sqrt{\frac{\rho_l}{\rho_g}} \times N_\mu^{0.8} \quad for \quad N_\mu \leq \frac{1}{15};\ \mathrm{Re}_l > 1635 \\ &\left|J_g\right| > \frac{\sigma}{\mu_l}\sqrt{\frac{\rho_l}{\rho_g}} \times 0.1146 \quad for \quad N_\mu > \frac{1}{15};\ \mathrm{Re}_l > 1635 \end{aligned} \qquad \textbf{Eqn. (3.66)}$$

Then, by substituting this critical velocity expression calculated from Ishii's expressions in the modified Weber expression, Eqn. (3.63), the final form of the expression proposed by Sawant is written as follows:

$$E = \left(1 - \frac{13N_{\mu}^{-0.5} + 0.3\left(\mathrm{Re}_l - 13N_{\mu}^{-0.5}\right)^{0.95}}{\mathrm{Re}_l}\right) \cdot \tanh\left[2.31\times10^{-4}\,\mathrm{Re}_l^{-0.35}\left(We - We_{crit}\right)^{1.25}\right] \qquad \textbf{Eqn. (3.67)}$$

Al-Sarkhi et al. [Al-Sarkhi, 2012b] found two problems in Sawant's way to calculate E:

1. The asymptotic value of the entrained fraction is always around 0.8, regardless how large is Re_l; consequently, not good predictions are obtained for Re_l greater than 4000 approximately.

2. The numerical results of maximum entrained fraction, E_{max}, becomes negative when $\mathrm{Re}_l < 13N_{\mu}^{0.5}$, situation which is encountered in the cases with low liquid flow rate, that is, for values of Re_l lower than 400 approximately.

An analysis of the existing data shows an asymptotic tendency for the maximum entrained fraction. The authors propose an approximate description through the next equation:

$$E_{\max} = E_{\max,\lim}\left[1 - \exp\left(\frac{\mathrm{Re}_l}{\mathrm{Re}_l^*}\right)^{0.6}\right] \qquad \textbf{Eqn. (3.68)}$$

where $E_{max,lim}$ is the asymptotic or limiting value of the maximum entrained fraction and Re_l* is a "time constant" in the form of a Reynolds number. This time constant is defined as the values of the liquid film Reynolds number when maximum entrainment fraction reaches 63.2% of its limiting value. This limiting value of the maximum entrained fraction, $E_{max,lim}$, have values slightly lower than 1. So, a good value for $E_{max,lim}$ would be 1.0. Regarding to Re_l*, the authors have compared the previously presented equation with experimental data and they determined a value of 1400 for Re_l*. So, the final form of the above expression would be

$$E_{\max} = 1\left[1 - \exp\left(\frac{\mathrm{Re}_l}{1400}\right)^{0.6}\right] \qquad \textbf{Eqn. (3.69)}$$

The authors also suggest a similar expression to Eqn. (3.68) for the calculation of the entrained fraction, with the proposed asymptotic shape. Then, the proposed expression to calculate E will be:

$$E = E_{\max}\left[1 - \exp\left(\frac{We}{We^*}\right)^{0.6}\right] \qquad \textbf{Eqn. (3.70)}$$

being We defined as in the Sawant's work, Eqn. (3.63), while We* is defined in the same way as Re_l*, the "threshold value" when the maximum entrainment fraction reaches 63.2% of its limiting value. Unfortunately, no model for We* is presently available.

3.4.2.2.2. Oliemans' correlation

The Oliemans' correlation [Mantilla, 2008] has been developed to calculate the entrainment in vertical annular flows from a regression analysis of the Harwell data bank. In this database air-water, air-ethanol, air-trichloroethane and water-steam fluid systems had been studied. The study covers pipe diameters from 0.06 to 3.2 cm, gas Froude numbers from 1 to 10, liquid Reynolds numbers in laminar and turbulent flow, gas densities lower than 56 kg/m^3 and surface tensions between 0.012 and 0.073 N/m. The correlation can be expressed as follows:

$$\frac{E}{1-E} = 10^{-2.52}\rho_l^{1.08}\rho_g^{0.18}\mu_l^{0.27}\mu_g^{0.28}\sigma^{-1.80}D^{1.72}J_l^{0.70}J_g^{1.44}g^{0.46} \qquad \textbf{Eqn. (3.71)}$$

3.4.2.2.3. Ishii and Mishima's correlation

The database employed to develop this correlation included air-water systems, with pipe diameters from 0.95 to 3.2 cm. The experiments were conducted under low pressure conditions (0.1-0.27 MPa), superficial velocities lower than 100 m/s, liquid Reynolds numbers between 370 and 6400 and gas densities from 1.2 to 4.8 kg/m^3. Ishii and Mishima [Mantilla 2008, Cioncolini 2010] proposed the following expression:

$$E = \tanh\left(7.25\cdot 10^{-7}\, We_g^{1.25}\,\mathrm{Re}_l^{0.25}\right) \qquad \textbf{Eqn. (3.72)}$$

where the Weber number We_g and the liquid Reynolds number Re_l are calculated as in Eqn. (3.51).

Due to the fact that the criterion chosen for the entrainment fraction calculation is based on a wave balance force, the correlation is limited to liquid Reynolds numbers greater than 2 for vertical downward flow, and 160 for vertical upward and horizontal flow, and this expression is only useful for low viscosity liquids (in particular, air-water systems). This correlation has been compared with many experimental data for air-water systems in the ranges of: $1 < P < 4$ atm; $0.95 < D < 3.2$ cm; $370 < Re_l < 64000$; and gas superficial velocities, $J_g < 100$ m/s, and the results have shown to be satisfactory correlated.

Another way to present this equation is shown by Baniamerian [Baniamerian, 2010], see Eqn. (3.75), in which the total liquid mass flux of entrained liquid (G_e) is obtained.

3.4.3. Total Liquid Mass Flux of the Entrained Liquid

The entrainment mass flux, G_e, is the total mass flow rate of entrained liquid per unit of interfacial area in the gas core. As in the previous section, the fully developed entrainment region is also the most widely studied in the literature and, consequently, many experimental correlations have been developed along the last decades. A summary of them is shown in Table 3.4 and some of the most widely used are compiled here below.

3.4.3.1. Okawa's Correlation

Okawa et al. [Okawa, 2003] obtained the next expression by assuming that the entrainment rate from roll wave is proportional to the interfacial shear force and inversely proportional to the surface tension force

$$G_e = \begin{cases} 4.79x10^{-4}\left(\frac{\rho_l}{\rho_g}\right)^{0.111} \rho_g \rho_l f_i J_g^2 \frac{\delta}{\sigma} & \mathrm{Re}_l \geq \mathrm{Re}_{ffOE} \\ 0 & \mathrm{Re}_l \leq \mathrm{Re}_{ffOE} \end{cases} \qquad \textbf{Eqn. (3.73)}$$

where f_i is the interfacial friction factor. As it has been shown previously, the roll wave mechanism does not take place when Re_l is smaller than a critical liquid film Reynolds number, Re_{ffOE}. For this reason, droplet entrainment is neglected below this limit; the value of 320 is adopted by the authors for Re_{ffOE}.

In this expression δ is the film thickness, but the author proposes to estimate this parameter from the balance between the interfacial shear force and the wall friction force acting on the liquid film:

$$\delta = \frac{1}{4}\sqrt{\frac{f_w \rho_l}{f_i \rho_g}}\frac{J_{lf}}{J_g} D \qquad \textbf{Eqn. (3.74)}$$

and f_w is the wall friction factor, evaluated by $\left(\max.\left(\frac{16}{\mathrm{Re}_{lf}}, 0.005\right)\right)$; f_i is the interfacial friction factor; the liquid film properties can be obtained from these of the liquid by multiplying by (1-E), being E the entrained fraction, but as a first approximation, it can be obtained from the liquid properties.

The validity range of the Eqn. (3.73) has a lower limit because of the fact that the roll waves are not formed when Re_l is smaller than the critical film Reynolds number, Re_{ffOE}, a value of 320 is adopted for this critical Reynolds number (the values varies from 100 to 500 approximately for vertical upward and horizontal flows, a in depth analysis of the onset of entrainment Reynolds number is shown in Berna et al. [Berna, 2014]).

Table 3.4. Summary of Entrainment Mass Flux correlations.

Reference	Correlation
Developing and fully developed entrainment regions	
Kataoka et al. [Kataoka, 2000]	- Smooth injection $G_e = 9.35x10^{-6}\,\xi \exp\left(-1.87x10^{-5}\,\xi^2\right)\rho_l J_l \,\mathrm{Re}_l^{0.5}\, We_g^{-0.25} E +$ $+ 0.022\rho_l J_l \,\mathrm{Re}_l^{-0.26}\left(\frac{\mu_g}{\mu_f}\right)^{0.26} E^{0.74}\left[1-\exp\left(-1.87x10^{-5}\,\xi^2\right)\right]^{0.74}$ - Generalized expression $G_e = 7.2x10^{-10}\,\frac{\mu_l}{D}\mathrm{Re}_l^{1.75}\, We_g (1-E)^{0.25}\left(1-\frac{E_z}{E}\right)^2 +$ $E_z/E \le 1$ (developing $6.6x10^{-7}\,\frac{\mu_l}{D}\mathrm{Re}_l^{0.925}\, We_g^{0.925}\left(\frac{\mu_g}{\mu_f}\right)^{0.26}(1-E_z)^{0.185}$ entrainment region) $G_e = 6.6x10^{-7}\,\frac{\mu_l}{D}\mathrm{Re}_l^{0.925}\, We_g^{0.925}\left(\frac{\mu_g}{\mu_f}\right)^{0.26}(1-E_z)^{0.185}$ $E_z/E > 1$ (fully developed entrainment region)
Stevanovic and Studovic [Stevanovic, 1995]	$G_e = 1.1\times10^4\,\delta^{2.25}\rho_l$ (developing entrainment region) D = 3.175 cm., α_{lf} = 0.0526, α_d=0.0005; u_g=40.1 m/s, u_l=2.75 m/s, u_d = 28.86 m/s; P = 1.7 bar
Fully developed entrainment region	
Okawa et al. [Okawa, 2003]	$G_e = 4.79x10^{-4}\left(\frac{\rho_l}{\rho_g}\right)^{0.111}\rho_g\rho_l f_i J_g^2\,\frac{\delta}{\sigma}$ $\mathrm{Re}_l \ge \mathrm{Re}_{ffOE}$ $\delta = \frac{1}{4}\sqrt{\frac{f_w\rho_l}{f_i\rho_g}}\,\frac{J_{lf}}{J_g}D$; $f_w = \max.\left(\frac{16}{\mathrm{Re}_{lf}}, 0.005\right)$
Ishii and Mishima [Baniamerian, 2010]	$G_e = G(1-x)\tanh\left(7.25\times10^{-7}\,\mathrm{Re}_l^{0.25}\, We_g^{1.25}\right)$ G = total mass flux; x =dynamic quality, $x = \frac{W_g}{W_g + W_l}$
Sugawara [Stevanovic, 1995]	$G_e = 1.07\,\frac{\tau_i \Delta h_{eq}}{\sigma}\,\frac{u_g\mu_l}{\sigma}\left(\frac{\rho_l}{\rho_g}\right)^{0.4}$ $\Delta h_{eq} = \begin{cases} k_s & \mathrm{Re}_g \ge 10^5 \\ k_s\left[2.136\log\left(\mathrm{Re}_g\right) - 9.68\right] & \mathrm{Re}_g < 10^5 \end{cases}$ (equivalent wave height)

	$k_s = 0.57\delta + 21.73\times10^3\delta^2 - 38.8\times10^6\delta^3 + 55.68\times10^9\delta^4$ (equivalent wave roughness)
Hutchinson and Whalley [Stevanovic, 1995]	$G_e = \begin{cases} -0.000265 - 0.171TDS + 19.25TDS^2 \\ +884TDS^3 - 8135TDS^4 + 21410TDS^5 \quad when\ TDS \le 0.1 \\ -0.376 + 8.97TDS - 9.901TDS^2 \\ +63.51TDS^3 - 101TDS^4 + 46.81TDS^5 \quad when\ TDS > 0.1 \end{cases}$ $TDS = \frac{\tau_i \delta}{\sigma}; \quad \tau_i = \frac{1}{2} f_i \rho_g (u_g - u_l)^2 \approx \frac{1}{2} f_i \rho_g u_g^2$
Hewitt [Baniamerian, 2010]	$G_e = 5.75\times10^{-5}\alpha_g \rho_g u_g \left[(\mathrm{Re}_l - \mathrm{Re}_{ffOE})^2 \frac{\mu_l^2}{D\sigma} \frac{\rho_l}{\rho_g^2} \right]^{0.316} \quad \mathrm{Re}_l \ge \mathrm{Re}_{ffOE}$ $\mathrm{Re}_{ffOE} = 160$; α_g = void fraction
Ueda [Kataoka, 2000]	$G_e = 3.54\times10^{-3} U^{0.57} \quad U \ge 120$; $U = \frac{\tau_i}{\sigma_l}\left(\frac{J_g}{\sigma_l}\right)^{0.6}$
Adechi and Issa [Adechi, 2004]	$G_e = 3.54\times10^{-3}\chi^{0.57} \quad \chi \ge 120$ $\chi = \frac{\tau_i}{\sigma_l}\left(\frac{\varphi \bar{u}}{\sigma_l}\right)^{0.6}$; ū = averaged liquid film velocity ; $\varphi = 1 - \left(1 - \frac{2\delta}{D}\right)^2$
Schadel [Baniamerian, 2010]	$G_e = 1.175\times10^{-4} J_g \mu_l (\mathrm{Re}_l - \mathrm{Re}_{ffOE}) \left(\frac{\rho_l}{\rho_g}\right)^{0.5} \quad \mathrm{Re}_l \ge \mathrm{Re}_{ffOE}$
Fernandes et al. [Fernandes, 2004] (Schadel' modified)	$G_e = \frac{k\mu_l}{4} J_g \sqrt{\rho_l \rho_g} (\mathrm{Re}_{lf} - \mathrm{Re}_{ffOE}) \quad \mathrm{Re}_{lf} \ge \mathrm{Re}_{ffOE}$
Lopez de Bertodano et al. [Lopez de Bertodano 2001] (Dykhno and Hanratty's modified)	$G_e = \frac{\mu_l}{D}\frac{k_A'}{4}(\mathrm{Re}_{lf} - \mathrm{Re}_{ffOE}) We_g \left(\frac{\rho_l}{\rho_g}\right)^{0.5}$ $\mathrm{Re}_{ffOE} = 80$; $k_A' = 2.0 \times 10^{-7}$ Freon-113 data : D = 0.953 cm ; W_g = 0.0028-0.028 kg/s ; W_l = 0.0053-0.038 kg/s; J_g = 10.7-126 m/s; J_l = 0.074-0.54 m/s; P = 140-660 kPa. Water data: D = 1 cm; W_g = 0.0085-0.059 kg/s; W_l = 0.0056-0.059 kg/s; J_g = 5.2-25.4 m/s; J_l = 0.05-0.35 m/s; P = 250-500 kPa.
Lopez de Bertodano et al. [Lopez de Bertodano 1998] (Kataoka and Ishii's modified)	$G_e = 4.47x10^{-7}\frac{\mu_l}{D}\left[We_g \left(\frac{\rho_l - \rho_g}{\rho_g}\right)^{0.5} (\mathrm{Re}_{lf} - \mathrm{Re}_{ffOE}) \right]^{0.925} \left(\frac{\mu_g}{\mu_f}\right)^{0.26}$ $\mathrm{Re}_{ffOE} = 80$; $k_A' = 2.0 \times 10^{-7}$ Freon-113 data: D = 0.953 cm; W_g = 0.0028-0.028 kg/s; W_l = 0.0053-0.038 kg/s; J_g = 10.7-126 m/s; J_l = 0.074-0.54 m/s; P = 140-660 kPa. Water data: D = 1 cm; W_g = 0.0085-0.059 kg/s; W_l = 0.0056-0.059 kg/s; J_g = 5.2-25.4 m/s; J_l = 0.05-0.35 m/s; P = 250-500 kPa.

3.4.3.2. Ishii and Mishima's Correlation

Ishii and Mishima's [Baniamerian, 2010] correlation is one of the most known expressions to estimate the entrainment mass flux. This correlation is

$$G_e = G(1-x)\tanh\left(7.25\times10^{-7}\,\mathrm{Re}_l^{0.25}\,We_g^{1.25}\right) \qquad \textbf{Eqn. (3.75)}$$

where G is the total mass flux; x is the dynamic quality, $x = \dfrac{W_g}{W_g + W_l}$; We_g is the gas Weber number; and Re_l is the Reynolds liquid number.

3.4.3.3. Fernandes' Correlation

Fernandes et al. [Fernandes, 2004] presents the Schadel's equation in a slightly different form:

$$G_e = \begin{cases} \dfrac{k\mu_l}{4} J_g \sqrt{\rho_l \rho_g}\left(\mathrm{Re}_{lf} - \mathrm{Re}_{ffOE}\right) & \mathrm{Re}_{lf} \geq \mathrm{Re}_{ffOE} \\ 0 & \mathrm{Re}_{lf} \leq \mathrm{Re}_{ffOE} \end{cases} \qquad \textbf{Eqn. (3.76)}$$

where k denotes the entrainment rate parameter. Fernandes explains that, even though the Schadel's results were for a vertical flow at high superficial gas velocities, can be assumed that it is a good description for horizontal flows as well. For an air water flow at near atmospheric conditions, Schadel found k ≈ 0.00045 m·s/kg and Re_{ffOE} ≈ 200 for a 25.4 mm pipe. For the air–water experiments of Al-Sarkhi and Hanratty, they found k in the range 0.0001–0.0006 m·s/kg, with higher values for higher u_g and lower values for lower pipe diameters. In Fernandes's work of gas-condensate experiments, they found values of k between 0.0006 and 0.0011 m·s/kg.

3.5. Study of Experimental Data and Adjustment Correlations

Caused by the large existing dispersion in the results provided by the correlations that characterize the entrained droplet properties, we decided to conduct a literature search of the existing experimental measurements and finally, from it, to develop new correlations for these key variables. This section presents most relevant studies conducted to determine droplet sizes in annular flow. First, some conclusions are drawn from the experimental data. Next, the behavior of several empirical correlations is analyzed and new improved correlations presented. We will continue presenting the comparison of all this correlations with the experimental data, following with a dimensional analysis of these empirical correlations and some conclusions obtained from this study. Finally, the comparison of the results obtained from the empirical correlations with the correlations involving the critical Weber number are presented, which is a very simple and fast way to obtain a first estimation of droplet sizes.

3.5.1. Droplet Sizes: Experimental Data and Correlations.

This section is dedicated to present all studies conducted to determine droplet sizes in annular flow. First part is devoted to present some conclusions drawn directly from the experimental data. Next section, from the available experimental data, analyzes several empirical correlations found in the literature and present new correlations to improve them. We will continue presenting the comparison of all this correlations with the experimental data, following with a dimensional analysis of these empirical correlations and some conclusions obtained from this study. Finally, the comparison of the results obtained from the empirical correlations with the correlations involving the critical Weber number are presented, which is a very simple and fast way to obtain a first estimation of droplet sizes.

3.5.1.1. Analysis of Droplet Sizes from the Experimental Data

The most important parameter determining droplet sizes is said to be gas velocity [Azzopardi, 1997; Kocamustafaogullari, 1994]. Liquid velocity also affects, but not as much as gas velocity. Figure 3.5 and Figure 3.6 show the variation of droplet mean diameter with gas and liquid velocities for Al-Sarkhi's [Al-Sarkhi, 2002] and Fore's [Fore, 2002] experimental data. As noted, when gas velocity increases droplet sizes decrease and vice versa; the opposite is true for the liquid velocity. Additionally, it seems that these two variables effect are not entirely independent: on one hand, the higher the liquid velocity, the smaller the impact of gas velocity, particularly when the latter is over 35 m/s; on the other, at low values of liquid velocity ($J_l < 0.05$ m/s), the higher impact of gas velocity is noted for lower gas velocities ($J_g < 23$ m/s).

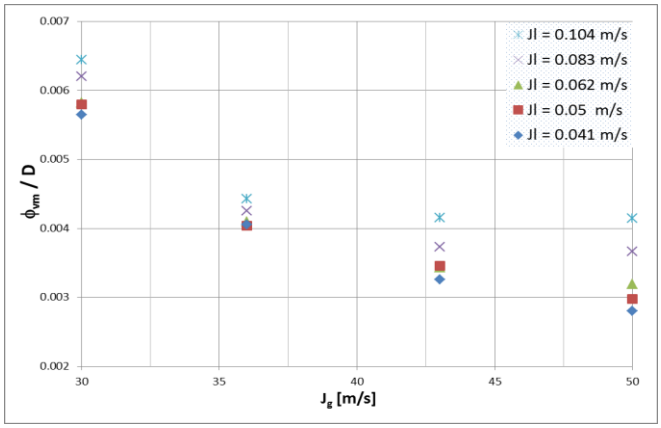

Figure 3.5. Al-Sarkhi's experimental data of Droplet Mean Diameter (Horizontal Flow, D=0.0254 m, P & T ambient), effect of gas velocity with constant liquid velocity.

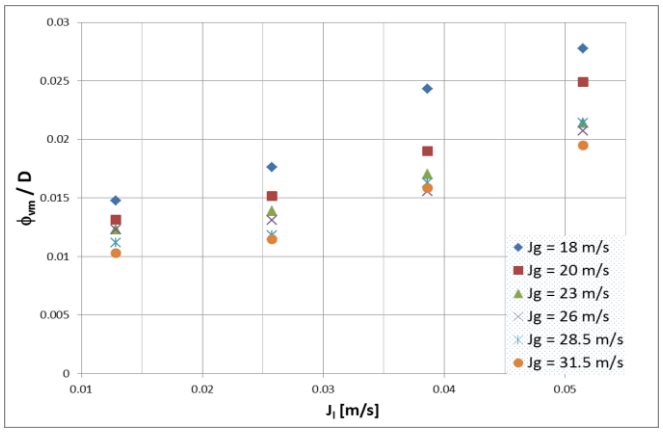

Figure 3.6. Fore's experimental data of Droplet Mean Diameter (Vertical Upward Flow, D=0.0508 m, P & T ambient), effect of liquid velocity with constant gas velocity.

3.5.1.2. New Correlations of the Droplet Sizes in Annular Flow

Many papers have been published over the last decades using different geometries and two-phase systems to measure droplet sizes. Based on geometry, those studies may be grouped in three types: horizontal, vertical upward and vertical downward. The first two are considered the most important ones; besides, for the latter type only a set of experimental measurements of droplet sizes that dates back in the 60's have been found. Then, the measurements here considered have been, firstly, the ones of horizontal flow (Paras and Karabelas [Paras, 1991], Simmons [Simmons, 2001] and Al-Sarkhi [Al-Sarkhi, 2002]) and, secondly, the ones of vertical upward flow ((Cousins and Hewitt [Tatterson, 1977], Lopes [Lopes, 1984], Fore and Duckler [Fore, 1995] and Fore et al. [Fore, 2002]).

The experimental measurements of all horizontal tests were carried out at ambient conditions. Regarding pipe diameters, these were: for Paras and Karabelas a diameter of 0.0508 m; for Al-Sarkhi 0.0254 m; and for Simmons 0.0953 m.

The experimental measurements of vertical data were carried out at the following conditions: Cousins and Hewitt's, Lopes' and the first set of Fore's data were carried out at ambient pressure and temperature conditions; the pipe diameters were 0.0095, 0.05075 and 0.0508 m respectively; the last two series of Fore's data were made in a pipe of 9.67 mm of hydraulic diameter at temperatures of about 38ºC and pressures of approximately 3.5 and 17 bars, respectively.

The above-mentioned set of experimental data has been correlated with several expressions presented along this paper. The Tatterson's correlation performance Eqn. (3.19), is shown in Figure 3.7. As noted, most data fall within the ±50% band of the correlation only for values of the nondimensional x axis less than 0.2. From there on data show a huge scattering, but even the closer ones to the correlation are out of the ±50%. The

correlation is able to predict the droplet diameter for the experimental data taken for vertical upward flow at ambient conditions of pressure and temperature. Nevertheless, it underestimates diameters under pressures and temperatures above ambient conditions (Fore series 3.5 and 17 bars). On the other side, it overestimates droplet diameters in horizontal pipes.

The next expression to be analyzed is the one proposed by Ishii and Kataoka [Ishii, 1983], Eqn. (3.22). The results are shown in Figure 3.8. It can be appreciated that the general trend of the experimental results are better followed than in the Tatterson's correlation, but still the Fore's high-pressure measurements and the horizontal flow measurements (Paras, Al-Sarkhi and Simmons) are slightly outside of the ±50% error band.

Another expression proposed by the same investigation group, Kataoka, Ishii and Mishima [Fore, 2002] is also presented, Eqn. (3.23). As noted (Figure 3.9) despite their intent to improve the above expression, the behavior is very similar.

The Kocamustafaogullari correlation [Kocamustafaogullari, 1994] has been also studied, Eqn. (3.29). As the author's original expression gave the maximum droplet size diameter, a ULLN statistical distribution function (b = 1.93 and λ= 0.75) to derive the mean diameter (ϕ_{vm} =0.341 × ϕ_{max}). Those are shown in Figure 3.10. As observed, no major improvements are achieved with this expression; a better fit than previous measures for horizontal flow measurements (Paras, Al-Sarkhi and Simmons), to say the most.

Finally, Patruno's expression has been presented [Patruno, 2010], Eqn. (3.26). Although this correlation has been developed for Exxol D60^{TM} (aliphatic hydrocarbon aromatized) at high pressure conditions, the author himself correlated the Fore's data, both at atmospheric pressure and at high pressure. Figure 3.11 shows that the correlation adequately predicts the experimental measurements of Fore at high pressure, but all other data are not properly predicted.

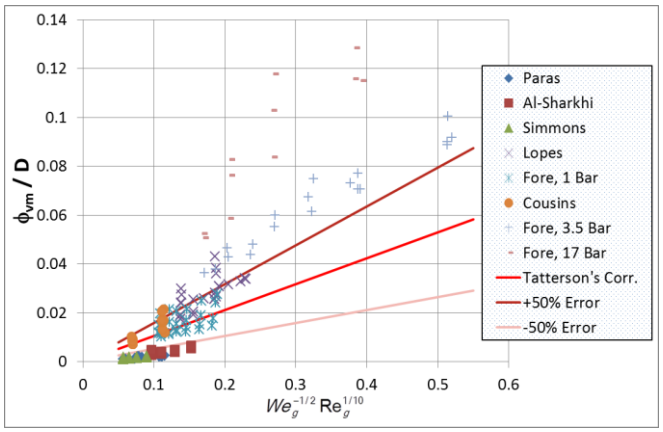

Figure 3.7. Comparison of experimental data with the correlation given by Tatterson et al. [Tatterson, 1977].

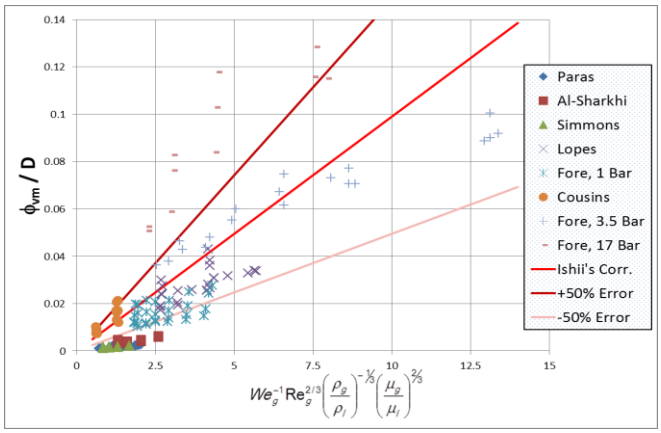

Figure 3.8. Comparison of experimental data with the correlation given by Ishii and Kataoka [Ishii, 1983].

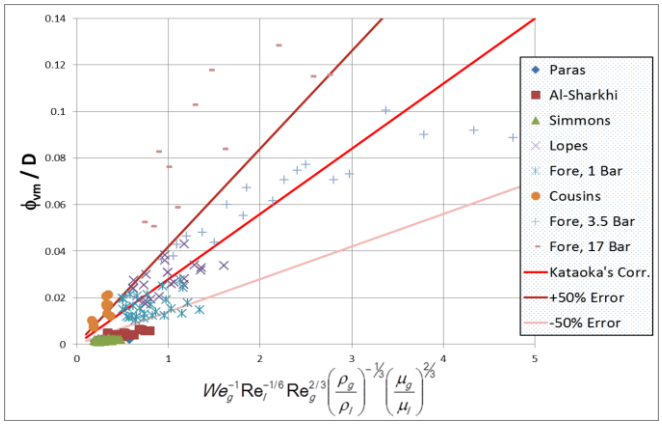

Figure 3.9. Comparison of experimental data with the correlation given by Kataoka [Fore, 2002].

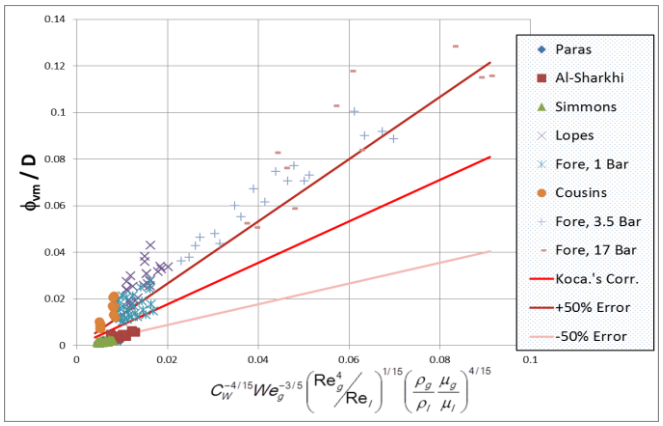

Figure 3.10. Comparison of experimental data with the correlation given by Kocamustafaogullari [Kocamustafaogullari, 1994].

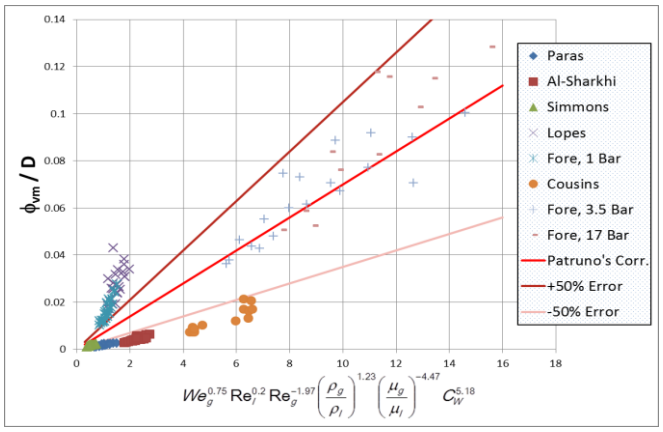

Figure 3.11. Comparison of experimental data with the correlation given by Patruno [Patruno, 2010].

As noted in the data shown above, the flow configuration is a major difference. So, despite the above correlations might be intended for a generic use, observations recommend to derive a flow configuration dependent correlation. These discrepancies have to be mainly caused by the differences in the effects produced by the gravity forces in vertical and horizontal pipes. Consequently, two new correlations are here proposed, one for horizontal data and another for vertical upward data.

The horizontal data set was found to be better adjusted by the next correlation:

$$\frac{\phi_{vm}}{D} = 2.634 \cdot We_g^{-0.23}\,\mathrm{Re}_g^{-0.54}\,\mathrm{Re}_l^{0.13} \qquad \textbf{Eqn. (3.77)}$$

where the Weber and Reynolds numbers are defined in terms of superficial velocities. The fitting of the new correlation with the horizontal data is presented in Figure 3.12. As can be seen, the new equation fits data much closer, almost all of them are between the ±25% error band, with a value for the Pearson product-moment correlation coefficient of R^2=0.902.

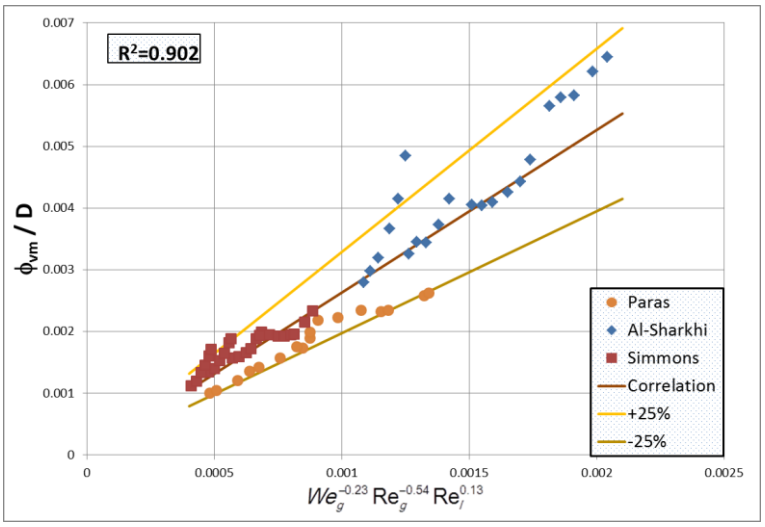

Figure 3.12. Comparison of horizontal experimental data with the new correlation.

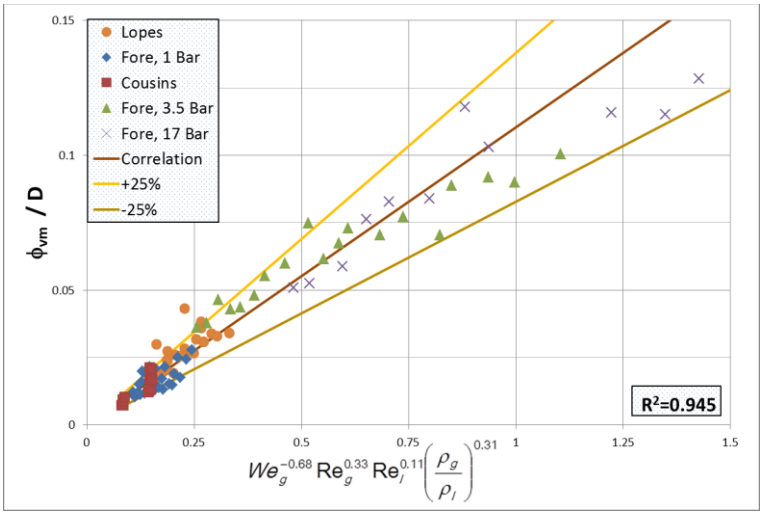

Figure 3.13. Comparison of vertical upward experimental data with the new correlation.

The vertical upward data set was found to be better adjusted by the next correlation:

$$\frac{\phi_{vm}}{D} = 0.11 \cdot We_g^{-0.68} \, \mathrm{Re}_g^{0.33} \, \mathrm{Re}_l^{0.11} \left(\frac{\rho_g}{\rho_l} \right)^{0.31} \qquad \textbf{Eqn. (3.78)}$$

with the same definition as in the previous equation for the Weber and Reynolds numbers. As can be seen in Figure 3.13, the new equation provide a good fitting of data, with most of measurements in between ±25% error band and a Pearson correlation coefficient even higher than the above expression's (R^2=0.945).

3.5.1.3. Analysis of the Droplet Size Correlations and Comparison with the Experimental Data

As the above equations are unfolded in terms of the fundamental kinetic variables and fluid properties, one may reach to an expression like:

$$\phi_{vm} = CONSTANT \cdot D^a \, J_g^b \, J_l^c \, \rho_g^d \, \rho_l^e \, \mu_g^f \, \mu_l^g \, \sigma^h \qquad \textbf{Eqn. (3.79)}$$

where the exponents are given in Table 3.5 for the correlations here considered. Note that the pipe diameter has been moved to the right side of the correlations to take it into account in the table. The correction factor, C_W has been $C_W = 0.028 N_\mu^{-4/5}$ in all the cases and $\rho_l - \rho_g \cong \rho_l$.

Table 3.5. Summary table of the exponents for each of the parameters involved in droplet size correlations.

Correlation	a	b	c	d	e	f	g	h
Tatterson, Eqn. (3.19)	6/10	-9/10	-	-4/10	-	-1/10	-	½
Ishii, Eqn. (3.22)	2/3	-4/3	-	-2/3	1/3	0	-2/3	1
Kataoka, Eqn. (3.25)	1/2	-4/3	-1/6	-2/3	1/6	0	-1/6	1
Patruno, Eqn. (3.26)	-0.02	-0.47	0.2	0.01	0.006	-2.5	0.126	2.358
Kocamustafaogullari, Eqn. (3.29)	0.6	-0.933	-0.067	-0.067	-0.386	0	0.0133	0.433
Tatterson Theoretical, Eqn. (3.30)	-	-1	-	-0.5	-0.25	-	-	0.75
Al-Sarkhi, Eqn. (3.33)	0.493	-1.014	-	-0.507	-	-	-	0.507
New Horizontal, Eqn. (3.77)	0.353	-1.01	0.127	-0.774	0.127	0.541	-0.127	0.233
New Vertical Upward, Eqn. (3.78)	0.756	-1.038	0.112	-0.042	-0.2	-0.327	-0.112	0.682

3.5.1.3.1. Comparison of the Empirical Correlations with the Experimental Data

As shown above, the most influencing variable on droplet size is the gas superficial velocity. To assess the ability of correlations to catch the experimental trend with respect to this variable, comparisons have been set in which the rest of variables have been kept constant and just the superficial gas velocity is variable.

Figure 3.14 shows the response of correlations when gas superficial velocity changes at a constant liquid velocity (0.104 m/s) for horizontal flows. Al-Sarkhi's data have been used. As observed, only the new correlation proposed follows accurately the experimental trend, whereas the rest of correlations overestimate them and, generally, show slopes far from data's. However, Azzopardi's, Tatterson's theoretical and Al Sarkhi's get a reasonable approximation.

Figure 3.15 shows the correlations compared to Fore's data, again for a variable superficial gas velocity at a constant liquid one (0.02573 m/s). Tatterson's correlation follows very closely the experimental measurements, although Kocamustafaogullari's and the new correlation give acceptable results.

Regarding Fore's high temperature and pressure data, the results are presented in Figure 3.16 and Figure 3.17. The correlation that better fits data at 3.5 bars is the one proposed in this paper; nonetheless, Ishii's and Kataoka's offer a reasonable agreement with data trends in the whole range explored of J_g. The rest of expressions underestimate the experimental results, even though approaching them as the gas velocity increases. At 17 bars, although data are scarce, it seems that the only acceptable behavior is the one of the correlation proposed in this paper and, just at high J_g, Patruno's correlation.

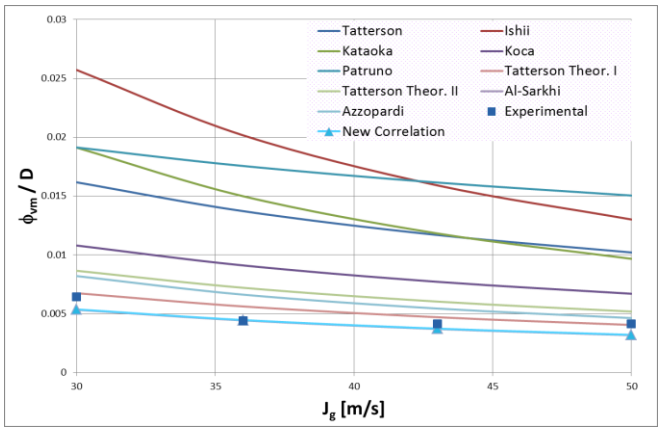

Figure 3.14. Comparison of droplet mean diameter of Al-Sarkhi's data (Horizontal Flow, D=0.0254 m, P & T ambient, J_l = 0.104 m/s) with several correlations.

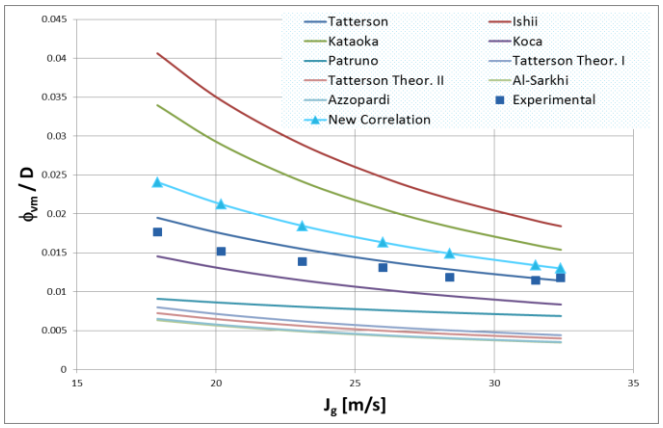

Figure 3.15. Comparison of droplet mean diameter of Fore's data (Vertical Upward Flow, D=0.0508 m, P & T ambient, J_l = 0.02573 m/s) with several correlations.

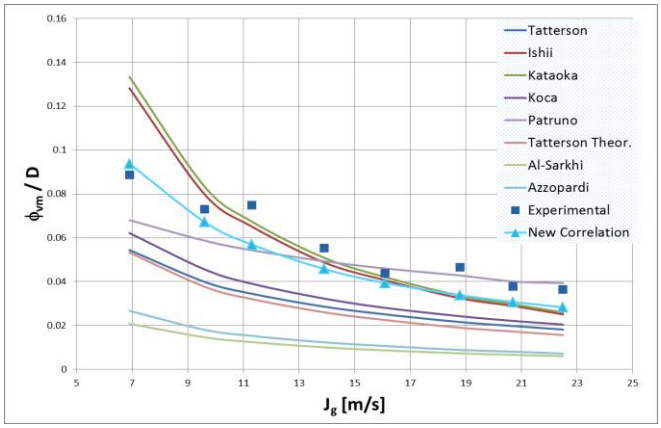

Figure 3.16. Comparison of droplet mean diameter of Fore's data (Vertical Upward Flow, D=0.00967 m, P ≅ 3.5 bars & T ≅ 38 ºC, J_l ≅ 0.03 m/s) with several correlations.

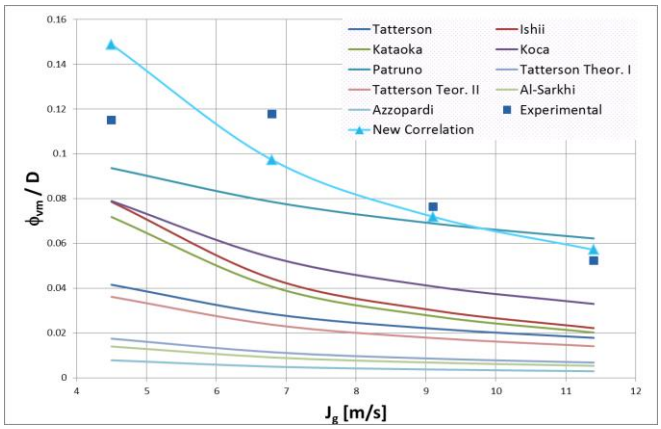

Figure 3.17. Comparison of droplet mean diameter of Fore's data (Vertical Upward Flow, D=0.00967 m, P ≅ 17 bars & T ≅ 38 ºC, J_l ≅ 0.06 m/s) with several correlations.

As explained above, the most influencing variable on droplet size is the gas superficial velocity, but it has been considered interesting to analyze how the different equations behave when analyzing the effect of the liquid superficial velocity. To assess the ability of these correlations to catch the experimental trend with respect to this variable, comparisons have been set in which the rest of variables have been kept constant and just the superficial liquid velocity is variable.

Figure 3.18 shows the comparisons at a constant gas velocity (50 m/s) for horizontal flows, Paras and Karabelas's data have been used. Only the new correlation, the Tatterson theoretical expression, Al-Sarkhi's and Azzopardi's correlations are able to follow accurately the experimental measurements, whereas the rest of correlations overestimate them. Also note that there is a slightly upward trend of dimensionless droplet size ratio with liquid velocity, which is also well captured, especially by the new correlation.

Figure 3.19 shows the response of correlations when gas liquid velocity changes at a constant gas velocity (9 m/s) at high pressure (17 bar) for vertical flows. Only the new correlation and Patruno's correlation follow accurately the experimental measurements, whereas the rest of correlations clearly underestimate them. Note that the upward trend of the dimensionless droplet size ratio with liquid velocity in the experimental measurements is also captured by both correlations, whereas the rest of correlations predict a negative slope.

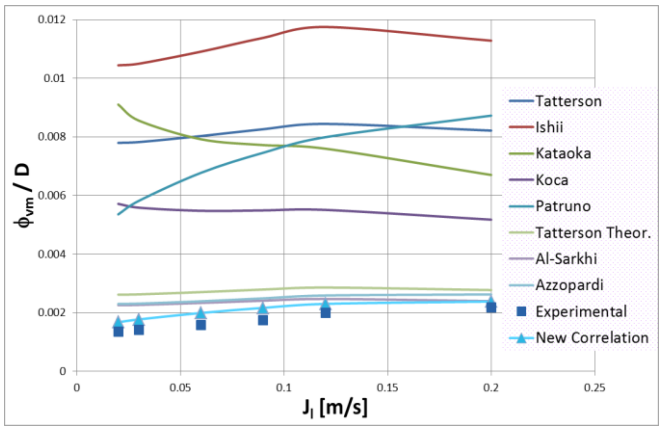

Figure 3.18. Comparison of droplet mean diameter of Paras's data (Horizontal Flow, D=0.0953 m, P & T ambient, $J_g \cong 50$ m/s) with several correlations.

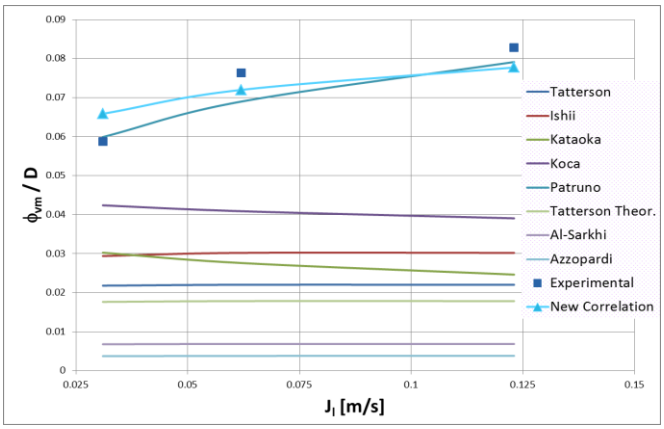

Figure 3.19. Comparison of droplet mean diameter of Fore's data (Vertical Upward Flow, D=0.00967 m, P ≅ 17 bars & T ≅ 38 ºC, $J_g \cong 9$ m/s) with several correlations.

3.5.1.3.2. Comparison of the New Correlations with the Expressions Involving the Critical Weber Number

All the expressions in section 3.2.1 have been studied and their results have been found out to be similar (i.e., same order of magnitude). Then in what follows, just the critical Weber number criterion (Eqn. (3.1) with $We_{crit} = 12$) is shown. Note that to derive mean size from the maximum one given by this criterion, a ULLN distribution for the droplet size (b=1.93; λ= 0.75). Figure 3.20 and Figure 3.21 show the predictions performance with respect to data for vertical upward and horizontal flow, respectively. As observed, the new correlations derived from annual flow data are more accurate than

critical Weber number criterion; in both flow configurations the linear correlation coefficient has much higher values: 0.921 versus 0.639, for vertical flow; and 0.874 versus 0.724, for horizontal flow. Nevertheless, in case that only gas velocity was available, critical Weber number criterion provides a reasonable approximation.

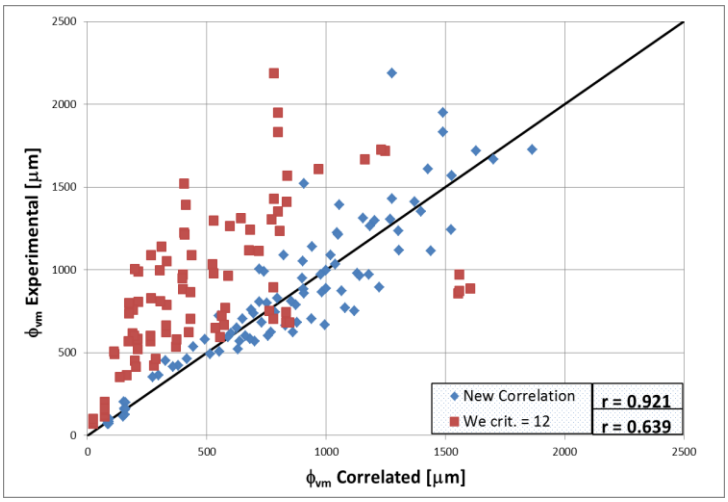

Figure 3.20. Comparison of the experimental data for the droplet sizes with the ones obtained with the Critical Weber number criterion model and with the new correlation for vertical upward flow conditions.

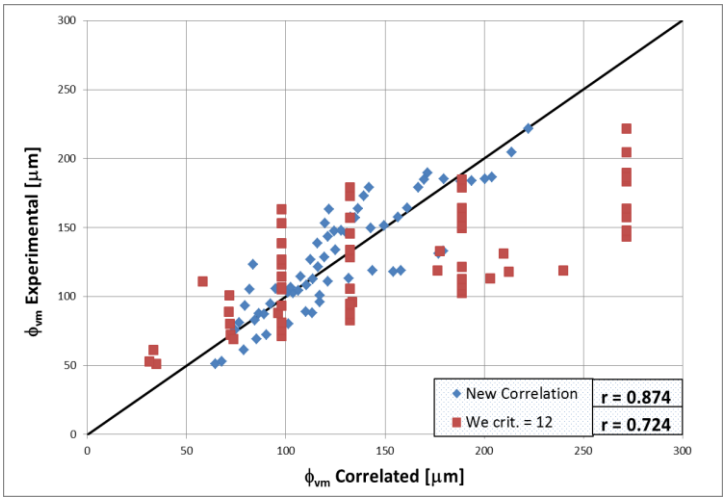

Figure 3.21. Comparison of the experimental data for the droplet sizes with the ones obtained with the Critical Weber number criterion model and with the new correlation for horizontal flow conditions.

3.5.2. The Entrainment Mass Flux: Experimental Data and Correlations.

Because of the already mentioned scattering in the results provided by the different correlations, which becomes even more pronounced in this case, we decided to conduct a search and subsequent analysis of experimental data related to this magnitude. Consequently, here below the data from which the expressions in section 3.4 were derived are analyzed and on their bases a new correlation is proposed. Finally, a comparison among other correlations and the new one is set.

3.5.2.1. Analysis of Entrained Fraction from the Experimental Data

The experimental series analyzed are Azzopardi's [Azzopardi, 1991], Simmons's [Simmons, 2001], Mantilla's [Mantilla, 2008] and Alamu's [Alamu, 2010]. The experimental conditions of each of them were: Azzopardi's data were taken with the laser diffraction technique in a 0.02 meter vertical upward flow at a pressure of 1.5 bars and at ambient temperature, the working fluids were air and water; Simmons's data were measured with a Malvern Spraytec 5008 in a 0.0953 meter horizontal pipe at ambient pressure and temperature, the working fluids were air and water; Mantilla's data were taken in two experimental facilities, namely, a 2-inches and a 6-inches horizontal flow loops, for the 2-inches experimental facility three experiments with different working fluids were carried out (air-water, air- water-butanol and air-water-glycerin) and air-water for the 6" facility, the measurements were taken at ambient temperature and pressures of 2 and 1 bar respectively; and Alamu's data were taken on a vertical pipe with an inner diameter of 19 mm, the used fluids were air and a mixture of water and glycerin (dynamic viscosity of 3.6 mPa s and density of 1097 kg.), at a pressure of 1.5 bars and ambient temperature.

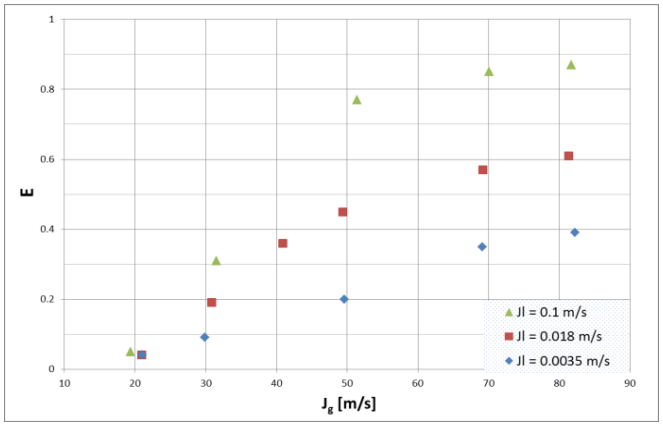

Figure 3.22. Mantilla's experimental Entrained Fraction data (Horizontal Flow, D=0.0486 m, P=2 bars, T ambient, Working fluids: Air-Water), effect of liquid velocity with constant gas velocity.

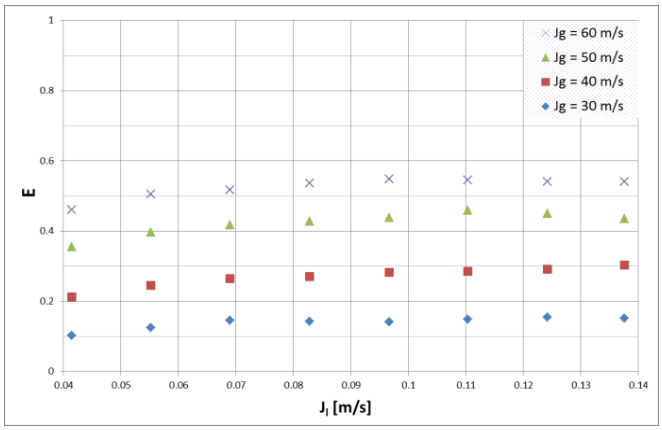

Figure 3.23. Azzopardi's experimental Entrained Fraction data (Vertical Upward Flow, D=0.02 m, P=1.5 bar, T ambient, Working fluids: Air-Water), effect of liquid velocity with constant gas velocity.

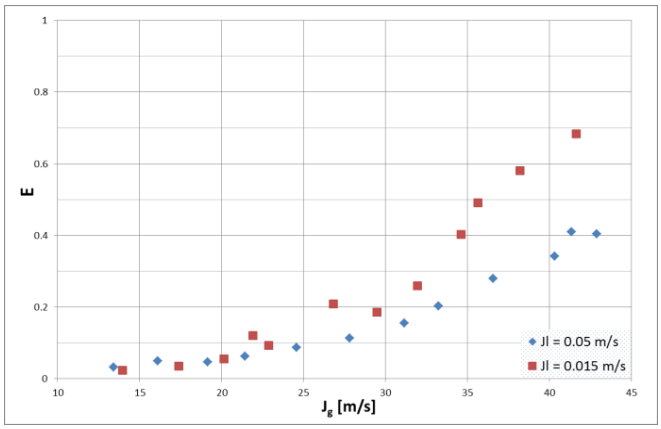

Figure 3.24. Alamu's experimental Entrained Fraction data (Horizontal Flow, D=0.0486 m, P=2 bars, T ambient, Working fluids: Air-Water-Glycerin), effect of liquid velocity with constant gas velocity.

From Figure 3.22 to Figure 3.24 display the entrained liquid fraction as a function of the gas and liquid superficial velocities, based on Mantilla's, Azzopardi's and Alamu's data. In the horizontal configuration (Figure 3.22) it is soundly observed that the higher gas velocity the higher entrainment. Likewise, for the same gas velocity, a liquid velocity increase results in a higher entrainment fraction too, although having a lesser effect. For vertical flow, in the range of conditions explored by Azzopardi's (Figure 3.23), the entrainment fraction growth with gas and liquid superficial velocities looks much more moderate, particularly with the liquid superficial velocity. Alamu's data trends (Figure 3.24) confirm these observations for Water-Glycerin mixtures.

3.5.2.2. New Correlation of the Entrained Fraction from Annular Flow

Entrainment has been correlated in terms of the entrained fraction (E). The dimensionless numbers which are considered to be the predominant in the entrainment phenomenon have been studied. Finally, based on all the data set previously introduced and using the dimensionless numbers which dominate this magnitude, the best correlation found is:

$$\frac{E}{1-E} = 5.51\cdot 10^{-7} \cdot We_g^{2.68}\,\mathrm{Re}_g^{-2.62}\,\mathrm{Re}_l^{0.34}\left(\frac{\rho_g}{\rho_l}\right)^{-0.37}\left(\frac{\mu_g}{\mu_l}\right)^{-3.71} C_W^{4.24} \qquad \textbf{Eqn. (3.80)}$$

being the Weber and Reynolds numbers defined in terms of superficial velocities. The expression of the Surface Tension Factor is as originally was defined by Ishii, Eqn. (3.27).

Data fitting by the correlation is presented in Figure 3.25. As can be seen in the figure, the data shows a large scattering that prevents this correlation from having higher accuracy than data. Despite that, most data fall in between ±50% (the Pearson product-moment correlation coefficient of R^2=0.666).

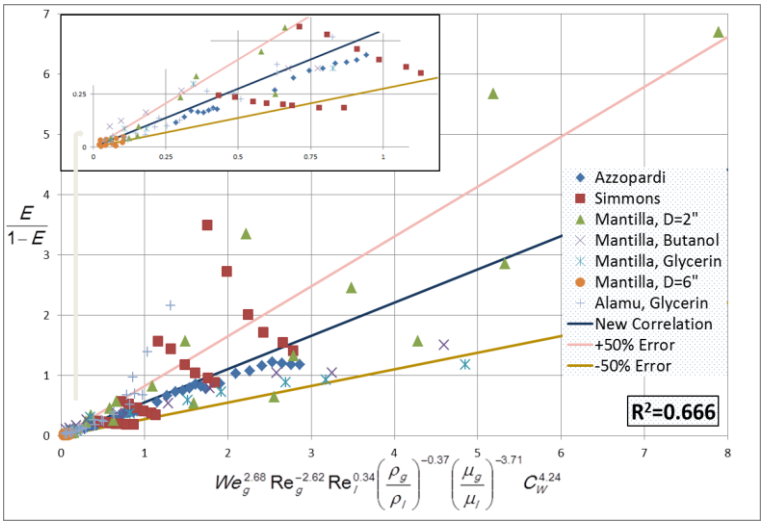

Figure 3.25. Comparison of the entrained fraction experimental data with the new correlation results.

3.5.2.3. Analysis of the Entrained Fraction Correlations and Comparison with Experimental Data

As on droplet size, the most influencing variable on entrainment fraction is the gas superficial velocity. Consequently, to evaluate the ability of correlations to capture the

experimental trend with respect to this variable, comparisons have been set keeping constant the rest of magnitudes and just the superficial gas velocity was varied.

Figure 3.26 shows the entrained fraction versus the gas velocity at a constant liquid velocity (0.06894 m/s) for vertical upward flows, Azzopardi's data are displayed. The correlations of Wallis, Oliemans, Zhang and Ishii give results similar to the expression derived, all of them being very similar to the experimental.

Figure 3.27 displays the entrained fraction versus the gas velocity at a constant liquid velocity (0.004 m/s) but for large pipes (6 inches), Mantilla's data are shown. The correlations of Nakazatomi and the proposed here accurately predict the experimental results; note that in this case all other correlations predict much higher values.

Figure 3.28 shows the response of correlations when gas superficial velocity changes at a constant liquid velocity (0.0159 m/s) for vertical flows, Simmons' data have been used. None of the correlations follow the experimental values, although at least the proposed correlation captures the trend, besides being closer to the experimental data at low gas velocities.

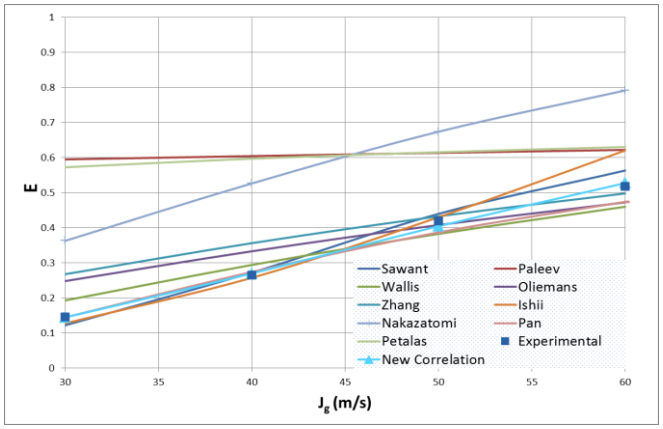

Figure 3.26. Comparison of Entrained Fraction of Azzopardi's data (Vertical Upward Flow, D=0.02 m, P=1.5 bar, T ambient, J_l=0.06894 m/s) with several correlations.

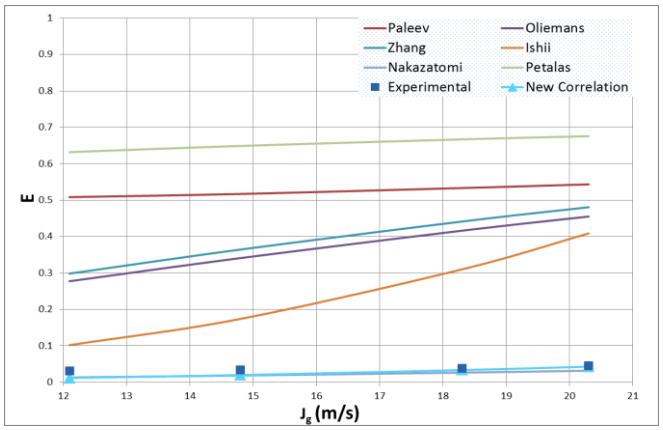

Figure 3.27. Comparison of Entrained Fraction of Mantilla's data (Horizontal Flow, D=0.153 m, P & T ambient, J_l=0.004 m/s) with several correlations.

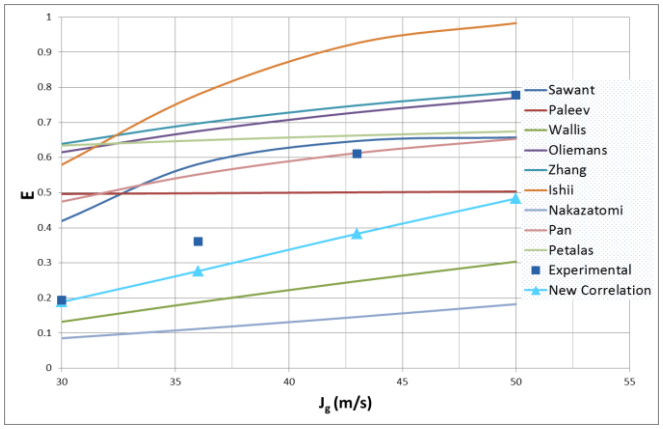

Figure 3.28. Comparison of Entrained Fraction of Simmon's data (Horizontal Flow, D=0.0953 m, P & T ambient, J_l=0.0159 m/s) with several correlations.

Figure 3.29 and Figure 3.30 present the comparison of Mantilla's data for mixtures of water-butanol and water-glycerin as working liquids, thus introducing the influence of the physical properties of working liquid in the entrained fraction expression. Mantilla's data for a water-butanol mixture are shown in Figure 3.29, only Nakazatomi's correlation alongside with the new correlation, accurately follow the experimental measurements. Figure 3.30 shows the results obtained for Alamu's experimental series (water-glycerin mixture). No correlation accurately predicts the experimental results, although the correlation developed in this paper has very similar values at low gas velocities, but moving away slightly with the increase of the gas superficial velocity.

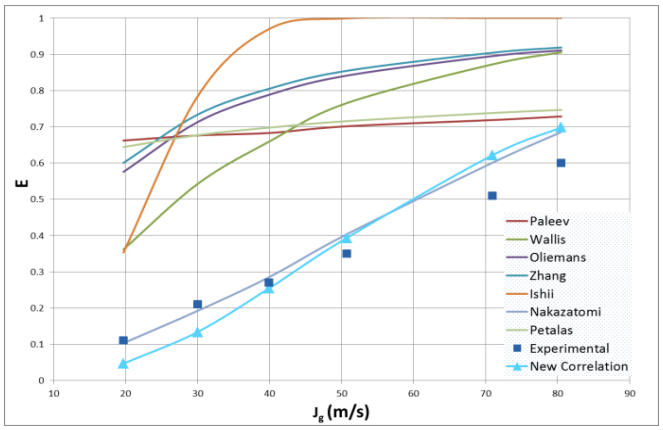

Figure 3.29. Comparison of Entrained Fraction of Mantilla's data (Horizontal Flow, air-water-butanol, D=0.0486 m, P=2 bar, T ambient, J_l=0.018 m/s) with several correlations.

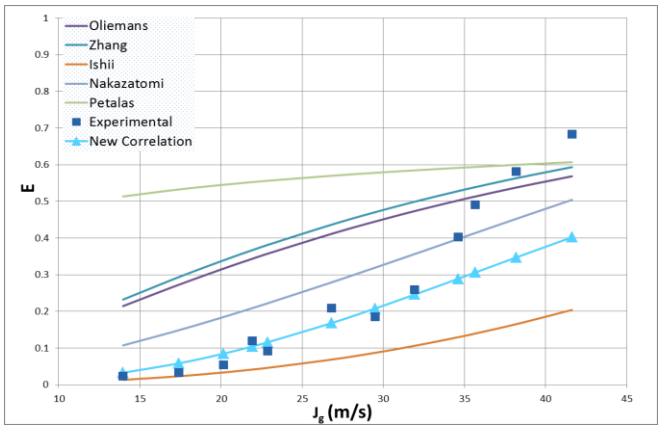

Figure 3.30. Comparison of Entrained Fraction of Alamu's data (Vertical Upward Flow, air-water-glycerin, D=0.019 m, P=1.4 bar, T ambient, J_l=0.15 m/s) with several correlations.

As explained above, the most influencing variable on entrained fraction is the gas superficial velocity, but it has been considered interesting to analyze how the different equations behave when analyzing the effect of the liquid superficial velocity. To assess the ability of these correlations to catch the experimental trend with respect to this variable, comparisons have been set in which the rest of variables have been kept constant and just the superficial liquid velocity is variable.

Figure 3.31 shows the comparison of correlations at a constant gas velocity (60 m/s) for Azzopardi's data. The correlation proposed in this paper give the best results, although other correlations like those of Sawant and Zhang give good results too.

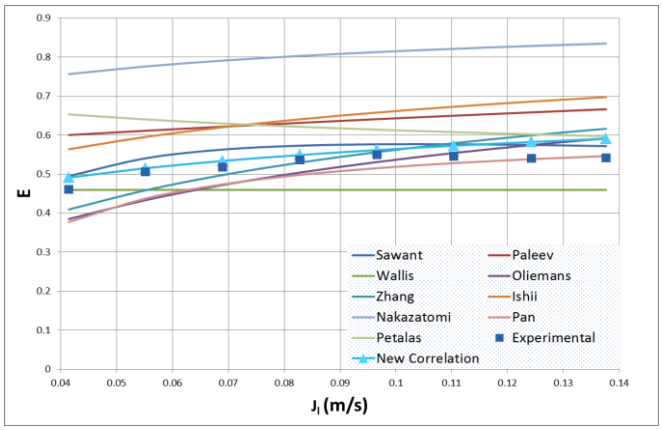

Figure 3.31. Comparison of Entrained Fraction of Azzopardi's data (Vertical Upward Flow, D=0.02 m, P=1.5 bar, T ambient, J_g=60 m/s) with several correlations.

As a conclusion, the new correlation derived show a consistent behavior when compared to most data and, anyway, it shows more consistent trends and accurate estimates. It is also noteworthy that contrary to some of the other correlations (i.e., Wallis, Sawant and Pan), the correlation is valid in a broad range of conditions and numerical stable in it.

3.6. Final Conclusions

A detailed characterization of the entrained droplets into the gas core is required for a thorough understanding of annular two-phase flow. An extensive review of the phenomena, together with a collection and analysis of data found in the open literature for key variables defining the entrained droplets, have been described in the present paper.

Regarding to droplet sizes we can say that, from the correlations analyzed in the present paper and from the correlations that we have developed, several conclusions can be obtained. The most important one is that droplet size distributions are strongly dependent on gas flow rates, being less dependent on liquid velocities. An increase in gas flow rate results in a decrease in droplet sizes and vice versa. That is to say, by increasing the gas velocity, the droplet size distribution is shifted toward smaller droplet sizes and the distributions are more centered around the mean.

The main conclusion that can be extracted from the droplet size correlations is that droplet sizes are inversely proportional to gas velocity (all correlations in the vicinity of -1).

Regarding the liquid superficial velocity, there is not a clear trend in the expressions in which appears, in some cases it produces the droplet size increase, and in others a decrease. Although, for both horizontal and vertical upward flow, the droplet sizes are directly proportional to superficial liquid velocity (exponent slightly higher than 0.1), which seems reasonable, because it is admitted that the relative velocity between gas and liquid will determine the droplet sizes, i.e., a higher liquid velocity would produce larger droplets because it increases with the decrease of relative speed. It has also been observed an increasing tendency of droplet sizes with the pipe diameter (exponents about 0.5).

Moreover, with regard to droplet velocities, to highlight that droplets tend to have a velocity around 80% of the gas velocity. The droplet mean velocity increases with the gas velocity and is almost independent of liquid velocity, although a small influence of the liquid is observed. So, despite being the droplet velocity in the vicinity of 80% in all cases, a small upward trend has been observed with the increasing in gas and liquid velocities until this 80% is reached.

It also has been observed that there is an increasing dispersion of the droplet velocity distributions with the increasing of the gas velocity. As it has been explained in the previous paragraph, greater gas velocities produce smaller droplets. For these smaller droplets, it has been seen that they travel in a wider range of velocities. This can be explained by the fact that smaller droplets will be most strongly affected by gas turbulence, which can cause acceleration and deceleration in the lateral direction, producing this variability in their speed. Larger droplets, being less susceptible to turbulence, will show a narrower range of velocities.

Finally, with regard to the amount of entrained droplets, it is important to comment that this phenomenon is very important and very difficult to determine in gas-liquid two-phase annular flow. This phenomenon causes the decrease of the liquid film thickness until its disappearance in the gas stream, leading to dry-out conditions. The entrainment process is caused by the high speed of the gas phase, which tends to shear-off the crests of the produced disturbance waves. These waves have been produced into the gas-liquid interface due to the difference in velocities between the liquid phase and the gaseous phase. The entrained fraction is the most adequate way to estimate the amount of water entrained as droplets into the gas stream. This magnitude shows a consistent trend, which is common in almost all works that have been found in the open literature, the entrained fraction increases with the increase of both the liquid and gas flow rates. But this magnitude is mostly influenced by gas superficial velocity.

Specifically, regarding the correlation developed in this study, remark the fact that our expression significantly improves the results given by the correlations found in the open literature. In addition, emphasize that the new expression has been obtained from experimental data that have been correlated, not only for air and water data, but also glycerin and butanol (which causes that there are significant changes in the physical properties of the working fluids), and in a wide range of pipe diameters too (from 1 to 15 cm approximately), which makes the correlation to have a wider applicability. Furthermore,

the correlation is presented as a function of dimensionless numbers, which also contributes to make their use more general.

Chapter 4

JET HYDRODYNAMICS

4. JET HYDRODYNAMICS

This chapter is an extended and updated version of the second section of the paper published in Nuclear Engineering and Design, Vol. 300, pp. 563-577, 2016 [Berna, 2016].

Introduction

Submerged gaseous jets into water pools are characterized by the interaction of inertia versus buoyancy forces, this kind of flows can exhibit diverse behaviors ranging from bubbly plumes to stable jets.

Studies carried out over the lasts decades have confirmed the existence of two regimes that characterize the development of the submerged gaseous flows after leaving the nozzle exit. In the case of low gas flow rate the bubbling regime is observed, this regime is characterized by the production of bubbles that break-up near the orifice and rise independently in the direction dictated by gravitational or density effects [Cieslinski, 2005].

Whereas, in the case of higher flow rates, submerged gaseous jets can be shown. Whenever a gas is injected with very high velocity through a nozzle into a water pool, the momentum and energy of the gas are transferred to the surrounding liquid, leading to three-dimensional complex flow structures, which are generally turbulent. This injection process is essentially an unsteady and turbulent process. Observations of Dai et al. [Dai, 2006] have shown that the injection process of high-speed gaseous jets in still water can induce large pressure pulsations upstream of the nozzle exit, and that the shock-cell structures in the over- and under-expanded jets can lead to strong changes in the hydrodynamic pressure. Shi et al. [Shi, 2010] have shown that the injection of supersonic gaseous jets into water causes large flow oscillation, which can be related to shock waves reflecting in the gas phase and, complementarily, Tang et al. [2011] has observed the back-attack phenomenon.

Between both kinds of flows exists a borderline, in which is complicated the measurements because of the unsteadiness effects, being similar to the pulsatile behavior of the bubbly regime [Loth, 1989; Loth 1990].

This PhD. Work is devoted to the high flow jets, namely the study of the characteristics of submerged high-speed gaseous jets. Only a reduced number of previous investigations have been focused in the exploration of the physics of these processes. From them can be highlighted, among others, the works of Loth and Faeth [Loth, 1989; Loth 1990], Gamble et al. [Gamble, 2001], Gulawani et al. [Gulawani, 2007], Someya et al. [Someya, 2011], Tang et al. [Tang, 2011], Weiland et al. [2013], Roger et al. [Roger, 2014], etcetera.

4.1. General Characteristics of Submerged Gaseous Jets

These unsteadiness effects can be reduced by the increase of the gas flow rate, finally reaching the region of the underexpanded jets. In this region the flow is sonic and the static pressure at the nozzle exit is greater than the ambient pressure. The equalization of both pressures, jet-surrounding water, occurs in a zone near the nozzle exit, in which shock waves and other compressible phenomena take place.

Near the exit, the jet is in a forced convection regime with fully turbulent motion causing significant fluctuations near the jet edge. As the jet moves upward, it entrains liquid and thus increases its mass flow. This causes velocities to decrease in the downstream direction (momentum conservation), so that buoyancy forces become more important, giving rise to a transition regime and eventually a purely bubbly plume. This balance forces conduct to different flow regions formed along the submerged gas jet trajectory, they will be discussed in the following paragraphs.

Several experimental studies have been conducted by different researchers over the lasts decades. As a result, some authors consider three regions in a submerged gaseous jet (Figure 4.1):

(1) Jet or momentum jet region, located at the nozzle exit. Region in which inertia forces of the submerge jet dominates buoyancy forces;

(2) Buoyant jet region, at the middle section of the jet. At the middle section of the jet, where buoyancy forces makes bend the jet towards the free surface. In that region the dissipation of the centerline jet velocity and the droplet entrainment continues;

(3) Plume region, at the end section of the jet. It begins when buoyancy forces dominate to the inertia forces and ends when liquid surface is reached.

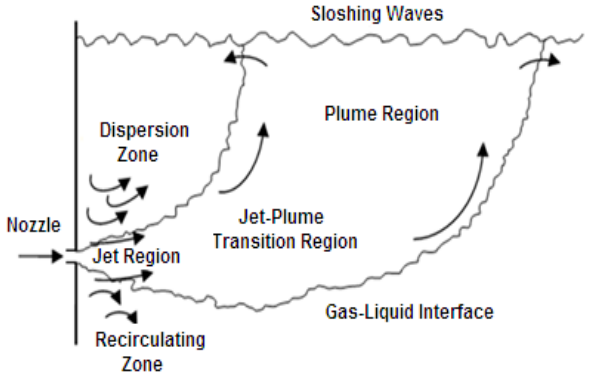

Figure 4.1. Schematic view of a submerged gas jet into a liquid bath.

Whereas other authors divide the jet region in three regions (Figure 4.2):

- Region I is the initial expansion zone. After the ejection, a gas jet in air expands rapidly and widely by under-expansion. In that region a depressurization will occur through a succession of shock and expansion wave reflections at the gas-liquid interface (gas and pool pressures match each other). After this rapid expansion, the jet expands linearly that is the beginning of next region.

- Region II is the region of flow establishment. It extends until the apex of the potential core (about four or five orifice diameters long). The so called potential core is the central portion of the flow in which the gas velocity remains constant and equal to the nozzle exit velocity and is surrounded by a turbulent mixing zone.

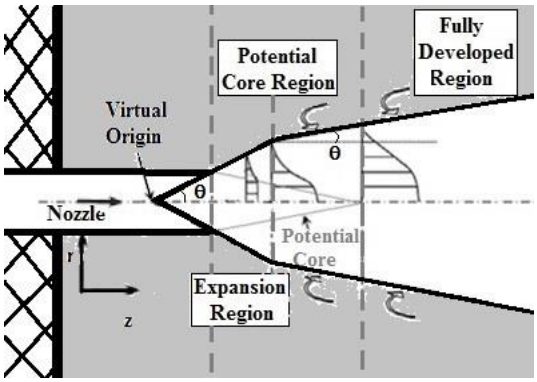

Figure 4.2. Schematic view of the jet region a submerged gas jet.

- Region III is the region of established flow. It extends beyond the apex of the potential core. It is characterized by a dissipation of the centerline jet velocity, by a spreading of the gas jet in the transverse direction and by the entrainment of drops from the surrounding water into the gas jet.

Recent studies carried out by Roger et al. [Roger, 2014] show that for highly underexpanded submerged gaseous jets the way in which they evolve present some peculiarities (Figure 4.3). This kind of jets present the following characteristics: a gaseous potential core, which is quite similar to that described earlier; a "drop layer" region in which the gas breaks the liquid structures and drags droplets from the gas-liquid interface; an outer zone where bubbles of gas emerge from it, carrying away part of the liquid, the final results is the formation of a "bubble layer" which expands radially as the jet evolves; and the near field, where the jet expands radially depending on the nozzle diameter, the stagnation pressure and the axial abscissa.

Characterization of these jet regions includes: flow conditions at the break zone, expansion angle models at the different jet regions and, the most important subject, the characterization of gas-liquid interface. That later aspect will determine the droplet distribution, size and velocity, and its amount.

The main jet features are here introduced: the jet expansion and developed angle, the end of the expansion zone, jet penetration and the initial jet velocity.

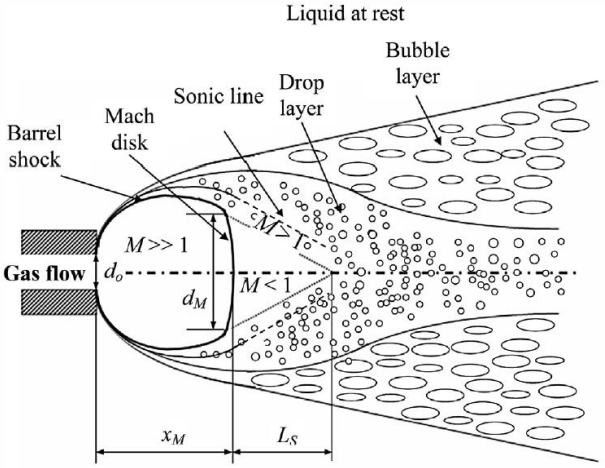

Figure 4.3. Schematic view of strongly underexpanded gaseous jets [Roger, 2014].

4.2. Unsteadiness of Jet Development Processes and flow Structures

The complexity of the processes that take place in the injection of a gaseous jet into liquid introduces an additional level of difficulty in the jet characterization, which is marked by his unsteadiness and pulsating behavior. This unsteadiness can produce continuity breaks of the submerged jet, this phenomenon is called pinch-off or back attack.

A development of "Back-Attack phenomenon" in supersonic gaseous jets was made by Tang et al. [Tang, 2011]. The converging-diverging Laval nozzles are used in Tang's article. In the Figure 4.4 can be shown the complete development of a gaseous jet injected into water. The phenomena which take place are: expansion, bulge, necking/breaking, and back-attack. A brief description of these four stages is shown below:

Expansion (Figure 4.4(a))

Due to the large density ratio between the injected gas and the surrounding water, when the gas enters the water, the initial pressure is not high enough to overcome the inertia effect of the water. Consequently, a gas bag enclosed by the surrounding water is formed near the nozzle exit. The pressure keeps increasing and, finally, when this pressure is high enough, the gas are able to expand freely, completing the expansion process.

Bulge (Figure 4.4(b))

Just after the expansion process, a small bulged bubble appears near the nozzle exit, as pointed by the red arrow in Figure 4.4(b). It will not collapse, and is usually swept away downstream. This bulged bubble will appear several times before necking/breaking and results in pressure oscillation.

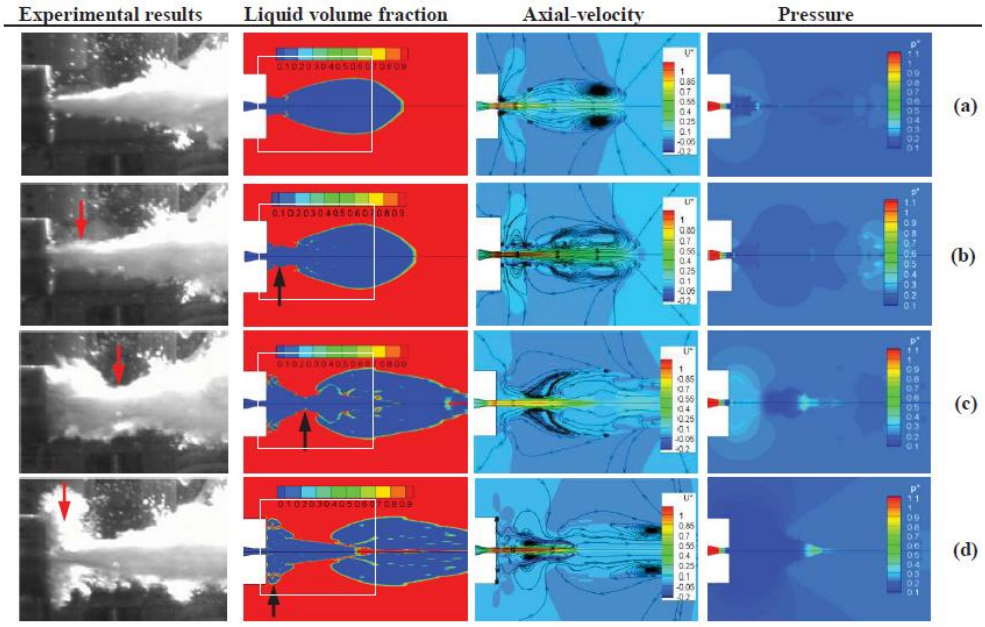

Figure 4.4. The flow structures of (a) expansion, (b) bulge, (c) necking/breaking, and (d) back-attack during the jet development (Ma=2, Under-expansion). The axial-velocity and pressure are normalized and the solid lines represent the streamlines) [Tang, 2011].

Necking/breaking (Figure 4.4c))

The injected gas keeps expanding and spreading away from the nozzle exit. This expansion causes the reduction of the jet pressure until lower values than the ambient, which causes a strengthening downstream from the tip. As a result, the difference in pressure between the jet and the surrounding water can change very abruptly, bearing to the gas bag instability. Then, the gas bag is compressed in the radial direction, which causes the collapse and separation of the gaseous jet into two parts (necking/breaking phenomena).

This necking/breaking will strengthen the jet diameter and hence the new gas supplied by the nozzle is hind, finding difficulties to pass through this area. As a result, the pressure between the nozzle exit and this breaking point will become much higher. Meanwhile, a shockwave will move towards the nozzle exit, producing a decrease in the

velocity. During this stage, a certain amount of the surrounding water has already been entrapped by the gaseous jet. This necking/breaking phenomenon plays a very important role in the unsteadiness and turbulence of the submerged gaseous jets. Highlight that this phenomenon cannot be observed in gas-gas jets due to their small density ratio.

Back-attack (Figure 4.4d))

The gas flow strengthening, described in the previous stage, and the resistance acting on the flow propagation will become stronger. Therefore, it will generate a backflow impacting on the nozzle surface, which can even block the nozzle exit, this is the so called "back-attack phenomena" or "pinch-off" as it is also named.

Other aspect that involves a higher level of complexity in the study of submerged gaseous jets is the injection process at low flow rates, added to the characteristic unsteadiness associated with gas injection into liquids. This unsteadiness involves oscillatory release of gas which can cause liquid to slug into the jet passage. This phenomenon is accompanied by appreciable fluctuations of static pressure in the surrounding areas of the nozzle exit and beyond the jet boundaries. Effects which often result in important levels of noise and vibration, even blocking the passage in the cases in which the gas reacts with the surrounding liquid.

4.3. Flow Conditions at the Nozzle Exit

First aspect to take into consideration, when studying a submerged gaseous jet, is if there are critical or subcritical flow conditions. The critical flow or sometimes called "Choked flow" is caused by compressible flow effects. The parameter that becomes "choked" or "limited" is the velocity or the mass flow rate. Choked flow is a fluid dynamic condition associated with the Venturi effect. When a fluid, at a given pressure and temperature, passes through a restriction (the throat of a convergent-divergent nozzle or a valve in a pipe) and enters into a lower pressure environment, the fluid velocity increases. At initially subsonic upstream conditions, the conservation of mass principle requires the fluid velocity to increase as it flows through the smaller cross-sectional area of the restriction. At the same time, the Venturi effect causes the static pressure, and therefore the density, to decrease downstream past the restriction. Choked flow is a limiting condition which occurs when the mass flow rate will not increase with a further decrease in the downstream pressure environment while upstream pressure is fixed. For homogeneous fluids, the physical point at which the choking occurs for adiabatic conditions is when the exit plane velocity is at sonic conditions or at a Mach number of 1. At choked flow, the mass flow rate can be increased by increasing the upstream pressure or by decreasing the upstream temperature.

To characterize the nozzle exit flow conditions different model has been studied, isentropic conditions model, friction losses model and the experimental friction losses

model of Bubnov [Bubnov, 1998]. This last model has been the final selection used in the present work.

4.3.1. Isentropic Conditions Model

For isentropic conditions (reversible process without losses), that is to say, energy friction loss term is equal to zero, the energy conservation equation is given by

$$de + d\left(\frac{1}{2}u^2\right) + d(Pv) = 0 \qquad \textbf{Eqn. (4.1)}$$

For isentropic process we now the following relations:

$$P\,\rho^{-\gamma} = cte = P_0\,\rho_0^{-\gamma} \qquad \textbf{Eqn. (4.2)}$$

$$\frac{T}{T_0} = \left(\frac{P}{P_0}\right)^{\frac{\gamma-1}{\gamma}} \qquad \textbf{Eqn. (4.3)}$$

$$c = \sqrt{\gamma RT} = \sqrt{\frac{\partial P}{\partial \rho}} \qquad \textbf{Eqn. (4.4)}$$

$$de + Pdv = dq = 0 \qquad \textbf{Eqn. (4.5)}$$

where γ is the isentropic expansion coefficient

$$\gamma = \frac{c_p}{c_v} \qquad \textbf{Eqn. (4.6)}$$

from Eqn. (4.1)

$$d\left(\frac{u^2}{2}\right) + v\,dP = 0 \qquad \textbf{Eqn. (4.7)}$$

using Eqn. (4.2)

$$d\left(\frac{u^2}{2}\right) + P_0\,\rho_0^{-\gamma}\gamma\,\rho^{\gamma-2}\,d\rho = 0 \qquad \textbf{Eqn. (4.8)}$$

Integration of this equation yields

$$\frac{u^2}{2} + \frac{\gamma}{\gamma-1}\left[\frac{P}{\rho} - \frac{P_0}{\rho_0}\right] = 0 \qquad \textbf{Eqn. (4.9)}$$

Rearranging the above expression and using

$$P = \rho RT \qquad \textbf{Eqn. (4.10)}$$

it is obtained

$$\frac{u^2}{2} = \frac{\gamma}{\gamma - 1}\left[RT_0 - RT\right] \qquad \textbf{Eqn. (4.11)}$$

The critical flux is obtained when the Mach number is equal to 1.

$$M = \frac{u}{c} = 1 \qquad \textbf{Eqn. (4.12)}$$

c is the local velocity of the sound in the gas.

Then

$$M^2 = \frac{u^2}{c^2} = 1 \qquad \textbf{Eqn. (4.13)}$$

Dividing Eqn. (4.11) by c^2 and rearranging

$$1 = \frac{2\dfrac{\gamma}{\gamma - 1}\left[RT_0 - RT\right]}{\gamma RT} = 2\frac{1}{\gamma - 1}\left[\frac{T_0}{T_{crit}} - 1\right] \qquad \textbf{Eqn. (4.14)}$$

rearranging

$$T_{crit} = T_0 \frac{2}{(\gamma + 1)} \qquad \textbf{Eqn. (4.15)}$$

and using Eqn. (4.3) critical pressure is

$$P_{crit} = P_0\left(\frac{2}{(\gamma + 1)}\right)^{\frac{\gamma}{\gamma - 1}} \qquad \textbf{Eqn. (4.16)}$$

and P_0 the pressure inside the steam generator tube.

The velocities at the break will be:

1- For critical condition (sonic velocity)

$P_1 < P_{crit}$

$$u_{crit} = \sqrt{\gamma R T_{crit}} = \sqrt{\gamma R T_0 \frac{2}{(\gamma+1)}} = c_0 \sqrt{\frac{2}{(\gamma+1)}} \qquad \textbf{Eqn. (4.17)}$$

2- For sub-critical condition (subsonic velocity)

$$P_1 > P_{crit}$$

$$u = \sqrt{\frac{2\gamma}{(\gamma-1)}\left[\frac{P_0}{\rho_0} - \frac{P_1}{\rho_1}\right]} = c_0 \sqrt{\frac{2}{(\gamma-1)}\left[1 - \left(\frac{P_1}{P_0}\right)^{\left(1-\frac{1}{\gamma}\right)}\right]} \qquad \textbf{Eqn. (4.18)}$$

By considering polytrophic processes (n≠1.4) similar equations are obtained, only the replacement of the isentropic by the polytrophic coefficient is needed.

4.3.2. Friction Losses Model

Another possibility is to consider a model which takes into account friction losses at the nozzle exit. In steady state conditions, the energy conservation equation is given by

$$de + d\left(\frac{1}{2}u^2\right) + d(Pv) + de_{friction} = 0 \qquad \textbf{Eqn. (4.19)}$$

Assuming that the energy friction loss term is

$$de_{friction} = d\left(\chi \frac{u^2}{2}\right) \qquad \textbf{Eqn. (4.20)}$$

where χ is the coefficient of friction loss at the break.

Then energy conservation equation from Eqn. (4.19) is given by

$$d\left((1+\chi)\frac{u^2}{2}\right) + v\,dP = 0 \qquad \textbf{Eqn. (4.21)}$$

using Eqn. (4.2)

$$d\left((1+\chi)\frac{u^2}{2}\right)+P_0\,\rho_0^{-\gamma}\,\gamma\,\rho^{\gamma-2}\,d\rho=0 \qquad \textbf{Eqn. (4.22)}$$

where γ is the isentropic expansion coefficient, Eqn. (4.7).

Integration of this equation yields

$$(1+\chi)\frac{u^2}{2}+\frac{\gamma}{\gamma-1}\left[\frac{P}{\rho}-\frac{P_0}{\rho_0}\right]=0 \qquad \textbf{Eqn. (4.23)}$$

rearranging the above expression and using Eqn.(4.18) we obtain

$$\frac{u^2}{2}=\frac{1}{(1+\chi)}\frac{\gamma}{\gamma-1}\left[RT_0-RT\right] \qquad \textbf{Eqn. (4.24)}$$

Using Eqn. (4.21) and dividing Eqn. (4.24) by c^2

$$1=\frac{2\dfrac{1}{(1+\chi)}\dfrac{\gamma}{\gamma-1}\left[RT_0-RT\right]}{\gamma RT}=2\frac{1}{(1+\chi)}\frac{1}{\gamma-1}\left[\frac{T_0}{T_{crit}}-1\right] \qquad \textbf{Eqn. (4.25)}$$

rearranging

$$T_{crit}=T_0\,\frac{2}{(\gamma+1)+\chi(\gamma-1)} \qquad \textbf{Eqn. (4.26)}$$

and using Eqn. (4.3), we obtain the critical pressure

$$P_{crit}=P_0\left(\frac{2}{(\gamma+1)+\chi(\gamma-1)}\right)^{\frac{\gamma}{\gamma-1}} \qquad \textbf{Eqn. (4.27)}$$

The velocities at the break will be:

1- For critical condition (sonic velocity)

$P_1 < P_{crit}$

$$u_{crit}=\sqrt{\gamma RT_{crit}}=\sqrt{\gamma RT_0\,\frac{2}{(\gamma+1)+\chi(\gamma-1)}}$$
$$=c_0\sqrt{\frac{2}{(\gamma+1)+\chi(\gamma-1)}} \qquad \textbf{Eqn. (4.28)}$$

2- For sub-critical condition (subsonic velocity)

$$P_1 > P_{crit}$$

$$u = \sqrt{\frac{2\gamma}{(1+\chi)(\gamma-1)}\left[\frac{P_0}{\rho_0} - \frac{P_1}{\rho_1}\right]}$$

$$= c_0 \sqrt{\frac{2}{(1+\chi)(\gamma-1)}\left[1 - \left(\frac{P_1}{P_0}\right)^{\left(1-\frac{1}{\gamma}\right)}\right]} \qquad \textbf{Eqn. (4.29)}$$

To estimate the value of the friction loss coefficient of a sudden expansion the Vennard formula has been used

$$\chi = \left(1 - \frac{w_0}{w_1}\right)^2 \qquad \textbf{Eqn. (4.30)}$$

where w_0 and w_1 denote the cross-sectional areas of the narrow and expanded portions of the flow.

4.3.3. Bubnov Model

The Bubnov model [Bubnov, 1998] has been chosen to characterize the flow conditions (pressure loss due to sudden expansion considered). Because it has been considered that provides better results, but more experimental tests has to be made to confirm his results.

A way to consider friction losses and polytrophic processes are presented in the paper of Bubnov [Bubnov, 1998], in which the energy conservation equation is as follows:

$$d\,e + d\left(\frac{C_\alpha\left(1 - C_\beta\right)}{2}u^2\right) + d\left(P\,v\right) = 0 \qquad \textbf{Eqn. (4.31)}$$

where C_α is the correction of the kinetic energy flow and C_β is the intensity of pulsating motions. The terms in Eqn. (4.31) are: first term the internal energy, second term the kinetic energy (including friction losses) and last term is the pressure work.

For isentropic processes there are the relations shown from Eqn.(4.10) to Eqn.(4.13). Then the energy conservation equation from Eqn. (4.31) and Eqn. (4.13) is given by

$$d\left(C_\alpha\left(1 - C_\beta\right)\frac{u^2}{2}\right) + v\,dP = 0 \qquad \textbf{Eqn. (4.32)}$$

using Eqn. (4.10)

$$d\left(C_\alpha\left(1-C_\beta\right)\frac{u^2}{2}\right)+P_0\,\rho_0^{-\gamma}\gamma\,\rho^{\gamma-2}\,d\rho=0 \qquad \textbf{Eqn. (4.33)}$$

integration of this equation yields

$$C_\alpha\left(1-C_\beta\right)\frac{u^2}{2}+\frac{\gamma}{\gamma-1}\left[\frac{P}{\rho}-\frac{P_0}{\rho_0}\right]=0 \qquad \textbf{Eqn. (4.34)}$$

rearranging the above expression and using Eqn. (4.18) we obtain

$$\frac{u^2}{2}=\frac{1}{C_\alpha\left(1-C_\beta\right)}\frac{\gamma}{\gamma-1}\left[RT_0-RT\right] \qquad \textbf{Eqn. (4.35)}$$

Using Eqn. (4.21) and dividing Eqn. (4.35) by c^2

$$1=\frac{2\dfrac{1}{C_\alpha\left(1-C_\beta\right)}\dfrac{\gamma}{\gamma-1}\left[RT_0-RT\right]}{\gamma RT}=2\frac{1}{C_\alpha\left(1-C_\beta\right)}\frac{1}{\gamma-1}\left[\frac{T_0}{T_{crit}}-1\right] \qquad \textbf{Eqn. (4.36)}$$

rearranging

$$T_{crit}=T_0\,\frac{2}{2+C_\alpha\left(1-C_\beta\right)(\gamma-1)} \qquad \textbf{Eqn. (4.37)}$$

and using Eqn. (4.11) we obtain the critical pressure.

Applying the equations of polytrophic processes and operating, we obtain the critical pressure:

$$P_{crit}=P_0\left(\frac{2}{2+C_\alpha\left(1-C_\beta\right)(\gamma-1)}\right)^{\frac{\gamma}{\gamma-1}} \qquad \textbf{Eqn. (4.38)}$$

The following empirical relation was obtained for a sudden flow expansion:

$$C_\alpha\left(1-C_\beta\right)=2.6135-1.4891\frac{w_0}{w_1} \qquad \textbf{Eqn. (4.39)}$$

where w_0 and w_1 denote the cross-sectional areas of the narrow and expanded portions of the flow.

Depending on the flow conditions, different expressions are recommended to estimate gas flow velocity:

1- For critical condition (sonic velocity)

$$P_1 < P_{crit}$$

$$u_{crit} = c_0 \sqrt{\frac{2}{2 + C_\alpha (1 - C_\beta)(\gamma - 1)}} \qquad \textbf{Eqn. (4.40)}$$

where $c_0 = \sqrt{\gamma R T_0}$

2- For sub-critical condition (subsonic velocity)

$$P_1 > P_{crit}$$

$$u = \sqrt{\frac{2\gamma}{C_\alpha (1 - C_\beta)(\gamma - 1)} \left[\frac{P_0}{\rho_0} - \frac{P_1}{\rho_1} \right]} = \\ = c_0 \sqrt{\frac{2}{C_\alpha (1 - C_\beta)(\gamma - 1)} \left(1 - \left(\frac{p_1}{p_0} \right)^{\frac{\gamma - 1}{\gamma}} \right)} \qquad \textbf{Eqn. (4.41)}$$

4.4. The Expansion Angle

The expansion or spreading angle is an important parameter to determine the way in which the submerged gaseous jet spreads downstream. After the ejection, an underexpanded gas jet in air expands rapidly and widely by underexpansion until the surrounding pressure is equal to the gas pressure. As it is presented by Epstein et al. [Epstein, 2001], after this rapid expansion the jet expands linearly.

As shown in Weiland's PhD. document [Weiland, 2010] the jet spreading angle or the expansion angle, parameter which indicates the degree of mixing and entrainment at the interface, has been found to be a function of both Mach number (initial jet velocity) and aspect ratio (ratio between nozzle length and area). Generally speaking, with the increase of both parameters the expansion angle increases, many experimental data have noted these statements. Weiland's experiments were carried out in a vertical pool, having injectors with a constant diameter and a varying throat to reach the desired Mach number.

Someya et al. [Someya, 2011] investigated horizontal submerged gas jets. They found that a jet large expansion occurred rapidly and extended about 3 mm from the inlet point; then, expansion progresses at a slower rate (i.e., a narrower angle). Figure 4.5 shows the

experimental expansion angles vs. stagnation pressure. The spread angle in the expansion region increased with pressure, whereas the expansion angle in the developed region slightly changed around an average value of about 7º.

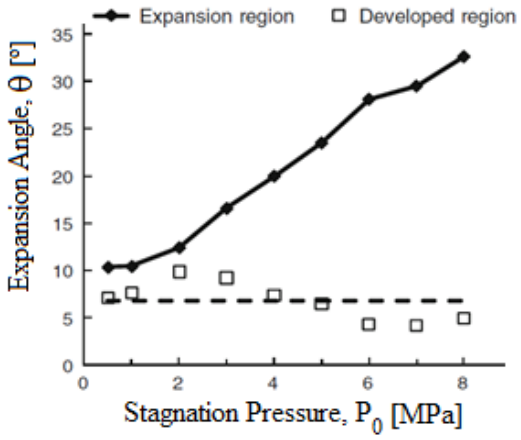

Figure 4.5. Expansion angle vs. stagnation pressure [Someya, 2011].

Roger et al. [Roger, 2014] studied strongly underexpanded gas jets submerged in liquids, they used argon, helium and nitrogen as injection gases and water and mixtures of water with glycerin as surrounding liquid. The experiments took place up to 18 MPa. They propose the following correlations for the expansion angle. In the case of the near field the jet expansion is given by:

$$\frac{d_{jet}}{d_0} = 1 + 0.43\left(\frac{P_a}{P_\infty}\right)^{0.5}\left(\frac{x}{d_0}\right)^{0.5} \qquad \textbf{Eqn. (4.42)}$$

this correlation predicts an increase in the jet diameter ratio of three or four times when the stagnation pressure varies from 2 to 18 MPa. Downstream of the near field zone the expansion angle is about 24º, having small influences the stagnation pressure and the physical properties of the working fluids. In the far field zone they propose the following correlation:

$$\frac{d_{jet}}{d_0} = \frac{d_{tr}}{d_0} + 2\tan\frac{\theta}{2}\left(\frac{x - x_{tr}}{d_0}\right) \qquad \textbf{Eqn. (4.43)}$$

The transition between both regions is characterized by the axial abscissa coordinate, x_{tr}, and by its corresponding jet diameter, d_{tr}, these points are obtained via the derivatives of Eqn. (4.42) and Eqn. (4.43).

Harby et al. [Harby, 2014] correlated their experimental measurements and propose the following correlation for the expansion angle:

$$\theta = 2.227 \cdot \ln(M_0) + 8.3953 \qquad \textbf{Eqn. (4.44)}$$

being M_0 the jet momentum flow rate at the nozzle exit, given in Newtons.

4.5. Jet Penetration

The penetration length can be defined as the distance reached by the jet when his bottom part cuts the imaginary line drawn horizontally from the jet nozzle exit.

Only a few studies have been made related to a high velocity jets discharging into a liquid pool. Hoefele in his Ph.D work [Hoefele, 1972] presents a penetration length figure of horizontal submerged gaseous jets as function of the Froude number. It is found that this relationship is in reasonable agreement with the experimental data obtained for gas jets in water, $ZnCl_2$ solution and "Thoulet's solution" but shows poor agreement for the mercury-air system. Figure 4.6 shows the Hoefele's results of gas jet penetration to several fluids.

In which Froude number is defined as:

$$Fr = \frac{\rho_g u_0^2}{(\rho_l - \rho_g) g d_0} \qquad \textbf{Eqn. (4.45)}$$

where u_0 and d_0 are the initial gas jet velocity and the orifice diameter respectively.

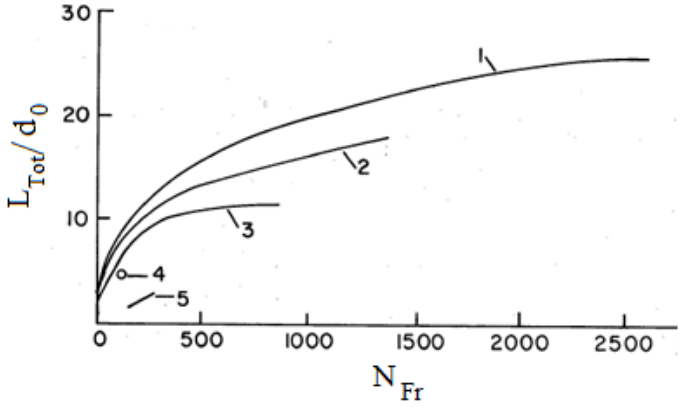

Figure 4.6. Variation of dimensionless length penetration of the submerged horizontal gas jet (1- Water; 2- $ZnCl_2$ solution; 3- Tula solution; 4- Liquid Ni_3S_2; 5- Hg) with Froude number [Hoefele, 1972].

Hoefele and Brimacombe [Hoefele, 1979] gave the following equation to calculate the penetration length for horizontal gas jets for an air/water system:

$$\frac{L_{Tot}}{d_0} = 10.7 Fr^{0.46} \left(\frac{\rho_g}{\rho_l} \right)^{0.35} \quad \textbf{Eqn. (4.46)}$$

where the Froude number is defined by Eqn. (4.45).

Carreau et al. [Carreau, 1986] propose for horizontal nitrogen sonic jets in still water the following correlation:

$$\frac{L_{Tot}}{d_0} = 1.34 Fr^{0.39} \quad \textbf{Eqn. (4.47)}$$

Harby et al. [Harby, 2014] correlated their experimental measurements and propose several correlations for the jet penetration. In particular they proposed two correlations to determine the jet penetration length until the end of the momentum region, that is to say, until the point in which the momentum regime ends, and another correlation to the buoyant regime, that is from the end of the momentum region until the point in which the pool free interface is reached.

The first correlation is function of the jet momentum at the nozzle exit, it is as follows:

$$L_M = 0.031 \cdot \ln(M_0) + 0.08 \quad \textbf{Eqn. (4.48)}$$

being M_0 the jet momentum flow rate at the injector exit, given in Newtons. This expression has a correlation coefficient of $R^2 = 0.97$. Another expression for the momentum region was found, in this case based on the dimensionless analysis:

$$\frac{L_M}{L_Q} = 2.29 Fr^{0.61} \quad \textbf{Eqn. (4.49)}$$

being L_Q the geometric length, which is defined as the square root of the nozzle area, $\sqrt{A_N}$ (m). In this case, the correlation coefficient has a value of $R^2 = 0.91$. The authors propose three new correlations for the buoyant region, the first of them is the following:

$$L_B = -40.52 \dot{m}^2 + 4.7 \dot{m} + 0.06 \quad \textbf{Eqn. (4.50)}$$

being $\dot{m}$ the inlet gas mass flow rate (kg/s). The correlation coefficient of this expression has a value of $R^2 = 0.89$. Another correlation as function of the inlet momentum is also proposed:

$$L_B = 0.031 \cdot \ln(M_0) + 0.076 \quad \textbf{Eqn. (4.51)}$$

which has a value of the correlation coefficient of R^2 = 0.93. Finally an expression as function of dimensionless number was proposed:

$$\frac{L_B}{L_Q} = 0.0007Fr^2 + 0.14Fr + 9.3 \qquad \textbf{Eqn. (4.52)}$$

which has a value of the correlation coefficient of R^2 = 0.97.

4.6. Characterization of the Liquid Phase

Regarding to the liquid phase, the key parameters are the liquid velocity and the liquid film thickness which is disturbed by the submerged gaseous jet. It is also important to estimate the interfacial forces present in the gas-liquid interface. In the next paragraphs these magnitudes will be estimated.

4.6.1. Interfacial Shear Stress and Liquid Velocity

The interfacial shear stress ($\tau_{friction}$) determines the momentum exchange between gas and liquid:

$$\tau_{friction} = \frac{1}{2} f_{gi} \rho_g \left(u_g - u_l\right)^2 \qquad \textbf{Eqn. (4.53)}$$

The gas-liquid interface in a parallel base flow is controlled by the instabilities of Kelvin–Helmholtz generated in inviscid theory by the velocity difference [Yecko, 2002]:

$$u_l = u_g \sqrt{\frac{\mu_g}{\mu_l}\frac{\rho_l}{\rho_g}} \qquad \textbf{Eqn. (4.54)}$$

The interfacial friction factor is approximated through Ohnuki's correlations [Spore, 2000].

$$f_{gi} = 1.84 f_{wg} \qquad \textbf{Eqn. (4.55)}$$

where

$$f_{wg} = \begin{cases} \dfrac{16}{\mathrm{Re}_g} & \mathrm{Re}_g < 2100 \\ \dfrac{0.079}{\mathrm{Re}_g^{0.25}} & 2100 < \mathrm{Re}_g < 10^5 \\ 0.0008 + \dfrac{0.05525}{\mathrm{Re}_g^{0.237}} & \mathrm{Re}_g \geq 10^5 \end{cases} \qquad \textbf{Eqn. (4.56)}$$

4.6.2. Liquid Film Thickness

In order to determine the liquid film thickness the superficial wave amplitude will be estimated first (Figure 4.7), to do so the next expression have been used [Mantilla, 2008],

$$\Delta h_w = 2C_w \frac{\mu_l}{\rho_l}\sqrt{\frac{\rho_l}{\rho_g}}\frac{1}{\sqrt{f_{gi}f_{li}}}\frac{1}{u_g - u_l} \qquad \textbf{Eqn. (4.57)}$$

being C_w a factor that accounts for the effect of the surface tension on the circulation/dissipation flow in the wave, which was defined by Ishii and Grolmes [Ishii, 1975], Eqn. (2.37).

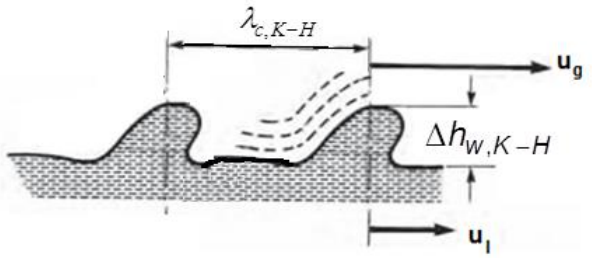

Figure 4.7. Schematic wave representation of the Kelvin-Helmholtz instability.

Moreover the critical wavelength, $\lambda_{c,K\text{-}H}$, for a Kelvin-Helmholtz instability can be defined as

$$\lambda_{c,K-H} = 2\pi\sqrt{\frac{\sigma_l}{g(\rho_l - \rho_g)}} \qquad \textbf{Eqn. (4.58)}$$

Finally, assuming that the perturbed liquid film thickness can be defined as the square root of the product of the last two variables,

$$\delta_l = \sqrt{\lambda_{c,K-H}\cdot\Delta h_{w,K-H}} \qquad \textbf{Eqn. (4.59)}$$

4.7. The Gas-Liquid Interface

The available information related with gas-liquid interface has not been carried out specifically for submerged jets but for annular flows, as many of the subjects seen previously, consequently the annular flow information is shown here. The gas-liquid interface of annular flows are covered by waves, a description of the waves that appear on the gas-liquid interface is shown in section "2.2. Waves on the Annular Flow", in which a review of the interfacial waves behavior is described. As far as high speed gaseous jets is concerned, it has been supposed an analogous behavior, i.e., the disturbance waves are the

dominant but small ripple waves exists too. Many recent studies with high spatial resolution [Alekseenko, 2009 & 2015; Setyawan, 2014; Cherdantsev, 2014; Dasgupta, 2017] confirm that disturbance waves are much more complex than a simply wave and the importance of the ripple waves. The disturbance waves are covered by ripple waves than can travel at a slower or faster velocity than the mother disturbance wave [Cherdantsev, 2014; Alekseenko, 2009]. These ripple waves are generated at the rear part of the disturbance waves. The waves that are slower than the mother disturbance wave disappear swallowed by the next disturbance wave, but the ones that are faster than the mother disturbance wave, as it reaches the vicinity of the top of the wave, are the main mechanism of liquid entrainment from the gas-liquid interface to the gas stream.

The velocity, width and curvature of the ripple waves generated in a disturbance wave vary markedly in the same "mother wave", but at higher gas velocities the ripple waves are narrower and more curved .On average the velocities of these "fast ripple waves" are about 20 – 30 % faster than the average velocity of the "mother disturbance waves" [Cherdantsev, 2014].

A recent experimental work related with the disturbance waves [Setyawan, 2014] displays the evolution of disturbance waves (Figure 4.8). Two sensors have been placed at a short distance (sensor 2 placed downstream of sensor 1) and the signal of sensor 2 has been delayed several milliseconds, so that the evolution of the interfacial waves can be measured. Several findings can be highlighted; in particular, four different phenomena have been detected: wave development (WD); wave coalescence (WC); wave break-up (BW); and droplet entrainment (DE). When the signal of sensor 2 is higher than those of sensor 1 the wave has growth (WD in Figure 4.8). When a single wave is detected in sensor 2 but two waves were detected in sensor 1 the waves have merged, wave coalescence (WC in Figure 4.8). The opposite situation, when two waves are detected in sensor 2 but only one single wave was detected in sensor 1 the wave has break-up takes place (BW in Figure 4.8). Finally, the most important phenomena for the present work, when the signal of sensor 2 is similar that the one of sensor 1 but with a smaller size which means that a portion of liquid has entrained into the gas stream, i.e., entrainment process (DE in Figure 4.8).

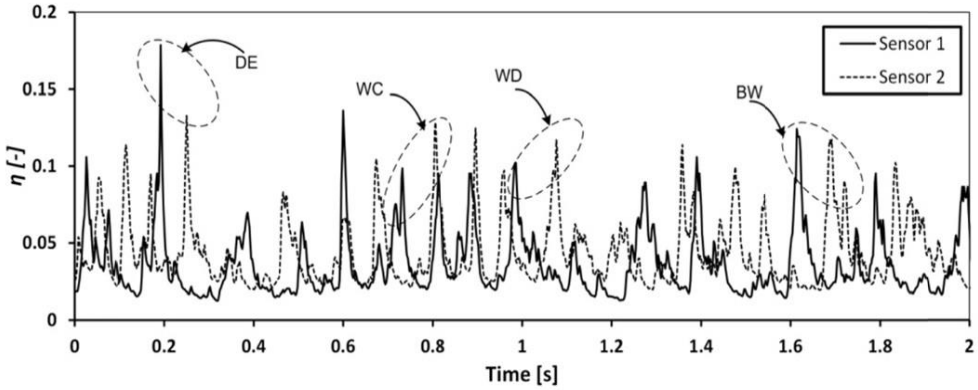

Figure 4.8. Time evolution of the disturbance waves [Setyawan, 2014].

4.8. The Entrainment Process

The process which takes place on the gas-liquid interface, due to the difference in velocity between the gaseous jet and the surrounding liquid, is a continuous exchange of mass, momentum and energy between both phases. A competition between the cohesive and disruptive forces (surface tension and aerodynamic forces respectively) will set up on the liquid surface, leading to perturbations in the surrounding liquid. The liquid in the vicinity of the interface continuously enters the gas core in form of droplets, in a process called liquid entrainment, primary break-up, primary disintegration, primary atomization or simply atomization. In the same way, the droplets which travel into the gas core continuously deposit on the film, in a process called droplet deposition. Then, the entrainment process is considered to be the result from a balance between the rate of droplets dragged from the liquid layer surrounding the submerged jet and the rate of deposition of droplets carried by the jet. In a fully developed flow these two processes are in a dynamic equilibrium, so that the total amount of liquid into the gas remains constant. In the following subsections a description of the entrainment-deposition processes are shown, as in previous sections, there is not available relevant information on this subject for submerged jets, so some annular flow findings are shown in the following paragraphs.

4.8.1. Droplet Entrainment-Deposition Mechanisms

Over the last decades, there have been many attempts by several researchers to describe the equilibrium between entrainment-deposition processes, but almost all of them are experimental correlations carried out in pipes under annular flow conditions.

The Kelvin-Helmholtz instability is the responsible for the entrainment of water droplets from a wavy liquid film into a gas stream. This mass transfer through the gas-liquid interface is complicated and entrainment fraction is a dynamic equilibrium between two competing effects, entrainment and deposition processes. The entrainment-deposition equilibrium is closely related to the waves occurring at the gas-liquid interface. There is a vast amount of experimental data and correlations available in the open literature to predict the amount of droplets carried by the gas stream, although most of them come from vertical or horizontal annular flow measurements. These entrainment-deposition predictions vary significantly among the different correlations, resulting in high uncertainties. The correlations do not incorporate wave characteristics, but dimensionless numbers; in addition, there are not overall mechanistic models for the prediction of entrainment-deposition equilibrium. Consequently, there is not a general model or expression to characterize the entrainment-deposition process but many correlations up to the present moment. In addition, there have been developed for annular flows, but they have been used here due to annular flows are the ones which present higher similarities with submerged jets.

4.8.1.1. The Entrainment Mechanisms

The entrainment process can takes place in several ways, depending on the flow conditions. Hydrodynamic and surface tension forces govern the evolution of the waves present on the gas-liquid interface, their motion and deformation. Under certain conditions, these forces lead to an extreme gas-liquid interface deformation, which results in the formation of several small liquid droplets coming from the break-up a wave portion. Droplets can be dragged from the gas-liquid interface to the gas core in different ways.

On the basis of the experimental data, there are five entrainment mechanisms which can occur in annular flows (Figure 2.4 and Section "2.3. The Onset Of Entrainment Process"). It is generally assumed that four of the five possible mechanisms of droplet entrainment can occur under co-current annular flow conditions. Being roll wave the dominant mechanism, the one that contributes most on the entrainment droplet process. In this mechanism the crest of the large amplitude roll waves of the gas-liquid interface are sheared off by the turbulent high velocity gas stream flowing over it.

Although recent studies [Cherdantsev, 2014] link the droplet entrainment process to the presence of "fast ripple waves". According to Chervantsev et al. three different mechanisms are possible to cause droplet entrainment: secondary entrainment, bag break-up and ligament break-up. Secondary entrainment is caused by the impacts of previous entrained droplets on the gas-liquid interface, Figure 4.9. While the other two mechanisms, bag and ligament break-up (mechanisms traditionally called wave undercut and roll wave respectively), are directly related with the disruption of fast ripples on disturbance waves, Figure 4.10.

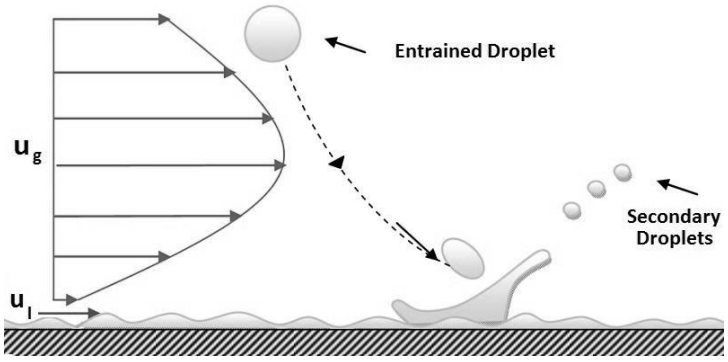

Figure 4.9. Schematic view of the secondary entrainment process.

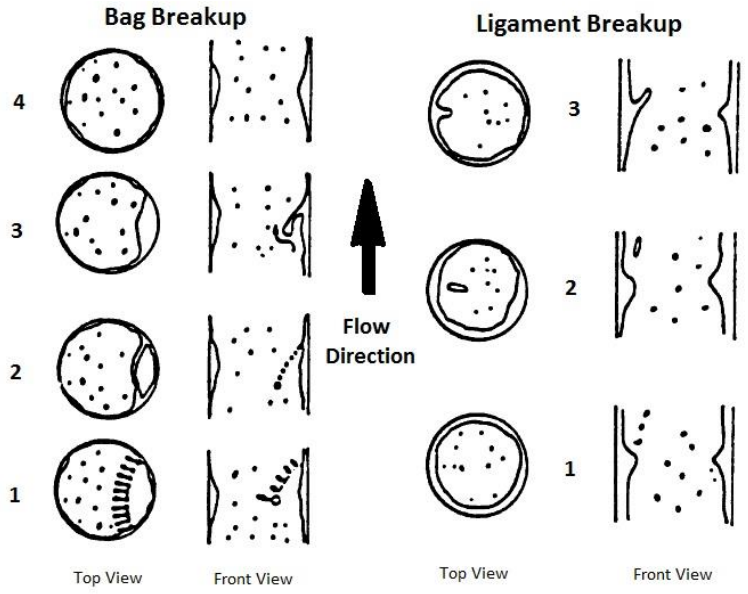

Figure 4.10. Schematic view of the two major Entrainment Mechanisms: bag and ligament break-up [Azzopardi, 1997].

The impacts of droplets can be classified in two major types regarding to the manner in which the film is perturbed, craters and furrows [Cherdantzev, 2017]. The first one, looks as a circular crater, while, the second one produces a long and narrow perturbation over the wavy interface. Regarding to their placement, craters usually take place on disturbance waves; meanwhile, furrows usually take place in the base film between disturbance waves. As far as occurrence probability is concerned, say that furrows impact mechanism probability is twice larger than that of the crater impact mechanism. This probability distribution is not strongly affected by the flow conditions in the experiments analyzed in the Cherdantzev's document.

The bag break-up occurs when the disruption of a whole front of a fast ripple wave occurs, whereas the ligament break-up occurs when two fast ripples interact [Chervantzev, 2014]. In the Cherdantsev's studies is said that the higher the gas and liquid velocities the greater the probability of the ripple wave to be disrupted. Although not all the ripple waves extinguish being scattered into entrained droplets. The authors give threshold value for the gas velocity (u_g = 16 m/s), under which no entrained droplets are detected, regardless of the presence of disturbance waves. Another difference with previous experimental observations, which usually stablishes differenced regions, is that the authors say that both mechanisms can occur at the same flow conditions, in fact at the same disturbance waves. Even though each of them have a higher the probability to occur under certain conditions, ligament break-up increases with gas and liquid flow rates, whereas bag break-up decreases with both variables. Situation which is understandable, given that at higher gas velocities

there are a greater number of ripple waves, so that the probability of interaction among them increases.

4.8.1.2. The Deposition Mechanism

In relation to deposition processes, three mechanisms can be identified in annular flows [Van't Westende, 2008]. First one is the gravitational effects, which produces a non-uniform droplet deposition along vertical direction. Gravity causes an enhancement of deposition at the bottom part and an inhibition and the top part. It also produces an asymmetric concentration profile of the entrained droplets (Figure 4.11a). Another one is associated with turbulent diffusion or turbophoresis, which is important for small particles that closely follow the turbulent motion of the gas phase (Figure 4.11b), the drag force tends to push the entrained droplets towards zones of low turbulence intensity. This mechanism has no preferential direction, depositing uniformly along the wall, providing a cylindrical symmetry distribution. The last mechanism is the free-flight or secondary flow (Figure 4.11c) whereby particles disengage from the turbulence and move to the wall.

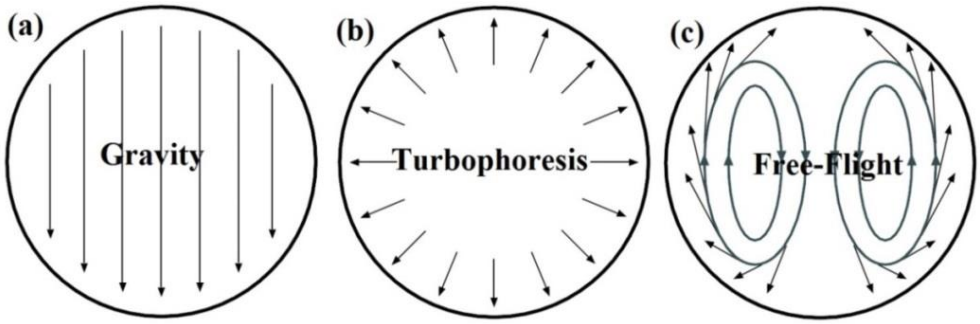

Figure 4.11. Deposition mechanism in horizontal annular flows [Van't Westende, 2008].

These entrainment-deposition mechanisms cause different entrainment flux profiles depending on flow conditions. In particular, the enhancement of the deposition at the bottom part, caused mainly by the gravity force, is clearly shown in Figure 4.12. On this figure the local droplet flux profiles are presented for a fixed superficial liquid velocity (u_l = 0.09 m/s). As can be seen in the figure, the higher the gas velocity is, the greater the homogeneity of the entrainment fluxes. A mapping of the entrainment droplet flux is shown in Figure 4.13, in which it can be observed the inhomogeneity on the axial coordinate for intermediate values of the gas velocity, showing a central region with lower entrainment droplet flux.

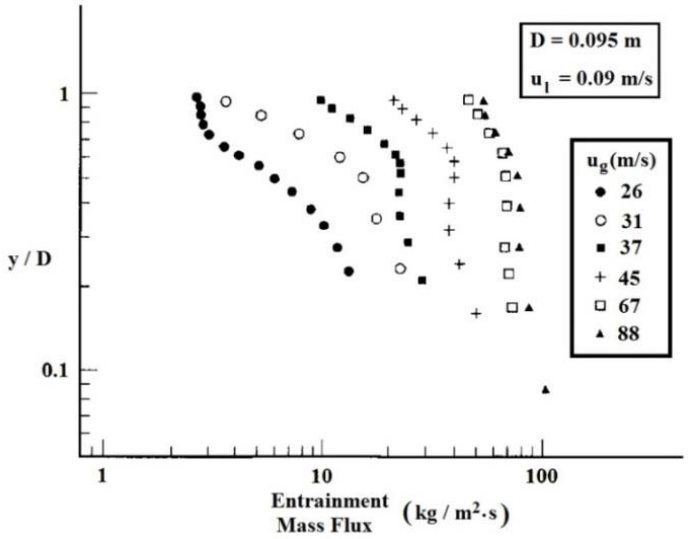

Figure 4.12. Vertical profiles dependency with the gas velocity for the mass flux of entrained droplets [Williams, 1996].

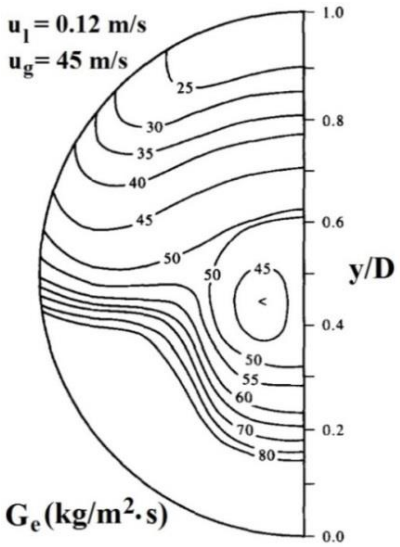

Figure 4.13. Contours of the entrained droplet flux, G_e [Williams, 1996].

With regard to the other two mechanisms, turbophoresis and free-flight, say that the most important parameter characterizing the behavior of a droplet in a turbulent fluid is the relaxation time, τ_d, $\left(\tau_d = \frac{\phi_d^2 \rho_d}{18 \mu_g} \right)$. The deposition rate per unit area is usually expressed by:

$$R_D = k_d C_B \qquad \textbf{Eqn. (4.60)}$$

where C_B is the bulk concentration and k_d is the deposition coefficient (units of velocity). The deposition rate depend on droplet sizes, small particles closely follow the flow lines, whereas big particles do not. Consequently several possibilities can takes place depending on droplets sizes [McCoy and Hanratty, 1977]:

1) For $\tau_d^+ = \tau_d U^{*2} \rho_g / \mu_g < 0.2$, particles closely follow the turbulent fluid motion. Under these circumstances deposition occurs by Brownian motion and k_d is defined in the same way as for fluid particles.

$$k_d^+ = \frac{k_d}{U^*} = 0.0889 Sc_p^{-0.704} \qquad \textbf{Eqn. (4.61)}$$

where U* is the friction velocity, defined as $U^* = U_g \sqrt{f_i / 2}$, and Sc_p is the Schimdt number, defined as $Sc_p = \frac{\mu_g}{\rho_g D_{diff,particle}}$, in which the diffusion coefficient is defined as $D_{diff,particle} = \frac{K_b T}{3 \pi \mu_g \phi_d}$, being K_b the Boltzmann constant ($K_b = 1.38054 \times 10^{-23}$ J / K), and T the absolute temperature.

2) When $0.15 < \tau_d^+ < 20$, particles do not follow fluid turbulence over the whole velocity field. Then, they impinge on the wall not only by the Brownian motion mechanism, but also by the inertial mechanism of free-flight. Between these two relaxation time values particles disengage from the turbulence in the viscous wall region where the magnitudes of the turbulent velocities are decreasing rapidly as the distance from the interface decreases. Thus, the average position from which a particle starts a free-flight to the wall increases as τ_d^+ increases. Since the turbulence increases rapidly with distance from the wall, the rate of deposition increases with increasing τ_d^+. The expression to estimate the deposition coefficient is

$$k_d^+ = \frac{k_d}{U^*} = 3.25 \times 10^{-4} \left(\tau_d^+ \right)^2 \qquad \textbf{Eqn. (4.62)}$$

There is a remarkably increase with air velocity and particle diameter (k_d varies with v^{*5} and ϕ_d^4 respectively).

3) When $1000 > \tau_d^+ > 20$ particles start a free-flight to the wall from a region outside the viscous wall layer where fluid turbulence is not varying rapidly with distance from the wall. Thus, k_d / U^* is not strongly affected by τ_d^+.

$$k_d^+ = \frac{k_d}{U^*} = 0.17 \qquad \textbf{Eqn. (4.63)}$$

4) For $\tau_d^+ > 1000$, for extremely large τ_d^+, particles move in unidirectional paths, so that deposition is strongly dependent on the velocity with which they entered the field.

$$k_d^+ = \frac{k_d}{U^*} = 20.7\left(\tau_d^+\right)^{-1/2} \qquad \textbf{Eqn. (4.64)}$$

As far as gravitational effects are concerned, in the case of submerged jets, and assuming analogous behavior to that discussed in the preceding paragraphs, it will have a homogeneous distribution of the entrained droplets along the radial direction. This situation is in this way, because the submerged jet injection takes place at high speeds, while as the jet evolves downstream his velocity decreases, so it will tend to a lower homogeneity distribution of the entrained droplets. This, as it has been mentioned at the beginning of this paragraph, assuming similar behavior to annular flow. Regarding to turbophoresis and free-flight mechanisms, the distribution function of the entrained droplets will be in the lasts two regions, mainly in the last one, so consequently the deposition mechanisms will be highly influenced by the gas velocity.

4.8.2. Total Mass of Entrained Water Droplets into the Submerged Jet

The total mass of water dragged by the submerged gas jet depends on the balance between the total amount of water torn from the gas-liquid interface and the one returned to it again. The liquid continuously crosses the gas-liquid interface, entering into the gas stream in form of water droplets in a process called liquid entrainment, and these dragged droplets continuously deposit on the film in a process called droplet deposition.

These entrainment and deposition processes are very important processes in the study of submerged jets. Particularly, in the case of horizontal injections, gravity imposes an asymmetric liquid distribution both, in the entrained droplets and in their surrounding liquid film. Consequently, the circumferential distributions of atomization and deposition are expected to be non-uniform. This non-uniformity, added to the previously mentioned pulsating jet behavior, non-confinement, among other difficulties, causes serious problems in experimental measurements as well as in modeling efforts. It is not surprising that data of deposition and atomization in submerged injections are very meager and that no reliable models are available yet. Therefore, expressions originally developed for annular flows, or modified expressions coming from them, have been used in this document.

This document takes into account both contributions, the droplet entrainment and their deposition throughout the jet spread process. To determine this total amount of water carried by the jet, firstly expressions which have been obtained from entrainment experiments in annular flow have been used. These correlations provide the ratio between the mass of entrained water against the total mass of water in the pipe, i.e., the equilibrium value of both processes entrainment-deposition. The direct application of these expressions to submerged jets present several difficulties, the first is that, in this case do not have a water flow value entering into the system, it is the jet itself which produces the movement of the surrounding water. Therefore, the total mass of water from the disturbed layer should be estimated (Section "4.7.2. Liquid Film Thickness"). A second difficulty is that these expressions were developed and apply directly to fully develop annular flows, that is, when the region under study is far from the injection area (Section "3.4.1. The Developing and Fully Developed Region Entrainment"). Consequently, a correction factor for developing flow region must be considered (Section "3.4.2.1. The Developing Entrainment Region"). In this sense, this thesis uses correlations to estimate the entrainment fraction in annular flows, Eqn. (3.80), applying correction factors of developing flow conditions, Eqn. (3.55). Thus, on the one hand, there is the expression for the entrainment fraction (balance between the entrainment-deposition processes thorough the gas-liquid interface), corrected by a factor which takes into account the not fully developed flow conditions.

While on the other hand, together with everything mentioned in the previous paragraph, there is the that fact that the jet is in a process of continuous spreading, consequently, a new contribution should be taken into account due to this continuous expansion. That is, this increase in the diameter will affect the value of the "balance" found so far. To take account of this situation a final term has been introduced, which will mainly affect the phenomenology of deposition processes. In particular, an exponential decay function has been used (characteristic form of relaxation processes), so that this term will affect the droplet population that come from upstream of the region under study. Summarizing, the total contribution is obtained as the entrainment fraction under fully developed conditions in annular flow with a correction factor because of developing flow conditions and another term which takes into account the mass of the upstream entrained droplets and still remaining in the submerged gas jet.

4.8.2.1. The Entrainment Mass Flux

Following the way already marked in the previous section, the annular flow correlations are the ones that best describe the behavior of submerged jets. In the same direction, the expression recently developed by Berna et al. [Berna, 2015a] is the expression which shows better results, Eqn. (3.80). A schematic view of the entrainment-deposition processes is shown in Figure 4.14.

As in the previous variables, a considerable number of correlations have been published over the last decades, a good summary of them can be found in sections: "3.4. The Amount of Entrained Droplets" and "3.5.2.2. New Correlation of the Entrained

Fraction from Annular Flow". Most of these correlations have been also tested in the actual model.

In the case under study, the selected expression should be corrected since all equations were obtained under fully developed annular flows conditions, not for submerged jets. Both of them present many analogies, but there are differences too. For instance, the annular flow takes place into a pipe, confined flow, while submerged jets occur in an open pool, not confined. Another difference is that, in submerged jets, there is a small distance to the nozzle exit, so that the flow is not fully developed, Eqn. (3.50), and in the nozzle exit there are not entrained droplets into the gas stream, they are progressively incorporated as the jet evolves downstream, Figure 4.15. In addition, the gas jet spreads downstream, so fully developed conditions in submerged jets will never be reached.

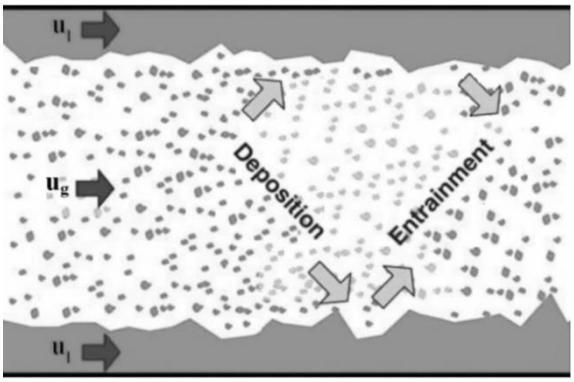

Figure 4.14. Schematic view of the entrainment-deposition balance in a horizontal pipe.

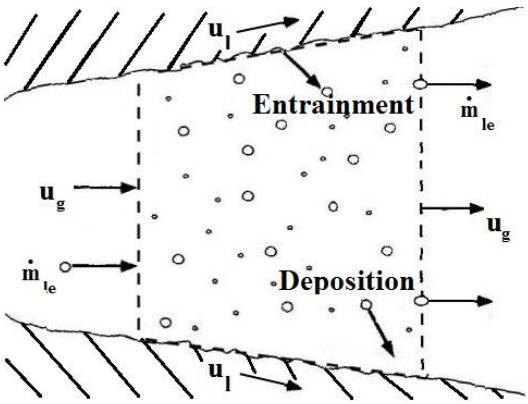

Figure 4.15. Schematic view of the entrainment-deposition balance as the submerge jet evolves downstream.

Nonetheless, this expression has been corrected to account for the flow development based on the work by Kataoka et al. [Kataoka, 2000], due to the fact that near the nozzle the entrained fraction is far from the equilibrium expression proposed for annular flows. Adopting a similar expression to the one proposed by Kataoka, Eqn. (3.55), but with a shorter transition to the "hypothetical" fully developed flow. This fully developed flow is never reached due to the continuous expansion downstream of the submerged gas jet. Then, the coefficient of the exponential has been maximized in order to have a quicker acceleration in the developing annular flow region, $2.75 \cdot 10^{-4}$ versus $1.87 \cdot 10^{-5}$:

$$E(z) = \left[1 - \exp\left(-2.75 \cdot 10^{-4} \frac{(z/D)^2 \, \mathrm{Re}_l}{We_g^{0.5}} \right) \right] E \qquad \textbf{Eqn. (4.65)}$$

being z the axial distance to the nozzle and D the jet diameter.

4.8.2.2. Droplet Deposition

All deposition processes described in section "4.8.1.2. The Deposition Process" can be summarized as part of the entrained droplets are unable to follow the eddy motion of the turbulent jet and, consequently, are projected to the gas-liquid interface, returning to the liquid pool, due to the relatively quiescent gas velocity near this gas-liquid interface. In the same direction that has been followed in the preceding paragraph, the amount of droplets that remain into the gaseous jet decreases exponentially as it evolves downstream, this is caused by the deposition processes. The used expression is

$$N_d(z) = N_{do} e^{\frac{-\Delta z}{l_c}} \qquad \textbf{Eqn. (4.66)}$$

where Δz is the distance in the axial jet direction from the cell in which the droplets have been dragged from the liquid interface; N_{do} is the "equilibrium" droplet population at a given distance from the nozzle; $N_d(z)$ is the droplet population at a given distance from the extraction region; and l_c is the characteristic length that accounts for the droplet motion towards the liquid interface.

4.8.3. The End of the Entrainment Region

Focusing on submerged gaseous jets, the above mentioned ongoing exchange of mass through the gas-liquid interface is in continuous variation as the submerged jet evolves, until a moment in which this dynamic interchange stops. This point is reached downstream of the gas jet injection nozzle, as it spreads and consequently his velocity decreases. The critical value below which entrainment is not possible mainly depends on two variables, liquid and gas velocities. Then, this point under which no entrainment can takes place, regardless of liquid conditions, is called "onset of entrainment" and the one related to gas velocities is called "entrainment inception velocity". A schematic view of these concepts was shown in Figure 2.5.

The dominant mechanism of liquid entrainment in low viscous fluids (i.e., water) is shearing-off of roll wave crests. Droplet entrainment would occur when interfacial shear stress exceeds surface tension. Figure 2.5 gives a conceptual illustration of entrainment. Based on the Ishii and Grolmes criteria [Ishii, 1975], the figure shows that there exists a lower limit of Re_l (Re_{ffOE}) under which roll-wave entrainment will not take place (no matter how high the gas velocity over the film is). The associated liquid velocity is usually called "onset of entrainment liquid velocity", u_{ffOE}. At the other edge, high Re_l, would result in a threshold gas velocity independent of Re_l (rough turbulent regime starts, in the range 1500 – 1750). In this case, the liquid Reynolds number used to evaluate these expressions is obtained from a "virtual" liquid film thickness, the perturbed surrounding liquid layer, δ_l (Section "4.7.2. Liquid Film Thickness").

A number of models have been published in the open literature. Here the Ishii and Grolmes equations have been selected as they provide a more detailed description of the entrainment domain. Nevertheless, other less sophisticated models have been tested, such as the Kutateladze's criterion or its improvement, which is shown in Crowe's book [Crowe, 2006]. It is worth mentioning that all these models had been developed for annular flows in pipes, so their application to submerged gaseous jets is an extrapolation that should be validated.

For the determination of the entrainment inception velocity the Ishii and Grolmes model has been used (Section 2.4.2. "Ishii and Grolmes model"). This model uses, for liquid Reynolds numbers higher than the onset of entrainment value, $Re_l > Re_{ffOE}$ ($Re_{ffOE} \approx 160$), the criterion shown in Eqn. (2.81) and, for the rough turbulent regime ($Re_l > 1635$), the expression shown in Eqn. (2.82).

Thus, once the point under no entrainment is possible has been determined, the next step will be to determine the total amount of water carried by the gas jet.

4.9. Characterization of the Entrained Droplets

In this section the entrained droplets are characterized, in particular its main characteristics once they have been formed are analyzed, such as its sizes and velocities, among other variables of interest. As in previous sections, due to data scarcity about submerged jets, the majority of findings displayed along these lines come from annular flow, which has a quite similar behavior. In particular, the information collected in chapter 3 has been used to carry out the calculations of submerged jets.

4.9.1. The Entrained Droplet Sizes

In the first instance, only knowing the average droplet size is sufficient for the study of the processes which takes place inside a submerged jet, in the current version of the SPARC code has implemented this variable. But, if you want to dig deeper into what happens to the drops which are dragged from the gas-liquid interface of the submerged jet, it is needed to know some aspects more. For example, the size distribution function of the

entrained droplet, the path followed by the entrained droplets from their initial to their final distribution size function and to note that although the small drop sizes are not broken but can oscillate, so that they have a spherical shape, fact that as to be taken into account un the hydrodynamics calculations. The latter two aspects are presented below, while a brief description of possible distribution functions of the entrained droplet sizes are shown in Appendix I.

4.9.1.1. Mean and Maximum Stable Sizes of the Entrained Droplets

The entrained droplets are surrounded by a gaseous phase which is moving at a high relative velocity; consequently the aerodynamic forces will cause the deformation and fragmentation of these droplets. Then the droplets with a diameter larger than the maximum stable size begin to oscillate, which finally results in the rupture of the droplet. Consequently, a distribution of smaller droplets is produced by the generation mechanisms [Crowe, 2006]. The break-up mechanisms can be expressed as a balance of forces between external stress forces and surface forces. External stress forces, which attempt to disrupt the droplet and surface tension forces, which try to avoid droplet deformation. Consequently, the Weber number, which is the ratio between these two forces, has to be considered.

The maximum stable size of entrained droplets in annular flows can be estimated through the most widely used criteria, which relates the non-dimensional Weber number with a critical empirical value, further details are found in section "3.2.1. The critical Weber number". Throughout this section, the most widely used expressions to estimate the critical Weber number are displayed. For low viscosity liquids, this critical Weber number ranges from 5 to 20 [Kolev, 2007], but the most widely used value found is 12. An extensive summary of the experiments carried out until the beginning of the decade of the 90 is presented in Wierzba's work [Wierzba, 1990], see summary Table 4.1. This criterion has been shown in Eqn. (3.1), among other expressions. Many of these expressions have been tested. Finally the selected expression is the suggested by Kolev, Eqn. (3.14) [Kolev, 2007].

The range of values of the critical Weber criterion, which takes a critical value of the Weber number to determine the maximum stable droplet size, comes from the balance between the surface tension and the drag force. Surface tension force holds the drops together against the drag force that tries to break-up them. Thereby is obtained:

$$F_D = F_\sigma$$

$$\frac{1}{2}\rho_g \frac{\pi\phi_{d,\max}^2}{4} C_D\left(u_g - u_d\right)^2 = \pi\phi_{d,\max}\sigma \qquad \textbf{Eqn. (4.67)}$$

$$We_{crit} = \frac{8}{C_D}$$

the critical Weber number of water droplets was defined in Eqn. (3.1).

Table 4.1. Summary of critical Weber number values obtained from different experimental facilities [Wierzba, 1990].

Reference	We_c	Exp. Fac.	Notes
Lenard (1904)	5.8	FF	Calc. for water u=8m/s; φ=5.5 mm
Merrington&Richardson (1947)	15.4-29.8	FF	Calc. by Hinze (1948)
Lane (1951)	10.8	VWT	Calc. from $u\varepsilon^2 d$=const. for water
Volynskii (1948)	11-15.8	HWT	Average value 14
Buhman (1954)	2.2-3.6	HWT	For water 2.6-3.5; (3.9-10.4)
Hinze (1955)	13	HWT	For gas oil
Krzeczkowski (1980)	11-38	HWT	For water 11
Nichiporenko et al. (1982)	10.9-17.7	HWT	For liquid metal, 17.7 for bag break-up
Wierzba (1985)	14	HWT	For water
Isshiki (1959)	9.26-29	SO	For water 11.1-14.6=f(φ)
Haas (1964)	11.2	SO	For mercury
Naida et al. (1973)	8.4-12.1	SO	Average value for tin 10.9
Yoshida (1985)	10-48	SO	For water 10-31=f(φ)
Hanson et al. (1963)	7.2-47.6	HST	For water 7.2-14.3=f(φ)
Simpkins (1971)	13	HST	For water
Gelfand et al. (1972)	12-16	HST	For liquid nitrogen
Simpkins & Bales (1972)	14	HST	For water
Gelfand et al. (1973)	10-50	HST	For water 10
Gelfand et al. (1974)	10	HST	For water and kerosene
Reichman & Temkin (1974)	7	HST	Calc. from $U\varepsilon^2 d$=const. for water
Korsunov & Tishin (1971)	15-32	CN	For transformer oil
Lopariev (1975)	14.6-99.6	VS	For low viscosity liquids 14.6-21
Caveny & Gany (1979)	20-30	CN	For Al/Al_2O_3 agglomerates
Boriov et al. (1986)	40-60	HST	For water and kerosene

FF: free fall experiments HWT: horizontal wind tunnel SO: suction orifices VS: venture scrubber
VWT: vertical wind tunnel HST: horizontal shock tube CN: convergent nozzle

An alternative approach to the critical Weber criteria is the direct correlation of the specific droplet sizes as a function of scenario characteristics (fluid properties and flow conditions), even though the available correlations had been developed for annular flows. Although it can be said that annular flow has many similarities with the submerged gaseous jets. Since it also has a continuous gaseous phase, within which the entrained droplets travel, and being surrounded by a liquid phase too. The annular flow correlations give as a

result bigger stable droplet sizes, due to the fact that this kind of flow is less aggressive. Then, due to the fact that no correlations are available for submerged gaseous jets, correlations developed for annular flow can be used, since it is a phenomenology which many similarities. Even though these expressions must be used cautiously, being clear about the conditions in which were developed. From the large number of available correlations, the selected has been the newly developed expression for horizontal annular flow shown in Berna's et al. paper, Eqn. (3.77) [Berna, 2015a].

Other possible way to estimate the entrained droplets sizes is to use expressions usually used in Venturi scrubbers, Figure 4.16. The conditions and phenomenology which takes place into these devices are quite similar to those of submerged jets. In Venturi scrubbers the liquid flow is injected at some point near the Venturi's throat, then, as a result of the high velocity of the gas stream in the throat narrowing, a portion of the injected liquid is atomized in small droplets. This atomizing process of the thin liquid film is quite similar to that which takes place in submerged jets. The most widely expression used in this kind of scrubbers is the Nukiyama and Tanasawa correlation [Fernández Alonso, 2001]:

$$\phi_{32} = \frac{0.585}{\left(u_g - u_l\right)}\sqrt{\frac{\sigma}{\rho_l}} + 1.683\cdot 10^{-3}\left(\frac{\mu}{\sqrt{\sigma\rho_l}}\right)^{0.45}\left(\frac{1000Q_l}{Q_g}\right)^{1.5} \qquad \textbf{Eqn. (4.68)}$$

which mainly depends on physical properties, relative velocity and ratio of the volumetric flow rates between both fluids. Even though this correlation was not originally developed for Venturi scrubbers, but for a liquid current introduced coaxially to a gas stream, it has been widely used for the characterization of these kinds of devices over the last decades. Several authors have pointed out that this correlation tends to overestimate the entrained droplets sizes, but in spite of it this expression is widely used nowadays.

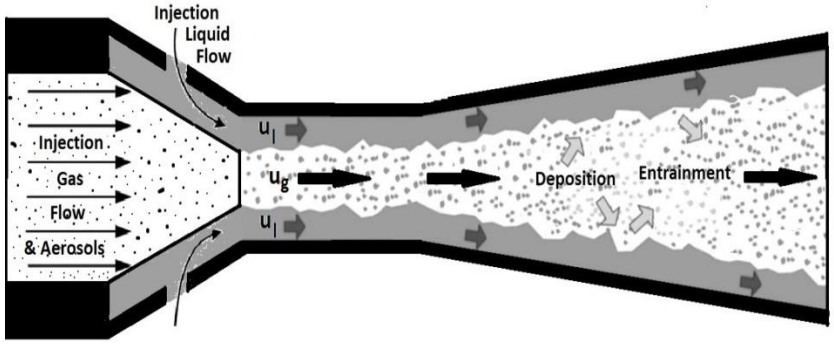

Figure 4.16. Schematic view of the entrainment-deposition processes in a Venturi scrubber.

Another more recent expression, developed by Boll et al. [Fernández Alonso, 2001], is also regularly used when studying Venturi scrubbers, this correlation is

$$\phi_{32} = \frac{4.22 \cdot 10^{-2} + 5.77 \cdot 10^{-3} \left(\frac{1000 Q_l}{Q_g} \right)^{1.922}}{\left(u_g - u_l \right)^{1.602}} \qquad \textbf{Eqn. (4.69)}$$

There are other attempts of approaches in the open literature to determine the sizes of the entrained droplets from a liquid film caused by very high gas velocity streams. For instance, Mayer [Kolev, 2007] proposed a correlation suitable for the interaction of a gas stream traveling at high velocity with a large liquid surface

$$\phi_{vm} = 9\pi \sqrt[3]{16} c_1 \left(\frac{\mu_l \sqrt{\sigma / \rho_l}}{c_1 \rho_g \left(u_g - u_d \right)^2} \right)^{2/3} \qquad \textbf{Eqn. (4.70)}$$

using for the parameter c_1, called sheltering parameter, a value of $c_1 = 0.3$. Whereas Wolfe and Anderson, whose compared Mayer's theory with their own data in the region $9 * 10^{-5} < 9\pi \sqrt[3]{16} c_1 \left(\frac{\mu_l \sqrt{\sigma / \rho_l}}{c_1 \rho_g \left(u_g - u_d \right)^2} \right)^{2/3} < 1.1 * 10^{-3}$, found for the sheltering parameter that the value which best fits was $c_1 = 0.18$.

Finally, after a large number of expressions tested, the correlations used in this work to determine droplet sizes have been the average of the two expressions quoted, Eqn. (3.1) and Eqn. (3.14). It has been combined the aggressiveness of the first group, sudden exposure to a high speed gaseous stream, with the smoothness of the second ones, expressions for fully developed annular flow.

4.9.1.2. Secondary Atomization of the Entrained Droplets

In contrast to primary atomization where a bulk fluid, usually in the form of a liquid jet or sheet, break-up for the first time and forms drops. Secondary atomization, secondary break-up or secondary disintegration, is a phenomenon in which a drop (which comes from primary atomization), immersed in an ambient flow field moving at a high relative velocity to it, break-up into smaller fragments due to the aerodynamic forces. The final distribution of droplet sizes will be determined by the gas and liquid properties in both, the primary and the secondary disintegration. This break-up process of single drops can be caused by either the relative velocity between the gas and liquid phases, the turbulence of the high speed gas phase or by a shock wave propagating in the ambient gas. In our case, there is a big difference in the velocities between the newly entrained droplets (the velocity of the entrained drops in the release point is usually considered to be approximately equal to the wave celerity, i.e., velocity of propagation of the gas-liquid interface waves) and the high speed gas stream, then drops break into small fragments due to the effect of these disruptive

aerodynamic forces caused by the relative velocity between both phases. Consequently, as mentioned earlier, it also exist maximum stable sizes of the entrained droplets in submerged gas jets. Therefore, when a gas stream extracts a large fragment of liquid from the gas-liquid interface, this will break into smaller fragments, with many similarities to that which takes place in the sprays. Then, the final maximum stable droplet sizes, that can be shown when droplets are suddenly exposed to a high speed gas stream, may not be their initial droplet sizes. The typical way to describe the aerodynamic break-up is through dimensionless numbers, in particular the Weber and Ohnesorge numbers. But most of the observations show that droplet break-up is almost independent of the Ohnesorge number for fluids with low values of the Ohnesorge number (Oh < 0.1), as it happens in the case of water droplets. Then, as it has been said on previous occasions, the critical value of the Weber number below which droplets are stable is about 11-13.

Since fragmentation of entrained droplets is the result droplet-ambient interaction, it depends on the flow conditions, i.e., different flow conditions lead to different break-up modes. A classification of the break-up models, widely accepted, could be as follows [Hsiang and Faeth, 1992; Pilch and Erdman, 1987]: vibrational, bag, multimode (often called bag-and-stamen), sheet-thinning and catastrophic.

The vibrational break-up mode (We < ≈11-12) is not always shown. This mode consists of oscillations at the natural frequency of the droplet, which produces only a few numbers of fragments, whose sizes are comparable to those of the parent droplet.

The bag break-up mode consists of formation of a thin hollow bag attached to a thicker toroidal rim, Figure 4.17. This mode occurs at low Weber numbers, the border lines depend on the author (for instance, 12 < We <50 [Kolev, 2007] or ≈ 11 < We < ≈ 35 [Ashgriz, 2011]). During this break-up mechanism the separation of the flow around the deformed droplet leads to a positive pressure difference between the leading stagnation point and the wake, which results in the formation of the bag, with a toroidal ring. After a while, the bag bursts into a multitude of fine fragments and, finally, the ring breaks forming a few larger fragments.

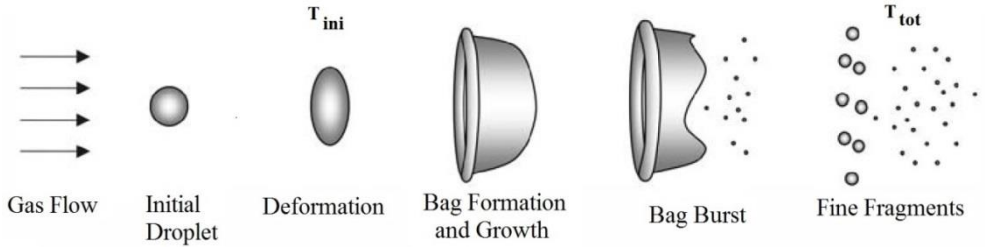

Figure 4.17. Schematic view of bag break-up mechanism.

Bag-and-stamen break-up (≈ 35-50 < We < ≈ 80-100) is quite similar to bag break-up, but with the addition of a stamen facing the flow direction. As in the bag break-up mode,

the bag is the first part of the droplet to disintegrate, followed by the rim and finally the stamen. The fragments are of multiple sizes.

In sheet stripping or sheet-thinning (≈ 80-100 < We < ≈ 350), a film is continuously eroded from the droplets surfaces. It disintegrates rapidly after being removed. Which result in a great amount of small droplets and, in some cases, remain a core of comparable size to that of the parent droplets.

Finally, during catastrophic break-up ((We < ≈ 350) the droplet surface is corrugated by waves of large amplitude and long wavelengths. They form a small number of large fragments that in turn break up into even smaller units. Some authors sub-divide this region into wave-crest stripping and catastrophic. They attribute mass removal from the drop surface via large amplitude-small wavelength waves.

An important aspect to take into account his that droplet break-up cannot be classified by the previously mentioned modes, in many cases the droplet break-up produces in multimode regimes, i.e., a combination of the primary modes. For this reason too, as the regime transition is actually a continuous process, the evaluation of the transition Weber number between modes is subjective and different authors have reported different magnitudes.

Only vibrational and bad break-up modes can take place under the present study conditions. The rest of break-up modes take place at higher Weber numbers, and none of them take place under the present study conditions. Further information of all these break-up mechanisms can be found in many publications, for instance, in Crowe's [Crowe, 2006] and Kolev's [Kolev, 2007] books or Gelfand's [Gelfand, 1996], Hsiang and Faeth's [Hsiang, 1992], and Pilch and Erdman's [Pilch, 1987] papers.

The break-up process does not occur instantaneously, but requires a short period of time. Two dimensionless break-up times are usually defined [Ashgriz, 2011], the initiation time (t^*_{ini}) and the total break-up time (t^*_{tot}). Defined as the moment in which the deformed droplet resembles an oblate spheroid and the moment in which all droplet fragments have reached a stable state, respectively. To quantify these two moments a characteristic time is defined [Ranger and Nicholls, 1969]:

$$t_{ref} = \frac{\left(\frac{\rho_l}{\rho_g}\right)^{0.5} \phi_0}{u_{r_0}} \qquad \textbf{Eqn. (4.71)}$$

where ϕ_0 is the initial droplet size and u_{ro} is the initial ambient velocity relative to the droplet.

A dimensionless time as been defined:

$$t^* = \frac{t}{t_{ref}}$$ **Eqn. (4.72)**

where t is time at which droplet deformation begin or at which break-up takes place. A simple correlation to determine these dimensionless times assumes that

$$t^*_{ini} \approx 1.5 \quad and \quad t^*_{tot} \approx 5.0$$ **Eqn. (4.73)**

also applicable when Oh < 0.1.

Gjesing et al. [Gjesing, 2009] propose a slightly different final break-up time, which depends on the value of the Weber number. His proposal is:

$$t^*_{tot} = \begin{cases} 6 & if \quad 3 \le We_d < 12 \\ 6(We_d - 12)^{-0.25} & if \quad 12 \le We_d < 18 \\ 2.45(We_d - 12)^{0.25} & if \quad 18 \le We_d < 45 \\ 14.1(We_d - 12)^{-0.25} & if \quad 45 \le We_d < 351 \\ 0.766(We_d - 12)^{0.25} & if \quad 351 \le We_d < 2670 \\ 5.5 & if \quad We_d \ge 2670 \end{cases}$$ **Eqn. (4.74)**

Even though, when the Ohnesorge number increases above 0.1, which is not the case of water droplets, it has been observed that the break-up time progressively increases with the Ohnesorge number [Hsiang and Faeth, 1992]:

$$t^*_{tot} = \frac{5}{\left(1 - \frac{Oh}{7}\right)}$$ **Eqn. (4.75)**

being developed for $We_d < 10^3$ and Oh < 3.5.

The degree of deformation of the entrained droplets can be correlated as function of the maximum droplets diameter and a reference characteristic time, $t_{ref,c}$, defined as:

$$t_{ref,c} = \frac{t_{ref}}{\left(1 - \frac{Oh}{7}\right)}$$ **Eqn. (4.76)**

Then, the correlation is as follows:

$$\frac{\phi - \phi_0}{\phi_{cro-\max} - \phi_0} = 0.615 \frac{t_{ref}}{t_{ref,c}}$$ **Eqn. (4.77)**

The maximum cross-stream diameter, $\phi_{cro\text{-}max}$, has been estimated as function of droplet Weber number:

$$\frac{\phi_{cro-\max}}{\phi_0} = 1 + 0.19 \cdot We_d^{1/2} \quad ; \quad Oh_d < 0.1 \; ; \; We_d < 10^2 \qquad \textbf{Eqn. (4.78)}$$

A more general evolution of the stages of droplet deformation and break-up is shown in Figure 4.18 [Crowe, 2006], also for Oh < 0.1.

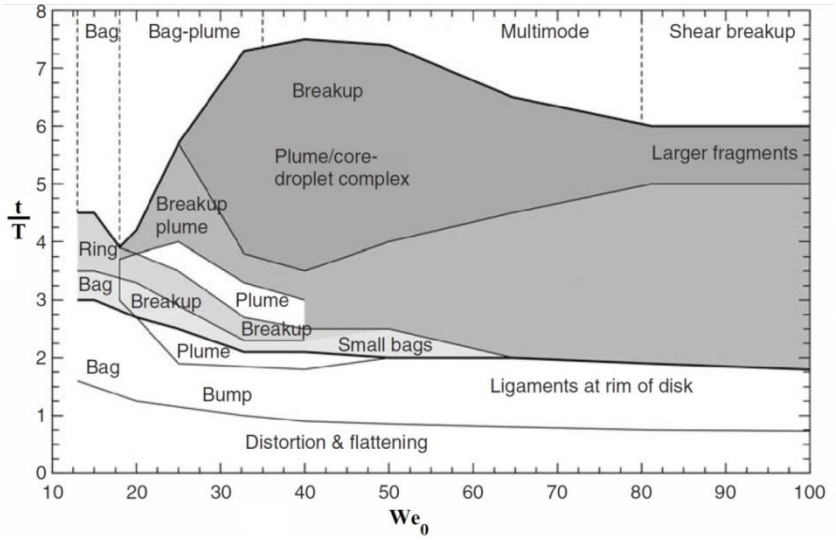

Figure 4.18. Stages of droplet deformation and break-up for various regimes of aerodynamic break-up [Crowe, 2006].

A correlation based on their experimental measurements for the Sauter mean diameter (SMD), ϕ_{32}, has been proposed by Hsiang and Faeth [Hsiang and Faeth, 1992]:

$$\phi_{32} = 6.2 \cdot \frac{\sigma}{\rho_g u_{r_0}^2} \left(\frac{\rho_l}{\rho_g} \right)^{1/4} \left[\frac{\mu_l}{\rho_l \phi_0 u_{r_0}} \right]^{1/2} We_d \qquad \textbf{Eqn. (4.79)}$$

Another correlation to estimate the SMD [Crowe, 2006], also for Oh < 0.1, is

$$\phi_{32} = 6.2 \cdot \phi_0 Oh^{1/2} We_d^{-1/4} \qquad \textbf{Eqn. (4.80)}$$

Other alternative correlation was proposed by Schmehl [Crowe, 2006]:

$$\phi_{32} = 1.5 \cdot \phi_0 Oh^{0.2} \left(\frac{1 + 0.7 Oh^{1.4}}{We_d} \right)^{0.25}$$ **Eqn. (4.81)**

Another expression to estimate the mean diameter of the resulting droplets is shown in Agard's work, which is based on the Anderson and Wolfe studies [Nikolaidis, 2008]:

$$\phi_{vm} = \left[\frac{136 \mu_l \sigma^{3/2} \phi_d^{1/2}}{\rho_g^2 \rho_l^{1/2} \left(u_{g_0} - u_{d_0} \right)^4} \right]^{1/3}$$ **Eqn. (4.82)**

Other researchers proposed formulations for the droplet size distributions after the secondary break-up [Liu, 2000]. They explain that a wide variety in the droplet sizes might be produced. Due to many modes are excited by the aerodynamic interactions of the droplets with the surrounding gas, added to the possibility of collisions and coalescences among the secondary droplets, both during and after the droplet break-up process.

The final velocity of the secondary droplets when the break-up process is finalized can be expressed as [Crowe, 2006]:

$$\frac{u_{r_0}}{u_r} = 1.0 + 2.7 \left(\sqrt{\frac{\rho_g}{\rho_l}} \frac{\phi_0}{\phi} \right)^{1/2}$$ **Eqn. (4.83)**

being the subscript r_0 referred to the initial gas-droplets velocity and the subscript r the relative velocity after the droplet break-up.

4.9.1.3. Aspect Ratio of the Entrained Droplets

Under high velocity gas streams the entrained droplets can break-up in smaller droplets. Even when the conditions for droplet break-up have not been reached, the entrained droplets have not a spherical shape but an oblate ellipsoid, spherical caps with or without a skirt or other shapes. Due to the fact that the entrained droplets are immersed within the gaseous stream, wherein the difference in the droplets-gas velocities is large, their shape is not spherical but ellipsoidal, i.e., an oblate shape as shown in Figure 4.19.

An important assumption is that the volume of the droplets is supposed to be preserved, i.e., $d_{//} \cdot d_{\perp}^2 \approx d_0^3$. To determine this aspect ratio of the entrained droplets is usually used the droplet Weber number. From the available expressions, found in the open literature, the one proposed by Loth [Loth, 2010] is shown below:

$$AR = 1 - 0.75 \tanh\left(0.07 We_d\right) \quad for \quad We_d < We_{crit}$$ **Eqn. (4.84)**

where the range of values of the critical Weber number has been analyzed in sections "4.9.1.1. Mean Size of the Entrained Droplets" and "3.2.1. The Critical Weber Number". The aspect ratio and the droplet Weber number are defined respectively as,

$$AR = \frac{\phi_{II}}{\phi_{\perp}}$$ **Eqn. (4.85)**

$$We_d = \frac{\rho_g \left(u_g - u_d\right)^2 \phi_d}{\sigma}$$ **Eqn. (4.86)**

being ρ_g, μ_l and σ are the gas density, water dynamic viscosity and water surface tension, respectively.

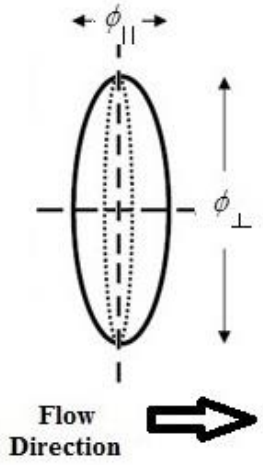

Figure 4.19. Schematic view for the aspect ratio of the entrained droplets.

The minimum value of the aspect ratio predicted by this expression is ¼ approximately and correlates quite well with the experimental data of Reinhart, as shown in Figure 4.20. The predictions of this correlation are also roughly consistent with the shape of the droplets disintegrating due to shock waves at very high Weber numbers.

Hsiang and Faeth [Crowe, 2006] proposed an empirical correlation to estimate the maximum deformation of a droplet, but in this case caused by a shock wave. The empirical correlation to determine the degree of deformation is

$$AR = \left(1 + 0.007 We_d^{1/2}\right)^{-3}$$ **Eqn. (4.87)**

The adjustment obtained by Schmehl [Schmehl, 2003] to determine the degree of deformation of a droplet by a shock wave based on the experimental data of Hsiang is shown below [Hsiang, 1995]:

$$
\begin{aligned}
We_d &< 0.6\left(1+0.8Oh^{0.8}+0.9\times10^{-4}Oh^{2.4}\right) \quad deformation < 5\%\,;\ Oh < 6\times10^{2} \\
We_d &= 1.1\left(1+0.7Oh^{0.85}+1.5\times10^{-4}Oh^{2.4}\right) \quad deformation < 10\%\,;\ Oh < 6\times10^{2} \\
We_d &= 2.3\left(1+0.75Oh^{0.8}+2.5\times10^{-4}Oh^{2.4}\right) \quad deformation < 20\%\,;\ Oh < 6\times10^{2} \\
3\left(1+15Oh^{1.2}\right) &< We_d < 13\left(1+1.7Oh^{1.4}\right) \quad droplets\ oscillations\,;\ Oh < 3\times10^{-1}
\end{aligned}
\qquad \textbf{Eqn. (4.88)}
$$

Correlations which indicate that an increase in the droplet viscosity slows the droplet deformation rate; however, the maximum droplet deformation is not substantially affected by the Ohnesorge number.

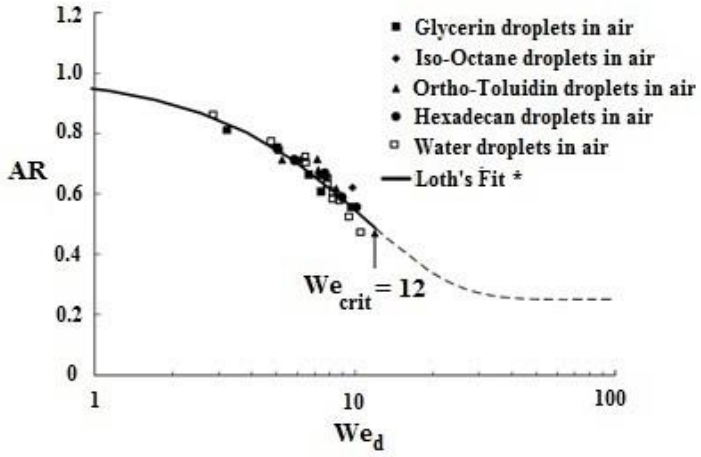

Figure 4.20. Aspect Ratio of Loth's correlation for deformable droplets in air for $Re_d > 600$, based on the Reinhart experimental data [Loth, 2010] (* the Loth's fit line is solid only up to the critical Weber number, maximum value of the Weber number previous to droplet break-up).

4.9.2. The Entrained Droplet Velocity Profile

The measurement of the velocity profile of the entrained droplets is a key parameter to characterize the submerged jets, as well as a challenging. Due to the limited number of expressions which were specifically developed for submerged jets, in this section we will show these expressions and other possible ways to estimate the droplet velocity profiles. In particular, three possible ways to determine this variable are developed throughout this section.

4.9.2.1. The Slip Ratio and the Stokes Number

Other possible way to estimate the entrained droplets velocity is through the Stokes number. This dimensionless number is a very important parameter where particles are suspended in a fluid flow. The Stokes number is defined as the ratio of the particle momentum response time (in our case the droplet response time, τ_d) over the flow system

time (τ_g), it has been defined in Eqn. (3.48), applicable for low Reynolds numbers. Another possible definition, more general is from Eqn. (3.43) and taking into account the fluid time scale, τ_g, which is determined from its characteristic length (D) and its characteristic velocity (u_g) of the system under investigation:

$$\tau_g = \frac{D}{u_g} \qquad \textbf{Eqn. (4.89)}$$

Consequently the Stokes number is:

$$Stk = \frac{\tau_d}{\tau_g} = \frac{4\rho_d \phi_d^2 u_d}{3C_D \,\mathrm{Re}_d\, \mu_g D} \qquad \textbf{Eqn. (4.90)}$$

The entrained droplet behavior can be classified depending on the Stokes number values: if Stk << 1, droplets response time is almost instantaneous to any change in the gas hydrodynamics; if Stk >> 1, droplets are hardly affected by changes in the submerged gas velocity. When the Stokes number is ≈ 1, both phases have similar reaction time to any condition fluctuation.

And, finally, proceeding as in section "3.3.2. The Stokes Number", leads to Eqn. (3.49). This expression provides results, as told above, that are strongly affected mainly by the carrier gas velocity and the size distribution of the entrained droplets.

4.9.2.2. Phenomena with Analogies with Submerged Jets, the Annular Flow Correlations

Other possible ways to estimate the entrained droplets velocities are from the experimental measurements carried out under annular flow conditions in pipes, as presented in section "3.3.3. Annular Flow Expressions", due to the fact that present many analogies with submerged gas jets.

The correlations found in the open literature of this regime, even though they were developed for fully developed annular flows. These expressions provide higher values than the predictions offered by the rest of correlations shown up to this moment for the velocities of the entrained droplets, being between 0.5 – 0.8 of gas superficial velocity [Lopes, 1987; Fore, 1995; Azzopardi, 1997]. In Lopes' article it is said that the slip ratio is of the order of 50% of the gas superficial velocity. Whereas Fore says that droplets at the centerline travel on average at 80% of the local mean gas velocity, Figure 3.3. All authors coincide to indicate that there is not shown an important sensitivity to the surrounding liquid velocity. While Azzopardi also says that mean droplets velocities are 80% of the gas velocity, but he added that the velocity profile of the entrained droplets follows the shape of the radial gas flow profile. Azzopardi speak about a trend for smaller droplets to travel at higher velocities than the ones with larger sizes. He also adds that the smaller droplets have higher velocity dispersion. This can be explained by two ways, firstly, by the fact that smaller droplets are most strongly affected by the gas turbulence, which can produce acceleration-

deceleration in the radial direction. Moreover, because of that larger droplets have shorter lifetimes and hence they reach lower velocities.

4.9.2.3. Correlations for Submerged Jets

Recent experiments with submerged gaseous jets [Someya, 2011] suggest that the entrained droplets travel in the gaseous phase at smaller velocities (between 1/30-1/60 the gas velocity). Unfortunately, these data are too scarce, as are the only ones to give such a small value for droplet velocity, consequently further investigation are needed to give them full credit. The correlation proposed by Someya et al. [Someya, 2011] is

$$u_d = 1.08\,p_0 + 3.35 \qquad \textbf{Eqn. (4.91)}$$

being p_0 the stagnation pressure, in their experiments varies from 0.5 to 8 MPa.

A very recent work proposes the following correlation for the determination of the entrained droplet velocity. This correlation uses the wave velocity of the gas-liquid interface (wave celerity, c), added to a percentage of the gas velocity to estimate the entrained droplet velocities [Berna, 2016]. The wave celerity is usually shown as a lower limit velocity to the entrained droplets, it is considered to be the initial velocity and release point of the entrained droplets [Mantilla, 2008; Van't Westende, 2008]. The Berna's expression is as follows

$$u_d = c + 0.15 \cdot u_g \qquad \textbf{Eqn. (4.92)}$$

being c the wave celerity (velocity at which the gas-liquid interface waves are travelling, Figure 4.21), defined as Kumar suggested, Eqn. (2.45) [Mantilla, 2008].

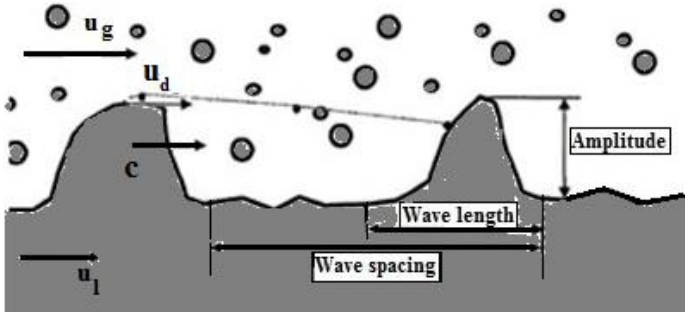

Figure 4.21. Schematic view of a unit disturbance wave.

This correlation provides predictions for the droplet velocities of 1/5 of the gas velocity, i.e., much higher velocities than those predicted by Someya's correlation.

Given the scarcity of expressions for submerged jets, it has been considered of great importance to conduct experimental series [Berna, 2017]. So that, these new experimental data series have been carried out in order to increase the limited information available

related with this subject as well as new correlations have been developed. The final expression for the estimation of the droplet mean velocity is shown below:

$$\mathrm{Re}_d = 4.024 \cdot 10^4 \, \mathrm{Re}_g^{0.2773} \qquad \textbf{Eqn. (4.93)}$$

All these expressions have been implemented and tested in the code, being the correlation used in the actual code version the one proposed in this PhD. document.

4.9.3. The Drag Coefficient of the Entrained Droplet

The drag coefficient, C_D, of rigid spheres has been widely studied and many semi-empirical correlations are available in the open literature. A selection of them is shown in Table 3.2, section "3.3.1. Force Balance Equation".

All the correlations shown in Table 3.2 suppose that particles have a spherical shape. But in our case, a water droplet suddenly exposed to an airstream, there is not a spherical shape but an oblate. In order to quantify the effect on the drag coefficient, there are several expressions available in the open literature.

For low Reynolds numbers of the water droplets the following correlations can be employed [Ashgriz, 2011]:

$$C_D = \frac{8}{\mathrm{Re}_d} \frac{3\mu_{rel} + 2}{\mu_{rel} + 1} \cdot \left(1 + \frac{\mathrm{Re}_d}{16} \frac{3\mu_{rel} + 2}{\mu_{rel} + 1} + \frac{1}{40} \left(\frac{3\mu_{rel} + 2}{\mu_{rel} + 1} \right)^2 \left(\frac{\mathrm{Re}_d}{2} \right)^2 \ln \frac{\mathrm{Re}_d}{2} \right) \quad for \quad \mathrm{Re}_d < 1 \qquad \textbf{Eqn. (4 94)}$$

$$C_D = \frac{1}{1 + \mu_{rel}} \left[\mu_{rel} \left(\frac{24}{\mathrm{Re}_d} + \frac{4}{\mathrm{Re}_d^{1/3}} \right) + \frac{14.9}{\mathrm{Re}_d^{0.78}} \right] \quad for \quad 0.5 < \mathrm{Re}_d < 200 \qquad \textbf{Eqn. (4.95)}$$

where $\mu_{rel} = \mu_d / \mu_l$ is the ratio of the viscosity of the droplet to the viscosity of the free stream

As far as high speed streams are concerned, Ortiz et al [Ortiz, 2004] present a correlation to determine the drag coefficient. For these flows the velocity is supersonic or high subsonic, which implies large Weber numbers. The correlation proposed is

$$C_D = 1.6 + 0.4 Oh^{0.08} We_d^{0.01} \qquad \textbf{Eqn. (4.96)}$$

being the Ohnesorge and Weber (free stream Weber number) numbers defined in Eqn. (3.7) and Eqn. (4.86).

The Ortiz's correlation was developed studying data of Ohnesorge number ranging from 0.002 to 44 and Weber numbers from 10^3 to $1.62 \cdot 10^5$.

In the case of water droplets the drag coefficient only depends on Weber number (0.002<Oh>0.003). Consequently the correlation reduces to

$$C_D = 1.6 + 0.25 We_d^{0.01} \qquad \textbf{Eqn. (4.97)}$$

But this correlation is essentially independent of Weber number, for instance, $We_d=10^3$-10^4-10^5 conducts to C_D = 1.868-1.874-1.881, i.e., the value of the drag coefficient of a water droplets exposed to a high speed stream is constant and $C_D \approx$ 1.87-1.88.

Another possibility to estimate the drag coefficient of a deformable droplet, also useful at high Reynolds numbers, is to use the empirical expression proposed by Schemhl [Pak, 2006]:

$$C_D = 0.28 + \frac{21}{\mathrm{Re}_d} + \frac{6}{\sqrt{\mathrm{Re}_d}} + \\ + We_d \left(0.2319 - 0.1579 \log \mathrm{Re}_d + 0.047 \log^2 \mathrm{Re}_d + 0.0042 \log^3 \mathrm{Re}_d\right) \qquad \textbf{Eqn. (4.98)}$$

The drag coefficient obtained by Eqn. (4.98) is plotted in Figure 4.22, in which the solid line represents the drag coefficient of a solid sphere and the dashed line indicates the drag coefficient of a disk, whereas the red lines represent the drag coefficient for deformed droplets at several Weber numbers. As is shown in the Figure 4.22, as the Weber number increases the drag coefficient values move from rigid sphere to disk drag coefficient values. The drag coefficient for We = 12 is used when the Weber number is over 12.

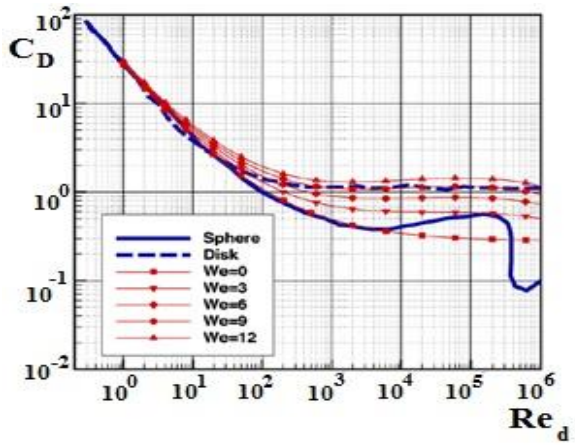

Figure 4.22. Effect of the obstacle shape in the Drag Coefficient [Pak, 2006].

The drag coefficient of oblate spheroids has been studied over the last decades by several authors. A simple correlation, which is derived from a linear interpolation between a solid sphere and a solid disk, was proposed by Liu et al. [Ashgriz, 2011]:

$$\frac{C_D}{C_{D-Sphere}} = 1.0 + 2.632 \cdot \left[1 - \left(\frac{\phi_0}{\phi_{cro}} \right)^2 \right] \qquad \textbf{Eqn. (4.99)}$$

being $C_{D\text{-}Sphere}$ the drag coefficient for a sphere at the same Reynolds number, and ϕ_{cro} the cross-stream diameter at a moment between the begin of the droplet deformation and the break-up.

4.10. Summary of Jet Hydrodynamics

Throughout this chapter the major aspects related to hydrodynamics of submerged jets has been addressed. In such a way that are directly shown here those aspects about which specific information of submerged jets is available. While for those about which there is not this information, it is shown the way as the key concepts have been adapted. This adaptation procedure is based on the annular flow findings displayed along the two previous chapters; remind that these flows are the ones with highest points in common with submerged jets.

Over this chapter the main characteristics of submerged jets are shown. In sections 1 and 2 the general characteristics of submerged jets are explained, showing the main regions in which jets can be divided, displaying of the complexity of injection and flow structures. Straightaway, in section 3, the three models used to characterize the conditions at the nozzle exist are shown. The next two sections display the expansion angle and the penetration length estimations. Immediately followed by the characterization of the liquid phase, mainly its velocity and thickness, both aspects have been shown along section 6. Proceeding to give some clues related with the gas-liquid interface along section 7, in order to show the extremely complex behavior of the interfacial waves. Sections 8 and 9 are focused on the analysis of the droplet entrainment process and their subsequent balance between atomization-deposition processes. In this section is estimated the total amount of droplets carried by the submerged jet, their sizes and velocities depending on the submerged jet conditions at the nozzle exit and along his spread downstream, the end of the entrainment region. Concentrating on droplet behavior, the section displays the maximum and mean droplet sizes; it also gives some sketches of secondary atomization process and droplet shapes, with the ultimate aim of showing the extreme complexity of the entrainment process.

Chapter 5

RELEASE AND TRANSPORT OF FISSION PRODUCTS– AEROSOL FORMATION AND GROWTH

5. RELEASE AND TRANSPORT OF FISSION PRODUCTS - AEROSOL FORMATION AND GROWTH

Introduction

The release of Fission Products (FPs) during a severe accident in a NPP involves a complex chain of events, which are strongly dependent on the temperature history, the fuel type, fuel burnup and the thermal-hydraulic conditions existing in the vessel and containment. The core degradation leads, as a result, to the emission of FPs, actinides and structural materials in form of gases and vapors into the reactor coolant system. Its emission is made in a wide variety of chemical forms, which depends on the equilibrium of the condensed phase existing into the fuel. Its equilibrium varies throughout the course of the severe accident, mainly because of temperature and oxygen potential variations. The majority of these radioactive materials that escape from the core will do in form of aerosols. Consequently, an important part of reactor accident analysis is the prediction of the behavior of these radioactive aerosols during its path through the vessel and the reactor coolant system. Aerosols consist of very small solid particles or liquid droplets suspended in the gaseous phase. These suspended solid or liquid particles typically have a range of sizes which go from 0.01 μm to 20 μm. The aerosols concentrations in a reactor accident are typically less than 100 g/m^3 and usually even less. At these small concentrations, the aerosols particles produce little or none effect in the gas hydrodynamics, but the gas dynamics can profoundly affect the behavior of these suspended particles.

Throughout this section the main source of radioactive materials which can be released during an accident, the fission products, together with the subsequent aerosol formation growth and transport mechanisms will be described.

5.1. Background of Primary System and Containment FP Release and Transport

The primary system FP release and transport did not play an important role before the Three Mile Island accident in 1979. Only three documents can be mentioned, first the TID-14844 [DiNunno, 1962], the WASH-1400 [U.S. NRC, 1975] and a German risk study [Gesellschaft für Reaktorsicherheit, 1979]. TID-14844 gives a set of assumptions in order to be able to estimate the consequences of an accident. In this first document, it is assumed that a percentage of the source terms escape from the primary circuit to the containment, in particular, 100% of the noble gases, 50% of the halogens and 1% of the solid FPs are assumed to be released. While the WASH-1400 report is the first systematic attempt to try to estimate the source terms in nuclear accidents which might lead to a melted core. Even though, due to the scarcity of data the assumptions on the release of FPs from the primary

circuit were unrealistic. A few years later and based on this document, the German risk study was concluded. This document was carried out for a representative 1300 MWe German PWR plant.

After the Three Mile Island accident, due to the low amount of released radioactive materials in comparison to the previous assumptions made in the cited reports, the international efforts increased noticeably. Becoming evident that the phenomena associated with the primary circuit FPs release and transport played an important role in the estimation of accident source terms. Some bear fruits of these efforts were: several US NRC NUREGs related with this subject NUREG-0772 [US NRC, 1981], NUREG-0956 [US NRC, 1986] and NUREG-1150 [US NRC, 1990]; the German risk study Phase B [Gesellschaft für Reaktorsicherheit, 1990]; among other reports in several countries. The most important steps forward in understanding the FPs behavior of all these studies were the performance of separate effects experiments to try to understand focusing on each phenomena, the development and evaluation of new computer codes and the design and the startup of large scale tests to investigate integrated phenomena. Good summaries of the FPs release and transport are shown in NUREG/CR-9163 [US NRC, 1994], on the State of the Art Report on Nuclear Aerosols [Allelein, 2009] and on the IRSN report on Nuclear Power Reactor Core Melt Accidents [Jacquemain, 2015].

5.2. Inventory of Fission Products and Actinides

Fission products are produced by irradiation of neutrons on fuel, which causes fuel fission reactions. Its yield depends on the type of product itself and on the type of fission (thermal neutrons for ^{235}U or ^{239}Pu, fast neutrons for ^{238}U, etc.). Consequently, the inventory of fission products can differ greatly depending on the type of LWR (BWR or PWR), the burnup rate (increases virtually in a near-linear shape in terms of mass or number of atoms), etc.

The most important types of accidents that can lead to core damage are the SBOs (Station Black Out), LOCAs (Loss Of Coolant Accident), ATWSs (Anticipated Transient Without Scram), etc. For PWR plants most probable accident types are: SBO sequences start with the loss of off-site power (LOSP); the LOCA sequences can be of large, intermediate, and small size with failure of the emergency core cooling systems (ECCSs); and SGTR events in combination with other failures. For BWR plants most probable accident types are: SBO with a turbine trip and followed by loss of all AC power; and ATWS.

The FPs inventory for a 900 MWe PWR is around 2 tons in normal operation. Table 5.1 lists the inventory of each FP and heavy nucleus together with its activity from the reactor Shut-Down (SD) to one month later [Jacquemain, 2015].

In Table 5.2 the FP inventory in normal operation of Peach Bottom NPP is shown (estimation of MELCOR code), its two units (Units 2 and 3) have a thermal power of 3514

MW, equivalent to about 1180 MWe each. Both reactors are a General Electric nuclear steam supply system (NSSS) of the BWR/4 product line housed within a Mark I containment [Leonard, 2007].

As a consequence of the great variety of parameters which affect the performance of the production processes of radioactive materials release, the composition of the FPs can be very different. All these conditions are dynamic, for instance, during the course of an accident the fuel rods can be exposed to very high temperatures, ranging from 600 to 2400 ºC, and the environment can change from highly oxidizing to moderately reducing. Consequently, in the next paragraphs a brief explanation of a possible composition of the released FPs in a PWR after an accident is shown.

Table 5.1. Total mass and change in activity with time of FPs and Actinides in a 900 MWe PWR[1] [Jacquemain, 2015].

		Activities as a fraction of the total activity			
Fission Products	**Total Mass at SD (kg) [2]**	**At SD**	**1 hour later**	**1 day later**	**1 moth later**
As	0.00739	0.20%	0.01%	0.00%	0.00%
Se	3.14	0.58%	0.02%	0.00%	0.00%
Br	1.16	1.17%	0.20%	0.00%	0.00%
Kr	22.1	2,32%	1.46%	0.03%	0.06%
Rb	20.3	3.22%	0.84%	0.01%	0.00%
Sr	55.1	4.50%	3.85%	2.57%	6.10%
Y	28.9	5.84%	5.11%	3.40%	8.16%
Zr	210	4.73%	3.83%	4.63%	10.30%
Nb	3.24	7.09%	5.68%	5.93%	13.18%
Mo	184	4.28%	2.28%	2.90%	0.01%
Tc	45.2	4.82%	2.50%	2.77%	0.01%
Ru	137	1.85%	3.11%	3.67%	10.27%
Rh	23.6	2.30%	3.42%	4.96%	10.26%
Pd	59.3	0.19%	0.33%	0.18%	0.00%
Ag	3.97	0.14%	0.11%	0.12%	0.05%
Cd	4.0	0.03%	0.02%	0.01%	0.00%
In	0.082	0.13%	0.03%	0.01%	0.00%
Sn	2.65	0.66%	0.15%	0.02%	0.01%
Sb	0.898	1.76%	0.68%	0.17%	0.06%
Te	26.2	3.85%	4.16%	2.88%	0.69%
I	12.7	5.70%	8.94%	6.39%	0.65%
Xe	307	4.33%	3.60%	5.12%	0.41%
Cs	161	3.82%	1.27%	0.46%	1.61%
Ba	82.1	4.67%	3.75%	3.46%	3.45%
La	69.9	4.71%	5.22%	3.57%	3.25%
Ce	163	3.61%	5.04%	7.41%	16.01%
Pr	62.1	3.10%	4.63%	5.49%	11.76%
Nd	207	0.68%	1.07%	1.25%	0.82%

Pm	12.4	0.65%	1.22%	1.65%	1.48%
Sm	35.7	0.21%	0.46%	0.54%	0.00%
Eu	8.9	0.08%	0.19%	0.29%	0.36%
Actinides					
U	69900	9.37%	3.91%	0.00%	0.00%
Np	31.5	9.37%	22.76%	29.86%	0.02%
Pu	589	0.05%	0.11%	0.19%	0.80%
Am	6.18	0.00%	0.00%	0.00%	0.00%
Cm	2.09	0.01%	0.03%	0.06%	0.21%
Total activity (Bq)		5.91E+20	2.42E+20	1.39E+20	3.30E+19

[1] 900 MWe PWR with UO_2 fuel enriched to 3.70% of 235U, 72.5 tons of initial uranium, with the fuel loaded into four regions of the core (burnup rate of the assemblies: 10.5 GWd/tU for the first region [one burnup cycle], 21 GWd/tU for the second region [two cycles], 31.5 GWd/tU for the third region (three cycles) and 42 GWd/tU for the last region [four cycles]).

[2] Total mass of the stable isotopes and the radioactive isotopes.

Table 5.2. Total mass of FPs for Low burnup and high burnup calculated with MELCOR code for an 1180 MWe BWR [Leonard, 2007].

Radionuclide Group	Element	Mass (kg) Low-Burnup	Mass (kg) High-Burnup
Noble Gases	Xe, Kr	361.8	876.5
Halogens	I, Br	14.0	34.0
Alkali Metals	Cs, Rb	207.8	506.0
Tellurium	Te, Se	33.2	81.5
Alkaline Earths	Ba, Sr	154.1	372.0
Platinoids	Ru, Pd, Rh	234.3	633.4
Early Transition	Mo, Tc, Nb	263.7	640.9
Lanthanides	La, Nd, Pr, Sm, Y, Pm, Eu, Am, Gd	485.7	1240.5
Cerium Group	Ce, Pu, Zr, Np	1213.1	2280.6

The chemical forms at which the FPs in the fuel matrix under nominal irradiation conditions of a PWR can be found are [Jacquemain, 2015]:

— Dissolved oxides, for nearly half the products, particularly Sr, Y, Zr, La, Ce and Nd.

— Oxide precipitates primarily for Ba and Nb.

— Metal precipitates for Mo, Tc, Ru, Rh and Pd.

— Dissolved atoms for the volatile FPs: Br, Rb, Te, I and Cs. However, the chemical state of these FPs is not fully known at the present time. The majority of them are probably present in the form of dissolved atoms and, above a certain temperature, they can migrate radially into the fuel pellets and condense in the colder sections, where they form more complex compounds with fuel elements or other FPs. For example, Cs can form compounds such as cesium molybdates and urinates, but it has never been confirmed experimentally.

— Dissolved atoms or inter-granular or intra-granular gas bubbles for the fission gases: Xe and Kr. It should be noted that gases that are accumulated at the grain boundaries are more easily released during accident events.

The chemical state of the FPs in the first three categories mentioned above is not fixed, so some of them may move from one category to another according to several variables, such as, the operating temperature, the oxygen content in the fuel (which increases with burnup as fission reactions tend to be oxidizing), and the burnup (which increases the concentration of FPs in the matrix). This is especially the case of Mo, which precipitates mainly in metallic form, but which may also be in oxidized form (especially on the surface of Mixed Oxide Fuel pellets, MOX), and for Nb and Sr whose oxides may be partly dissolved and partly precipitated in the fuel.

With regard to fission gases, as fuel is irradiated, fission gases form atoms within the grain structure of the UO_2, these atoms diffuse towards the grain boundaries or precipitates in the form of nanometric intra-granular bubbles, but these bubbles might be redissolved under the influence of fission spikes. The fission gasses that arrive at the grain surface accumulate until coalesce to form larger bubbles, filling the inter-granular space. Some of them can escape from the fuel and reach the free volume of the fuel rod. So, at the instant that an accident occurs, the fission gases are distributed in three forms:

— Atoms of gas dissolved in the fuel matrix.

— Intra-granular gas bubbles of gas with low mobility.

— Inter-granular gas bubbles.

The inter-granular gases are the first released phase, often referred to as ‘burst release’, in addition to the gas fraction that had already been released into the fuel rod plenum during normal operational irradiation (whose range reaches at most 10%, depending on the burnup, the irradiation power and the fuel type). This release occurs at the beginning of the temperature rise (around 1000°C, although this temperature may be lower in the case of high burnup fuels). The atoms of gas dissolved in the matrix are released in the second place. Finally, the nanometric intra-granular bubbles are released in the last place, often only at the point at which the fuel melts.

The non-gaseous fission products are released through two processes:

— Diffusion towards the grain boundaries of the FPs in solution in the fuel matrix and in the form of precipitates, once the limit of solubility has been reached.

— Mass vaporization transfer process that carries out of the grain boundaries the FPs, which allows the formation and release of several species (CsI, molybdates, zirconates and uranates of caesium, Ba, Sr, etc.)

The release of these FPs conducts to potential chemical interactions with the fuel cladding and/or structural components which may also reduce the volatility of some elements by the formation of more refractory compounds. Finally, even once FPs have escaped from the core, an important portion condenses in cooler areas within the structure of the upper head before, especially in the case of the less volatile FPs.

Summarizing, the major parameters that determine the amount of FPs released from the core are:

— Temperature: which is the key parameter at least up to the loss of core integrity.

— Oxidizing or reducing conditions: the kinetics of volatile FPs release are accelerated under oxidizing conditions, in addition, the total release of some FPs is also very sensitive to the oxygen potential. For instance, Mo release increases in the presence of steam, Ru with the presence of air, whereas the release of Ba, Sr, Ro, Ce, Eu and Np increases under reducing conditions.

— Interactions with the cladding and/or structural components: for instance, the presence of tin in the cladding delays the emission of the volatile elements Te and Sb. Ba (which made a major contribution to the residual power via its descendant ^{140}La) is also partially trapped in the cladding and in the internal core steel structures.

— Burnup enhances the FPs release: through the kinetics of the volatile FPs reactions and through the increase in the release of low volatile elements such as Nb, Ru, Ce and Np.

— Type of fuel: the FPs releases from MOX fuels tend to be higher than those of UO_2.

— Morphology of the fuel during its in-vessel degradation process: an increase in the FPs release (caused by the increase in the surface area/volume ratio the change) takes place during the transition from a ‘degraded fuel rod’ to a ‘debris bed’ geometry, while the opposite occurs during the transition from a ‘debris bed’ to a ‘molten pool’ (due to the formation of a solid crust on the molten corium pool surface).

Summarizing, mainly from the VERCORS analytical experiments and the PHEBUS programme integral tests, a classification in four decreasing volatilities classes of FPs can be established [Pontillon, 2010a,b&c]:

— Volatile fission gases and FPs (Kr, Xe, I, Cs, Br, Rb, Te, Sb and Ag). Almost all of them released even before the formation of the molten pool. Release accelerated under oxidizing conditions.

— Semi-volatile fission products (Mo, Ba, Y, Rh, Pd and Tc). Very high level of release, in some circumstances equivalent to the volatile FPs. Its release can be almost total, but are very sensitive to the oxidizing/reducing conditions and have large degree of retention by the structures in the upper head structures.

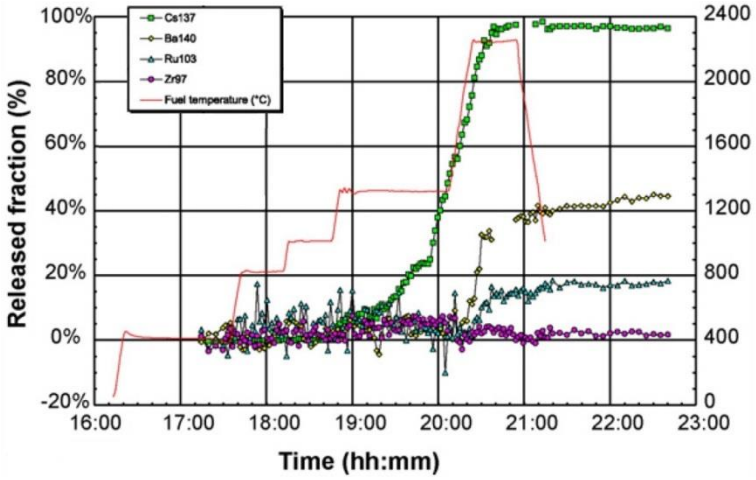

Figure 5.1. Illustration of the behavior of an isotope included in each of the four volatilities classes of FPs according to VERCORS test [Pontillon, 2010a].

— Low-volatile FPs (Sr, Nb, Ru, La, Ce, Eu and Np). Low level of release, up to 10% during the fuel rod degradation phase, however it can be higher for high burnup fuels. The retention in the upper head structures is expected to be high.

— Non-volatile FPs (Zr and Nd). No significant release has been measured experimentally.

With regard to the release of actinides say that U and Np behaves as low-volatile FPs and Pu as non-volatile FPs.

Figure 5.1 displays the VERCORS tests measurements of the FPs release versus time for each of the four FPs volatility groups (via a representative isotope of each group). The fuel temperature is also shown in order to highlight the temperature ranges in which FPs release starts and accelerates.

5.3. Degradation of the Reactor Core during a Severe Accident

An accidental scenario takes place when the fluid of the primary circuit is partially lost or its flow stops, then the core overheats and the remaining fluid starts boiling, this steam leads to an oxidizing atmosphere. Consequently uncovered parts of the fuel rods suffer a great rise in temperature due to the residual heat. This head up, added to the

oxidizing atmosphere, can lead to significant and/or irreversible degradation of the vessel. Control rods suffer degradation processes previously than fuel rods, degradation can be via melting (alloys of silver-indium-cadmium, Ag-In-Cd) or oxidation (boron carbide, B_4C). The degradation mechanisms are mechanical and chemical. In summary, the sequence of major phenomena involved in the core degradation process are: the cladding failure (zircaloy cladding begin to distort at 700 ºC approximately); the melting of the control rods (for instance, silver-indium-cadmium alloys melt at temperatures of about 800 ºC); the cladding oxidation and hydrogen formation (start at temperatures of approximately 1000 ºC); zircaloy melting and fuel dissolution (when zircaloy melts the UO_2 fuel partially dissolves on it); corium flow (molten materials solidificate in colder areas, which may conducts to reductions in the coolant flow, which affects the cooling of the degraded core); oxidation of molten mixtures (the zircaloy continues is oxidation along its path through the core); and finally, formation of a corium pool in the reactor core or into the lower head (when melting point of UO_2 is reached, 2800 ºC, a "molten pool" is formed in the reactor core, it expands reaching the baffle or the core support plate, finally flowing into the lower head). Figure 5.2 shows, in a schematically form, the major phenomena involved during the core degradation process.

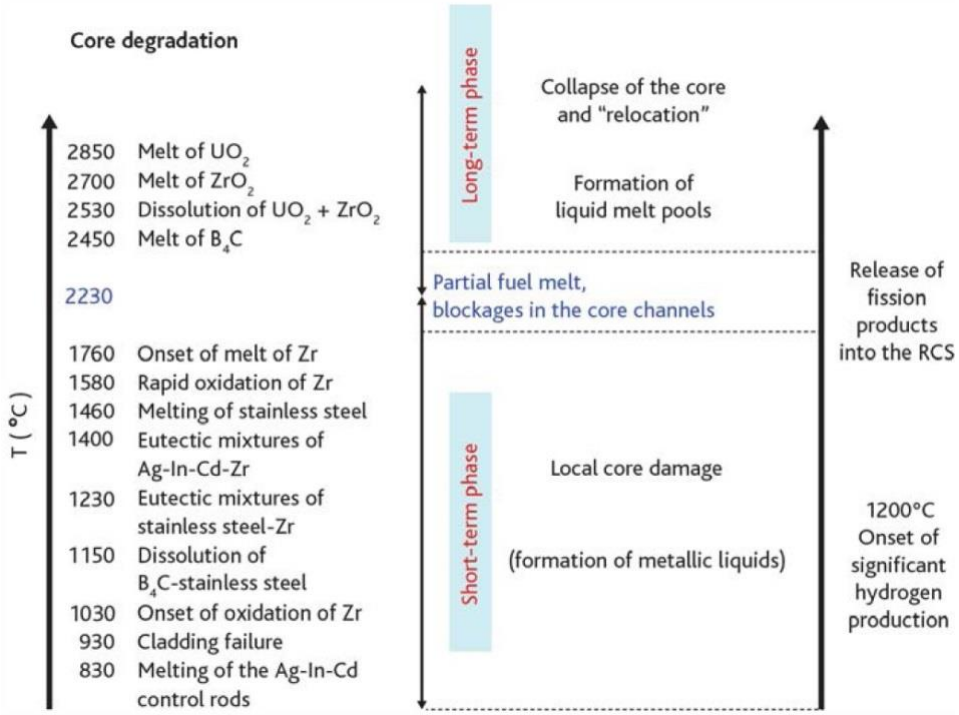

Figure 5.2. Major phenomena during the degradation process of reactor core materials [Jacquemain, 2015].

The oxidation and failure of the core starts with the oxidation and failure of the rod cladding. Under normal operation, the zircaloy cladding is at about 350 ºC, when the temperature in the core reaches 700-900 ºC, the cladding begin to deform. This deformation and subsequent failure can differ depending on the pressure differences between the inner and outer parts of the cladding, Figure 5.3. If the pressure in the core is lower than that of the gases of the fuel rods, Figure 5.3 (a), then the cladding swells until it bursts, phenomenon called usually "ballooning". This phenomenon can cause a mechanical failure of the cladding previously to its oxidation. If the pressure in the core is higher than that of the gases of the cladding, Figure 5.3 (b), then the cladding is pushed towards the fuel pellets, which promotes the formation of a eutectic of UO_2-Zr, with a melting point of 1200-1400 ºC. In Figure 5.3 is displayed a summary of the phenomenology which takes place during the fuel cladding failure.

With regard to hydrogen release and cladding oxidation, the zirconium of the fuel rods cladding oxidizes when contains superheated steam, this oxidation reaction starts at about 1000 ºC and is considerably accelerated at 1500 ºC (absorption of oxygen by the cladding and the oxide layer thickness are governed by the Arrhenius law, exponentially increasing with temperature). This oxidation reaction is strongly exothermic; the released heat is comparable to that of the residual power. In addition the molecular hydrogen produced may escape from the Reactor Coolant System (RCS) and react with air, which may lead to explosion which can affect the containment integrity.

As a result, not all fuel rod cladding failures occur before their oxidation, then results that oxidized fuel rod cladding can lose its integrity caused by other mechanisms which take place at high temperatures; these mechanisms are not well known. The latest experimental evidences show that zirconia layer breaks at 2300-2500 K or when its thickness is lower than 300 mm approximately, but the rupture mechanism is poorly understood. Before the zirconia layer failure, when the zircaloy melting point is reached, the UO_2 fuel (melting point at 3100 K approximately) is partially dissolved by the liquid metal (remains inside up to the point in which fuel rods loss its integrity). When the molten materials flow outside of the failed rods their solidification in colder region may result in the reduction of flow cross sections, affecting the vessel cooling (several variables affect this solidification process, for instance, the molten mixture viscosity, which depends on temperature, degree of oxidation, etc.). As the temperature increases the zircaloy continues oxidizing. If the molten mixture reaches the melting point of the UO_2 a "molten pool" is formed in the core (in fact several hundred degrees below because of the formation of eutectic liquids). These molten materials can go out of the core reaching the lower head and, due to its low surface/volume ratio, are very difficult to cool.

As far as FPs is concerned, its release starts with the failure of the fuel cladding. In the initial stage the FPs trapped into the cladding – fuel gap and the most volatile escape. With the progression of the accident other FPs are released (depending on temperature, oxygen potential, burn up and type of fuel, etc.). Even though there are still uncertainties about the composition of the FPs release depending on the boundary conditions of the accident. In the next section a brief description of the FPs formation process is displayed.

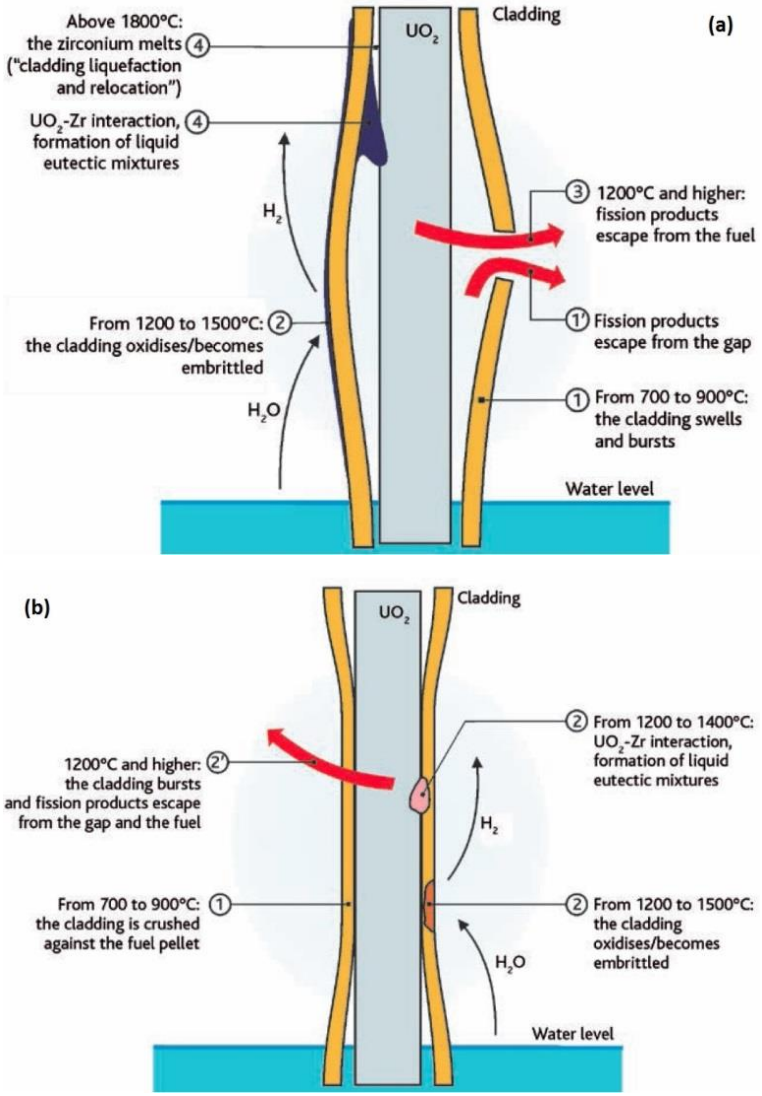

Figure 5.3. Mechanisms of degradation of the fuel cladding during severe accidents: (a) low pressure (b) high pressure [Jacquemain, 2015].

The containment concrete basemat come into direct contact with the corium, then the reactor pit begins to decompose due to the high amount of heat emitted, this phenomenon is known as molten core – concrete interaction (MCCI). On one side, the molten core – concrete interaction produce the erosion of the concrete and, additionally, the large amount of gases produced make the containment pressure to raise, finally, both aspects can lead to

the containment failure. The containment penetration time can be from one to several days, depending on the corium quantity and on the concrete type (siliceous or calcareous), on the basemat thickness, composition of the corium, etc. Besides, the residual heat released by the FPs exceed the heat that can be removed by the basemat (concrete has a very low thermal conductivity and a great thickness), then the corium temperature increases and the concrete basemat fails by erosion or ablation (the siliceous and silico-calcareous at 1600 K approximately, and the calcareous at temperatures several hundred degrees higher). The aerosol produced during the MCCI affects the rest of aerosols and changes the resulting aerosol release.

The degradation of the core may reach several levels, from intact rods to complete corium pool. All these phenomena which take place during a severe accident does not occur in an ordinate way but simultaneously and in several parts of the core. Being his description out of the scope of this document, more details are shown in the IRSN report on Nuclear Power Reactor Core Melt Accidents [Jacquemain, 2015].

5.4. Aerosol Formation

During the successive stages of a severe accident in a LWR, which probably can end with the core melting, the radioactive materials (which mainly include FPs and structural materials) released are in form of aerosols and vapors. Their composition, total amount and release timing are strongly dependent on their dominant source, control rod and fuel burst chronology, cladding oxidation, fuel heat up and geometric evolution along the accident, molten pool formation and characteristics, etc. In addition, their chemical form depends on an equilibrium between them and the condensed phase of the fuel. This equilibrium varies as the accident evolves, mostly by the temperature, pressure and oxygen potential. In their path they also encounter a great variety of environments, mainly changes in temperature and carrier gas composition. The structural materials also play and important role. As a result, most of the radioactive materials produced during a severe accident can escape from the core in form of aerosols. These aerosol particles can be formed in two ways in an accidental sequence [Allelein, 2009]:

- the mechanical comminution of materials, and

- the condensation of vapors, both on nucleation kernels forming fine particles (homogenous nucleation) and on pre-existing particles (heterogeneous nucleation).

Mechanical comminution processes that produce aerosol particles in reactor accidents include:

• entrainment of solid particles or liquid droplets in high velocity gas flows,

• droplets ejection by gases bubbling through liquids,

• shock waves such as those produced in energetic interactions of molten materials with coolants, and

• high pressure melt ejection from the reactor coolant system.

Mechanical processes rarely produce very fine particles (usually minimum size about 1-2 μm) that can remain suspended in the gas phase over extended periods of time. Moreover, most of the mechanical processes that can be sources of aerosols are not of long duration and, therefore, are not able to be sources of aerosols throughout the long periods of time in which an accident occurs. An exception is the production of aerosols by the bursting of bubbles of gas dispersing through liquids, but this mechanism is not so important. Consequently, mechanical processes as source of aerosols have been largely ignored in most analyses of reactor accident.

Nucleation of aerosol particles from supersaturated vapors is the most important source of aerosols in reactor accidentals sequences. The vapors rich in radioactive materials (mainly FPs) are formed from high temperature materials from the core debris materials. These vapors become oversaturated as they are transported from the vicinity of the core to colder regions. These supersaturated vapors can be nucleation points of aerosol particles.

Even when steam is composed of a single species of condensable species the vapor nucleation is a very complicated physical process. Nucleation can occur homogeneously from the vapor when the supersaturation ratio (ratio of the actual partial pressure divided by the equilibrium partial pressure of the species) exceeds a value of 4 - 10. Nucleation is a kinetic process and there is not an abrupt onset point, it is generally considered that nucleation occurs when the production rate > 1 particle /cm^3-s.

As for the heterogeneous nucleation say that, due to the ions presence, it can occurs with lower degrees of supersaturation than that of homogeneous nucleation. The gas phase in a nuclear reactor accident will be intensely irradiated, so there will exists a relatively high ions concentration, which will act as nucleation points, so some heterogeneous nucleation points will exist. But, the higher supersaturation ratio will exists when superheated vapors escape from the high temperature zone, existing in the vicinity of core debris, towards colder regions, even higher than 10^4. It is likely that both, heterogeneous and homogeneous nucleation, will occurs simultaneously.

While the theory of nucleation of complex vapors produced in reactor accidents is much more complicated than the theory for single pure vapors described above. In fact, a general theory of nucleation for complex vapors has not been developed yet.

Then, as a result of all the successive stages in the degradation of the core during a severe accident in an LWR, a release of vapor and aerosol particles takes place. All the fission products and structural materials that are released from the core mainly do in the form of vapors. These vapors cool down during its path through the primary circuit, specifically in the upper part of the pressure vessel and in the reactor cooling system, the main phenomena involved in the formation and transport of aerosols are shown in Figure 5.4. The condensation of the vapors is governed mainly by aerosol physics, with the exception of iodine and ruthenium, which may continue in gaseous form, the chemistry of these highly radiotoxic elements is complex.

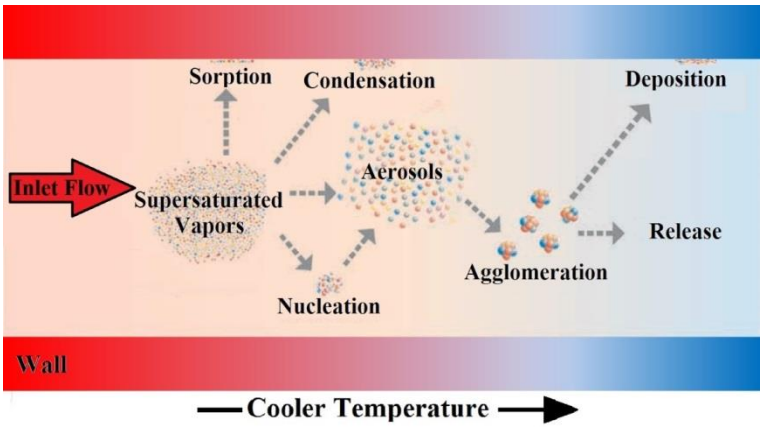

Figure 5.4. Aerosol formation and transport phenomena.

The aerosol composition differs depending on the dominant source, either the fuel and control rod burst events, oxidation of the cladding, reflooding of the degraded core, etc. Its composition also depends on temperature variations and oxygen potential during the course of the accident, through the displacement of the equilibrium reactions of aerosol formation. Aerosol particles might be formed by a wide variety of processes, such as, chemical reactions, attrition of solids, resuspension, etc. Given sufficient time in a quasi-steady state environment (path followed by the aerosols until they reach the break), the aerosols are subjected to particle growth by agglomeration, coagulation and gravitational deposition-resuspension processes onto surfaces. All these processes will develop an aerosol size distribution function that is approximated quite well by a log-normal distribution. Then, the aerosols features under severe accident conditions that will affect the nature of the salient aerosols are mainly their formation processes, growth, shape, equilibrium between deposition-resuspension processes and equilibrium between agglomeration/de-agglomeration processes.

5.5. Growth and Transport of Aerosols in the Primary Circuit

The aerosols formed in the Reactor Pressure Vessel (RPV) can be transported through the primary circuit previously to be emitted to the containment or even to the surrounding environment, if a containment failure occurs during the accident or the aerosols are able to bypass the containment building. Consequently, all the processes that can take place within the path followed by the aerosols in the primary system determine the nature, magnitude and timing of the radioactive aerosol emission. Along this path, the amount of FPs can be attenuated due to a great variety of aerosol and vapor removal mechanisms. The major phenomena suffered by the aerosols throughout their way inside the primary coolant circuit are described in the next paragraphs.

In addition to the physical phenomena, the chemistry of some FPs has to be taken into consideration. In particular, the iodine and ruthenium chemistry is of major importance, due to the great amount of chemical forms, their reactivity and mainly due to their radiotoxicity. For instance, iodine can presents in atomic and molecular forms (I and I_2 respectively), hydroidic (HI), or in metallic compounds of cesium, rubidium, silver, indium and cadmium mainly. The ruthenium reacts with air, forming dioxide of ruthenium (RuO_2), which oxidizes to RuO_4 through an equilibrium chemical reaction. That is, a percentage remains in form of dioxide (solid form, which can deposit onto steel pipes of the primary circuit). While the rest, in metastable form of RuO_4, is laden by the carrier gas along the primary circuit to the free volume of the containment.

Several research efforts have been carried out to try to study severe accidents with melted core and particularly to study the chemical of iodine and ruthenium, for instance, experimental programs like VERCORS, PHEBUS-FP or EPICUR and simulation codes like the SOPHAEROS module of the ASTEC code, the ICARE modulus of the CATHARE code or MELCOR code [Jacquemain, 2015]. But not definitive results can be concluded, only verification of the complexity of the iodine chemistry.

5.5.1. Agglomeration

Once the aerosol particles are formed by their random movement, as they are suspended in a fluid, they might collide due to their relative motion induced by several causes, such as, fluid non-homogeneities (generated by shear or turbulence forces), Brownian motion, external forces (gravity, electrostatic, Van der Waals, etc.), concentration or temperature gradients, etcetera. Two different situations may occur when two particles collide. The colliding particles preserve their identity and shape, or coagulate, that is, the colliding particles merge and lose their identity. This merger phenomenon is called agglomeration or coagulation.

Brownian agglomeration is more significant for small particles, free molecular regime (Knudsen number >> 1) and in the transitional regime (Knudsen number ≈ 1). Small particles mobility is very large, but this effect is mitigated by the reduced target area they present. Brownian agglomeration is more effective when come into play very small particles with larger ones. In general, models are derived from the theory of Brownian diffusion with correction factors for the free molecular regime for nonspherical particles [Allen, 2001].

Gravitational agglomeration occurs as a result of the dependence of the aerosol terminal velocity with its dimensions. Particles with slow sedimentation velocity (usually smaller) are captured by the more settling velocity particles (usually larger). This agglomeration mechanism is proportional to the difference in velocities and the sum of their projected areas. The disparity arises when the resulting collision effectiveness has to be quantified [Allen, 2001].

Turbulent agglomeration can be subdivided in two processes: turbulent shear agglomeration and turbulent inertial agglomeration [Allen, 2001]. Turbulent shear can

produce that particles following different flow path-lines collide with each other (particles on different streamlines are travelling at different velocities). Turbulent inertial agglomeration results when particle trajectories depart from flow streamlines and such departures cause collisions.

Probably the most significant uncertainty in this area is related to particle shape. It is common to associate two aerosol shape factors: one related to their mobility properties and another related to collision properties. Spheres are the most compact particle shapes and therefore any deviation from this shape has some impact on motion resistance and on likelihood of colliding to each other. Particles in presence of high steam humidity conditions tend to collapse into compact shapes due to the influence of the surface tension of water. However, the primary circuit is generally highly superheated, so that compaction is only likely to occur near the break under certain accident sequences (cold leg break or SGTR event). However, it might have other species abundant enough to cause a compaction effect, but there is not enough experimental evidences corroborating this point. Therefore, high shape factors, such the ones of agglomerates in the form of long chains, probably can be excluded. However, shape factors and their evaluation remain still under significant uncertainty.

Another important property that has to be considered is the hygroscopicity of the aerosol particles. If the aerosol is hygroscopic the aerosol can absorb water molecules and form droplets, so that particles increase in size and the gravitational settling deposition mechanism is accelerated, for instance cesium hydroxide is hygroscopic.

5.5.2. Deposition

Aerosol deposition will takes place along their path through the primary circuit, due to several mechanisms, such as, sedimentation (gravitational settling), inertial impaction (projection onto surfaces by flow-geometry changes and turbulent eddies), Brownian diffusion, thermophoresis, diffusiophoresis and electrophoresis. Among these deposition mechanisms, not all of them are certain to be significant, since they are scenario dependent. Brownian diffusion will be important if aerosol particles remain small after its formation. From the rest of named phenomena, probably only thermophoresis will produce significant deposition whatever the accident sequence.

Brownian diffusion is more relevant for the surrounding areas of the nucleation points and particles remain small, i.e., within the reactor vessel. For laminar flow, the classic approach, Fick's law, can be used, but only in the limit of stagnation. Therefore, empirical models of deposition are used, being the most commonly employed the Gormley and Kennedy's [Gormley, 1949]. For turbulent flows, phenomenology changes, turbulence brings particles close enough to the wall so that the diffusion goes on to become the dominant transport mechanism [Davies, 1966]. This mechanism affects above all highly submicron particles having a small contribution in the deposition for the rest.

Thermophoresis is a phenomenon that does not have a great dependence on particle size, although its importance is greater for submicron particles. It occurs as a result of

unbalanced collisions between gas molecules and aerosol particles. A particle immersed in a temperature gradient undergoes a force directed towards colder temperatures, which is counteracted by the force of hydrodynamic drag. Highly conductive particles (e.g., metallic particles) are less affected by thermophoresis than those made of more insulating materials. For larger particles, a thermal gradient can be established within the particle, which conducts to a considerable increase in complexity. Several models are available in the literature, the most commonly used is the Brock formula, further information can be shown in several publications [Talbot, 1980; Muñoz-Bueno, 2005; Housidas, 2005].

Diffusiophoresis takes place when particles are dragged by a net flow of steam towards an area where it condenses. This condensation is characterized by Stefan velocity. A correction function of the gas composition (mixture of steam and non-condensable gases) and the particle flow regime (via the Knudsen number) has to be taken into account, the Loyolka's model is the most commonly used [Loyolka, 1971]. Only certain sequences of accidents lead to vapor condensation on surfaces in the primary circuit, those involving lower temperatures, such as cold leg breakage or SGTR. As a matter of fact, diffusiophoresis never occurs alone, but it must necessarily be accompanied by thermophoresis, therefore there is deposition by thermo-diffusiophoresis.

Radioactive aerosols self-charge electrically, due to the predominance of α and β^- decays, they are very small and develop a positive charge (the theoretical work of Clement and Harrison [Clement, 2000] and experimental of Gendarmes et al. [Gendarmes, 2001]). The first of them indicates that the particle charging is very sensitive to two factors: the small particle sizes considerably limit their ability to self-charge, while its high concentration also contributes to reduce its self-charge. While, on the other, aerosols confinement can help this self-charge. Then it implies that limited self-charging can occur, with the only exception of regions with particularly confined flow.

The particles are deposited by the influence of gravity (sedimentation), being its terminal or settling velocity proportional to the square of its radius. In turbulent flows, the particles are deposited through the laminar boundary layer, while in a laminar flow around the whole flow layer. The gravitational sedimentation is not particularly significant in the primary circuit due to the small particle sizes (low sedimentation rate) and their short residence time (high speed).

The particles can be projected on surfaces due to its inertia (inertial impaction), changes in the flow direction when encountering obstructions or obstacles, such geometries are common in the primary circuit. The phenomenon of inertial impaction clearly becomes important with increasing particle size, so that the submicron particles are not affected substantially by this phenomenon. Since few particles become large enough in the primary circuit, this is not a dominant deposition mechanism.

Regarding to experimental measurements, the tests carried out in the Phébus FP circuit [Haste, 2013] shows that the aerosol deposition is mainly concentrated in the zones in which temperature decreases strongly, i.e., just above the bundle (fluid colds from 2000 to 700 °C approximately) and in the hot leg of the SG (fluid colds from 700 to 150 °C

approximately). In the vertical line the deposition mechanisms are enhanced too, due to the simultaneously developing flows and changes in geometry.

5.5.3. Resuspension

Particles, which previously have been deposited on surfaces of the primary circuit, can be resuspended, returning to the gas stream under some circumstances. This phenomenon may occur if the removal forces affecting the particles are greater than the ones that try to stick on them to the surface. Usually, resuspension is caused by a sudden increase in gas flow rate and by shocks or vibrations of the deposition surfaces. Events that probably will lead to resuspension could be for instance, core cooling (associated with attempts to quench the core), relocation of molten material (core debris falls from the core to the lower plenum), accidental or intentional depressurization (rupture of the reactor pressure vessel, primary circuit depressurization), violent fuel-coolant or hydrogen explosions (steam explosions, hydrogen combustion). Resuspension can happen even if the flow rate is constant. The result of this resuspension processes is the decrease in the retention of radionuclides into the primary circuit.

An estimation of the forces that bind the particles to the surface is important to estimate the particle resuspension. The Van der Waal force is the most important for dry particles, even though other electrostatic forces can also help to keep particles attached to the surface, but its effect is much weaker [Allelein, 2009]. If there is liquid material, the surface tension can become the dominant adhesion force. In addition, sintering and chemical bonding can further increase the resistance of the deposit layer. In principle, it is possible to calculate the Van der Waals force for smooth spherical particles. However, it is very sensitive to the particle shape and surface roughness (it has been observed experimentally that adhesion strength decreases an order of magnitude when the surface roughness is increased from 0.2 nm to 0.7 nm), making impossible the direct calculation of the adhesion force in reactor safety applications. Experimentally has been observed that adhesion force approximately follow a log-normal distribution for single particle. Another variable to take into account for thick deposit layers is the particle porosity, resuspension increases with the increase in porosity (increase in the number of contact points as the porosity of the deposit decreases).

The forces detailed above must be overcome so that resuspension occurs. The forces that produce resuspension can be divided into lift forces, which are in the normal direction to the surface, and drag forces, which tend to move parallel to the surface. Drag forces are much stronger than the lift ones. These parallel forces are needed to provide enough energy to overcome the forces holding the particles attached to the surface. Whereas the normal forces, i.e., lift forces have to move particles out of the reach of the conservative forces.

Another important parameter in many resuspension models is the diameter of the deposited particles. From several studies carried out with monolayer deposits, it has been found that the flow rate necessary to cause resuspension decreases as the particle sizes increase, since the drag force affecting the particles increases with size. However, in this case the resuspended particles are large agglomerates that would tend to redeposit

immediately. Consequently, the particles primary size cannot be used directly as a parameter, when resuspension is modeled.

In some studies it has explained that only long-term resuspension is related to the increase in the flow rate. However, other experiments showed that resuspension during acceleration of the flow, even in short term, is significantly reduced. While other studies have found that increasing the flow acceleration the resuspension rate increases in short term, but substantially decreases in the long term, whereby, based on these studies it is concluded that resuspension in short and long term are based on the same phenomenon and cannot be treated separately. Consequently, due to these discrepancies further investigations are needed.

The impact of particles carried by the fluid on the aerosol deposits can significantly increase the resuspension from the surface. The explanation comes from the fact that the momentum of a particle is about three orders of magnitude greater than that of the gas. Experimentally has been found that gas streams containing at least micron particles were substantially more efficient than pure gas flows to cause resuspension of deposited particles. While for submicron particles, no increase in resuspension rate has been shown.

Summarizing, several works, taking into account all the previously mentioned subjects, have been carried out over the last decades, in which monolayer and multilayer resuspension models have been developed [Wen, 1989; Biasi, 2001; Theerachaisupakij, 2003], but some lacks of knowledge have to be filled yet.

5.6. The Containment Influence on Aerosol Behavior

The FPs, actinides and structural materials are released into the containment at different locations and with different timings. All the aerosols enter into the containment through a leak or break before the vessel failure and from the core cavity when the core is melted. In such a way that, the aerosol amount and size distribution differ considerably. During the core degradation phase the highest amount of aerosols is released into the containment, reaching even above 1 g/m^3. The most important variables for the aerosol behavior are the relative humidity, the gas temperature, the condensation rates (wall and volume condensation) and the local atmosphere flow velocity.

The natural circulation, driven by the differences in the local gas densities, dominates the mixing phenomenon that takes place in the containment atmosphere. Only during the initial blow down phase and with H_2 deflagrations the forced convection appears in the containment. Consequently, the aerosol particles are laden by the carrier gas; in such a way that large particles (like condensate droplets) have a noticeable slip ratio with the gas, i.e., reduction of velocity which leads to settling. These condensate droplets drag the deposited aerosols, washing it from the walls (soluble aerosols are washed down more efficiently than insoluble aerosols) and carrying them to the containment sump. This washing down mechanism determines the FP heat distribution between the surfaces and the containment

sump. To make even more difficult the study of the aerosols behavior, part of the aerosols that are washed down to the containment sump, if the water begins to boil, may return to the containment atmosphere.

Agglomeration - deposition processes of aerosols in the containment are important. Growth of aerosols due to agglomeration process is relevant in the containment when the aerosol concentration is not very high (below 1 g/cm^3). Particularly the Brownian agglomeration is the dominant mechanism, being also relevant the gravitational agglomeration, and agglomeration by turbulent inertia and turbulent diffusion. Deposition of aerosols on the containment surfaces depends on geometry, size distribution, density, thermal-hydraulic conditions, etc. Small aerosol particles have considerable deposition by diffusion. Diffusiophoresis is the only important phoretic mechanism in a LWR, being almost independent of aerosol size. Part of these aerosols deposited on the containment surfaces can be resuspended under certain conditions, for instance, H_2 combustion may result in high flow rates near the surfaces, therefore being likely that any of the previously deposited aerosols would be resuspended.

To study the behavior of most of the FPs released into the containment from the core, only the physical phenomena shown previously have to be taken into account. But for two specific cases, iodine and ruthenium, the chemical phenomena have to be considered. Iodine and ruthenium are highly radiotoxic FPs, which can be released to the containment in significant quantities and show a specific behavior. They have a very complex chemistry in their gas and liquid phases; they can react easily with containment structural surfaces (metallic and painted surfaces). In addition, their interactions with air and water radiolysis products, which are present in the containment atmosphere and sump, play an important role too.

As far as iodine is concerned, it can combine with many other FPs (cesium, silver, indium, rubidium and cadmium) and can be present in atomic form (I), molecular form (I_2) and hydroidic acid (HI), all of them in gaseous phase at the conditions of an accident. Even though, the majority of the iodine injected into the containment is washed down to the sump. All of them are soluble, except silver iodide (AgI), the soluble compounds form I^- ions. Due to the large quantity of FPs into the aqueous phase, the radiolysis of water occurs (including OH^-, O_2^-, etc.), then a large number of chemical reactions occur, resulting in the thermally and radiolytic oxidation of the iodine ions into volatile I_2 (depending on several parameters, the most important the pH of water, alkaline media results in very low production of I_2). Added to radiolytic products of water, organic materials are present too (which come from structural paintings). Iodine reacts with organic radicals producing volatile organic iodides, such CH_3I, or low volatile compounds (with high molecular weights). In regard to the insoluble silver iodide, if there is enough excess of silver (which can be released from the silver-indium-cadmium control rods) then the ion iodine concentration reduces, which results in a very low production of molecular iodine.

Regarding ruthenium chemistry, it can be significant in the presence of air, situation which can takes place, for instance, if there is a break in the reactor vessel. The ruthenium

is released mainly in the form of dioxide vapor (RuO_2) in presence of air, when cools down passes to tetroxide vapor (RuO_4), which deposits as solid dioxide, but this reaction is kinetically limiting, so that some part of the ruthenium remains as tetroxide (gaseous in the containment conditions). The final result is that an important ruthenium proportion may be released to the containment and, due to its high radiotoxicity (similar to that of the iodine in the short term and to that of the cesium in the mid-term), it is important to take ruthenium into account.

5.7. Aerosol Behavior in the Secondary Circuit of a PWR

Accidents which involve the secondary circuit of a PWR plant are of two types, accidents in which there are major leaks or complete breaks of one or more SG U-tubes (SGTR accidents) and accidents in which the secondary line breaks (SLB) which almost immediately leads to the rupture of SG tubes (SLB which induces a SGTR). As shown in Section 1.2.2., "Steam Generator Tube Rupture Accident Scenarios", many degradation processes can take place in a SG which can lead to SG tube cracking. Another important subject, also shown on Section 1.2.2., is that in an SGTR accident the containment can be bypassed, because of the blow down of the secondary circuit or via the relief valves of the secondary circuit. Consequently, an open path to the surrounding environment can exist, releasing FP to the atmosphere.

As stated in section 1.2.2., the SGTR event can be spontaneous or induced, for instance, in the risk assessment studies two types of severe accidents involving SGs can occur. Firstly, an operational design basis fault caused by a SGTR scenario with leads to core damage and, secondly, a core damage sequence which brings to high pressure and temperature conditions in the primary circuit that could lead to a SGTR event. During both SGTR accidents, whether spontaneous or induced, the secondary side of the affected SG can be flooded or dry. This has a significant effect on the capture mechanisms, deposit and release of aerosols. In both cases, there are many mechanisms in the secondary side of a SG which can lead to the reduction of the aerosols release, taking for granted that this aerosol release to the environment are smaller in the case of flooded SGs. For instance, the most significant capture mechanisms are: inertial impaction, interception, Brownian diffusion, phoretics (thermophoresis, diffusiophoresis and electrophoretic), condensation, gravitational settling, etc. Among them, the more significant capture mechanisms, either in the secondary side of a SG or in a pool, will be widely studied in the next section.

For these reasons, several European projects have focused to make improvements in understanding the retention mechanisms in the secondary side of SGs, i.e., in the study of SGTR events. For instance, the PSAERO and HORIZON experiments in Finland, the PECA experiments in Spain and ARTIST project in Switzerland have been carried out over the last decades [Allelein, 2009]. In addition, certain models have been developed, in particular the SPARC90-Jet code developed along this PhD work.

5.8. Effects of Thermal-hydraulics on Aerosol Behavior

The thermalhydraulic conditions are of major importance in aerosol behavior in both, primary circuit and containment. Along the next two subsections some clues of the influence of thermalhydraulics on the aerosol behavior will be shown.

5.8.1. Influence of Thermal-hydraulics of the Primary Circuit on Aerosol Behavior

Thermal-hydraulic data are very important to be able to calculate the aerosol transport processes along the primary circuit. In fact, the thermal-hydraulic conditions are input data to perform the calculations of this PhD. work, i.e. pool scrubbing and SGTR events calculations.

Thermal-hydraulic conditions refer to the evaluation of the velocity field of the carrier fluid (usually steam), the temperature field (including the structural temperatures), pressure field, the evaluation of the concentration of the different components of the carrier gas (usually steam and hydrogen) and the concentration of the transported material (including the aerosols, which can have a relative importance in the thermal-hydraulics).

The velocity field is important due to the fact that provides the carrier gas velocity and hence the velocity of the laden aerosols. The velocity field is very important to estimate the particle size distribution. This velocity is determinant in many of the aerosol growth and transport mechanisms (agglomeration, deposition, resuspension, etc.). For example, the greater the velocity field through the primary circuit is, the shorter the time for agglomeration process to occur, which results in a smaller particle size distribution.

The temperature field is important not only for the calculation of the flow velocity field, but for the determination of the carrier gas, aerosol and structural materials properties (thermal conductivity, diffusivity, wall and fluid temperature evolution, etc.).

The pressure field is important for the same reasons that the temperature field, being of special interest the overall systems pressure (containment, primary and/or secondary). For instance, pressure is important in a wide range of aerosol dynamics calculations and in order to determine the condensation temperature of the carrier gas, which leads to biphasic flows, changing the deposition mechanisms behavior.

5.8.2. Influence of Thermalhydraulics of the Containment on Aerosol Behavior

The thermalhydraulic conditions of the containment are important when characterizing the aerosol behavior. The aerosol entering the containment from the melted core through a leak or by a break are made by pressure balancing in the early stages of the accident, whereas in the later phases is accomplished by natural circulation processes.

Condensation processes of aerosols is other of the aspects that has to be considered. Two condensation processes take place, volume and wall condensation. The volume condensation (condensation of steam on the aerosol) appears when the relative humidity is

higher than that of saturation conditions (for hygroscopic aerosols even takes place at somewhat below saturation conditions). This phenomenon differs from one zone to another, more significant near steam sources and close to cold regions.

With regard to wall condensation, aerosols are deposited by diffusiophoresis onto the wall. Wall condensation mainly depends on steam saturation ratio in the containment atmosphere and the difference in temperature between the bulk and wall.

The FP decay heat strongly influences thermal-hydraulics, because they are a considerable heat source. This heat is partially released to the atmosphere, and partly to the containment structures and sump. The decay heat released to the atmosphere decreases the humidity, whereas the heat released to the sump enhances the evaporation (reaching under certain conditions saturation conditions) increasing the humidity. Consequently all these effect has to be considered in order to have a comprehensive and accurate analysis of the aerosol behavior.

5.9. The General Dynamic Equation of Aerosols

The mathematical expression of the aerosol dynamics processes, which takes into account for the major mechanisms of aerosol formation, growth and transport (sorption/desorption, nucleation, condensation, agglomeration, diffusion, etc.). This equation is essentially a mass/population balance into a control volume on the aerosol size distribution and, it is referred to as the general dynamic equation (GDE) for aerosols. The GDE is an integro-differential equation which usually does not have an analytic solution. The GDE gives the changes in the aerosol size distribution over time and position.

The expression of the distribution function that accounts for the balance of the different aerosol species present in the system are [Williams, 1990]:

$$\frac{\partial}{\partial t} n(v,\vec{r},t) = -\nabla\left[\vec{U}(v,\vec{r},t)n(v,\vec{r},t)\right] - \nabla \cdot D_{diff}(v,\vec{r},t)n(v,\vec{r},t)$$
$$-\frac{\partial}{\partial v}\left[I(v,\vec{r},t)n(v,\vec{r},t)\right] + \frac{1}{2}\int_0^v K(u,v-u,\vec{r},t)n(v-u,\vec{r},t)\,du \qquad \textbf{Eqn. (5.1)}$$
$$-n(v,\vec{r},t)\int_0^\infty K(u,v,\vec{r},t)n(v,\vec{r},t)du + Q(v,\vec{r},t)$$

where $\vec{U}$ is the vector sum of the fluid and particle velocities; D_{diff} is the diffusion coefficient; $I(v,\vec{r},t)$ is the rate of increase/decrease in volume of the particle due to condensation/evaporation; $K(u,v,\vec{r},t)$ is the coagulation kernel factor, which accounts for the agglomeration rate of a particle of volume u with another with volume v; $Q(v,\vec{r},t)$ is a source term which came from the FP release and which also can be due to homogenous

nucleation. Point that $\vec{U}$ and D_{diff} depend on the total particle volume, the parameters U, D_{diff}, I, K and Q depend on position and time.

As it has been told earlier, the GDE does not have an analytic solution in most of the realistic cases. Given the complexity of solving the GDE several approaches have been developed over the years, for instance, discrete, spline, modal and sectional approaches, from which the lasts two are the most commonly used.

For the modal approach the distribution function of the aerosol sizes is evaluated using analytic functions which represent the different domains or the modes of the distribution. The analytic functions are arbitrarily chosen, but the lognormal and the gamma distribution functions are the most commonly used. The most important disadvantages of this approach are that the aerosol distribution form is imposed so as the number of modes. Whereas the major advantage is that the number of variables is reduced, only three variables are needed (particle number, geometric median diameter and standard deviation) to describe each mode.

In the case of the sectional approach, the continuous aerosol size distribution is divided in a finite number of class sizes or bins. Within each of these bins an aerosol property is held constant, which depends on the goals of the study. In nuclear applications, mass conservation is one of the main parameters for a correct evaluation of the source term, consequently, the distribution function is usually expressed in terms of mass, assuming constant aerosol density.

Summarizing, in order to determine the evolution of the size distribution of the aerosols along their path through the primary circuit the general dynamic aerosol equation has to be solved, and then all the different phenomena presented throughout the previous sections have to be taken into account. Even though, for the calculations of the SPARC90-Jet code, up to the present moment, only the initial size distribution of aerosols is needed. Consequently, this initial distribution has to be previously known or must be determined, so it is important to study the different processes which lead to the aerosol size distribution just before the break or the discharge nozzle, in order to be able to accurately characterize them.

5.10. The Aerosol Size Distribution

Summing up everything mentioned throughout this chapter, the main contributions to aerosols, of the different elements present in the core, are uranium, tin (oxide from Zircaloy oxidation), silver, cadmium, indium and fission products contribution (typically between 10 and 40 %). According to several researchers [Kissane, 2008; Allelein, 2009; Lind 2010b] the typical aerosol composition is, in approximately in equal parts, metal (Ag, In and/or Cd from 15 to 40 %, if they are part of the control rod materials), metal oxide (tin oxide, uranium dioxide and zirconium dioxide) and a mixture of fission product species (great diversity of compounds: metal oxides, salts, ternary compounds, hydroxides, etc.). This

aerosols composition will be base for any of the potential LWR accident sequences. Most of the materials transported to the hot leg are multi-component aerosols, with mainly the exception of iodine (mainly in gaseous/vapor form). Whereas, for the cold leg, all materials are transported in aerosol form, also with the exception of iodine, in gaseous/vapor form too.

In nuclear accident scenarios, the number of aerosol particles carried by the gas stream can be very high, exceeding 10^{13} particles / m^3. Consequently, it is almost impossible to predict aerosol behavior by calculating the dynamics of individual particles. Instead of individual calculations, aerosols must be considered in a collective sense, that is to say, aerosols have to be taken as a continuous or discrete distribution of particle sizes.

Regarding to their size and structure the information is less reliable, but for the hot leg, it seems that these particles are relatively compact agglomerates with aerodynamic mass median diameter (AMMD) of approximately 1–2 μm, a standard deviation of about 2 and with a near-lognormal distribution. These statements are confirmed by the PHÉBUS test measurements, which were carried out at 700 ºC in the hot leg during fission product tests. Recent ARTIST tests indicated that, when aerosol agglomerates bigger than a determined size suffer a large shear force, their size distribution shift towards smaller stable sizes, for instance, agglomerates of an initial mass median diameter of 3-4 μm suffered de-agglomeration up to 2 μm, from this value, further de-agglomeration did not happened [Allelein, 2009].

Finally, in order to determine the aerosol distribution function in a pool discharge or at a break in a SG the log-normal distribution can be used. This distribution function fits well the available data for the size distribution of aerosols subjected to particle growth by agglomeration and gravitational deposition onto surfaces in quasi-steady state conditions. The probability density for particles having sizes in the interval ϕ_p to $\phi_p + d\phi_p$ is:

$$f_v(\phi_p) = \frac{1}{\sqrt{2\pi}Ln\lambda}\exp\left[-\left(\frac{Ln\phi_p / \mu}{\sqrt{2}Ln\lambda}\right)^2\right]dLn\phi_p \qquad \textbf{Eqn. (5.2)}$$

being

μ the mean particle size

λ the geometric standard deviation

In order to estimate the capacity of the aerosols capture mechanisms, an initial distribution of aerosol sizes has to be implemented in the input file of the code. So consequently, these values of the aerosol sizes are important parameters to be determined. This aerosol size distribution function is obtained by knowing or estimating the mean aerosol size and its geometric standard deviation and from these two parameters the probability density of each aerosol size interval is obtained, Eqn. (5.2), or knowing the exact aerosol size distribution. The predictions for the distribution of aerosol sizes made by

several codes can also be used, for instance, SOPHAEROS' code results. As a first approximation, typical values of the lognormal parameters can be used to determine the probability density of the aerosol sizes too, for instance, mean particle sizes of 2 μm and geometric standard deviation of 2.

5.11. Summary of the Release and Transfer Processes of FPs from the Core to the Environment

In summary, the sequence of processes involved in the release and transfer of the FPs from the core to the environment during a severe accident with core melting is shown in Figure 5.5.

As shown in Figure 5.5, the release of FPs from the core depends on several aspects (mainly fuel type and boundary conditions during the accident), which determine the nature, magnitude and timing of the released FPs. Then, these FPs scatter through the primary coolant circuit, in which several variables (boundary conditions in the RCS, chemical interactions and chemical reactions among them and with the surfaces of the RCS) affect their original nature, magnitude and timing. Once they are in the primary circuit, the FPs, can be released to the containment, through leakage or a break in the RCS. Or even can bypass the containment and reach the surrounding areas of the NPP, for instance, in a severe accident of a PWR with a break in the SG the aerosols can be released through a relief valve of the secondary circuit. If the FPs does not bypass the containment, several mechanisms can change once again their nature, magnitude and timing. The boundary conditions of the containment, the chemical interactions or chemical reactions of FPs and the mitigation means used are of major importance to determine the distribution of FPs. In the containment, after the failure of the vessel, the behavior of FPs is affected by the presence of new aerosols from boiling of sump water or by the aerosol interactions with the concrete. Finally, if a containment failure or bypass takes place (for instance, leakage, filtered venting or melting of the concrete basemat) the FPs are released to the environment.

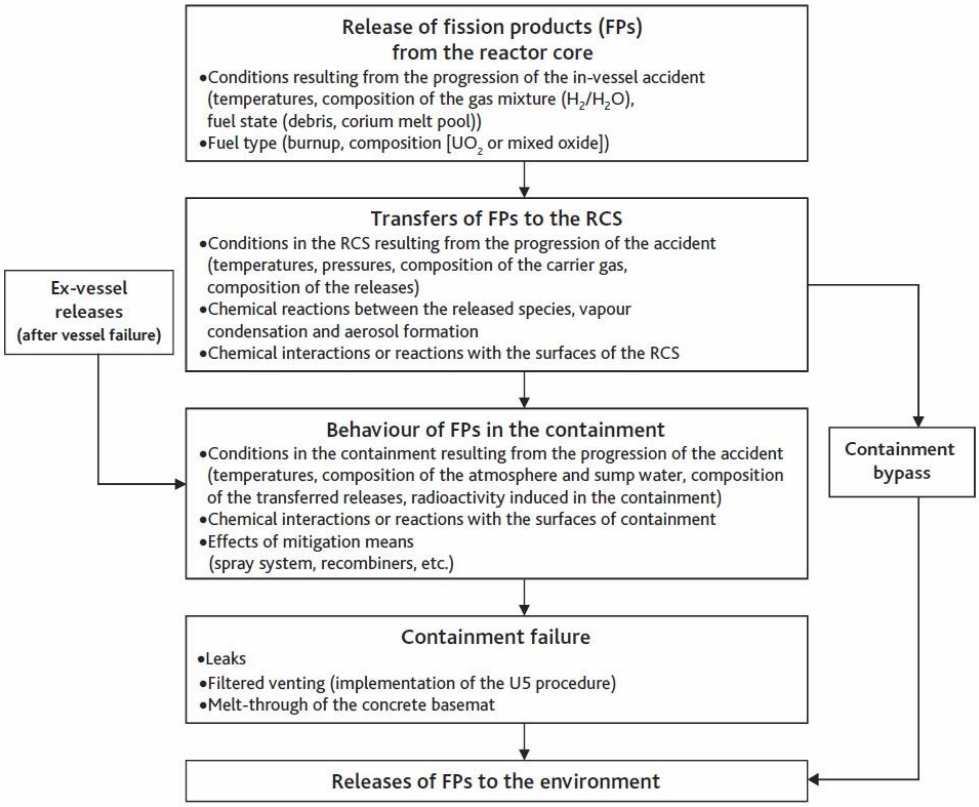

Figure 5.5. Release and transport of FPs from the core to the environment [Jacquemain, 2015].

NUREG-1465 of the US-NRC, as a result of its research efforts in severe accident sequences, proposes the existence of five general phenomenological phases in an accident progression, similar for all NPPs despite the differences in plant design and accident sequences [Soffer, 1995]. These five general phases or progression stages of a severe LWR accident are:

- Coolant Activity Release, begins with a postulated break or leak in the RCS which cannot be accommodated by the reactor core cooling systems. The phase ends with the fuel cladding failure.

- Gap Activity Release, the phase begins with the commence of the fuel cladding failure. The loss of fuel geometry accompanied by the gradual melting and slumping of the core materials to the bottom of the core vessel leads to the total release to the containment of noble gases and significant fractions of volatile FPs (like iodine and cesium) accumulated during operation in the fuel cladding gap and fuel rod plenums.

- Early In-Vessel Release, starts when the release of FP's to the containment is significant. Their amounts are strongly influenced by the residence time of the radioactive materials within the RCS during core degradation. This phase comprises the core degradation and ends with the failure of the bottom head of the reactor vessel.

- Ex-Vessel Release, starts when the molten core debris exits out of the reactor vessel (core debris expelled from the reactor vessel into the reactor cavity and subsequent failure of the bottom head of the reactor vessel). In such a way that, the release of FPs come mainly from the molten core debris interaction with the structural concrete, but also could include releases caused by high pressure melt expulsion phenomena and even ex-vessel steam explosions.

- Late In-Vessel Release, usually takes place simultaneously with the previous phase but with a longer duration. During this phase continues the release of radionuclides from the core into the containment. And additionally, starts the release of part of the FPs, which previously were deposited in the RCS during the early in-vessel phase.

These five phases of a severe accident have a specific duration and involve the release of inventories of FPs depending on the accident progression, which depends on the type of plant (BWR or PWR), the plant design, the type of accident, etc. In table 5.3 the duration of the five phases using MELCOR 1.8.5. code for BWR and PWR reactors is displayed, further information is shown in SANDIA report SAND2011-0128 [Powers, 2011]. For the development of the source term a wide variety of accident sequences in both BWR (Grand Gulf and Peach Bottom plants) and PWR (Surry and Sequoyah plants) reactors have been considered, further data are available in the SANDIA laboratory document [Powers, 2011].

Table 5.3. Comparison of source terms for high and low burnups and BWR and PWR reactors [Powers, 2011].

Phases	BWR		PWR	
	Low-Burnup	High-Burnup	Low-Burnup	High-Burnup
Gap Release	0.2 ± 0.03	0.16 ± 0.01	0.33 ± 0.12	0.22 ± 0.04
Early In-Vessel Release	8.8 ± 1.1	8.0 ± 1.1	5.3 ± 1.2	4.5 ± 2.4
ExVessel Release	1.6 ± 0.5	2.9 ± 0.8	9 ± 10	4.8 ± 1.3
Late In-Vessel Release	12 ± 2	12 ± 2	130 ± 20	143 ± 8

* Uncertainties refer to the estimation of medians with nonparametric statistics applied to a small set of the accident analyses

Chapter 6

AEROSOL CAPTURE MECHANISMS – THE DECONTAMINATION FACTOR

6. AEROSOL CAPTURE MECHANISMS – THE DECONTAMINATION FACTOR

This chapter is an extended and updated version of the third section of the paper "Enhancement of the SPARC90 code to pool scrubbing events under jet injection regime", published in Nuclear Engineering and Design, Vol. 300, pp. 563-577, 2016 [Berna, 2016].

Introduction

The aerosols produced during the accident, whose formation and growth processes were described in the previous chapter, can escape from the primary circuit of a LWR and might escape to the environment.

Though, if there is a water volume in the aerosols escape pathway, a discharge in the shape of submerged jet can occur, whether in a suppression pool (during an accident with loss of power, SBO, in a water reactor boiling BWR) or in the secondary of a steam generator (in an accidental breakage sequence tube / s in U in a steam generator, SGTR, in a pressurized water reactor, PWR). So that there is a capture of aerosols in those volumes, being reduced the amount of them that escape outside. Usually these sequences have been considered only for BWRs and for low discharge velocities, but these may also take place at higher velocities and, as mentioned previously, in PWRs.

In particular these aerosols can escape during a SGTR (steam generator tube rupture) event in a PWR. This kind of accidents might be a major source of accidental release of radioactive aerosols into the surrounding environment due to its potentiality to by-pass the reactor containment. During these accidents the aerosols interact and form particles which grow in size due to vapor condensation, coagulation and agglomeration of the colliding particles. All these agglomeration/break-up processes occur mainly within the transporting flow, much greater length traveling inside the pipes of the primary circuit until the break is reached than in the secondary of the SG. But not only the aerosol particles can suffer these processes, also the entrained water droplets, due to relative motion among them, have the opportunity to collide. In this case only the jet region has to be considered. The secondary side of the SG has a good potential for aerosol scrubbing along these tube rupture accidents. Several capture processes take place during these scrubbing events, the most important of them are usually the mechanical interactions between particle-droplet (inertial impaction, interception and Brownian diffusion), but under certain circumstances other processes can be relevant, such are, the phoretic processes (thermophoresis, diffusiophoresis, electrophoresis). For all these processes the aerosol characteristics, i.e., size, shape, hygroscopicity, etc., are the key factors for the effectiveness of these removal processes, playing gas hydrodynamics an essential role too.

Throughout this section the main aerosol capture mechanisms will be described, along with all aspects related to aerosols interactions and between aerosol- water droplets, also discussing the interactions between the own water droplets.

6.1. The Aerosol Capture Mechanisms

Once the aerosols size distribution function has been characterized, the next step will consist in determining the main capture processes that can take place, i.e. the collection mechanisms.

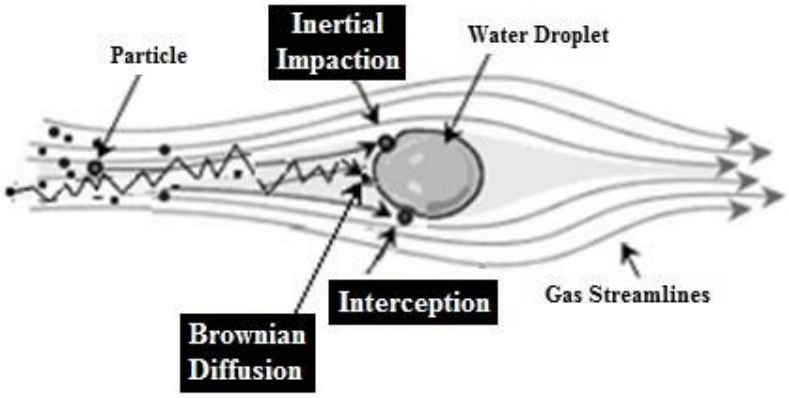

Figure 6.1. Sketch of droplet-particle mechanical interaction.

Single droplet may collect particles by using one or more of the several collection mechanisms, such as inertial impaction, interception, Brownian diffusion, electrostatic attraction, diffusiophoresis, thermophoresis, etc. Although all these capturing mechanisms might play some role in the scenario under consideration, at the present stage of the work the attention has been focused on those related to droplet-particle mechanical interactions (Figure 6.1), that is: inertial impaction, interception and Brownian diffusion. This has been done in this way because, in some publications is shown that the main contribution to collection efficiency consists of these three mechanisms [Slinn, 1983]. In Figure 6.2, it is shown a typical curve of the collection efficiency versus aerosol particle size of a particle removal device. In this figure, it is seen that within the mechanical collection mechanisms, Brownian diffusion dominates for small aerosols, sizes smaller than 0.1 μm, being very unimportant to sizes greater than 1.0 μm and insignificant for particles larger than 10 μm. Similarly, interception becomes more important in the vicinity of the μm, losing importance in favor of inertial impaction for larger values.

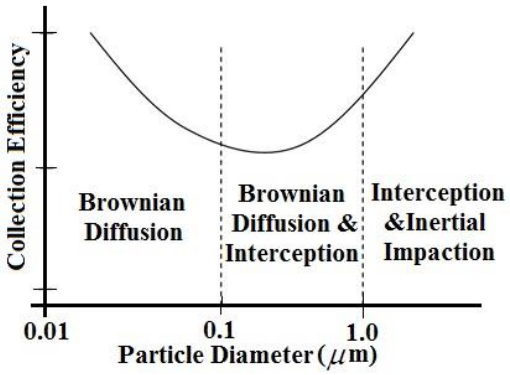

Figure 6.2. Sketch of droplet-particle mechanical interaction.

To calculate the collection efficiency two main ways are possible, one consist of consider that the collection mechanisms are independent, that is to say, the total contribution can be regarded as the sum of each particle removal mechanism, then the collection efficiencies are additive:

$$\eta = \sum_{\substack{all \\ mechanisms}} \eta_{mechanism} \qquad \textbf{Eqn. (6.1)}$$

Which is the simplest expression to calculate the particle removal, but independency of the collection efficiency is not completely true. So, it is needed to consider the coupling among the different aerosol capture mechanisms, this coupling has been done taking into account the combined effects by each mechanism sequentially [Allelein, 2009]:

$$\eta = 1 - \prod_{\substack{all \\ mechanisms}} \left(1 - \eta_{mechanism}\right) \qquad \textbf{Eqn. (6.2)}$$

Despite that only the contributions of the three main capture mechanisms have been considered in this doctoral work, a section has been devoted to the presentation of some of the remaining capture mechanisms, which under certain conditions can be important. Given that them might be taken into consideration in future code improvements.

The expressions presented throughout this section for aerosol scrubbing by the entrained droplets have been taken from the domain of wet scrubbers, as droplet hydro conditions are probably closer to submerged jets than the annular flow ones.

6.1.1. Inertial Impaction

The aerosol particles tend to driven away from the obstacles, in our case the entrained droplets, following the streamlines. But, if the inertia of these carried particles is high enough, they have trajectories which depart from the streamlines. Consequently, heavy

particles might be removed from the carrier flow due to sudden changes of direction caused by the presence of obstacles. Particle inertial would make them move away the gas streamlines and eventually collide with the obstacle.

Among the different available expressions in the literature, many of them have been tested, for instance the widely used, Calvert equation [Rudnick, 1986]:

$$\eta_{impact} = \left(\frac{Stk_p}{Stk_p + 0.35} \right)^2 \qquad \textbf{Eqn. (6.3)}$$

This expression is valid for high relative velocities, which for the case of gas between 20 to 160 m/s, highlight that this expression was originally developed for scrubbers. But, finally the one proposed by Slinn [Flagan, 1988], which is more elaborated and provides better results, has been the employed here,

$$\eta_{impact} = \left(\frac{Stk_p - S_{impact}}{Stk_p + \frac{2}{3} - S_{impact}} \right)^{3/2} \left(\frac{\rho_d}{\rho_p} \right)^{1/2} \qquad for\ Stk_p > S_{impact} \qquad \textbf{Eqn. (6.4)}$$

where

$$S_{impact} = \frac{1.2 + \frac{1}{12} Ln\left(1 + \frac{\mathrm{Re}_d}{2} \right)}{1 + Ln\left(1 + \frac{\mathrm{Re}_d}{2} \right)} \qquad \textbf{Eqn. (6.5)}$$

where Stk_p is the particle Stokes number [Crowe, 2006],

$$Stk_p = \frac{C_c \rho_p \phi_p^2 (u_g - u_d)}{9 \mu \phi_d} \qquad \textbf{Eqn. (6.6)}$$

being C_c the Cunningham slip-correction factor, which has several possible expressions for its calculation, but all of them are quite similar, being their general form:

$$C_c = 1 + \frac{2\lambda}{\phi_p} \left[A_1 + A_2 \exp\left(- A_3 \frac{\phi_p}{\lambda} \right) \right] \qquad \textbf{Eqn. (6.7)}$$

several possibilities for the values of coefficients A_1, A_2 and A_3 are shown in Table 6.1. In which λ is the gas mean free path and ϕ_p is the flow reference length-scale, which is equal to the obstacle diameter. The quotient between λ and ϕ_p is usually called the momentum transfer Knudsen number:

$$Kn = \frac{2\lambda}{\phi_p} \qquad \textbf{Eqn. (6.8)}$$

Table 6.1. Coefficients of the Cunningham Correction Factor.

Author	A_1	A_2	A_3
Crowe [Crowe, 2006]	1.17	0.525	0.39
Jung [Jung, 2002]	1.247	0.42	0.435
Davies, [Davies, 1945]	1.257	0.4	0.55

For air at $1.01 \cdot 10^5$ Pa (1 atm) and 293 K (20°C) the mean free path is $\lambda_{ref} = 0.0664$ μm, while for air at other conditions the following formula can be used, it was proposed by Willeke [Crowe, 2006],

$$\lambda = \lambda_{ref}\left(\frac{1.01\cdot 10^5}{P}\right)\cdot\left(\frac{T}{293}\right)\cdot\left(\frac{1+\frac{110}{293}}{1+\frac{110}{T}}\right) \qquad \textbf{Eqn. (6.9)}$$

where pressure, P, is in Pa and temperature, T, in K. For other gases, different from air, an accurate determination of the mean free path from kinetic theory via Eqn. (6.9) is difficult. It is possible to resort to the theory that relates the mean free path to gas macroscopic properties. A good approximate formula is

$$\lambda = \left(\frac{\mu_g}{P}\right)\cdot\left(\frac{\pi RT}{2M}\right)^{1/2} \qquad \textbf{Eqn. (6.10)}$$

where P is the gas pressure in kPa, R is the Universal gas constant (kJ/k mole-K) and M is the gas molecular weight in kg/kmol and T the temperature in K. Using this expression for air molecules at ambient conditions (T = 298 K, P = 10^5 Pa and $\mu_g = 1.8\cdot 10^{-5}$ kg m^{-1} s^{-1}) the mean free path is $\lambda_g = 6.51\cdot 10^{-8}$ m.

Another quite different expression for the mean free path is obtained through the consideration of the number of target objectives and their cross sectional area:

$$\lambda = \frac{1}{\sqrt{2}\, n\, \sigma} \qquad \textbf{Eqn. (6.11)}$$

where n is the number of target molecules per unit volume, and σ is the cross sectional area for collision:

$$\sigma = \pi\, d_{colis,mol}^2 \qquad \textbf{Eqn. (6.12)}$$

being the molecular cross sectional area $\approx 10^{-19}$ m^2 at ambient conditions.

Langmuir [Pulley, 1997] presented his results for Venturi scrubbers. For potential flow around a spherical drop (drop Reynolds number $Re_d \to \infty$) he proposed the following expression:

$$\eta_{impact,p} = \left(\frac{Stk_p}{Stk_p + 0.5} \right) \qquad \textbf{Eqn. (6.13)}$$

Whereas for viscous flow ($Re_d \to 0$):

$$\eta_{impact,v} = \left[1 + \frac{0.75 Ln(2Stk_p)}{(Stk_p - 1.214)} \right]^{-2} \qquad \textbf{Eqn. (6.14)}$$

In most applications the selection of the appropriate flow field to the situation is quite easy, for instance in spray towers the droplets quickly accelerate to high Reynolds numbers and consequently the potential flow equation is used. But, for example, in the Venturi scrubbers the droplets initially have a high relative velocity to the gas but then they are accelerated towards gas velocity, that is, the flow field therefore changes as the drop passes through the Venturi. Langmuir suggested an interpolation formula for the transition between viscous and potential flow to estimate the collection efficiency due to inertial impaction:

$$\eta_{impact} = \frac{\left[\eta_{impact,v} + \eta_{impact,p} (Re_d / 60) \right]}{\left[1 + (Re_d / 60) \right]} \qquad \textbf{Eqn. (6.15)}$$

This equation assumes that the collection efficiency is the arithmetic mean of $\eta_{impact,p}$ and $\eta_{impact,v}$ at a Reynolds number of 60.

Another similar expression for inertial impaction in spray systems is presented in Allelein et al. [Allelein, 2009], but in this case the viscous and potential terms are as follows:

$$\eta_{impact,p} = \begin{cases} 0 & for\ Stk_p \le 0.08334 \\ 8.57 \left(\dfrac{Stk_p}{Stk_p + \delta} \right)^2 (Stk_p - 0.08334) & for\ 0.08334 < Stk_p < 0.2 \\ \left(\dfrac{Stk_p}{Stk_p + \delta} \right)^2 & for\ Stk_p \ge 0.2 \end{cases} \qquad \textbf{Eqn. (6.16)}$$

$$\eta_{impact,v} = \begin{cases} 0 & for\ Stk_p \le 1.214 \\ \dfrac{1}{\left(1 + \dfrac{0.75\,Ln(2\,Stk_p)}{Stk_p - 1.214}\right)^2} & for\ Stk_p > 1.214 \end{cases} \qquad \textbf{Eqn. (6.17)}$$

being δ an uncertainty constant, $0.25 < \delta < 0.75$.

6.1.2. Interception

The collection mechanism by interception is an extension of the inertial impaction mechanism. Interception takes place when aerosol particle radius is larger than distance between the streamline followed by the aerosol particle and the surface of the obstacle (in the present case, the water droplets). Lots of expressions are available in the open literature and, many of them have been tested in the present work, for instance the Zhao and Zheng's correlation [Zhao, 2008], Slinn's correlation [Flagan, 1988], etc.

A simple expression is the one proposed by Zhao and Zheng [Zhao, 2008], in which the collection efficiency produced by interception is modeled by next expression

$$\eta_{intercep} = \left(1 + \frac{\phi_p}{\phi_d}\right)^2 - \frac{\phi_d}{\phi_d - \phi_p} \qquad \textbf{Eqn. (6.18)}$$

Another expression to the interception mechanism, a little bit elaborated, is the proposed by Slinn among other authors [Zhao, 2006]. The expression is as follows:

$$\eta_{intercep} = 4\frac{\phi_p}{\phi_d}\left[\frac{\mu_g}{\mu_l} + \left(1 + 2\left(\frac{\mathrm{Re}_d}{2}\right)^{1/2}\right)\frac{\phi_p}{\phi_d}\right] \qquad \textbf{Eqn. (6.19)}$$

Finally the selected correlation was the one proposed by Jung and Lee's [Jung, 1998], which is as follows:

$$\eta_{intercep} = \frac{1-a}{J + bK}\left[\frac{\phi_p/\phi_d}{1 + \phi_p/\phi_d} + \frac{1}{2}\left(\frac{\phi_p/\phi_d}{1 + \phi_p/\phi_d}\right)^2 (3b + 4)\right] \qquad \textbf{Eqn. (6.20)}$$

where $a = \left(r_d/r_g\right)^3$ being r_d is the sphere radius and r_g is the boundary radius (jet radius);

$b = \dfrac{\mu_l}{\mu_g}$; $J = 1 - \dfrac{6}{5}a^{1/3} + \dfrac{1}{5}a^2$ and $K = 1 - \dfrac{9}{5}a^{1/3} + a + \dfrac{1}{5}a^2$.

Following the same path as in the previous section, in Allelein's work [Allelein, 2009] it is shown the following correlations:

$$\eta_{intercept} = \frac{\left[\eta_{intercept,v} + \eta_{intercept,p}\left(\mathrm{Re}_d / 60\right)\right]}{\left[1 + \left(\mathrm{Re}_d / 60\right)\right]} \qquad \textbf{Eqn. (6.21)}$$

being in this case the viscous and potential terms as follows:

$$\eta_{intercep,v} = \left(1 + \frac{\gamma \phi_p}{\phi_d}\right)^2 \left[1 - \frac{1.5}{\left(1 + \frac{\gamma \phi_p}{\phi_d}\right)} + \frac{0.5}{\left(1 + \frac{\gamma \phi_p}{\phi_d}\right)^2}\right] \qquad \textbf{Eqn. (6.22)}$$

$$\eta_{intercep,p} = \frac{3\gamma \phi_p}{\phi_d} \qquad \textbf{Eqn. (6.23)}$$

Brockmann [Allelein, 2009] has reviewed information available on dynamic and collision shape factors in reactor containment atmospheres. He concludes that in humid environments where spheroidization occurs, collision shape factor, γ, can vary between 1 and about 4.

6.1.3. Brownian Diffusion

Brownian motion is the random movement of particles suspended in a fluid; these particles collide among themselves and with the particles of the fluid. Due to the Brownian diffusion of particles the droplets can capture small particles of aerosols by diffusion. In this case several expressions have been tested too. For instance the one of Zhao and Zheng [Zhao, 2006], which is as follows

$$\eta_{j,k}^{diff} = \frac{4}{\left(\frac{\mathrm{Re}_{d,j}}{2}\right) Sc_k} \left[1 + 0.4\left(\frac{\mathrm{Re}_{d,j}}{2}\right)^{1/2} Sc_k^{1/3} + 0.16\left(\frac{\mathrm{Re}_{d,j}}{2}\right)^{1/2} Sc_k^{1/2}\right] \qquad \textbf{Eqn. (6.24)}$$

where the Schmidt number is

$$Sc_k = \frac{\mu_g}{\rho_g D_{diff,k}} \qquad \textbf{Eqn. (6.25)}$$

and the diffusion coefficient

$$D_{diff} = \frac{K_b T C_c}{3\pi \mu_g \phi_p} \qquad \textbf{Eqn. (6.26)}$$

where K_b is the Boltzmann constant (=1.38054×10^{-23} J/K); T is the gas absolute temperature; C_c is the particle Cunningham slip-correction factor, defined in Eqn. (6.7).

Finally the correlation selected to consider the collection efficiency by this diffusion motion is the one given by Jung and Lee [Jung, 1998]. They obtained an analytic solution for a multiple fluid sphere system using the extended Kuwabara free vorticity model which includes the effects of induced internal circulation inside a liquid droplet and of neighboring collectors.

The diffusion efficiency for the solid sphere system (b→∞) is given by

$$\eta_{diff} = 2\left(\frac{3\pi}{4Pe}\right)^{2/3}\left[\frac{(1-a)}{K}\right]^{1/3} \qquad \textbf{Eqn. (6.27)}$$

the coefficients a, b and K are defined as in the impaction mechanism and Pe is the Peclet number, which is defined as,

$$Pe = \frac{\phi_d u_d}{D_{diff}} \qquad \textbf{Eqn. (6.28)}$$

being D_{diff} as defined in Eqn. (6.26).

So far, it has been obtained the Brownian diffusional collection efficiency for the cases of solid spheres (b→∞). For the liquid sphere case whose viscosity ratio is intermediate, it does not appear to be possible to obtain an analytic expression. Therefore, it would be taken a path for obtaining a semi-empirical correlation equation. The possibilities to the values of the viscosity ratio, $b = \frac{\mu_l}{\mu_g}$, are:

- b ≥ 100,

$$\eta_{diff} = 2\left(\frac{\sqrt{3}\pi}{4Pe}\right)^{2/3}\left[\frac{(1-a)(3b+4)}{J+bK}\right]^{1/3} \qquad \textbf{Eqn. (6.29)}$$

- 100> b > 1,

$$\eta_{diff} = 0.7\left[\frac{4}{\sqrt{3}}\left(\frac{1-a}{J+bK}\right)^{1/2} Pe^{-1/2} + 2\left(\frac{\sqrt{3}\pi}{4Pe}\right)^{2/3}\left[\frac{(1-a)(3b+4)}{J+bK}\right]^{1/3}\right] \qquad \textbf{Eqn. (6.30)}$$

- $b \leq 1$ (bubble case),

$$\eta_{diff} = \frac{4}{\sqrt{3}}\left(\frac{1-a}{J+bK}\right)^{1/2} Pe^{-1/2} \qquad \textbf{Eqn. (6.31)}$$

where the coefficients a, b, J and K are defined as in the previously, the same as in the case of the Peclet number. Remark that the expression which has been used in the present PhD work is the second one, viscosity ratio between 1 and 100, which is the case of water droplets traveling into the gaseous jet.

For this second case Kim et al. [Kim, 2001] uses the Jung and Lee's expression, but for the calculation of the Cunningham slip correction factor uses the Lee and Liu's expression:

$$C_c = \begin{cases} \dfrac{3.328\lambda}{\phi_p} & for\ \ Kn > 2.6\ \ or\ \ \phi_p < 0.05\,\mu m \\ 2.609\sqrt{\dfrac{2\lambda}{\phi_p}} & for\ \ 1.5 < Kn < 2.6\ or\ 0.05 < \phi_p < 1.0\,\mu m \end{cases} \qquad \textbf{Eqn. (6.32)}$$

expression which distinguishes depending on the Knudsen number and the particle size.

6.1.4. Collection Efficiency by Other Mechanisms

Theoretically, Slinn's formula is likely to underestimate the collection efficiency since it includes only a subset of the mechanisms that influence particle collection. This expression only takes into account the three main mechanisms, but in fact the other mechanism can be important to droplets smaller than 1 micrometer. A number of studies have suggested that thermophoresis, diffusiophoresis, and electric charges may increase the collection efficiency for particles in the 0.01−1 μm diameter range.

6.1.4.1. Thermophoresis

Thermophoresis, which is caused by uneven heating of particles in ambient temperature gradients, drives particles towards evaporating and sublimating hydrometeors. The thermophoresis occurs when the collection surface, in our case the entrained droplet, is at a substantially lower temperature than the aerosol carried by the gas stream. This thermophoretic force is more important in the warmer area; consequently, this imbalance produces a force that drags the particles towards the cold droplets.

Then, the collection efficiency of this mechanism can be written in terms of a temperature parameter and two coefficients depending on the Knudsen number [Porcheron, 2011]:

$$\eta_{thermoph} = 4K_{TA}f_h\left(T_g - T_s\right)\frac{\mu_g}{\rho_g T_g V_{thermoph}\ \phi_d} \qquad \textbf{Eqn. (6.33)}$$

where

K_{TA} is the thermophoresis coefficient (depending on the ratio of the atmosphere thermal conductivity to particles thermal conductivity)

f_h is the ventilation coefficient

V_{therm} is the thermophoretic velocity (is a terminal velocity)

The so called Talbot interpolation formula, employed for the calculation of the thermophoretic deposition velocity, is as follows:

$$V_{thermoph} = \frac{\dfrac{2\mu_g C_s(\nu)}{\rho_g \chi}\left(\dfrac{k_g}{k_p} + C_t Kn\right)}{(1+3C_m Kn)\left(1+\dfrac{2k_g}{k_p}+2C_t Kn\right)} \nabla LnT \qquad \textbf{Eqn. (6.34)}$$

where

$C_s = 1.128$

$$C_m = \frac{(2-\alpha_m)}{\alpha_m}$$

$$C_t = \frac{15}{8}\frac{(1-\alpha_t)}{\alpha_t}$$

α_m is the momentum accommodation coefficient

α_t is the thermal accommodation coefficient

k_g is the thermal conductivity of the gas phase

k_p is the thermal conductivity of the aerosol particles

Kn is the Knudsen number, defined in Eqn. (6.8).

According to Andronache et al. [Andronache, 2006], which works are centered in the study of the scavenging of ultrafine particles of rainfall, the thermophoretic and contribution to collection efficiency can be expressed as follows:

$$\eta_{thermoph} = \frac{4\alpha_{th}\left(2+0.6\,\mathrm{Re}^{1/2}\,\mathrm{Pr}^{1/3}\right)\left(T_g - T_s\right)}{V_{thermph}\ \phi_d} \qquad \textbf{Eqn. (6.35)}$$

where

T_g is the gas jet temperature [K]

T_s is the temperature of the droplet surface [K]

$V_{thermphp}$, is the droplet terminal velocity [m/s]

α is given by $\alpha_{th} = \dfrac{2C_c\left(k_g + 5\lambda/\phi_p k_p\right)k_g}{5P\left(1+6\lambda/\phi_p\right)\left(2k_g + k_p + 10\lambda/\phi_p k_p\right)}$

C_c is the particle Cunningham slip-correction factor

k_g thermal conductivity of gas jet [J/m*s*K]

k_p thermal conductivity of particle [J/m*s*K]

P pressure [Pa]

λ the mean free path of gas molecules [m]

Pr is the Prandtl number of gas $\mathrm{Pr} = \dfrac{c_p \mu_g}{k_g}$

c_p heat capacity of gas [m^2/s^2*K]

In the particular case under study, severe accident in a nuclear reactor, such temperature differences can be quite large in the coolant system. Consequently, very hot aerosols and gases emerge from the core region of the reactor and encounter large areas of cool surface. So the contribution of this capture mechanism can be significant under certain circumstances.

6.1.4.2. Diffusiophoresis

Diffusiophoresis moves particles towards diffusionally-growing hydrometeors due to water vapor concentration gradients. When a concentration gradient exists, the aerosol moves in the diffusion flux direction of the heavier gas component. This gradient appears in the steam condensation processes, in particular, occurs when condensation takes place on cold water, inducing a steam flow towards the droplets.

This mechanism is not usually encountered under reactor accident scenarios, since the condensation of large amounts of vapor on surfaces does not take place. Although, diffusiophoresis can takes place in the containment under accident conditions.

The diffusiophoretic collection efficiency can be written as [Porcheron, 2011]:

$$\eta_{diphusioph} = 4 f_h \frac{\sqrt{M_w}}{X_i \sqrt{M_i} + X_w \sqrt{M_w}} \frac{D}{u_w \phi_d} Ln\left(\frac{P - P_{sat}}{P_g}\right) \qquad \textbf{Eqn. (6.36)}$$

where

f_h is the ventilation coefficient

M_w is the water molecular weight [kg/mol]

M_i is the water molecular weight of the aerosol i [kg/mol]

X_i is the molar fraction of the aerosol i

X_w is the water molar fraction

D is the diffusion coefficient [m^2/s]

P is the pressure [Pa]

Another expression to estimate the diffusiophoretic contribution to the collection efficiency proposed by Andronache et al. [Andronache, 2006], which has been developed for the study of the scavenging of ultrafine particles of rainfall. Their expression is:

$$\eta_{diffusioph} = \frac{4\beta_{dph}\left(2 + 0.6\,\mathrm{Re}^{1/2}\, Sc_w^{1/3}\right)\left(\frac{p_s^0}{T_s} - \frac{p_g^0\, RH}{T_g}\right)}{V(\phi_p)\phi_d} \qquad \textbf{Eqn. (6.37)}$$

where

p_s^0 vapor pressure of water at temperature T_s [Pa]

p_g^0 vapor pressure of water at temperature T_g [Pa]

RH relative humidity [%]

β is given by $\beta_{dph} = \frac{T_g D_{diff,water}}{P}\sqrt{\frac{M_w}{M_g}}$

$D_{diffwater}$ water vapor diffusivity in the gas [m^2/s]

M_w water molecular weight

M_g gas molecular weight

Sc_w is the Schimdt number for water in gas, $Sc_w = \frac{\mu_g}{\rho_g D_{diff,water}}$

6.1.4.3. Electrical Charge

Deposition of aerosol carried by the gas stream may be enhanced due to electrophoresis; this capture mechanism is a complex process which depends on aerosol decay activity, size, concentration and confining geometry. The radioactive aerosols can be electrically charged, due to the dominance of α decay (this kind of processes generally strip out electrons from the aerosol particles) whereas in β- decay a positive charge develops though very small particles that can develop a small negative charge.

The contribution of electric charge to the collection efficiency is based on the concept that a droplet with a charge Q_r attracts an aerosol particle with an opposite charge q_p and this process enhances the capture efficiency by the raindrop of aerosol particles close to the raindrop's surface [Wang, 2010]. The electrostatic collection efficiency is expressed as

$$\eta_{ec} = \frac{16KC_cQ_rq_p}{3\pi\mu_gV(\phi_p)\phi_d^2\phi_p} \qquad \textbf{Eqn. (6.38)}$$

where

$K=9x10^9$ [Nm^2/C^2]

Q_r mean charge of the droplets [C]

q_r mean charge of the particles [C]

Q_r and q_r are assumed to be opposite charges

A parameterization has been proposed for the mean droplets and particles charges:

$$Q_r = a\alpha\phi_d^2 \Leftrightarrow q_r = a\alpha\phi_p \qquad \textbf{Eqn. (6.39)}$$

where

$a=0.83x10^{-6}$

α [C/m^2] is an empirical parameter that varies between 0, which corresponds to neutral particles, and 7, which corresponds to highly electrified particles (corresponding to highly electrified clouds with thunderstorms [Andronache, 2006]).

6.2. Particle-Particle Interactions

Understand particle interactions are of particular interest in the case of submerged jets, because in the above studied capture mechanisms it is considered that an entrained droplet can capture an aerosol particle depending on many parameters. A key parameter, in almost all the expressions of the different aerosol capture mechanisms, is the size of both the obstacle and the laden particle. Consequently, the initial size distribution and its evolution must be determined for both, droplets and aerosols.

6.2.1. Aerosol-Aerosol Interactions

As shown in chapter 5 "Release and Transport of Fission Products – Aerosol Formation and Growth" aerosols suffer a great variety of complex processes along their path through the primary system. Aerosols change in size and form, from their formation up to their release, taking place both chemical and physical phenomena. Consequently, a major parameter that must be determined is the initial aerosol size in the discharge process and it also can be of interest to study the importance of aerosol interactions throughout this process.

The agglomeration / de-agglomeration processes take place due to the relative motion between aerosol particles. This relative motion can be caused by several reasons, for instance, the Brownian motion, fluid inhomogeneities (such turbulence or external forces, like Van der Waals, electrostatic or gravitational forces). These collisions can lead to the formation of bigger particles, i.e., agglomerates or clusters, or it can lead to the aerosol break-up in smaller particles, de-agglomeration mechanisms. Examples of agglomeration mechanisms are the Brownian agglomeration, gradient agglomeration, turbulent agglomeration, diffusional agglomeration, etc. The break-up of agglomerates can be mainly caused by the aerodynamic stresses acting on them.

The different possibilities, in order to take into account the aerosol sizes, are to consider: an aerosol constant size as a starting point (usually the discharged aerosols are characterized by their mean size value); to use as a input an aerosol size distribution function, a log-normal distribution function is the widely used (Appendix I); and, the most complex way, to try to estimate effects of agglomeration / de-agglomeration processes which take place as the submerged jet evolves (i.e., start with an aerosol size distribution function which changes as the jet spreads downstream). At the present stage of the SPARC90-Jet code development an aerosol size distribution function is used as input.

6.2.2. Droplet-Droplet Interactions

The different relative velocity of the entrained droplets dragged by the gas stream due to their size, shape, moment of extraction from the gas liquid interface, etc., creates the opportunity for droplet collisions.

The collision between water droplets does not necessarily result in the droplet coalescence. When water droplets collide they may recoil, splatter or otherwise be disrupted. The greatest diversity of collision behaviors occurs for droplets when they are nearly of equal size. A criterion for coalescence is that the collision energy has to be less than 15 ergs ($1.5 \cdot 10^{-6}$ J). In the case of submerged jets, this condition is usually not reached, so a collision efficiency has to be considered. But even when the energy criterion is satisfied, the efficiency with which collision of droplets results in coalescence is not unity. A commonly cited expression for efficiency collection for coalescence during water droplet collisions is [Powers, 1993]:

$$\eta_{collision} = \frac{\phi_d(i)^2}{[\phi_d(i)+\phi_d(j)]^2} \quad for\ \phi_d(i) > \phi_d(j) \qquad \textbf{Eqn. (6.40)}$$

This expression for the collision efficiency leading to droplet coalescence indicates that the minimum efficiency is 0.25. But experimental measurements show that lower efficiencies can occur, Figure 6.3. In particular, the collection efficiency by collision falls below the calculated with the Eqn. (6.40) when droplets are of similar size. An alternate expression, which is also shown in the figure, is given by:

$$\eta_{collision} = \begin{cases} 1 - \dfrac{8\phi_d(j)}{\phi_d(i)} & for\ \phi_d(j)/\phi_d(i) < 0.125 \\ 0 & otherwise \end{cases} \qquad \textbf{Eqn. (6.41)}$$

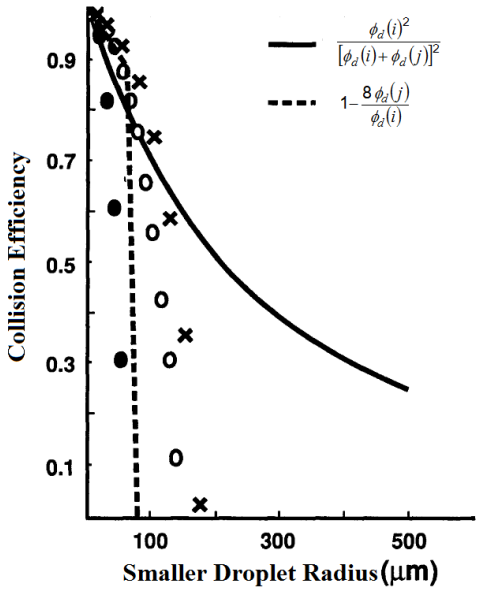

Figure 6.3. Comparison of Collection Efficiency of a 500 μm droplet.

In summary, modeling the phenomena involved in droplet collisions is very difficult due to the high variety of potential outcomes. Nevertheless, in further SPARC90-Jet code enhancement, it might be investigated the consequences on the droplet size distribution in the submerged jet. Even though, up to this moment, a mean value of the entrained droplets depending on the jet and surrounding area conditions is considered. The different possibilities to consider the sizes of the entrained droplets are: a constant size depending on the jet and surrounding water conditions (section 3.2 "Droplet Sizes", in which the different expressions found in the open literature for annular flow are shown); to use a droplet size

distribution function, a log-normal distribution function, as for the case of aerosols, is the widely used (Appendix I); and, the most elaborated way, to estimate the effect of droplet-droplet collisions in the evolution of the droplet size distribution.

6.3. The Decontamination Factor

The usual way to estimate the scrubbing efficiency has been in terms of a Decontamination Factor (DF), which is defined by as the ratio of the aerosol mass flow rate entering the system to the one that goes out of the system,

$$DF = \frac{\dot{m}_{in}}{\dot{m}_{out}} = \frac{1}{1-\eta} \qquad \textbf{Eqn. (6.42)}$$

being η the particle collection efficiency $\left(\eta = \dot{m}_{ret}/\dot{m}_{in}\right)$.

6.3.1. Building the Overall Decontamination Factor

Owing to the decontamination process is composed of several stages, the particles DF of a given size is the product of the elementary DF's corresponding to each stage or cell:

$$DF = \prod_n DF_n(k) \qquad \textbf{Eqn. (6.43)}$$

being k the particle size index and n the stage number.

In the general case, the system inlet, the airborne fission products corresponds to a particle distribution whose size is due to the deposition, transportation and characteristics of the upstream primary circuit. For experimental systems particle distribution depends on the aerosol generator. The usual assumption is that there is no interaction between particles of different sizes (the transit time is too short to allow significant agglomeration) and all decontamination mechanisms are linear (no effect of aerosols on gas and liquid velocity fields). Consequently, it is not necessary to know the airborne concentration of each size class, just knowing the mass fraction.

Let $F_0(k)$ be the mass fraction at the inlet of the particles of a given size. Then the overall DF is given by:

$$\frac{1}{DF} = \frac{\dot{m}_{out}}{\dot{m}_{in}} = \frac{1}{\dot{m}_{in}} \sum_k \dot{m}_{in}(k) \frac{\dot{m}_{out}(k)}{\dot{m}_{in}(k)} = \sum_k F_0(k) \cdot \frac{1}{DF(k)} \qquad \textbf{Eqn. (6.44)}$$

being,

$$F_0(k) = \frac{\dot{m}_{in}(k)}{\dot{m}_{in}} \qquad \textbf{Eqn. (6.45)}$$

The mass fraction at any other stage is given by:

$$F(k)=\frac{\dot{m}_{out}(k)}{\dot{m}_{out}}=\frac{\dot{m}_{out}(k)}{\dot{m}_{in}(k)}\frac{\dot{m}_{in}(k)}{\dot{m}_{out}}=\frac{1}{DF(k)}\cdot DF\cdot F_0(k) \qquad \textbf{Eqn. (6.46)}$$

6.3.2. Inertial Capture by the entrained Droplets of the Submerged Gas Jet

In the Epstein model, the fundamental mechanism in the inertial capture by the entrained droplets is the velocity difference between the gas phase and the liquid droplets.

The airborne mass in the class size k collected by an individual droplet per second is:

$$\dot{m}_{jk}(z)=-\frac{\pi\phi_{d,j}^2}{4}\left[u_g(z)-u_{d,j}(z)\right]\cdot c_p(k,z)\cdot\eta_{jk}(z) \qquad \textbf{Eqn. (6.47)}$$

where $\phi_{d,j}$ is entrained droplet diameter with discrete size class j, $c_p(k,z)$ is the mass concentration of particles in the size class k at the axial location z and η_{jk} is the collection efficiency of particles in the size class k by the droplets of class j.

Assuming now that there is no screening between the droplets, the mass flow rate of particles in the size class k collected within an axial mesh z, z+dz is:

$$d\dot{M}_k(z)=-\sum_{j=1}^{n(z)}N_{d,j}(z)\cdot\dot{m}_{jk}(z)\cdot dV \qquad \textbf{Eqn. (6.48)}$$

where n(z) is the droplet size distribution in the axial position z and dV is a gas jet differential volume, $dV=\pi R^2(z)dz$.

Then, the mass of airborne particles of size class k collected by the water droplets per unit time and length is:

$$\frac{d\dot{M}_k(z)}{dz}=-\sum_{j=1}^{n(z)}\frac{\pi\phi_{d,j}^2}{4}\left[u_g(z)-u_{d,j}(z)\right]\cdot\eta_{jk}(z)\cdot c_p(k,z)N_{d,j}(z)\pi R^2(z) \qquad \textbf{Eqn. (6.49)}$$

The mass flow rate of airborne particles of size class k which are dragged by the gas jet through the gas surface is:

$$\dot{M}_k(z)=\pi R^2(z)\alpha(z)u_g(z)\,c_p(k,z) \qquad \textbf{Eqn. (6.50)}$$

Dividing Eqn. (6.49) by Eqn. (6.50):

$$\frac{1}{\dot{M}_k(z)}\frac{d\dot{M}_k(z)}{dz}=-\sum_{j=1}^{n(z)}\frac{\pi\phi_{d,j}^2}{4}\frac{\left[u_g(z)-u_{d,j}(z)\right]}{\alpha(z)u_g(z)}\cdot\eta_{jk}(z)N_{d,j}(z) \qquad \textbf{Eqn. (6.51)}$$

defining,

$$\gamma(k,z)=\sum_{j=1}^{n(z)}\frac{\pi\phi_{d,j}^2}{4}\frac{\left[u_g(z)-u_{d,j}(z)\right]}{\alpha(z)u_g(z)}\cdot\eta_{jk}(z)N_{d,j}(z) \qquad \textbf{Eqn. (6.52)}$$

Then,

$$\frac{d\dot{M}_k(z)}{\dot{M}_k(z)}=-\gamma(k,z)dz \qquad \textbf{Eqn. (6.53)}$$

Integrating,

$$\left[Ln\dot{M}_k(z)\right]_{z_i}^{z_i+\Delta z}=-\int_{z_i}^{z_i+\Delta z}\gamma(k,z)dz \qquad \textbf{Eqn. (6.54)}$$

Consequently,

$$\dot{M}_k(z_i+\Delta z)=\dot{M}_k(z_i)\exp\left(-\int_{z_i}^{z_i+\Delta z}\gamma(k,z)dz\right) \qquad \textbf{Eqn. (6.55)}$$

Finally the DF in the stage i:

$$\frac{\dot{M}_k(z_i)}{\dot{M}_k(z_{i+1})}=\exp\left(+\int_{z_i}^{z_i+\Delta z}\gamma(k,z)dz\right)=DF_i(k) \qquad \textbf{Eqn. (6.56)}$$

Decontamination Factor, DF, of airborne particles of size class k is eventually estimated as the product of individual contributions of each axial node (i):

$$DF(k)=\frac{\dot{M}_k(z_1)}{\dot{M}_k(z_2)}\frac{\dot{M}_k(z_2)}{\dot{M}_k(z_3)}\cdots\frac{\dot{M}_k(z_n)}{\dot{M}_k(z_{n-1})}=\prod_{i=1}^{N}DF_i(k)=$$
$$=\exp\left(\sum_{i=1}^{N}\int_{z_i}^{z_i+\Delta z}\gamma(k,z)dz\right)\approx\exp\sum_{i=1}^{N}\gamma(k,z_i)\Delta z_i \qquad \textbf{Eqn. (6.57)}$$

being γ(k,z) defined in Eqn. (6.52).

6.4. Summary of Aerosol Capture

Throughout this chapter the aerosol collection mechanisms have been studied, in particular, the following mechanisms have been analyzed: inertial impaction, interception, Brownian diffusion, electrostatic attraction, diffusiophoresis, and thermophoresis. Focusing

on those related to droplet-particle mechanical interactions, i.e. inertial impaction, interception and Brownian diffusion, due to the fact that they are considered to be the dominant mechanisms under the conditions of the present work.

Consequently, the collection efficiency of these three mechanisms has been considered to be not fully independent so consequently coupling has been considered. With regard to inertial impaction, which is the dominant mechanism for particles larger than 1 μm approximately, the widely used Calvert's expression has been studied among others, Eqn. (6.3) to Eqn. (6.17). For particles smaller than 0.1 μm the Brownian diffusion is the dominant mechanism, several expressions have been studied too, Eqn. (6.28) to Eqn. (6.32). Whereas for the interception mechanism, which is important for intermediate particle sizes, the expressions analyzed are displayed from Eqn. (6.18) to Eqn. (6.23). Information of other mechanisms has been collected too, but only the three mechanisms of mechanical interactions have been taken into consideration from this moment on. Remind that all these expressions come mostly from wet scrubbers, as there are not specific expressions which were developed for the study of aerosol capture processes in submerged jets.

The current chapter continues with other possible interactions, in particular, section 2 gives some clues about particle-particle and droplet-droplet interactions, bringing to light other aspects susceptible to be taken into account in future works.

The chapter ends with the calculation of the aerosol scrubbing efficiency, based on the aerosol capture mechanisms, section 3. This aerosol collection efficiency is determined from the decontamination factor (DF), which is the ratio of aerosol mass flow rate entering-going out of the system, Eqn. (6.43), it can also been obtained from the collection efficiency. In summary, the DF has been estimated for each of the particle classes using the Epstein's model, i.e., as the product of the contributions in each calculation node, Eqn. (6.57), and finally, the overall DF is obtained from the addition of each particle class averaged with its mass fraction, Eqn. (6.44).

Chapter 7

ORIGINAL SPARC90 AND NEW SPARC90-JET CODES

7. ORIGINAL SPARC90 AND NEW SPARC90-JET CODES

This chapter is an extended and updated version of the fourth and fifth sections of the paper "Enhancement of the SPARC90 code to pool scrubbing events under jet injection regime", published in Nuclear Engineering and Design, Vol. 300, pp. 563-577, 2016 [Berna, 2016].

Introduction

The modelling of pool scrubbing made by the original SPARC90 code has been based on splitting the aqueous bulk in two main regions: the entrance zone and the bubble rise zone (Figure 7.1a). While, the new developed SPARC90-Jet code extends the above description by adding a new way of modeling particle removal phenomena at the entry region (Figure 7.1b). To do so, the submerged gas jet responsible for particle injection has to be hydrodynamically described.

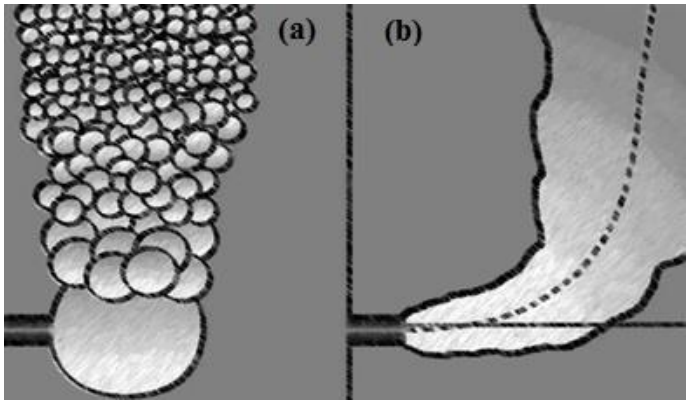

Figure 7.1. Schematic View of the two existing conceptual approaches: (a) Globular Regime; (b) Jet Injection Regime.

7.1. The Original SPARC90 code

Several specific codes for pool scrubbing were developed from the middle 80s until the early 90s, such are SPARC90 [Owczarski, 1991], BUSCA [Ramsdale, 1991] and SUPRA [Wassel, 1985]. All of them modeled gas injection under the "globule regime", so that gas-liquid interactions under jet injection regime are missing.

The SPARC90 (Suppression Pool Aerosol Removal Code) was developed by the Pacific Northwest Laboratory (PNL) as a prototypical code. This initial code version was

developed to calculate the aerosol capture by the wet well of a BWR during accident events in which aerosol scape from the degraded core. Throughout the following years the code improvements were carried out.

The SPARC90 code is written in FORTRAN. The code needs an input file, in which should be included, among others, the geometric and thermo-hydraulic conditions of the pool and the thermo-hydraulic conditions and composition of the injected gas. From these data SPARC90 calculates the total DF, and the decontamination factor as a function of aerosol particle size. From this input file the code provides an output file, which consists of two parts: a copy of the input file and the output calculations. The calculated output also consists of two parts: the essential information about the particle size distribution at the pool surface, and the bubble parameters and other information related to the overall particle distribution and gas conditions.

The SPARC90 code incorporates five aerosol scrubbing models and two thermal-hydraulic models [Owczarski, 1985]. The aerosol scrubbing process is described by: convective flows from the condensation of steam, growth of soluble particles by water vapor sorption, gravitational settling (sedimentation), inertial deposition due to circulation of the bubble surface and diffusional deposition. The thermal-hydraulic model consists of two parts, in the first one, the model for the equilibrium pool temperature is described. This is the steady-state temperature of the pool in thermal and vapor equilibrium with the gas leaving the pool. The second part is the model for steam evaporation into the bubble as it rises. This incoming steam is the result of the steam maintaining vapor equilibrium as the bubble rises. This steam influx retards all particle deposition mechanisms, and it is especially important in pools near the boiling point.

All these models have been designed and applied for the determination of aerosol pool trapping during vent discharge processes in the suppression pools of BWR reactors under severe accident conditions. Such discharge occurs at low gas velocities. However, there are accident sequences, like SGTR core meltdown sequences, at which particle laden gases reach the aqueous ponds at very high velocities and new particle removal mechanisms become effective right at the nozzle or break inlet.

A qualitative discussion of hydrodynamic processes, thermal-hydraulic processes and retention mechanisms associated with aerosol capture when passing through the suppression pool from a submerged vent to the pool surface is shown in this section, consult the code manual for detailed information [Owczarski, 1991].

7.1.1. Hydrodynamic Processes

In SPARC90 the inlet gases can enter into the pool through a variety of vents in the various BWR systems. During steady flow, the gases leaving the vent form large globules that break up into a swarm of small bubbles within a few globule diameters from the vent (Figure 7.2). The size of the initially formed globule depends on the vent type (e.g., horizontal vent, downcomer, or T-quencher) and it also depends on the composition of the

gas flow rate (condensable versus non-condensable fraction of gases). Just after the injection, the unstable globule breaks up as it rises.

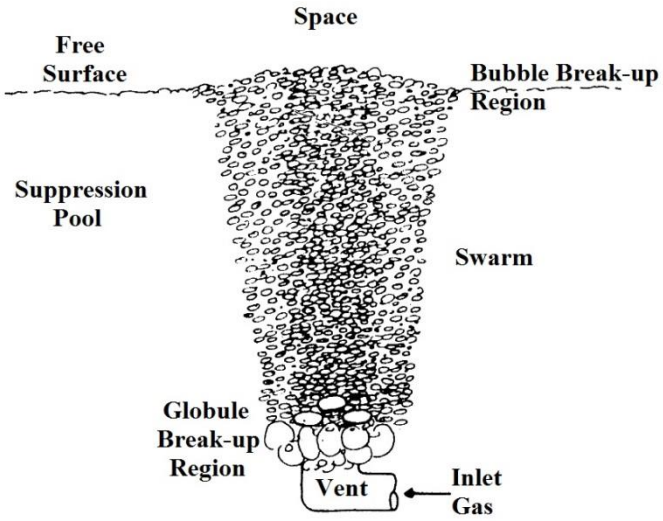

Figure 7.2. Schematic View of Suppression Pool During Scrubbing.

7.1.2. Thermalhydraulics

Three different aspects of thermal hydraulics are involved in the SPARC90 calculations: heat transfer to/from the gas phase, mass transfer to/from the gas phase, and the work of the expanding gas phase as the bubble rises. The thermal hydraulics of these pool/gas interactions also affects particle capture mechanisms.

Regarding to heat transfer, it is considered that the gas entering the pool through the vents rapidly equilibrates to the pool temperatures it breaks up into bubbles. When the entering gas is in hot dry conditions, it evaporates water from the pool and hinders particle capture, whereas high steam fractions in the inlet gas would enhance particle capture.

As the bubble swarm rises throughout the rising plume, vapor transfers into the bubble to try to maintain vapor equilibrium. This entering vapor not only hinders particle capture by the pool, but also adds to the swarm volume and provides more steam for particle growth by condensation.

The condensation processes of water vapor on particles occur if the vapor pressure of the bubble is greater than the vapor pressure of wet particles. Dissolved particles have lower vapor pressure than wet insoluble particles; therefore, the growth potential of soluble particles exists even under sub-saturated atmospheres.

7.1.3. Aerosol Capture Mechanisms

The aerosol capture mechanisms which take place during the swarm formation are caused by the following events:

- Excess steam (above the pool vapor pressure) condensation moves particles to the surface.

- Vent exit gas temperatures higher than pool temperatures, which cause thermophoretic deposition.

- High vent exit velocities, which cause inertial impaction on the water pool.

- Bubble formation, which involves curved surface motion and potential particle capture.

The aerosol removal during the bubble rise period is caused by inertial deposition, sedimentation and diffusion. The shape that best represents the stable bubbles during this rise period is an oblate spheroid, the larger bubbles are flatter than the smaller ones. For each bubble size, the relative velocity of gas to liquid determines his shape. This relative velocity greatly aids the aerosol capture processes. These capture processes are: by centrifugal forces, by the destruction of the diffusion boundary layers of the outwardly diffusing particles (Brownian) and the inwardly diffusing water vapor.

The effectiveness of iodine species capture in a suppression pool has been considered separately in the SPARC90 code. The main conclusions that can be extracted are the facts that I_2 and Hl would be captured with high DFs, and organic iodides would be captured lightly until the pool was saturated.

7.1.4. The Entrainment Process

The water-aerosol droplets are produced when swarm bubbles break up at the pool surface forming new aerosol particles. If the entrainment particle production rate multiplied by duration times pool concentration produces significant quantities of aerosol radionuclides from materials previously trapped in the pool, an entrainment model should be included. However, due to the insignificancy of this process no entrainment model has been included in the code.

7.2. The Enhanced SPARC90 Code Implementation

The SPARC90-Jet model, presented in the previous sections, has been implemented as a subroutine of the original SPARC90 Fortran code [Owczarski, 1991]. This section outlines the fundamentals, major hypotheses and changes introduced into the code in order to estimate particle removal during gas injection in pools under jet regime. To do so, a simplified and reliable approach to submerged jet hydrodynamics has been intended to describe both the gas-liquid and the drop-particles interactions. This section summarizes this update process of the SPARC90 code and the way in which the code is organized to capture the phenomena which take place under high velocity injection conditions (SPARC90-Jet). It is basically based on the state-of-the–art equations for jet

hydrodynamics and aerosol removal (remind that the old version was only developed for low velocity injection regimes) presented earlier.

7.2.1. The SPARC90-Jet Organization and Development

Regarding the programming of the SPARC90-Jet, when the jet option is activated the new subroutine of the SPARC90-Jet is called, this subroutine continues to be active until gas jet velocity is below the onset of the entrainment zone, moment in which is considered that the gaseous jet extinguishes. From this point, the code performs the same calculations as the original code, that is, the rising plume decontamination factor, although starting from different conditions. But with a significant difference, in our case, the globule formation region has been removed, consequently only the rising plume in which the bubbles evolve with a single diameter to represent the swarm exists, for non-condensable gases this value corresponds to the volume mean diameter, i.e. 0.72 cm.

The structure of the SPARC90-Jet is sequentially programmed in two main different parts: hydrodynamics and aerosol scrubbing by droplets. In order to implement the expressions developed in sections 2 and 3 within SPARC90, the jet entrainment zone is split in a number of nodes (Figure 7.3).

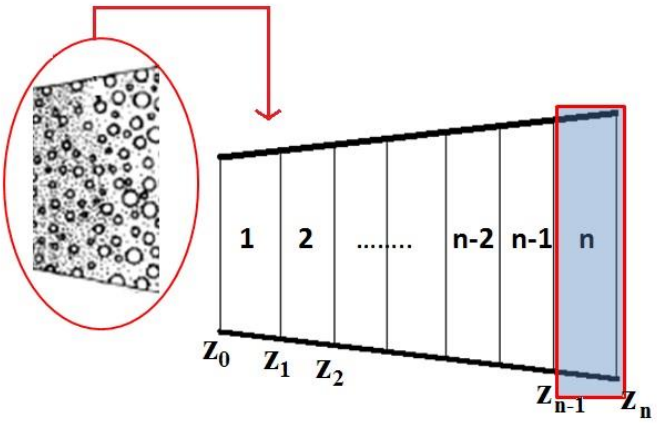

Figure 7.3. Schematic view of the jet nodalization.

The new subroutines of the SPARC90 code have been implemented in a highly modular way in FORTRAN programming language (through Visual Studio).

The SGTR subroutine contains the encoding of the model. The rest of subroutines contain auxiliary variables and perform intermediate calculations. It is highly modular, because all the input variables and all the intermediate calculations generated through the model have been packed in separate modules (Table 7.1). Each one of them includes specific functions related to the nature of the variables under study. The total number of

subroutines are 13 (1 the main subroutine and 12 auxiliary which are called for intermediate calculations).

Table 7.1. Structure of the subroutine SGTR.

Subroutine	**Description**
SGTR	Main subroutine, from which all other subroutines are called, in it all the intermediate steps are implemented.
thermal	Calculates the gas jet and water properties according to the variables introduced with the input file
cc	Calculates the jet critical values, difference between critical or subcritical conditions
ifss	Calculates the interfacial friction factor and the interfacial shear stress and from these values the gas and liquid Reynolds numbers, the surrounding liquid velocity and the perturbed liquid film thickness
eiv	Calculates the entrainment inception velocity, velocity under which no entrainment is possible
ed	Calculates the droplet entrainment, the entrainment mass flux of each cell is calculated in this subroutine
ds	Calculates the droplet sizes, this subroutine calculates the diameter of the entrained droplets in each cell
dv	Calculates the droplet velocities, this subroutine calculates the velocities of the entrained droplets the current cell
moco	This subroutine solves the momentum conservation equation, giving as a result the new value of the submerged jet velocity in each cell
dvvf	Calculates the droplet velocities of the previous cell in the current cell and the void fraction of the current cell
edc	Calculates the variables related with the mass and number of droplets total number of entrained droplets in the current cell (total mass of droplets, total number of droplets, concentration of droplets)
realconc	Calculates the droplets from the previous cell which still remain in the current cell
newcdce	Calculates the collected mass per second in each cell, giving the Decontamination Factor of the current cell, internally this subroutine calculates the contribution of each of the collection mechanisms considered

7.2.2. The Code Input and Output Files

This section provides details of the SPARC90-Jet input and output files. In particular, the organization of the input file and his requested variables, which are needed for the code calculation. The output file organization and the variables which are provided by this file are also shown in this section.

7.2.2.1. The Input File Organization and Requirements

The input file is read in using a free-field format. The data entered in this file consist of pool conditions (physical parameters existing in the pool), inlet gas composition and conditions, aerosol particle properties, mass flow rate of the inlet particles and carrier gas, and SPARC-90 calculation parameters (vent parameters, calculation steps parameters, etcetera). An example of an input file is shown in Appendix II.

7.2.2.2. The Output Files Description

In the output file are shown many variables, see Appendix II. The code prints six variables concerning the pool exit conditions as function of the particle bin number (remind that maximum bin number is 20), i.e.:

- particle dry diameter
- particle wet diameter
- particle mass flow rate, dry
- particle mass flow rate, wet
- number of particles
- particle bin Decontamination Factor DF

In addition, other 18 quantities are displayed, among others: number of median particle radii (wet and dry), particle geometric standard deviation, overall DF, etcetera.

Additionally, the new code version provides an extra file in which the main variables concerning the jet hydrodynamics are displayed. These key variables are: the values of the stagnation and the critical pressures; the values of the entrainment inception velocity (above which no entrainment can takes place); the velocity profile throughout the jet; and, the main characteristics of the entrained droplets (i.e., diameter, velocity, entrainment mass, number and void fraction).

7.2.3. Solving of the Conservation Equations by the Code

The determination of the axial velocity profile is a key issue to characterize the gaseous jet. To achieve this modeling, the Epstein model [Epstein, 1990] has been used as a starting point. This model considers three conservation equations: gas mass conservation, liquid mass conservation and momentum conservation.

Attending to the entrained droplets, say that total amount of droplets dragged by the gas stream in the cell n, $\dot{m}_l(n)$, is given by:

$$\dot{m}_l(n) = (2\pi \bar{R}(z)\Delta z)\ \rho_l v_e(n) \qquad \textbf{Eqn. (7.1)}$$

where $v_e(n)$ is the entrainment velocity in the cell n (this velocity is an effective drag velocity, that is to say, the extraction velocity of droplets minus the deposition velocity of droplets), this velocity is obtained from Ricou and Spalding theory [Ricou, 1961]

$$v_e(n) = e_0\, u_g(n) \sqrt{\frac{\rho(n)}{\rho_l}} \qquad \textbf{Eqn. (7.2)}$$

where the entrainment coefficient, e_0, varies from 0.058 to 0.116, and the density in cell n, $\rho(n)$, is given by

$$\rho(n) = \alpha(n)\rho_g + [1-\alpha(n)]\rho_l \qquad \textbf{Eqn. (7.3)}$$

then, the liquid mass conservation equation can be written as:

$$\frac{d}{dz}\left[\rho_l(1-\alpha(z))u_l(z)\pi R^2(z)\right] = 2\pi \bar{R}(z)\rho_l v_e(z) \qquad \textbf{Eqn. (7.4)}$$

being $\bar{R}(z)$ the average jet radius of each cell.

Integration over the limits of node n (z_{n-1}, z_n) yields to:

$$\rho_l(1-\alpha(n))u_l(n)R^2(n) - \rho_l(1-\alpha(n-1))u_l(n-1)R^2(n-1) = 2\bar{R}(n)\rho_l v_e(z)\Delta z \qquad \textbf{Eqn. (7.5)}$$

from where, taking into account that the liquid phase velocity ,u_l, is the droplet velocitiy, u_d. Then, solving for the liquid fraction one has

$$(1-\alpha(n)) = (1-\alpha(n-1))\frac{u_d(n-1)R^2(n-1)}{u_d(n)R^2(n)} + \frac{2\, v_e(n)\bar{R}(n)\Delta z}{u_d(n)R^2(n)} \qquad \textbf{Eqn. (7.6)}$$

The continuity condition imposes that the product of the entrained droplet velocities by the cell radius squared in adjacent cells are very similar, therefore Eqn. (7.6) can be written as:

$$(1-\alpha(n)) = (1-\alpha(n-1)) + \frac{2\, v_e(n)\bar{R}(n)\Delta z}{u_d(n)R^2(n)} \qquad \textbf{Eqn. (7.7)}$$

Applying this recurrence relation along the submerged jet[7],

$$(1-\alpha(n)) = \sum_{k=1}^{n} \frac{2\, v_e(k)\bar{R}(k)\Delta z}{u_d(k)R^2(k)} \qquad \textbf{Eqn. (7.8)}$$

Solving from the previous equation the void fraction the following expression is reached

$$\alpha(n) = 1 - \sum_{k=1}^{n} \frac{2\, v_{e,j}(k)\bar{R}(k)\Delta z}{u_{d,j}(k)R^2(k)} \qquad \textbf{Eqn. (7.9)}$$

Moreover, there is the gas jet momentum conservation equation, which is given by

$$\frac{d}{dz}\left[(1-\alpha(z))\rho_l u_l^2(z)\pi R^2(z)\right] + \frac{d}{dz}\left[\alpha(z)\rho_g u_g^2(z)\pi R^2(z)\right] + \tau_{friction} 2\pi R(z) = 0 \qquad \textbf{Eqn. (7.10)}$$

being $\alpha(z)$ the void fraction, $u_l(z)$ the liquid velocity, $u_g(z)$ the gas velocity, R(z) the jet radius, all of them in the axial coordinate z, and $\tau_{friction}$ is the friction shear stress force between the gas jet and the surrounding water.

The first term in Eqn. (7.10) is due to the momentum flux of entrained droplets, the second is due to the gas momentum flux and the third term is produced by the friction losses.

Note that several assumptions have been made: jet conical shape; no phase change and constant velocity along the radial coordinate; a gas jet expansion zone is considered, in which pressure equals the pool pressure [Bubnov, 1998].

Integration of the Eqn. (7.10) over cell n gives:

$$(1-\alpha(n))\rho_l u_l^2(n)R^2(n) + \alpha(n)\rho_g u_g^2(n)R^2(n) + \tau_{friction} 2\bar{R}(n)\Delta z = (1-\alpha(n-1))\rho_l u_l^2(n-1)R^2(n) + \alpha(n-1)\rho_g u_g^2(n-1)R^2(n-1) \qquad \textbf{Eqn. (7.11)}$$

Moreover, at the inlet region, the initial gaseous jet momentum is given by:

[7] In the general case, in which a droplet size distribution function would be considered in each cell, the Eqn. (7.9) will be written as:

$$\alpha(n) = 1 - \sum_{j=1}^{N_{sizes}} \sum_{k=1}^{n} \frac{2\, v_{e,j}(k)\bar{R}(k)\Delta z}{u_{d,j}(k)R^2(k)}$$

$$M_0 = \rho_0 u_0^2 \, \pi R_0^2 \qquad \textbf{Eqn. (7.12)}$$

being the gas density along the submerged gaseous jet equal to the inlet gas density, $\rho_g = \rho_0$ (actually not at the nozzle exit, but just after the initial jet expansion).

Therefore, it can be written for any cell n:

$$(1-\alpha(n))\rho_l u_l^2(n) R^2(n) + \alpha(n)\rho_g u_g^2(n) R^2(n) + \sum_{k=0}^{n} \tau_{friction,k} \, 2\,\bar{R}(k)\Delta z = \rho_0 u_0^2 R_0^2 \qquad \textbf{Eqn. (7.13)}$$

By substituting the expression of the void fraction, Eqn. (7.8), in the above equation and dividing by R^2 (n) one has:

$$\alpha(n)\rho_g u_g^2(n) + \sum_{k=1}^{n} \frac{2\, v_e(k)\bar{R}(k)\Delta z}{u_d(k) R^2(k)} \rho_l u_d^2(n) + \sum_{k=1}^{n} \tau_{friction,k} \, 2 \frac{\bar{R}(k)}{R^2(n)} \Delta z = \rho_0 u_0^2 \frac{R_0^2}{R^2(n)} \qquad \textbf{Eqn. (7.14)}$$

Using the gas mass conservation equation:

$$\frac{d}{dz}\left(\rho_g \alpha(z) u_g(z) \pi R^2(z)\right) = 0 \qquad \textbf{Eqn. (7.15)}$$

Integration over the node n with limits z_{n-1} and z_n yields to:

$$\alpha(n) u_g(n) R^2(n) - \alpha(n-1) u_g(n-1) R^2(n-1) = 0 \qquad \textbf{Eqn. (7.16)}$$

then, from the boundary condition at the entrance, $\alpha(0) = 1$, it can be written:

$$\alpha(n) u_g(n) R^2(n) = \alpha(0) u_g(0) R^2(0) = u_0 \, R_0^2 \qquad \textbf{Eqn. (7.17)}$$

which can be written as:

$$\alpha(n) u_g(n) = u_0 \, \frac{R_0^2}{R^2(n)} \qquad \textbf{Eqn. (7.18)}$$

Substituting this expression into Eqn. (7.14) and solving for the gas velocity in the node n, finally we have:

$$u_g(n) = u_0 - \frac{R^2(n)}{\rho_0 u_0 R_0^2} \sum_{k=1}^{n} \frac{2\, v_e(k)\bar{R}(k)\Delta z}{u_d(k)R^2(k)} \rho_l u_d^2(n) - \frac{1}{\rho_0 u_0 R_0^2} \sum_{k=1}^{n} \tau_{friction,k}\, 2\,\bar{R}(k)\Delta z \qquad \textbf{Eqn. (7.19)}$$

then, with the reorganization of the last expression one comes to

$$u_g(n) = u_0 - 2\frac{\rho_l}{\rho_0}\frac{\Delta z}{u_0}\frac{R^2(n)}{R_0^2} \sum_{k=1}^{n} \frac{v_e(k)\bar{R}(k)}{u_d(k)R^2(k)} u_d^2(n) - 2\frac{\Delta z}{\rho_0 u_0 R_0^2} \sum_{k=1}^{n} \tau_{friction,k}\, \bar{R}(k) \qquad \textbf{Eqn. (7.20)}$$

7.2.4. Main Assumptions of the SPARC90-Jet Code

In addition to the approximations associated with the expressions developed in the current section, this improved version of the SPARC90 code has implemented several approximations, among which, the following can be emphasized:

1) Constant conical expansion ratio of the submerged gaseous jet along the injection direction.

2) Thermal exchanges between the gas jet and the surrounding water have not being taken into account, neither sensible nor latent heat transfer. This approximation would be rough in case that water temperature is well below saturation.

3) Only the three main mechanisms which might cause particle depletion at the entry region have been considered (inertial impaction, interception and Brownian diffusion). Thermophoresis and diffusiophoresis have been neglected, which might result in the DF under-prediction (particularly, for submicron particles), electrophoresis can have some importance under certain circumstances.

4) Aerosols agglomeration/de-agglomeration processes have not been taken into account, it is assumed that interaction among aerosols cannot take place during the jetting region.

5) Droplets coalescence/break-up processes have not been taken into account, it is assumed that interaction among droplets cannot take place during the jetting region.

6) A mean diameter of the entrained droplets in each cell has been used, that is, only one constant diameter for the entrained droplets has been considered in each cell. Next step will be to consider a particle size discrete distribution function, among which the most appropriated for the present conditions seem to be the Log-Normal Distribution.

7) Correlations for jet hydrodynamics have been mainly chosen from expressions developed for annular flows (for instance, correlations of droplet sizes, entrained fraction, etc.), due to the lack of information about submerged gaseous jets.

8) Correlations for aerosol scrubbing by the entrained droplets have been chosen from those developed for wet scrubbers, due to the lack of information about submerged gaseous jets.

Consequently, the new model developed so far and presented in this document should be considered as preliminary, existing still pending improvements in several areas, which will be carried out in subsequent works, though an important step has been taken with the development of the SPAR90-Jet code. For the development of some of these improvements it is necessary to conduct extensive experimentation specifically on submerged jets. To thereby, on the one hand, use the experimental data to develop expressions specific to submerged jet, while on the other, to provide experimental data to validate the results predicted by the new code SPARC90-Jet. The first set of experiments should focus on two aspects, determination of jet hydrodynamics and aerosol capture processes. While the second group, should focus on the measurement of DF's. For both aspects, the present code should be viewed not as a final version, but subject to revisions and improvements, as well as it is also subject to more extensive validation against experimental databases. So as soon as new data become available, works of development and validation of a new version of SPARC90-Jet will be carried out.

7.3. Summary of the New SPARC90-Jet Code Implementation

The chapter begins with a brief presentation of the original SPARC90 code, section 1. After showing this short description of the old code, the chapter continues with the description of the new code, section 2. The SPARC90-Jet model has been implemented as a subroutine of the original SPARC90 Fortran code. Along this chapter it is outlined the fundamentals, major hypotheses and changes introduced into the code in order to estimate particle removal during gas injection in pools under jet regime. To do so, a simplified and reliable approach to submerged jet hydrodynamics has been developed to describe both the gas–liquid and the droplet-particles interactions. This chapter summarizes this update and implementation processes of the SPARC90 code to capture the major phenomena which take place under high velocity injection conditions (SPARC90-Jet), it is based on the state-of-the–art equations for jet hydrodynamics and aerosol removal (remind that the its old version was only developed for low velocity injection regimes) shown in the previous chapters.

Regarding the programming of the SPARC90-Jet, when the jet option is activated the new subroutine of the SPARC90-Jet is called, this subroutine continues to be active until gas jet velocity is below the onset of the entrainment zone, moment in which is considered that the gaseous jet extinguishes. From this point, the code performs the same calculations as the original code, that is, the rising plume DF, although starting from

different conditions. But with a significant difference, in our case, the globule formation region has been removed, consequently only the rising plume in which the bubbles evolve with a single diameter to represent the swarm exists, for non-condensable gases this value corresponds to the volume mean diameter, i.e. 0.72 cm.

The structure of the SPARC90-Jet is sequentially programmed in two main parts: hydrodynamics and aerosol scrubbing by droplets. The program is highly modular, in such a way that for each of these two main parts several subroutines carry out with the intermediate information needed to make further calculations. In order to implement the expressions developed in previous chapter within SPARC90, the jet entrainment zone has been split into a large number of nodes. The chapter ends with the enumeration of the major assumptions which have been made throughout the code implementation, subsection 7.2.4.

Chapter 8

HYDRODYNAMIC RESULTS PROVIDED BY THE ENHANCED SPARC90-JET CODE

8. HYDRODYNAMIC RESULTS PROVIDED BY THE ENHANCED SPARC90-JET CODE

Introduction

This chapter focuses on the characterization of the key variables needed to determine the submerged jet properties. Additionally, several studies linking the main parameters of the submerged jet with the characteristics of aerosol particles and, finally, their correlation with the collection efficiency have been carried out. Due to the lack of experimental data of the hydrodynamics of the submerged jet, it has been not possible to perform a confrontation against experimental data. Only the comparison between the results provided by the SPARC90-Jet code for all the tests under study has been shown. But despite this experimental data gaps, it has noted a number of submerged jet characteristics that seem to evolve in a logical manner. This chapter is organized as follows: first the presentation of SPARC90-Jet output file, secondly the results and their discussion, ending with a summary of the main obtained results.

8.1. The extra output file of the SPARC90-Jet

In addition to the output file provided by the old version of SPARC90 code the new version provides an extra file in which many variables of the jet are shown, an example of an output file is shown in Appendix II. This file is organized as follows:

- Determination if injection takes place under critical or subcritical conditions.

- Value of the entrainment inception velocity (which determines the end of the entrainment region and the end of the jet regime).

- Velocity profile of the submerged jet (diffusion zone and average velocity).

- Droplet characteristics (diameter, velocity, entrainment mass, number of entrained droplets and void fraction).

8.2. Results and Discussion of the SPARC90-Jet Calculations for the Jet Hydrodynamics

The experimental data series which have been used to assess the SPARC90-Jet code performance are: ACE [Escudero, 1995], LACE [Escudero, 1995], POSEIDON [Dehbi, 2001] and RCA [López-Jiménez, 1996]. The injection process of these four experimental programs (ACE, LACE, POSEIDON and RCA) take place under subcritical conditions and the entrained inception velocity is in the neighborhood of 15-20 m/s. Consequently this

section will concentrate on the other two groups of variables provided by the SPARC90-Jet code, i.e. submerged jet velocity profile and characteristics of the entrained droplet.

Throughout this section the main predictions of the SPARC90-Jet code will be shown. The following four figures, Figure 8.1 to Figure 8.4, show the main results provided by the code. In particular the axial distance versus jet and droplet velocities, and also versus the rest of entrained droplet parameters, i.e. diameter, total mass and number, all of them for the four experimental data series are displayed. An important comment related with the jet hydrodynamics, jet velocities and the rest of variables, is the fact that a "virtual" jet velocity is calculated by the code. This has been done in this way because of the unsteadiness and pulsating behavior of the submerged jet; consequently, there are periods of time in which no jet exists, followed by periods of time with a jet behavior of the injected gas. The criteria used has been to consider a jet with the characteristics needed to overcome the pressure of the pool, in such a way that the overexpansion takes place, as shown in the Someya's article [Someya, 2011] and using the expressions proposed by the Bubnov's model [Bubnov, 1998]. In this way, during these jet periods concentrate all the aerosol capture processes.

The penetration length, defined as distance when the jet bottom cuts an imaginary line drawn horizontally from the jet nozzle exit, presented in Eqn. (4.45) to Eqn. (4.52). In the four experimental data series analyzed this distance varies between 2 and 6 centimeters approximately, depending primarily on discharge conditions, amount and characteristics related to the entrained droplets and on physical properties of gas and liquid phases. The penetration length coincides approximately with the onset of entrainment point, moment in which the onset of entrainment velocity is reached by the jet. Consequently, in this work these distances are considered to be equal, i.e. penetration length, distance at which the entrainment process ends (distance from the nozzle exit to the onset of entrainment point) and end of the jet region. Along the penetration length the jet reduces his velocity until the entrainment inception velocity is reached (values are around 15-20 m/s), this calculations have been performed in the code via Eqn. (2.81) and Eqn. (2.82).

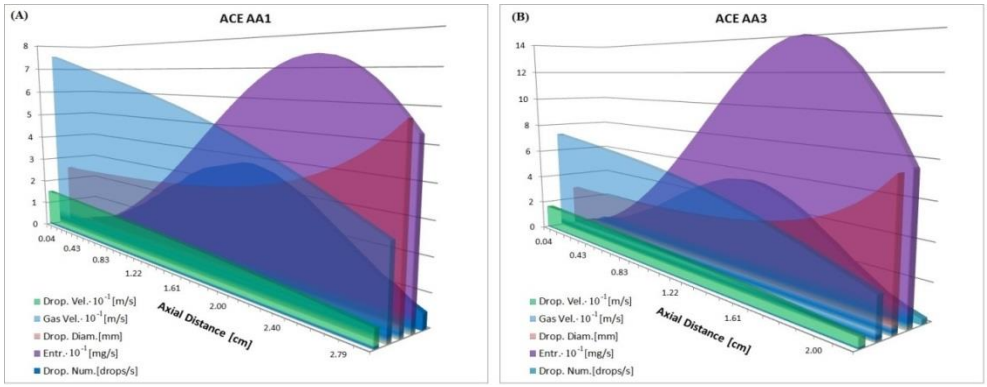

Figure 8.1. View of the main parameters calculations provided by the SPARC90-Jet code for the ACE experimental series: (A) ACE AA1; (B) ACE AA3.

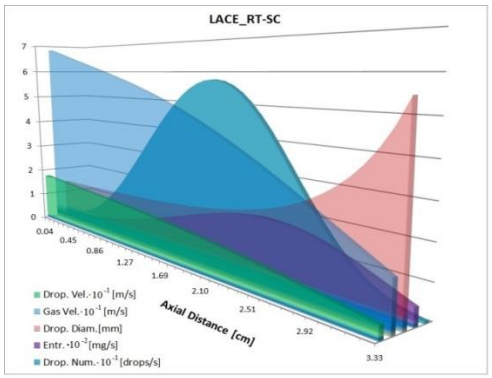

Figure 8.2. View of the main parameters calculations provided by the SPARC90-Jet code for the LACE experimental series.

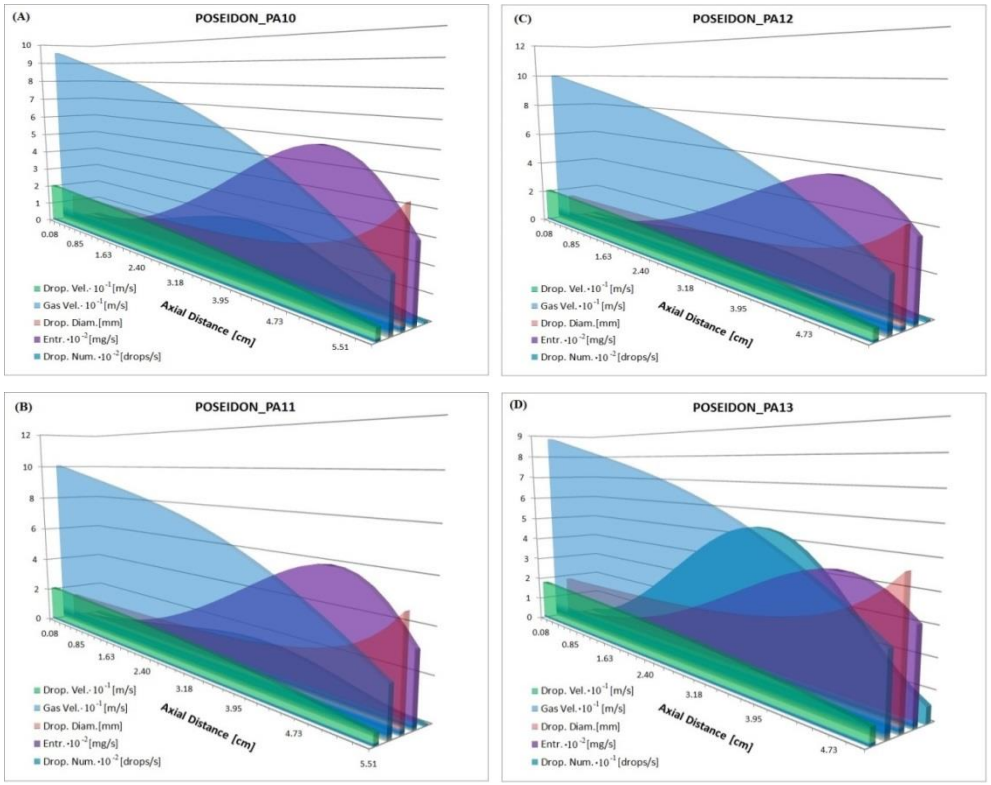

Figure 8.3. View of the main parameters calculations provided by the SPARC90-Jet code for the POSEIDON experimental series: (A) POSEIDON PA10; (B) POSEIDON PA11; (C) POSEIDON PA 12; (D) POSEIDON PA 13.

Referring now to the description of the main parameters related to the entrained droplets, I will start with the characterization of the velocity at which these entrained droplets are carried by the submerged jet. In order to estimate the droplets velocities the employed expression has been Eqn. (4.92). In which his main contribution depends on gas velocity (in this work a 15% of gas velocity has been selected) but it is also considered that are influenced by the celerity of the waves that travel on the gas-liquid interface. The selection of this expression has been done after having tested many different possibilities.

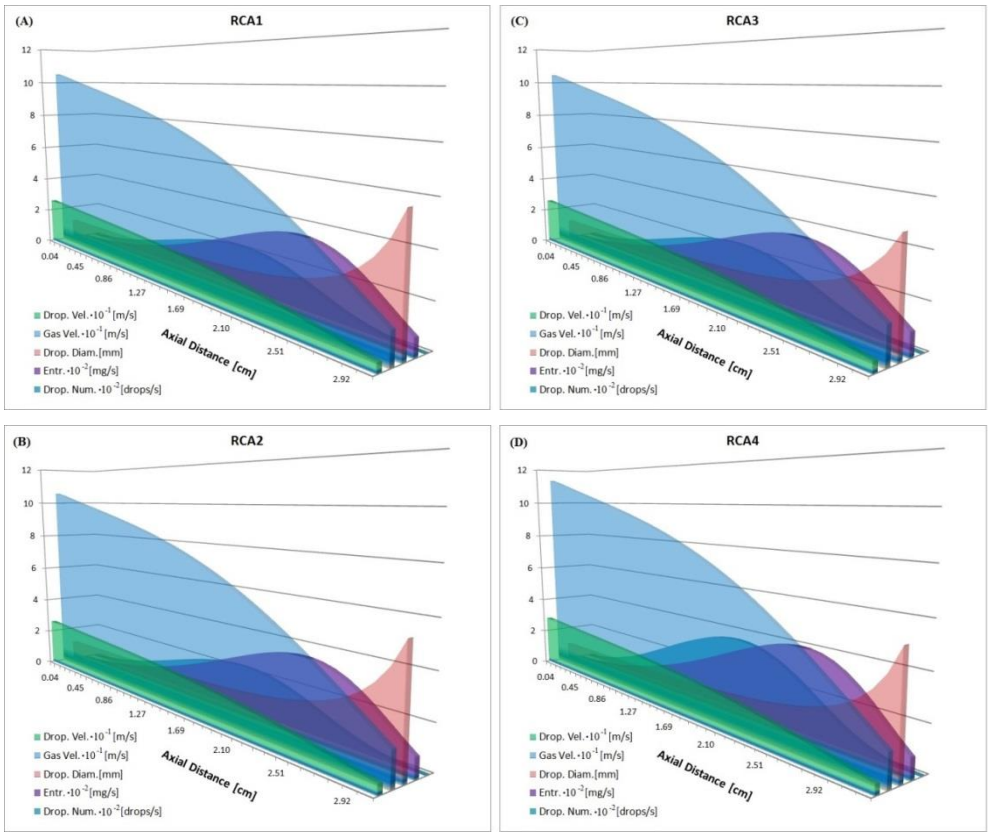

Figure 8.4. View of the main parameters calculations provided by the SPARC90-Jet code for the RCA experimental series: (A) RCA 1; (B) RCA 2; (C) RCA 3; (D) RCA 4.

As for the entrained droplets diameters, due to the not excessively high jet velocities for the four experimental data series at the injection nozzle (all of them under subcritical conditions and far from critical conditions), say that the droplet sizes are in the vicinity of the millimeter, increasing their size as the jet spreads reaching values of about 4 to 6 millimeters. From the large amount of the expression studied (all this expressions came

from annular flow or sudden exposure to high speed gas stream, due to the lack of specific information concerning submerged jets), shown in section "3.2 Droplet sizes" the selected expressions have been Eqns. (3.14) and (3.76), with the aim to combine the aggressiveness of a sudden exposure to a high speed gaseous stream, with the smoothness of the expression for fully developed annular flow.

The entrained fraction of droplets is another of the key variables studied. In order to determine this variable, many expressions found in the open literature have been tested. All these tested expression are displayed in section "3.4. The amount of the entrained droplets".

Finally, three expressions have been employed to determine the total amount of entrained droplets: the first of them, Eqn. (3.80), which estimates the entrained fraction of droplets in equilibrium conditions for annular flow (used this kind of correlations due to the lack of information specifically developed for submerged jets); the second one, Eqn. (4.65), which is a correction factor also developed in annular flow, used to study the flow developing region, which in fact for submerged jets is the whole jet region; and finally, the third expression, Eqn. (4.66), which takes into account the fact that the entrained droplets continue traveling carried by the submerged jet, reducing progressively his amount as the submerged jet spreads. Regarding to the total number of entrained droplets say that this quantity is estimated directly through the total mass of the entrained droplets and their size.

As was mentioned earlier, the amount of the entrained droplets and their traveling velocity are the key variables to estimate the jet behavior. As far as capture mechanisms processes are concerned, in addition to jet hydrodynamics, all the aspects related with aerosol characteristics must be consider, aspect which will be developed in the subsequent chapter.

Focusing on the comparisons between each of the key variables for all of the experimental data series, in the Figure 8.5 is shown the decrease of the submerged jet velocity as it evolves downstream. As it can be seen in the figure, there is not a direct relation between the initial gas jet velocity and his penetration length. These differences are caused by the total amount (entrained fraction) and velocities at which these entrained droplets are accelerated. Both variables depend not only on the initial gas velocity but also on gas and liquid properties, i.e. gas and liquid temperatures and pressures. Then, as a consequence, a higher injection velocity does not correspond necessarily with higher penetration length; this statement is justified in Figure 8.6 and Figure 8.7. If POSEIDON and RCA experimental series of both figures are compared, it is shown that a lower decrease in the gas velocity takes place in the four POSEIDON experimental series respect to the RCA experiments, this is caused by their lower final droplet velocity, added to the delay of the entrainment process (lower amount of entrained droplets). This dependency on gas and liquid properties is clearly shown in ACE experiments, in which ACE AA3 experiment has a higher injection velocity but a lower penetration length than ACE AA1. This aspect is easily justified by the differences in the gas and liquid properties, higher pressures and temperatures for both phases in ACE AA3 experiment, which produces, as a result, mainly a higher mass of the entrained droplets.

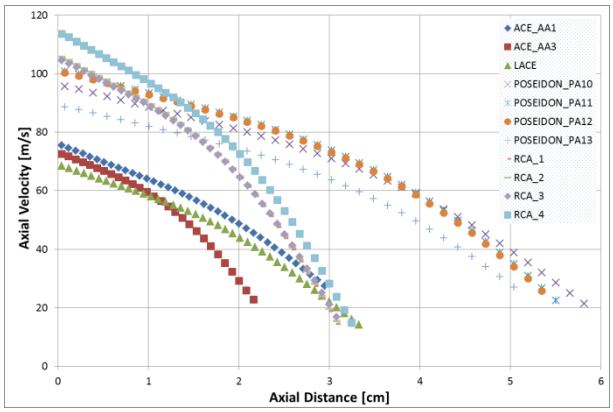

Figure 8.5. Gas jet velocity vs. axial distance calculations provided by the SPARC90-Jet code for the four experimental data series.

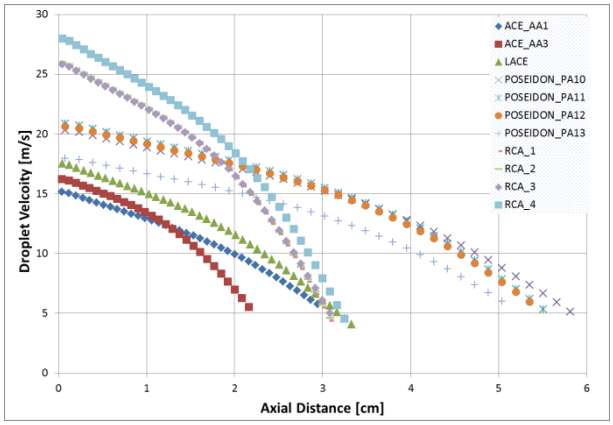

Figure 8.6. Entrained droplets velocity vs. axial distance calculations provided by the SPARC90-Jet code for the four experimental data series.

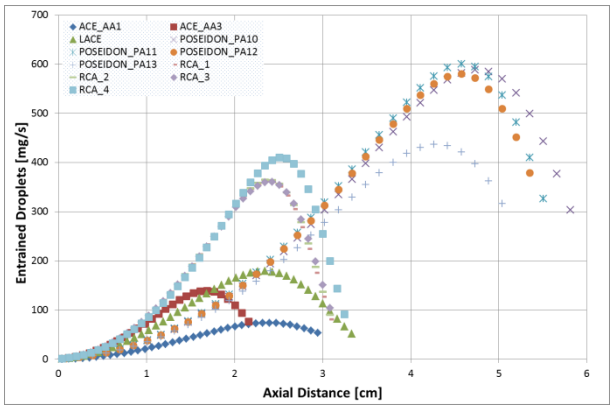

Figure 8.7. Entrained Fraction vs. axial distance calculations provided by the SPARC90-Jet code for the four experimental data series.

Respecting to the entrained droplet sizes, this magnitude is detailed in Figure 8.8, as it is shown in the figure the droplet size of the entrained droplets increase as the submerged jet evolves downstream. That is to say, there is an inversely proportional relation between the gas velocity and the size of the entrained droplets, Figure 8.9. This proportionality can be clearly shown in this figure, in which for all the experimental series there are a similar trend of the entrained droplet sizes with the gas velocity, in fact with the normalized gas velocity. This droplet size origin mainly depends on the gas velocity and on a lesser extent on gas and liquid physical properties.

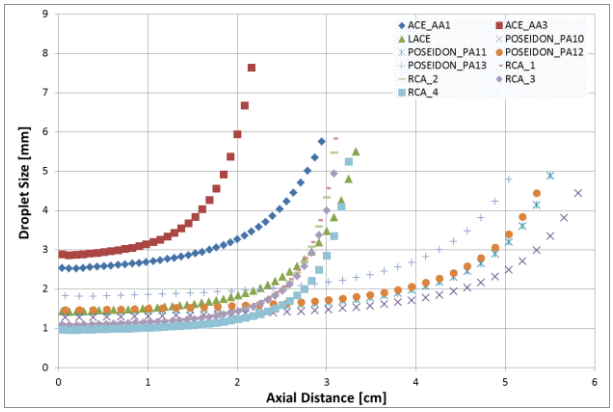

Figure 8.8. Droplet Size vs. axial distance calculations provided by the SPARC90-Jet code for the four experimental data series.

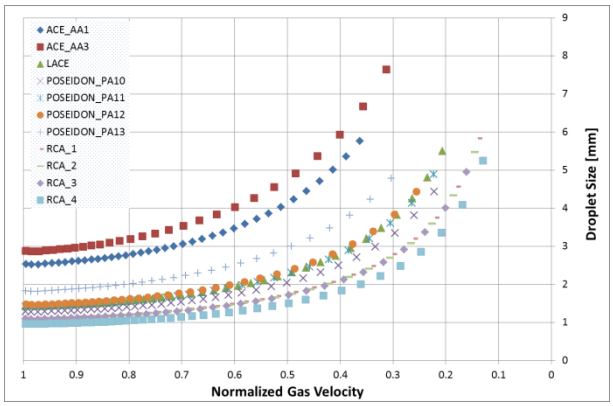

Figure 8.9. Droplet size vs. Normalized gas velocity calculations provided by the SPARC90-Jet code for the four experimental data series.

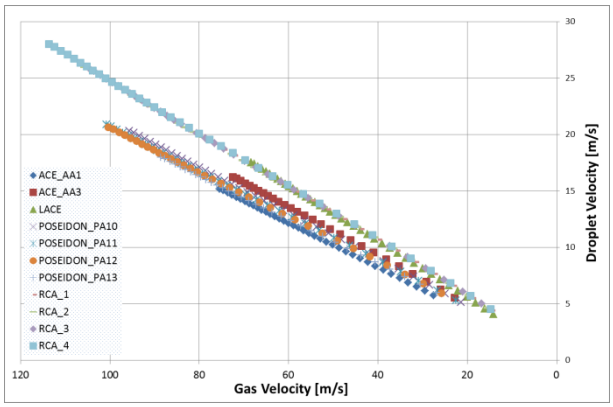

Figure 8.10. Droplet vs. Gas velocities calculations provided by the SPARC90-Jet code for the four experimental data series.

In order to appreciate more clearly the tendency with the gas velocity of the rest of variables, which is the dominant variable, the same path as marked in Figure 8.9 has been followed in the next group of figures. Figure 8.10 shows the linearity between the entrained droplets and the gas velocities for all the experimental data series, in this case the velocities have not been normalized because higher droplet velocities produce a quicker decrease in the gas velocity (the gas momentum is used in accelerate the entrained droplets). Even though, there are slightly different values and slopes depending on gas and liquid properties. For instance, RCA and LACE experiments present higher droplet velocity predictions and slightly higher decreasing slopes than the rest of experimental series, probably caused by the effect on the physical properties produced by their higher values of the pool and jet pressures. While the predicted droplet velocity, as function of gas velocity, is quite similar for the rest of experimental data series.

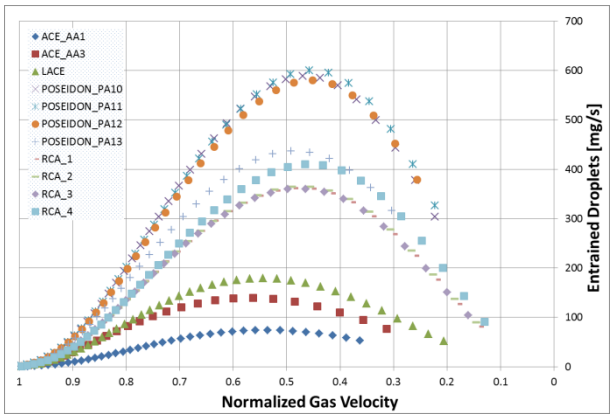

Figure 8.11. Entrained droplets vs. Normalized gas velocity calculations provided by the SPARC90-Jet code for the four experimental data series.

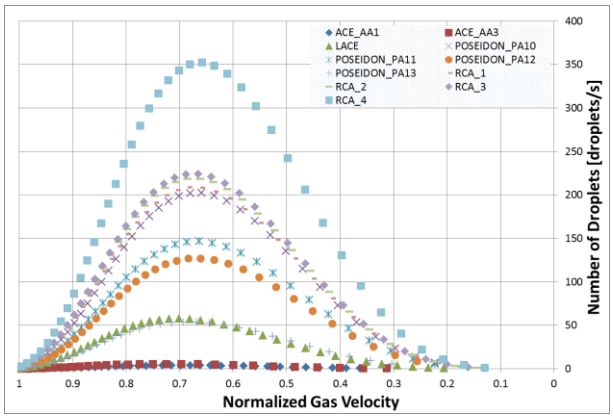

Figure 8.12. Total number of entrained droplets vs. Normalized gas velocity calculations provided by the SPARC90-Jet code for the four experimental data series.

With regard to the total mass of the entrained droplets, Figure 8.11, say that there is a bell shape for all the experimental series, being the total amount of the dragged water more or less significant depending mainly on the gas velocity. Although, with an important influence of gas and liquid properties (primarily by the pressure effects on the physical properties of both phases). In all tests, the total mass of the entrained droplets starts in zero at the nozzle exit, increasing as the submerged jet spreads downstream, reaching the maximum value at about 0.6-0.4 of the normalized gas velocity. These maximums values are located more delayed in the tests with higher penetration lengths. The predicted number of droplet, Figure 8.12, also have a bell shape, but with his maximum value advanced respect to the total mass of droplets (0.7-0.6 of the normalized gas velocity). This advance

in his maximum values is due to his dependency on the droplet size, Figure 8.9. For instance, for the RCA experiments, the entrained fraction becomes significant quite early and the velocities at which these droplets are accelerated are high enough, consequently the decrease of the jet velocity is the quickest of all the data series. While in the POSEIDON tests, the entrained fraction becomes significant somewhat later and, the droplet velocities are slightly lower, consequently the decrease of the jet velocity is the lowest of all the data series.

8.3. Summary of Submerged Jet Hydrodynamic Results

Submerged jet hydrodynamics is a key aspect to study the aerosol capture mechanisms. In this summary, the trends found with the simulations performed with the new SPARC90-Jet code will we shown.

The total amount of the entrained droplets and their traveling velocity determine most of the jet capture capabilities, aerosol capture depends on both magnitudes. As the number of droplets carried by the submerge jet the aerosol capture are enhanced, whereas, as the entrained droplets velocity increases the aerosol capture is reduced. Higher number of entrained droplets means higher number of obstacles against which the aerosol particles can collide. While higher droplets velocities means, firstly, further decrease in the jet momentum (required to accelerate them to that velocity) and, secondly, less velocity difference between the entrained droplets and the carried aerosols (which also results in lower efficiency of the collection mechanisms). In SPARC90-Jet calculations has been shown that droplet velocities are directly proportional with gas velocity (Figure 8.10). Whereas the total mass of the entrained droplets begin in zero at the injection nozzle, increasing along the axial distance, reaching his maximum at about 0.7-0.5 of the normalized gas velocity (Figure 8.11).

With regard to droplet sizes, say that, as it is generally accepted, the entrained droplet sizes increase with the decrease in the carrier gas velocity, statement confirmed by the results of SPARC90-Jet, as shown in the Figure 8.9. Even though, as it has been explained in the previous paragraph, the total mass of entrained droplets decreases with the gas velocity decrease.

Consequently, the jet hydrodynamic is determined not only by the injection velocity, but by the physical conditions of the liquid phase and gas phase, as confirmed by RCA and POSEIDON experiments. In particular, the penetration length of RCA experiments, in which the submerged gas injections take place at higher velocities than POSEIDON experiments, result in lower values compared to POSEIDON experiments.

Chapter 9

CONFRONTATION OF THE EXPERIMENTAL DECONTAMINATION FACTOR AGAINST SPARC90 AND SPARC90-JET RESULTS

9. CONFRONTATION OF EXPERIMENTAL DECONTAMINATION FACTOR AGAINST SPARC90 AND SPARC90-JET RESULTS

This chapter is an extended and updated version of the sixth section of the paper "Enhancement of the SPARC90 code to pool scrubbing events under jet injection regime", published in Nuclear Engineering and Design, Vol. 300, pp. 563-577, 2016 [Berna, 2016].

Introduction

An indirect validation of the hydrodynamic and aerosol capture modeling has also been conducted, this validation works have been made through comparisons against data from experiments dealing with the decontamination capability of aqueous ponds under representative severe nuclear accident conditions. Due to the few experiments that met the jet injection regime and given the not introduction of thermally mass transfer processes of the present version of SPARC90-Jet only a few experiments can be used. In this sense, only the experiments which meet these requirements can be employed, and therefore, a reduced number of experimental series have been used in this work, those are the following: ACE [Escudero, 1995], LACE [Escudero, 1995], POSEIDON II [Dehbi, 2001] and RCA [López-Jiménez, 1996]. Although, improvements and extension of SPARC90-Jet are expected in the future; however, a final model version will require a more extensive and sound database against which to compare.

9.1. Experimental Pool Scrubbing Scenarios

In order to assess the capabilities of the SPARC-Jet, a literature survey on pool scrubbing experiments has been carried out to build up a database on jet injection regime. However, just few of those experiments met the jet regime conditions ($We_g \geq 10^5$). In addition, due to the neglect of thermally driven mass transfer in the current version of SPARC-Jet, the experiments to be selected should not contain a high steam molar fraction, so that steam condensation does not affect the pool decontamination capability substantially. This screening out reduces the experimental programs providing useful data to ACE, LACE, POSEIDON II and RCA.

ACE experiments were framed within an international project led by EPRI [Escudero, 1995]. Similarly to previous tests, they analyzed the influence of gas flow rate, steam fraction, submergence and aerosol size (Table 9.1). The only experimental sets having Weber numbers over 10^5 were the AA1 and AA3 experiments.

Table 9.1. Summary of the main tests variables.

ACE Experimental conditions										
TESTS	Nozzle	Gas Data				Aerosol Data		Pool Data		
	D_N (cm)	P(bar)	T (ºC)	$\dot{m}$ (g/s)	X_s	ϕ_p (μm)	$\dot{m}$ (g/s)	P(bar)	T (ºC)	S (m)
AA1	0.95	1.21	138	2.20	0.012	2.37	7.75E-03	1.0	26	1.38
AA3	0.95	1.32	150	2.16	0.013	2.50	1.03E-02	1.0	82	2.62

LACE Experimental conditions										
TESTS	Nozzle	Gas Data				Aerosol Data		Pool Data		
	D_N (cm)	P(bar)	T (ºC)	$\dot{m}$ (g/s)	X_s	ϕ_p (μm)	$\dot{m}$ (g/s)	P(bar)	T (ºC)	S (m)
RT-SC-01/02	1.00	3.39	150	5.53	0.10	1.7	1.82E-05	3.0	110	2.50
RT-SC-P/01	1.00	3.39	150	5.36	0.11	5.6	1.82E-05	3.0	110	2.50

POSEIDON II Experimental conditions									
TESTS	Nozzle	Gas Data			Aerosol Data		Pool Data		
	D_N (cm)	T (ºC)	$\dot{m}$ (g/s)	X_s	ϕ_p (μm)	$\dot{m}$ (g/s)	P(bar)	T (ºC)	S (m)
PA10	2.00	222	38.33	0.04	0.3	1.17E-02	1.0	80	4.00
PA11	2.00	256	38.33	0.04	0.3	1.52E-02	1.0	75	2.00
PA12	2.00	237	34.72	0.0	0.3	1.61E-02	1.0	72	1.00
PA13	2.00	270	34.72	0.0	0.3	1.49E-02	1.0	63	0.30

RCA Experimental conditions									
TESTS	Nozzle	Gas Data				Aerosol Data	Pool Data		
	D_N (cm)	P(bar)	T (ºC)	$\dot{m}$ (g/s)	X_s	ϕ_p (μm)	P(bar)	T (ºC)	S (m)
RCA1	1.00	≈ 2.8	120	7.20	0.0	3.25	2.3	120	0.25
RCA2	1.00	≈ 2.8	120	7.20	0.0	4.02	2.3	120	0.50
RCA3	1.00	≈ 2.8	120	7.20	0.0	3.46	2.3	120	1.25
RCA4	1.00	≈ 2.8	120	7.20	0.0	4.03	2.3	120	2.50

LACE España Project was founded in 1987 as a Spanish participation in the international research program LACE [Escudero, 1995]. As in the previous experiments, the main objectives were the analysis of discharge events in pools. Only two experiments met the jet regime, RT-SC-0/02 and RT-SC-P/01 (Table 9.1).

POSEIDON II program carried out a total of 17 experiments [Dehbi, 2001]. They analyzed pool scrubbing dependence on carrier gas steam fraction, flow rate, particle size and submergence (Table 9.1). The chosen tests were PA10, PA11, PA12 and PA13 ($We_g \approx 5.5 \cdot 10^6 - 8 \cdot 10^6$), because of their low or null steam fraction, 0,04 for the first two and zero for the last two.

RCA experiments [López-Jiménez, 1996] were carried out in PECA facility located at CIEMAT (Centro de Investigaciones Energéticas, Medioambientales y Tecnológicas). They were focused on the jet injection regime ($We \approx 2.9 \cdot 10^6 - 3.6 \cdot 10^6$) in hot pools. Four different experiments were performed with particles of around 4 μm of AMMD (Aerodynamic Mass Median Diameter) and submergences from 0.25 m to 2.5 m (Table 9.1).

9.2. Results and Discussion of the Rising Plume, Jet and Overall Decontamination Factor

This section presents the analytical calculations results of the SPARC90-Jet code for the experimental data shown in the previous section. With a view to assess the capability of the newly development of the SPARC90-Jet code his results will be compared to the experimental data and with the old version of SPARC90.

The comparison of the four groups of experimental data studied in the present work (ACE, LACE, POSEIDON II and RCA) with the simulation results of the old SPARC90 version and with the ones of the newly developed SPARC90-Jet version is shown in Table 9.2 and Figure 9.1. As can be observed in both cases, table and figure, the experimental trends are well captured by the SPARC90 and SPARC90-Jet codes, although there are significant differences for both codes in some of the analyzed tests.

The following lines are devoted to the estimation of uncertainties existing into the SPARC90-Jet code calculations. Several methods could be used in order to quantitatively take into account the uncertainty sources which are associated with SPARC90-Jet code. The statistic of order method [Wilks, 1941], which is widely extended, has been the selection made in this paper. According to ASME [ASME; 2009] three main uncertainty sources exist in a code, these are: model uncertainties (mainly related with geometry and modelling assumptions, constants, coefficients or empirical correlations implemented in the model, etc.) input parameters uncertainties (errors associated with geometry, initial and boundary conditions, material properties, etc.) and numerical uncertainties (associated with the code numerical solving process, i.e., discretization error, iterative solving of equations, etc.). In the case of SPARC90-Jet code, we have focused on the model uncertainties, due to

the fact that errors associated with input parameters and numerical code uncertainties have been shown as of minor importance after an initial analysis. Sensitivity and PIRT (Phenomena Identification Ranking Technique) studies have been carried out; these techniques have shown that model expressions related with entrained droplets (entrainment fraction, diameter and velocity) and aerosol capture by inertial impaction are the ones of major importance. Applying to them the Wilks methodology [Wilks, 1941; Wald, 1943], i.e., performing 93 random simulations for each test (all the key expressions vary randomly between their maximum and minimum values, these extreme values were estimated during the sensitivity and PIRT analysis, taking into account of the information available from the literature and estimations based on national laboratory sources). After all this procedure a confidence interval for the output variable under study, DF, has been determined (Table 9.2).

Table 9.2. Summary of the experimental results and the obtained with SPARC90 and SPARC90-Jet codes.

TEST		Aerosol	Experimental DF		SPARC90 DF	SPARC90-Jet DF			
			min.-max.	Mean		Jet	Rising Plume	TOTAL	Uncertainty min.-max.
ACE	AA1	Cs	145.0-160.0	58.12*	14.70	2.198	13.84	30.41*	27.21-33.22*
		Mn	12.0-33.0						
		I	47.0-80.0						
	AA3	Cs	320.0-330.0	157.0*	33.23	2.315	30.60	70.83*	61.61-75.0*
		Mn	75.0-140.0						
		I	180.0-220.0						
LACE	RT-SC-01/02	CsI	116.0-128.0	122.0	9.50	14.33	11.32	162.2	119.1-229.6
	RT-SC-P/01	CsI	491.0-526.0	508.5	21.90	14.10	32.63	460.2	338.5-650.1
POSEIDON II	PA10	SnO_2	8.22-12.98	10.60	1.196	6.174	1.173	7.242	5.738-8.793
	PA11	SnO_2	3.95-6.75	5.35	1.150	4.190	1.081	4.529	4.028-5.636
	PA12	SnO_2	2.80-4.04	3.42	1.055	3.909	1.033	4.038	3.407-4.834
	PA13	SnO_2	1.94-3.24	2.59	1.026	2.599	1.006	2.615	2.326-2.832
RCA	RCA1	Ni	12.4-13.2	12.80	10.33	11.24	1.246	14.00	10.41-18.18
	RCA2	Ni	16.0-40.5	28.25	11.73	11.91	2.148	25.58	20.96-38.24
	RCA3	Ni	46.6-80.0	63.30	13.72	13.01	5.692	74.06	55.43-100.4
	RCA4	Ni	719.0-1220.7	969.9	25.72	22.03	16.35	360.2	246.8-504.3

* Weighted with the aerosol composition at the nozzle exit

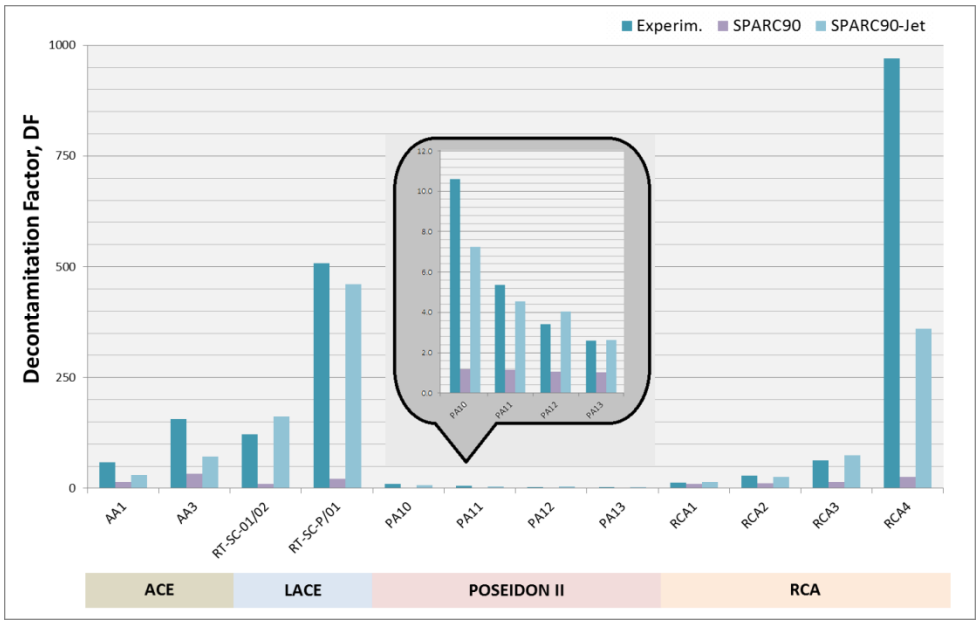

Figure 9.1. General summary of the DF experimental data and results of SPARC90 and SPARC90-Jet codes.

As far as the comparison between the results provided by both versions of SPARC90, we must stress that there is a significant improvement in all tests analyzed, up to the point that the new SPARC90-Jet version provides significantly better results for all tests in study. The new simulation results are closer to the experimental data in all cases.

We must emphasize that, despite the cited appreciable differences that seem to exist in the comparison of the DF for some experimental data and SPARC90-Jet results, actually they are not so important. If the values of the aerosol collection efficiency, η, are represented instead of the DF values (Figure 9.2), one can notice that differences in DFs are certainly negligible in terms of mass retention efficiency.

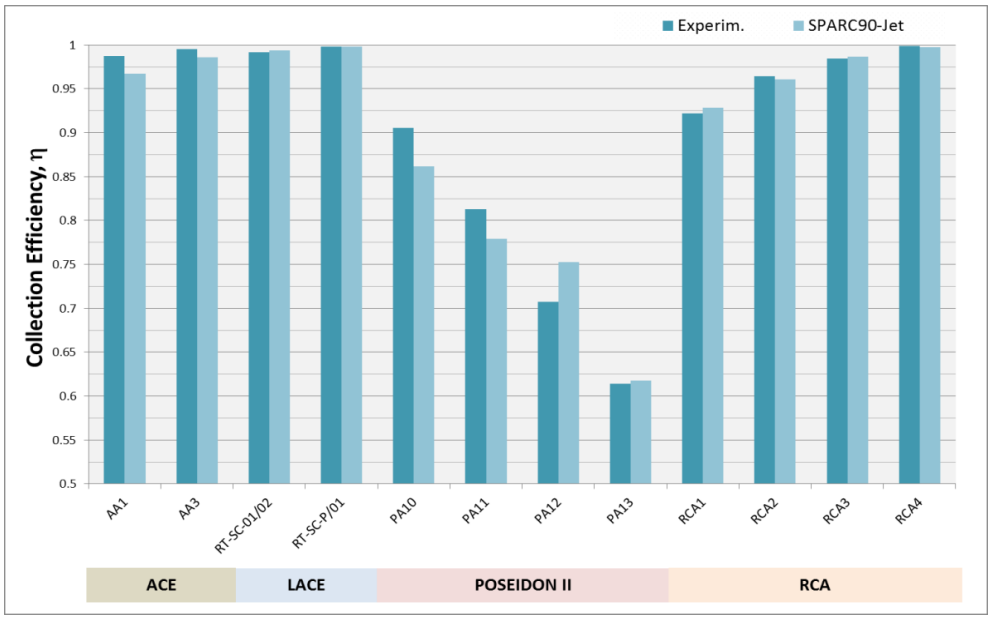

Figure 9.2. General summary of the Collection Efficiency experimental data and results of SPARC90 and SPARC90-Jet codes.

Regarding to DF dependency with test inlet variables and boundary conditions of the studied tests, say that, aerosol sizes and pool depth are of vital importance. Particle size is considered to be a factor of major influence on DF values, an increase in particle size leads to an increase in the DF. Digging deeper in the dependency of DF with aerosol size, this increasing tendency is clearly shown in LACE experimental data (Figure 9.3). Both experiments took place in almost the same conditions, the only significant difference was the aerosol size distribution. As can be seen in the figure, smaller aerosol distributions give as a result smaller DFs (tests RT-SC-01/02, ϕ_p = 1.7 μm versus RT-SC-P/01, ϕ_p = 5.6 μm). This tendency is clearly shown in the experimental data, being very well captured by the SPARC90-Jet version, but being not well captured in the old version of SPARC90. Consequently, an important advance has been reached in the present improvement of the code. This trend is confirmed by the lower submergence tests (i.e., PA13, RCA1 and RCA2), which are shown in Figure 9.4, the contribution of jet and rising plume regions to the DF have been displayed separately, along with the total DF and the experimental data, from this figure it can be said that higher values of DF are reached for larger sizes of aerosols in both regions. Even though, in the rising plume there is not virtually decontamination (DF ≈ 1), having only a slight increasing slope with aerosol sizes.

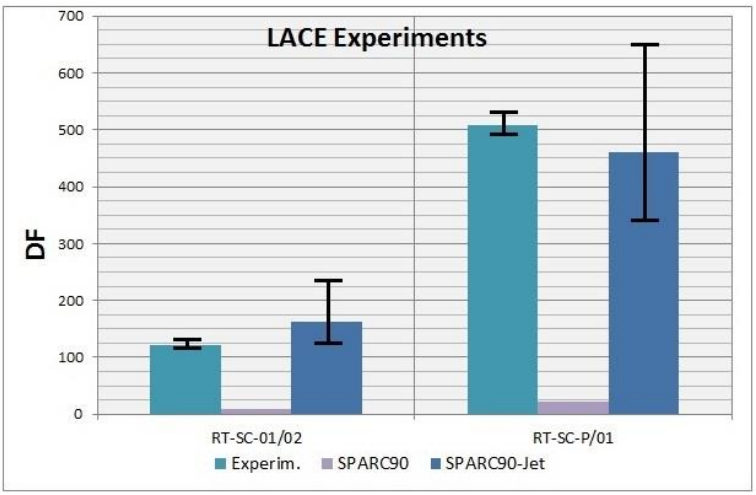

Figure 9.3. DF experimental data and results of SPARC90 and SPARC90-Jet codes for LACE experiments.

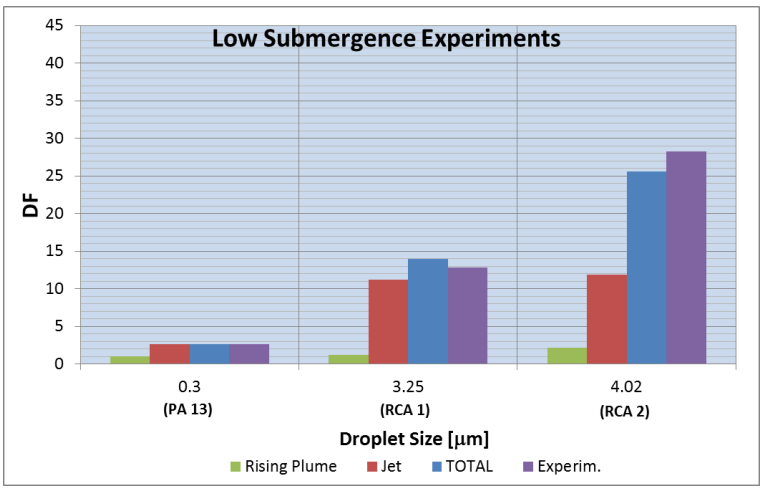

Figure 9.4. Experimental data vs SPARC90-Jet results (Total, Jet and Rising Plume regions) of the DF for the low submergence experiments.

The pool depth, submergence, is another key variable to take into account to determine the DF, as it is shown in Figures 9.5 and 9.6. The four POSEIDON II experiments studied here (Figure 9.5) took place in almost the same conditions (small aerosol size ≈ 0.3 μm, high jet and pool temperatures ≈ 250 – 75 ºC respectively, low or cero condensable gases and pressures near the atmospheric values), apart from submergence, which varies from 4.0 to 0.3 meters in the four experiments (PA10 – 4.0 m,

PA11 – 2.0 m, PA12 – 1.0 m and PA13 – 0.3 m). The upward trend of DF values with the increase of pool depth, which is seen in the experimental data, is quite well captured by the new code version. While for the old version, the DF values remain almost constant along all tests (only a very small upward tendency). This increasing tendency of DF values with submergence is due to the fact that the height of water above the injector determines the residence time of the aerosols.

The same conclusion as the expressed in the previous paragraph can be extracted from the four RCA experiments (Figure 9.6), even though in this case the aerosol sizes and pool and jet pressures were higher than in POSEIDON II experiments (aerosol sizes ≈ 4.0 μm, jet and pool pressures ≈ 2.8 – 2.3 bars respectively). We must highlight the fact that DF has a significantly higher value in RCA experiments than in POSEIDON II experiments, this results is mainly caused by the higher aerosol size (this statement will be discussed in next paragraphs). The confirmation of the assertion made earlier, increasing DF with pool depth, can be clearly seen in Figure 9.6 (RCA1 – 0.25 m, RCA2 – 0.5 m, RCA3 – 1.25 m and RCA4 - 2.5 m).

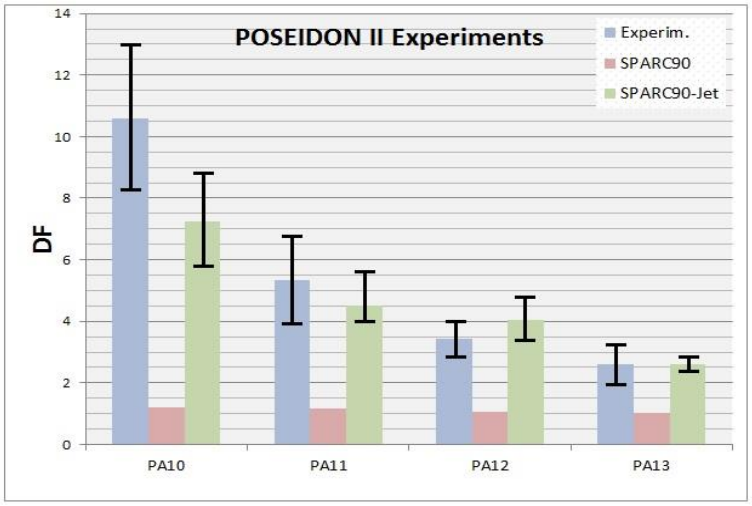

Figure 9.5. DF experimental data and results of SPARC90 and SPARC90-Jet codes for POSEIDON II experiments.

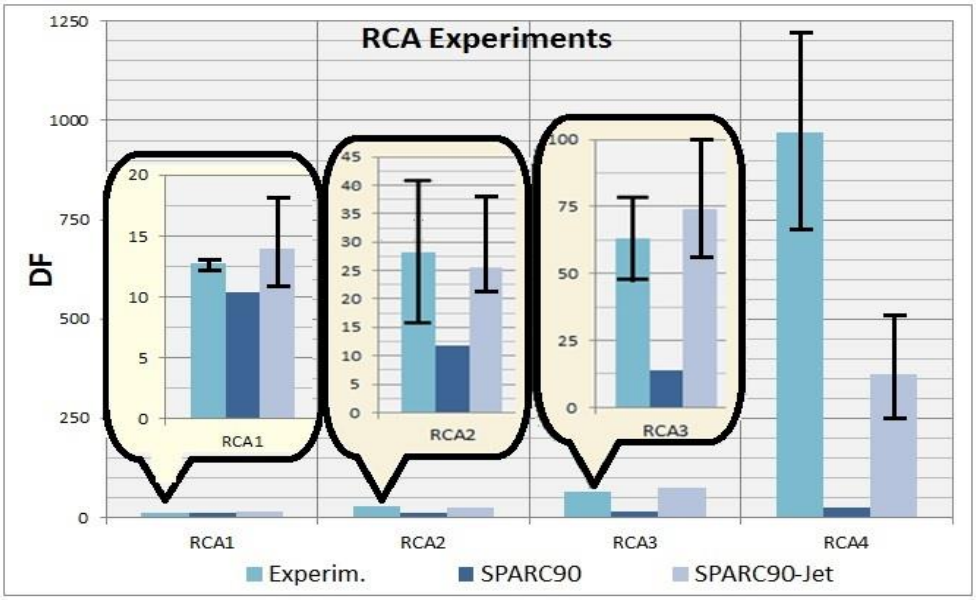

Figure 9.6. DF experimental data and results of SPARC90 and SPARC90-Jet codes for RCA experiments.

It seems intuitive to believe that, aerosol capture processes caused by changes in submergence, mainly or only take place in the rising plume. But if Figure 9.7 is seen, in which the contributions of the rising plume and jet regions for RCA experiments have been broken down, it is observed that the effect of submergence is seen in both regions. While it is true that this effect is observed in a more pronounced way in the rising plume region. But what it is most surprising, for POSEIDON II experiments, there is an increasing tendency with submergence, but this is not caused by the rising plume region (which is true that has a very slight upward trend), but for the jet region, as seen in Figure 9.8. This situation might be caused by the aerosol sizes, small ones have very small collection efficiency in the rising plume but still significant in the jet region.

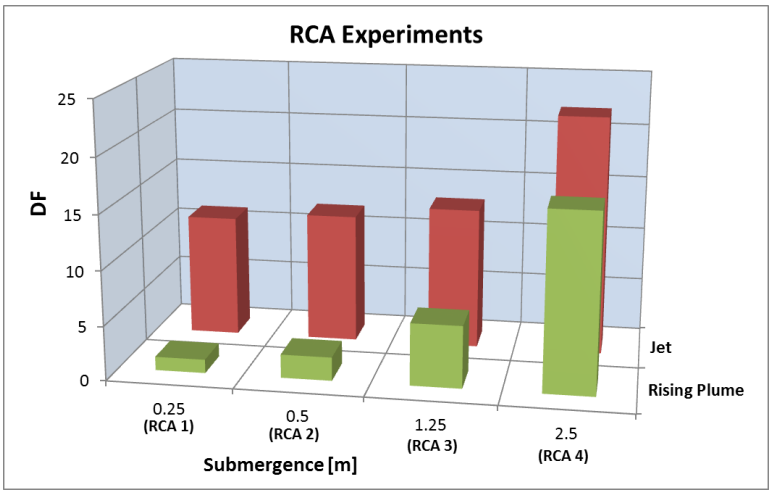

Figure 9.7. Contributions of the Injection and Rising Plume regions to the DF for RCA experiments according to SPARC90-Jet code.

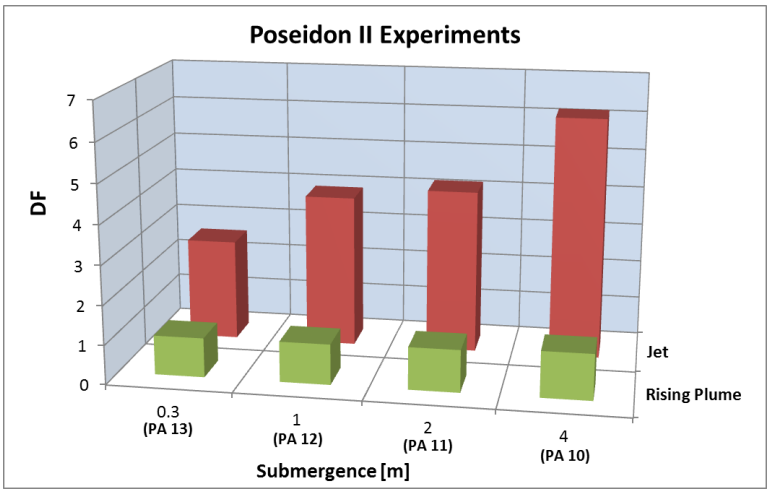

Figure 9.8. Contributions of the Injection and Rising Plume regions to the DF for POSEIDON II experiments according to SPARC90-Jet code.

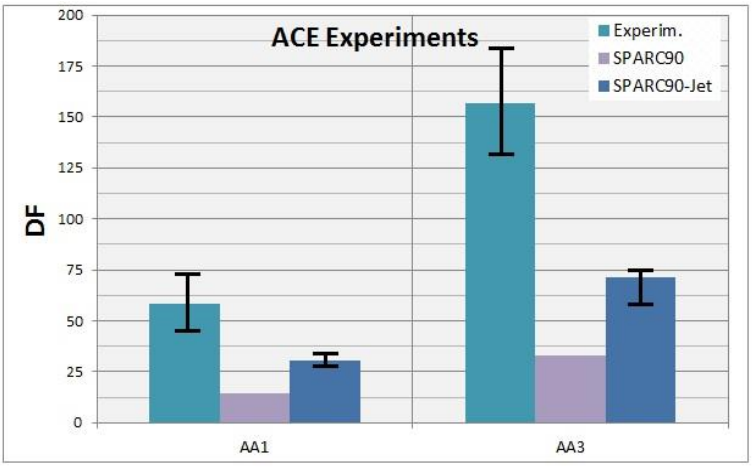

Figure 9.9. DF experimental data and results of SPARC90 and SPARC90-Jet codes for ACE experiments.

Figure 9.9 shows the results of ACE experiments. In this case the experimental conditions of both experiments were quite different (submergence 1.38 – 2.62 m, gas and pool temperatures 138 – 150 ºC and 26 – 82 ºC respectively for AA1 and AA3 tests) and added to these different experimental conditions there was a mixture of aerosols (MnO, CsOH and CsI). So many effects were combined to give as a result an experimental DF for each case. But despite this complexity, there are satisfactory results with the new version of the code, which improve significantly those of the old version, even though the predicted DF's are significantly lower.

Finally, to close up this section of confrontation of SPARC90-Jet code with his old version and against the experimental data, we must highlight that SPARC90-Jet provides much better results than his previous version, being closer to the experimental data for all the studied tests, despite the fact that in certain tests the error bars of the experimental data and the calculations of the SPARC90-Jet code does not overlap. Although, remind once again that the old SPARC90 code version was not intended for jet discharge processes, but only for globular discharges, so it is not surprising the poor results of the old version in the majority of the experimental tests under study. And we conclude that the main effects on DF are the injection pressure (either directly or through the submergence) and the aerosol sizes, having both of them an upward tendency, i.e. higher values of these variables gives as a results higher values of DF. But further investigations are needed to confirm these conclusions and to try to capture new trends dependent with other input variables.

9.3. Summary of Submerged Jet Decontamination Factor Results

The theoretical results offered by the SPARC90-Jet code have been compared with four experimental programs, ACE, LACE, POSEIDON and RCA, allowing the validation of the models and strengthening its reliability. This chapter begins with the general description of these four pool scrubbing experimental programs. Next, the results and discussion for the DF calculations are displayed.

This confrontation has been satisfactory, as it has been shown in the previous section, the experimental data and the simulations follow the same trends.

In summary, we must highlight some major insights, such as the capability of SPARC90-Jet to capture the increasing DF with aerosol diameter and with pressure-submergence, catching not only the experimental trend but also the magnitude. Finally, emphasize the substantial improvement achieved with regard to the old SPARC90 code version, which has been clearly shown when comparing the SPARC90 and the SPARC90-Jet results against the available experimental data. All the previously comments have been said with caution due to the model developed so far should be considered as preliminary and subject to improvements in several areas, added to the need to compare against a more extensive experimental database. Though, the results are encouraging, as the experimental trends are quite well captured, the final goal has not been reached yet.

Chapter 10

FINAL REMARKS, CONCLUSIONS AND FURTHER WORK

10. FINAL REMARKS, CONCLUSIONS AND FUTURE WORK

The PhD work carried out during the lasts 6 years approximately is expounded in the present thesis report. The work consists of an in depth investigation of jet discharge processes in aqueous ponds. The discharged jet carries aerosols in its bosom, so that the associated aerosol capture processes have also been studied. The work culminates with the implementation of a theoretical model for the calculation of the Decontamination Factor (DF) under jet injection regime conditions.

The theoretical model has been implemented as a complementary part of the original SPARC90 code, so that the new SPARC90-Jet code maintain the SPARC90 code capabilities, but it has been enhanced with new ones. In such a way that, this new code version is able to determine the aerosol retention capabilities, through the DF, regardless of the submerged discharge velocity. So that, at the current time the code is able to carry through with the calculations of the aerosol retention efficiency of a pool discharge or at the break stage of a wet steam generator under hypothetical severe accident SGTR conditions independently of the discharge conditions, low or high discharge velocities. But in addition to this theoretical work, experiments concentrated in some of the major aspects of submerged jets have been carried out in the scope of this PhD work, particularly the ones about which less specific information was available.

In order to summary and end the PhD report, this final chapter has been arranged in three subsections. The first one encapsulates a brief summary, made chapter by chapter. Next subsection shows the major findings of this work. To conclude this final chapter, there is a brief description of several further works, which can probably be carried out in the future.

10.1. Remarks Chapter by Chapter

Chapter 1 shows a contextualization of the work addressed throughout this PhD. In particular, a short description of BWR and PWR are shown, followed by some brief strokes of SG's characteristics. After this general description of LWRs, the chapter concentrates on aerosol description, behavior and possible capture mechanisms under nuclear accident scenarios, pool scrubbing and SGTR. Then, the submerged gas jets are described, since aerosol discharge processes occur under these flow conditions. The following section shows the initial SPARC90 code, which is one of the first attempts to describe aerosol capture mechanisms. The final section of the chapter focuses on the description of the objectives and motivation of this PhD work.

In chapter 2, the determination of the key variables of annular flows related with the gas-liquid interface properties has been carried out. An extensive review of the available gas-liquid interface information, together with a collection and analysis of experimental data found in the open literature for these key variables have been made. The decreasing

dependency of the liquid film thickness with both, the gas and the liquid velocities has been verified, in addition, a correlation as function of dimensionless numbers has been developed. As far as wave celerity is concerned, his direct dependency with gas velocity and his inverse proportionality with the liquid velocity have been validated. Added to the development of a new correlation with also improves the adjustment to experimental data. Regarding to wave frequency, say that the direct proportionality with gas and liquid velocities have been checked. As in the previous cases, a new correlation has been developed, with a better fitting of the experimental data.

In chapter 2 are also shown some aspects related with the entrainment of droplets. In particular, the major variables influencing the starting point of the entrainment process have been determined. The onset of entrainment point is the threshold value, i.e., value under which no entrainment of droplets can takes place. These critical values are so important in submerged discharges at high speeds because demarcate the endpoint from which this entrainment phenomenon is no longer produced and which also roughly coincides with the end of the jet region, i.e., point which delimitates the transition from jet region to rising plume region.

Chapter 3 is devoted to describe the most important variables which have to be considered in order to characterize the entrained droplets, in particular their sizes, velocities and total amount. Together with this variable description, the collection and analysis of experimental data found in the open literature for key variables defining the entrained droplets has been carried out. Speaking about droplets sizes, say that this magnitude is strongly affected by the gas flow rate, being less dependent on liquid velocity, with an inverse proportionality. A new correlation, which also improves the adjustment to experimental data of the previously existing correlations, has been developed. The droplet velocity has also been studied throughout this work, the main conclusion is the fact that droplet velocities are almost independent of liquid velocity and their velocity, in the vicinity of the pipe centerline, is around 80 % of gas velocity, although a small upward trend has been observed with the increase in gas velocity until this 80% is reached. With regard to the total amount of entrained droplets, say that this magnitude is very difficult to determine, but the verification of his upward trend with both the liquid and gas flow rates has been confirmed. Regarding the correlation developed in this study, it is remarkable the fact that the new expression significantly improves the results given by the correlations found in the open literature.

While in chapter 4 the aspects related to hydrodynamics of submerged jets are developed. In such a way that, those phenomena for which specific information is available, are fully developed here. While, for those phenomena in which this information is not available or does not exists, it is shown the strategy that has been followed. The parent processes used come from the annular flows studies, which were carried out in the two previous chapters. Remind that these kind of flows are the ones with highest points in common with submerged jets. Throughout this chapter the main characteristics of submerged jets are developed, showing the main regions in which jets can be divided, some sketches of the equations that characterize them, along with the displaying of the

complexity of injection and flow structures. Straightaway the equations to characterize the conditions at the nozzle exist are shown, determining the expansion angle and the penetration length. Immediately followed by the characterization of the liquid phase, proceeding next to analyze the droplet entrainment process and their subsequent balance between atomization-deposition processes, determining the total amount of droplets carried by the submerged jet, their sizes and velocities depending on the submerged jet conditions at the nozzle exit and along his spread downstream.

Throughout chapter 5 and 6 the aerosol formation and collection mechanisms have been studied. In particular, chapter 6 focuses in the aerosol capture mechanisms, and the following mechanisms were analyzed: inertial impaction, interception, Brownian diffusion, electrostatic attraction, diffusiophoresis, and thermophoresis. Focusing on those related to droplet-particle mechanical interactions, i.e. inertial impaction, interception and Brownian diffusion. These expressions come mostly from wet scrubbers, as there is no information specifically developed for aerosol capture processes in submerged jets. The chapter ends with the calculation of the aerosol scrubbing efficiency, which is determined from the decontamination factor (DF), ratio of aerosol mass flow rate entering-going out of the system.

Chapter 7 focuses on the SPARC90 code. At the beginning of the chapter a short description of the original code, which was originally designed for calculating discharge processes at low velocities, is shown. Next, the organization and development of the new subroutines, which take into account the injections at high velocities, is displayed. Summarizing, this new version of the SPARC90 code is focused on high gas velocity injection regime. The development of the new code has been done by choosing up-to-date equations from the open literature, jet hydrodynamics has been modeled and suitable aerosol equations have been adopted.

Chapters 8 and 9 focuse on the comparison of the available experimental data against the SPARC90 code results. Chapter 8 concentrates on results related with the jet hydrodynamics whereas chapter 9 focuses on the DF's results. Along chapter 9, the theoretical results offered by the SPARC90-Jet code have been compared with four experimental programs, allowing the validation of the models and strengthening its reliability. This confrontation has been satisfactory, the experimental data and the simulations follow the same trends. We must highlight some major insights, such as the capability of SPARC90-Jet to capture the increasing DF with aerosol diameter and with pressure-submergence, catching not only the experimental trend but also the magnitude in the majority of them. Finally, emphasize the substantial improvement achieved with regard to the old SPARC90 code version, which has been clearly shown when comparing the SPARC90 and the SPARC90-Jet results against the available experimental data.

10.2. Conclusions

The research work performed within this PhD can be divided in two main research lines. The first one, consists of an in depth investigation devoted to characterize submerged gas jet hydrodynamics. Whereas in the second one, the most influential aerosol capture phenomena has been studied. Finally, from these two subjects the DF can be determined.

With regard to this section of conclusions, it has been divided in three subsections. A summary of the qualitative findings related with the jet hydrodynamics is shown in the first one. Whereas the second one focuses in the description of the qualitative findings of the aerosol capture processes. Finally, along the third subsection, the comparison between the experimental data and, the old SPARC90 and the new SPARC90-Jet codes calculations for the DF are shown.

10.2.1. Conclusions on Jet Hydrodynamics

A though characterization of the submerged gas discharge process which takes place when a gas flow is coming out from a nozzle or hole submerged into water has been carried out with an extensive bibliographic search.

The initial intention was to compare de SPARC90-Jet code results against experimental data, but unfortunately there is not specific information about what happens inside the submerged gas jet. Consequently, only comparisons against processes which present analogies to submerged jets have been carried out. Among the final remarks derived from this work and mentioned in the previous section, the following ones may be highlighted:

- The mass flow rate affects quantitatively some important features of the submerged jet. As can be presupposed intuitively, as the mass flow rate is increased the momentum exchange between the submerged jet and the surrounding quiescent water is intensified, i.e., some quiescent water is eventually entrained into the gas jet. In addition, high mass flow rates result in higher values of the jet penetration length.
- The jet hydrodynamics is not only determined by the injection velocity-mass flow rate, but by the physical conditions of both, the liquid and gas phases. This aspect has been revealed in the experiments analyzed, having, for example, greater penetration lengths with lower discharge velocities.
- The disturbance waves, present in the gas-liquid interface, have been characterized for annular flows. Having developed correlations for his major variables, the wave frequency and celerity, they have been defined as function of dimensionless numbers in order to give generality to them. In particular, the wave celerity has been employed as a release point of the entrained droplets.
- As far as sizes of the entrained droplets are concerned say that are strongly dependent on gas flow rates. There is an inverse proportionality between size

distributions of the entrained droplets and gas mass flow rate, i.e., an increase in the gas velocity shifts the entrained droplets size toward smaller values and their distributions are more centered around the mean.

- Concerning droplet velocities, there is limited values of droplet velocities in submerged jets. The correlations based on annular flow data predict high values of droplet velocities, 0.5-0.8 of gas velocity near the centerline, whereas the limited previous data of submerged jets predicts low values, 1/30-1/60 of the gas velocity. Recent studies carried out by our research group indicate that droplet velocities are around 0.15-0.2 of gas velocity. All of these lines have been tested, providing better results the last of them.
- In relation to the amount of entrained droplets start by highlighting the importance and difficulty of his measurement in a submerged jet, since these entrained droplets will produce the aerosol capture throughout the jet region. Having only information of this variable inside pipes, all these correlations indicate that there is a direct proportionality between gas flow and amount of entrained droplets. Although the processes taking place in a submerged jet are far more complex than those of pipes, this complexity leads to three-dimensional complex flow structures with unsteady and pulsating behavior.

All these conclusions must be corroborated through future investigations to confirm these conclusions due to the scarcity of studies focused on the study of jet hydrodynamics.

10.2.2. Conclusions on Aerosol Capture

An in depth characterization of the aerosol capture process which takes place when a gas flow is coming out from a nozzle or hole submerged into water has been carried out with an extensive bibliographic search.

The SPARC90-Jet code results were compared and validated against the limited experimental data available in the literature, this process has provided valuable information to understand the jet-surrounding water behavior when aerosol particles are carried by the gas jet. From such an understanding, useful approaches for aerosol capture modeling have been derived. The major points of interest obtained can be summarized as follows:

- Collection of aerosols by single droplets may takes place by one or more of the several collection mechanisms, such as inertial impaction, interception, Brownian diffusion, electrostatic attraction, diffusiophoresis, thermophoresis, etc. Of all these mechanisms, the ones related with droplet-particle mechanical interactions are the most important in a submerged jet, in particular inertial impaction dominates for aerosol sizes bigger than 1.0 μm approximately, which is the case of the experimental data series under study.
- Particle size has been confirmed as a factor of major influence on DF values, an increase in particle size conducts to an important increase in the DF.

- The pool depth, submergence, is another key variable to determine the DF, an increase in submergence conducts to an increase in the DF. As it seems intuitive, the increase in the aerosol capture efficiency caused by changes in submergence, mainly or only should take place in the rising plume region. But it has been observed that the effect of submergence changes is seen in both regions. While it is true that this effect is more pronounced in the rising plume region.
- A large value of the inlet pressure conducts to higher values of DF, with similar effects than submergence.

All these conclusions must be corroborated through future investigations, in order to confirm these conclusions. Additionally, new trends dependent on other input variables could be found.

10.2.3. Confrontation of the Experimental DF Data against SPARC90 and SPARC90-Jet codes Predictions

In the two previous subsections have been listed the most remarkable findings of the two major aspects needed for the characterization of submerged jets. While along this last subsection, the calculations provided by the old SPARC90 and the new SPARC90-Jet code versions have been compared against the scarce experimental data when available.

Along the following lines the major insights related with the Decontamination Factor are listed, which comes from section "9.2. Results and Discussion of the Rising Plume, Jet and Overall Decontamination Factor". In particular, the comparison of its values provided by both codes and the experimental data, together with the major variables that influence its value are shown below:

- As can be observed in the experimental data, aerosol sizes is a factor of major influence on DF values, an increase in particle size conducts to an important increase in the DF. Small diameter aerosol particles (ϕ_p < 1 μm approximately) leads to low values of the DF (i.e., in the vicinity of 1), while large aerosol diameters (ϕ_p > 5 μm approximately) leads to high values of DF (DF > 100 approximately). This experimental trend is well captured by the new SPARC90-Jet code, while the old SPARC90 code is almost unable to find this experimental trend.
- Submergence has been confirmed to be another factor of major influence on DF values, an increase in depth of the discharge conducts to an important increase in the DF. This experimental trend is also well captured by the new SPARC90-Jet code, while the old SPARC90 code is almost unable to find this experimental trend, in particular, for small diameter aerosols the old code has a value of 1 approximately independently of the submergence. The pressure, not only due to the submergence, seems to have an important influence in the DF values. This last statement has to be taken even with more caution, since this variable has not been changed in a separated form in the experiments.

- As it intuitively seems, submergence dominates DF values in the rising plume, i.e., aerosol capture processes mainly takes place in the rising plume region, but it has an increasing tendency in the jet region too. There also is an upward tendency for small aerosol particles, but surprisingly, it is mainly caused by the jet region.
- Highlight that the SPARC90-Jet code provides much better results than SPARC90, being closer to the experimental data for all the studied tests.
- In certain tests the experimental data results and of the SPARC90-Jet calculations are not so close. But actually, the differences are not so important, if the aerosol collection efficiency is seen.

In summary, the influence in the DF values of the two major variables is well captured by the SPARC90-Jet code, not only the trend but also the magnitude. While the SPARC90 code catches neither the value nor the tendency in most of the experimental series. Particularly bad are the results provided for the experiments with small aerosol diameters (below 1 μm approximately). But remind that the original SPARC90 code was not intended for jet discharge processes, but only for globular discharges, consequently it is not so surprising the poor results of the old version in the majority of the experimental tests under study. To conclude remembering that all these statements have to be taken with caution because further investigations are needed.

10.3. Code Constraints and Further Works

As shown previously the aerosol capture processes, pool scrubbing phenomena, might take place mainly in the secondary side of a broken steam generator in a SGTR accident in a PWR plant, or in the suppression pools in a BWR plant during a SBO event. Therefore, in order to approach to the real situation several possible improvements and extension of SPARC90-Jet are expected in the future; however, a final version will require sets of specific experiments on submerged gaseous jets and a more extensive and sound database against which to compare. As a matter of fact, this is the key issue to develop further any model of jet injection scrubbing, data scarcity. So experimentation is of vital importance, so as to have expressions specifically developed for submerged jets and to have a larger database against which compare the code results. In addition, there are still many aspects of SPARC90-Jet code still susceptible to be improved, either because they rely on assumptions which need of further confirmation, on user experience and on own experimental results which are under analysis or because the available experimental data for the validation started in this document is not as extensive as desirable. The main gaps or assumptions of the present version of the SPARC90-Jet code can be summarized as follows:

- Constant conical expansion ratio along the spreading direction.
- Thermal exchanges gas jet - surrounding water have not been taken into consideration.

- Three main mechanisms of particle depletion have been considered (inertial impaction, interception and Brownian diffusion). Thermophoresis and diffusiophoresis might have importance for submicron particles. Electrophoresis can have some importance under certain circumstances.
- Droplets agglomeration/de-agglomeration processes have not been taken into account, it is assumed that interaction among droplets cannot take place.
- In the same direction, aerosol particle agglomeration and fragmentation of aggregates can play an important role, and in the present version has not been considered.
- The consideration of distribution functions of the entrained droplets is another simplification; in particular the Log-Normal Distribution seems to be the best option. Up to this moment the mean diameter of the entrained droplets in each cell has been used.
- Annular flow correlations have been mainly chosen to characterize the submerged jet hydrodynamics. Because of the lack of information specifically developed for submerged jets.
- Wet scrubber correlations have been chosen to estimate aerosol capture. Because of the lack of information specifically developed for submerged jets.

These are the major comments regarding simplifications and assumptions made in the current version of the code. In addition, in order to study adequately both accidental sequences, SGTR and SBO's, the effect of steam on discharges must be considered. While specifically for SGTRs, the effects of obstacles must also be taken into account. So that other important aspects that must be taken into account, and which need to be addressed in the future, are:

- The consideration of discharge processes with presence of condensable gases. Discharges with only condensable gases and mixtures of condensable-noncondesable gases must be considered.
- The introduction of obstacles. These obstacles correspond to the presence of the rest of the rod bundle of a SG, which will have an important influence in the case of a SGTR.

Another pending task, which can be made in the future, is the enhancement of the SPARC90-Jet code capabilities in order to be able to study the aerosol capture performance of Venturi scrubbers. These studies are of importance due to the recent applications of Venturi scrubbers in the filtered containment venting systems (FCVS). The Venturi scrubbers are high efficiency gas cleaners, in which the aerosols carried by the gas are removed by the entrained droplets formed during the atomization of the liquid inflow, the entrainment process takes place mainly in the Venturi throat.

The future possibility to increase in the capabilities of the SPARC90-Jet code, with an acceptable effort, is under study due to the high amount of similarities between a submerged jet and Venturi scrubbers used in FCVS. In fact, most of the collection

efficiency expressions for aerosol scrubbing found and which have been used here comes from wet scrubbers.

Therefore, a long way to go is still pending in order to reach the most ambitious marked objectives, but throughout this thesis a significant improvement in the calculation tools of the decontamination factor has been developed. Three future ways to improve the SPARC90-Jet code capabilities has been presented, consideration of discharges with noncondensable gases, presence of obstacles and enhancement of the code to study Venturi scrubbers. Up to now, promising results of the SPARC90-Jet code results has been obtained for the experimental data which met the code capabilities, i.e., pool discharges of non-condensable gases. The present research, in addition to the above mentioned promising results, has highlighted different open tasks that should be addressed in future research works. Mainly the need of experimental efforts in both, submerged jet hydrodynamics and aerosol particle removal, has been confirmed.

Published Papers

PUBLISHED PAPERS

This section collects the publications in journals and conferences that have been performed from the work presented in this thesis, or which are directly or indirectly related with the carried out work.

International Journals

- C. Berna, J. E. Juliá, A. Escrivá, J. L. Muñoz-Cobo, J. V. Pastor, C. Micó – "**Experimental investigation of the entrained droplet velocities in a submerged jet injected into a stagnant water pool"** – Experimental Thermal and Fluid Science, Vol. 82, pp. 32-41, April 2017.

- C. Berna, A. Escrivá, J. L. Muñoz-Cobo, L. E. Herranz – "**Enhancement of the SPARC90 code to pool scrubbing events under jet injection regime"** – Nuclear Engineering and Design, Vol. 300, pp. 653-677, April 2016.

- C. Berna, A. Escrivá, J. L. Muñoz-Cobo, L. E. Herranz - **"Review of droplet entrainment in annular flow: Characterization of the entrained droplets"** - Progress in Nuclear Energy, Vol. 79, pp. 64-86, March 2015.

- C. Berna, A. Escrivá, J. L. Muñoz-Cobo, L. E. Herranz - **"Review of droplet entrainment in annular flow: Interfacial waves and onset of entrainment"**- Progress in Nuclear Energy, Vol. 74, pp. 14-43, July 2014.

National Journals

- M. Sánchez, J. Pérez, S. Carlos, J. F. Villanueva, F. Sánchez, C. Queral, M. J. Rebollo, J. Rivas-Lewicky, G. Verdú, S. Gallardo, R. Miró, A. Querol, J. L. Muñoz-Cobo, A. Escrivá, C. Berna, F. Reventós, J. Freixa, V. Martínez, – **"Mejora y mantenimiento de códigos termohidráulicos de sistema en base a resultados de los experimentos OECD (PKL, ROSA y ATLAS) y su aplicación a plantas españolas. Proyecto CAMP-España"** – Revista de la Sociedad Nuclear Española, Nº 373, pp. 37-42, Mayo 2016.

- C. Berna, A. Escrivá, J. L. Muñoz-Cobo, J. M. Posada – **"Migración al código TRACE en su versión v5.0 p3 del modelo de planta de la central nuclear de TRILLO"** – Revista 41 Reunión Anual de la Sociedad Nuclear Española, Coruña, ESP, Nº 365, pp. 18, Septiembre 2015.

- C. Berna, A. Escrivá, J. L. Muñoz-Cobo, L. E. Herranz– **"Aumento de las capacidades del código SPARC para el estudio de procesos descarga de aerosoles a altas**

velocidades" – Revista 41 Reunión Anual de la Sociedad Nuclear Española, Coruña, ESP, Nº 365, pp. 63-64, Septiembre 2015.

- C. Berna, A. Escrivá, J. L. Muñoz-Cobo, L. E. Herranz, G. Bandini, S. Perez-Martin - **"Validación del código RELAP Sodio mediante la simulación de datos experimentales de la instalación CABRI"** – Revista 41 Reunión Anual de la Sociedad Nuclear Española, Coruña, ESP, Nº 365, pp. 64, Septiembre 2015.

- C. Berna, A. Escrivá, J. L. Muñoz-Cobo, J. M. Posada – **"Simulación de un disparo de turbina desde máximo nivel de potencia sin disparo del reactor en la planta de TRILLO con el código TRACE v5.0 p3"** – Revista 40 Reunión Anual de la Sociedad Nuclear Española, Valencia, ESP, Nº 354, pp. 125-126, Septiembre 2014.

-C. Berna, A. Escrivá, J. L. Muñoz-Cobo, L. E. Herranz - **"Desarrollo del modelo del reactor PHENIX con el código termohidráulico RELAP5-Na y simulación del transitorio PHENIX-EOL de circulación natural"** Revista 40 Reunión Anual de la Sociedad Nuclear Española, Valencia ESP, Nº 354, pp. 120, Septiembre 2014.

- L. E. Herranz, S. Pérez, G. Bandini, F. Jacq, C. Parisi, C. Berna - **"Development and validation of the ASTEC-Na thermal-hydraulic models"** – Revista 40 Reunión Anual de la Sociedad Nuclear Española, Valencia, ESP, Nº 354, pp. 15, Septiembre 2014.

- C. Berna, A. Escrivá, J. L. Muñoz-Cobo, L. E. Herranz – **"Desarrollo de Nuevas Correlaciones para Flujo Anular"** – Revista 39 Reunión Anual de la Sociedad Nuclear Española, Reus, ESP, Nº 343, pp. 104, Septiembre 2013.

- C. Berna, A. Escrivá, J. L. Muñoz-Cobo, A. Romero – **"Estudio de la extracción de calor residual por un generador de vapor en presencia de incondensables modelado con TRACE: experimento PKL III G1.1."** – Revista 38 Reunión Anual de la Sociedad Nuclear Española, Cáceres, ESP, Nº 332, pp. 76, Octubre 2012.

- C. Berna, A. Escrivá, J. L. Muñoz-Cobo, L. E. Herranz - **"Estudio de los Procesos de Captura de Aerosoles en Piscina para Inyecciones de Jets Gaseosos a Altas Velocidades: Mejoras del Código SPARC90"** – Revista 38 Reunión Anual de la Sociedad Nuclear Española, Cáceres, ESP, Nº 332, pp. 99, Octubre 2012.

- A. Escrivá, J. L. Muñoz-Cobo, C. Berna, L. E. Herranz – **"Adecuación del código SPARC90 para la simulación de la captura de aerosoles por rotura en el generador de vapor"** – Revista 37 Reunión Anual de la Sociedad Nuclear Española, Burgos, ESP, Nº 321, pp. 60, Septiembre 2011.

International Conferences

- C. Berna, A. Escrivá, J. L. Muñoz-Cobo, L. E. Herranz – "**Study of pool scrubbing under jet injection regime"**. 12th International Conference on Heat Transfer, Fluid Mechanics and Thermodynamics HEFAT2016, Malaga, Spain - Paper and Oral Presentation – July 2016.

- C. Berna, J. E. Juliá, A. Escrivá, J. L. Muñoz-Cobo, J. V. Pastor – "**Experimental characterization of the entrained droplet velocities into a submerged gaseous jet"**. 12th International Conference on Heat Transfer, Fluid Mechanics and Thermodynamics HEFAT2016, Malaga, Spain - Paper and Oral Presentation – July 2016.

- J. L. Muñoz-Cobo, A. Miquel, C. Berna, A. Escrivá – "**Spatial and time evolution of non linear waves in falling liquid films by the harmonic expansion method with predictor-corrector integration"**. 12th International Conference on Heat Transfer, Fluid Mechanics and Thermodynamics HEFAT2016, Malaga, Spain - Paper and Oral Presentation – July 2016.

- J. L. Muñoz-Cobo, A. Escrivá, C. Berna – "**Influence of the spacer location and the direct heating in the single and two phase region on the development of in-phase instabilities of BWR"**. 12th International Conference on Heat Transfer, Fluid Mechanics and Thermodynamics HEFAT2016, Malaga, Spain - Paper and Oral Presentation – July 2016.

- A. Miquel, J. L. Muñoz-Cobo, C. Berna, A. Escrivá – "**Comparison of polynomial chaos expansion methods for uncertainty quantification in CFD simulations"**. 12th International Conference on Heat Transfer, Fluid Mechanics and Thermodynamics HEFAT2016, Malaga, Spain - Paper and Oral Presentation – July 2016.

- G. Bandini, S. Ederli, C. Parisi, P. Palestra, M. Haselbauer, S. Perez-Martin, W. Hering, L. E. Herranz, C. Berna, A. Escriva, J. L. Muñoz-Cobo – **"Pre-test analyses for the experimental sodium loop KASOLA with ASTEC-Na and benchmarking with other codes"** . Proceedings of ICAPP 2015, Nice, FRA - Paper and Oral Presentation – May 2015.

- C. Berna, A. Escrivá, J. L. Muñoz-Cobo, L. E. Herranz – **"Development of new correlations for annular flow"** - Computational Methods in Multiphase Flow VIII, Valencia, ESP – ISSN 1743-3533 – Paper and Oral Presentation - April 2015.

-C. Berna, A. Escrivá, J. L. Muñoz-Cobo, L. E. Herranz – **"Enhancement of the SPARC90 code capabilities for pool scrubbing under jet injection regime"**

Computational Methods in Multiphase Flow VIII, Valencia ESP – ISSN 1743-3533 – Paper and oral Presentation - April 2015.

- L. E. Herranz, E. Fernández, C. López, C. Berna – **"Modeling Hydrodynamics of Submerged Gas Jets under Anticipated Conditions in Severe Nuclear Accidents"**. - 8th International Conference on Multiphase Flow ICMF 2013, Jeju, Korea – Paper and oral presentation – May 2013.

- C. Berna , A. Escrivá, J. L. Muñoz-Cobo – **"Analysis with TRACE Code of PKL III Test G 1.1&G1.1a"** - The 15th International Topical Meeting on Nuclear Reactor Thermalhydraulics, NURETH-15, Pisa, Italy – Paper and oral presentation - May 2013.

- C. Berna, A. Escrivá,, J. L. Muñoz-Cobo – **"Analysis with TRACE Code of PKL III Test G 1.1&G1.2"** - Joint PKL2-ROSA2 workshop on analytical activities related to OECD/NEA PKL and ROSA projects, Paris, FRA – Oral presentation - October 2012.

- C. Berna, A. Escrivá, J.L. Muñoz-Cobo, L. E. Herranz – **"Pool Scrubbing under Jet Injection Regime: An Enhancement of the SPARC90 Code"** – Proceedings of ICAPP 2012, Chicago, USA - Paper and oral presentation - June 2012.

- J. L. Muñoz-Cobo, A. Escrivá, C. García, C. Berna, J. Melara – **"Decay ratio calculation in the frequency domain with the LAPUR code using 1D-kinetics"** - PHYSOR 2012 – Advances in Reactor Physics – Linking Research, Industry, and Education Knoxville, Tennessee – Paper and oral presentation - April 2012.

National Conferences

- C. Berna, J. E. Juliá, A. Escrivá, J. L. Muñoz-Cobo, J. V. Pastor – **"Visualización de las trayectorias de las gotas arrastradas al interior de un chorro gaseoso sumergido mediante la técnica de fluorescencia inducida sobre un haz LASER plano"** – 42 Reunión Anual de la Sociedad Nuclear Española, Santander, ESP – Ponencia - Septiembre 2016.

- C. Berna, D. Blanco, A. Escrivá, J. L. Muñoz-Cobo – **"Simulación con TRACE de un transitorio de Station Blackout en la instalación experimental PKL"** – 42 Reunión Anual de la Sociedad Nuclear Española, Santander, ESP – Ponencia - Septiembre 2016.

- C. Berna, D. Blanco, A. Escrivá, J. L. Muñoz-Cobo, M. García, J. M. Posada – **"Últimos avances en la modelización y simulación de transitorios mediante el código TRACE V5.0 P4 de la planta nuclear de TRILLO"** – 42 Reunión Anual de la Sociedad Nuclear Española, Santander, ESP – Ponencia - Septiembre 2016.

- J. L. Cuadros, J. L. Muñoz-Cobo, C. Berna, S. Chiva, A. Escrivá, G. Monrós– **"Estudio del flujo anular aire agua co-corriente en tubería vertical ascendente"** – 42 Reunión Anual de la Sociedad Nuclear Española, Santander, ESP – Ponencia - Septiembre 2016.

- C. Berna, A. Escrivá, J. L. Muñoz-Cobo, J. M. Posada – **"Migración al código TRACE en su versión v5.0 p3 del modelo de planta de la central nuclear de TRILLO"** - 41 Reunión Anual de la Sociedad Nuclear Española, Coruña, ESP – Ponencia - Septiembre 2015.

- C. Berna, A. Escrivá, J. L. Muñoz-Cobo, L. E. Herranz – **"Aumento de las capacidades del código SPARC para el estudio de procesos descarga de aerosoles a altas velocidades"** - 41 Reunión Anual de la Sociedad Nuclear Española, Coruña, ESP – Ponencia - Septiembre 2015.

- C. Berna, A. Escriva, J. L. Muñoz-Cobo, L. E. Herranz, G. Bandini, S. Perez-Martin – **"Validación del código RELAP Sodio mediante la simulación de datos experimentales de la instalación CABRI"** - 41 Reunión Anual de la Sociedad Nuclear Española, Coruña, ESP – Ponencia – Septiembre 2015.

- C. Berna, A. Escrivá, J. L. Muñoz-Cobo, J. M. Posada – **"Simulación de un disparo de turbina desde máximo nivel de potencia sin disparo del reactor en la planta de TRILLO con el código TRACE v5.0 p3"** - 40 Reunión Anual de la Sociedad Nuclear Española, Valencia, ESP – Poster - Septiembre 2014.

- C. Berna, A. Escrivá, J. L. Muñoz-Cobo, L. E. Herranz - **"Desarrollo del modelo del reactor PHENIX con el código termohidráulico RELAP5-Na y simulación del transitorio PHENIX-EOL de circulación natural"** - 40 Reunión Anual de la Sociedad Nuclear Española, Valencia ESP – Ponencia- Septiembre 2014.

- L. E. Herranz, S. Pérez, G. Bandini, F. Jacq, C. Parisi, C. Berna– **"Development and validation of the ASTEC-Na thermal-hydraulic models"** - 40 Reunión Anual de la Sociedad Nuclear Española, Valencia, ESP – Ponencia- Septiembre 2014.

- C. Berna, A. Escrivá, J. L. Muñoz-Cobo, L. E. Herranz – **"Desarrollo de Nuevas Correlaciones para Flujo Anular"** -39 Reunión Anual de la Sociedad Nuclear Española, Reus, ESP – Ponencia- Septiembre 2013.

- C. Berna, A. Escrivá, J. L. Muñoz-Cobo, A. Romero – **"Estudio de la extracción de calor residual por un generador de vapor en presencia de incondensables modelado con TRACE: experimento PKL III G1.1."** - 38 Reunión Anual de la Sociedad Nuclear Española, Cáceres, ESP – Ponencia- Octubre 2012.

- C. Berna, A. Escrivá, J. L. Muñoz-Cobo, L. E. Herranz – **"Estudio de los Procesos de Captura de Aerosoles en Piscina para Inyecciones de Jets Gaseosos a Altas Velocidades: Mejoras del Código SPARC90"** - 38 Reunión Anual de la Sociedad Nuclear Española, Cáceres, ESP – Ponencia- Octubre 2012.

- A. Escrivá, J. L. Muñoz-Cobo, C. Berna, L. E. Herranz – **"Adecuación del código SPARC90 para la simulación de la captura de aerosoles por rotura en el generador de vapor"** - 37 Reunión Anual de la Sociedad Nuclear Española, Burgos, ESP – Ponencia- Septiembre 2011.

References

REFERENCES

- Adechi D., & Issa R. I., "**Modelling of annular flow through pipes and T-juntions**". Computers and Fluids, Vol. 33, pp. 289-313 (2004).
- Al-Sarkhi A., & Hanratty T. J., "**Effect of pipe diameter on the drop size in a horizontal annular gas-liquid flow**". International Journal of Multiphase Flow, Vol. 28, pp. 1617-1629 (2002).
- Al-Sarkhi A., Sarica C., & Magrini K., "**Inclination Effects of Wave Characteristics in Annular Gas-Liquid Flows**". AIChE Journal, Vol. 58, pp. 1018-1029 (2012a).
- Al-Sarkhi A., Sarica C., & Qureshi B., "**Modeling of droplet entrainment in co-current two-phase flow: A new approach**". International Journal of Multiphase Flow, Vol. 39, pp. 21-28 (2012b).
- Alamu M. B., "**Investigation of Periodic Structures in Gas-Liquid Flow**".. PhD. Thesis University of Nottingham (2010).
- Alekseenko S., Cherdantsev A. V., Cherdantsev M. V., Isaenkov S. V., & Markovich D. M., "**Study of formation and development of disturbance waves in annular gas-liquid flow**". International Journal of Multiphase Flow, Vol. 77, pp. 65-75 (2015).
- Alekseenko S., Antipin V., Cherdantsev A., Kharlamov S., & Markovich D., "**Two-Wave Structure of Liquid Film and Wave Interrelation in Annular Gas-Liquid Flow with and without Entrainment**". Physics of Fluids, Vol. 21 Nº1, N^{er} 061701 (2009).
- Alekseenko S., Antipin V., Cherdantsev A., Kharlamov S., & Markovich D., "**Investigation of Waves Interaction in Annular Gas-Liquid Flow Using High-Speed Fluorescent Visualization Technique**". Microgravity Science Technology, Vol. 20 Nº1, pp .271 (2008).
- Allen E., Smith P., & Henshaw J., **"A review of particle agglomeration"**. AEA Technology plc, AEAT/R/PSEG/0398 (2001).
- Alipchenkov V. M., Nigmatulin R. I., Soloviev S. L., Stonik O. G., Zaichik L. I., & Zeigarnik Y. A., "**A Three-Fluid Model to Two-Phase Dispersed-Annular Flow**". International Journal of Heat and Mass transfer, Vol. 47, pp. 5323-5338 (2004).
- Allelein H.-J., Auvinen A., Ball J., Güntay S., Herranz L. E., Hidaka A., Jones A. V., Kissane M., Powers D., & Webber G., **"State of the art report on nuclear aerosols"**. NEA/CSNI/R (2009).
- Andreussi P., Asali J. C., & Hanratty T. J., "**Initiation of Roll Waves in Gas-Liquid Flows**". AIChE Journal, Vol. 31 Nº1, pp. 119-126. (1985).
- Andronache C., Gronholm T., Laakso L., Phillips L., & Venalainen A. "**Savenging of ultrafine particles by rainfall at a boreal site: observations and model estimations**". Atmospheric Chemistry and Physics, Vol. 6, pp. 4739-4754. (2006).

- Arnold C. R., & Hewitt G. F., "**Further developments in the photography of two phase gas-liquid flow**". Journal of Photographic Science, Vol. 15, pp. 97-114 (1967).
- Asali J. C., & Hanratty T. J., "**Ripples generated on a liquid film at high gas Velocities**". International Journal of Multiphase Flow, Vol. 19, No. 2, pp. 229-243 (1993).
- Asali J. C., Hanratty T. J., & Andreussi, P., **"Interfacial drag and film height for vertical annular flow"**. American Institute of Chemical Engineers Journal, Vol. 31, No. 6, pp. 895-902 (1985).
- Ashgriz N., "**Handbook of atomization and sprays**". Springer Science & Business Media (2011).
- ASME, **"Standard for verification and validation in computational fluid dynamics and heat transfer"**, ASME V V 20 (2009).
- Azzopardi B. J., "**Mechanisms of Entrainment in Annular Two-Phase Flow**". UKAEA report AERE-11068 (1983).
- Azzopardi B. J., "**Drops in annular two-phase flow**". International Journal of Multiphase Flow, Vol. 23, pp. 1-53. (1997).
- Azzopardi B. J., **"Gas-Liquid Flows**". Begell House Inc., New York (2006).
- Azzopardi B. J., Piearcey A., & Jepson D. M., **"Drop size measurements for annular two-phase flow in a 20 mm diameter vertical tube"**. Exp. Fluids, Vol. 11, pp. 191-197 (1991).
- Baniamerian Z., & Aghanajafi C., "**Simulation of entrainment mass transfer in annular two-phase flow using physical concept**". Journal of Mechanics, Vol. 26, No.3, pp. 385-392. (2010).
- Belt R. J., Van't Westende J. M. C., Prasser H. M., & Portela L. M., "**Time and spatially resolved measurements of interfacial waves in vertical annular flow**". International Journal of Multiphase Flow, Vol. 36, pp. 570-587 (2010).
- Berna C., Escrivá A., Muñoz-Cobo J. L., & Herranz L. E., **"Pool Scrubbing under Jet Injection Regime: An Enhancement of the SPARC90 Code"**. Proceedings of ICAPP'12, Chicago, USA (2012).
- Berna C., Escrivá A., Muñoz-Cobo J. L., & Herranz L. E., **"Review of droplet entrainment in annular flow: interfacial waves and onset of entrainment"**. Progress in Nucear. Energy, vol. 74, pp. 14-43 (2014).
- Berna C., Escrivá A., Muñoz-Cobo J. L., & Herranz L. E., **"Review of droplet entrainment in annular flow: characterization of the entrained droplets"**. Progress in Nuclear. Energy, vol. 79, pp. 64-86 (2015a).
- Berna C., Escrivá A., Muñoz-Cobo J. L., & Herranz L. E., **"Enhancement of the SPARC90 code capabilities for pool scrubbing under jet injection regimes "**. Computational Methods in Multiphase Flow VIII, WIT Press, pp. 273-285 (2015b).

- Berna C., Escrivá A., Muñoz-Cobo J. L., & Herranz L. E., **"Enhancement of the SPARC90 code to pool scrubbing events under jet injection regime"**. Nuclear Engineering and Design, vol. 300, pp. 563-577 (2016).
- Berna C., Juliá J. E., Escrivá A., Muñoz-Cobo J. L., & Pastor J. V., **"Experimental Investigation of the Entrained Droplet Velocities in a Submerged Jet Injected into a Stagnant Water Pool"**. Experimental Thermal and Fluid Science, Vol. 82, pp. 32-41 (2017).
- Biasi L., de los Reyes A., Reeks M.W., & de Santi G.F., **"Use of a simple model for the interpretation of experimental data on particle resuspension in turbulent flows"**. Journal of Aerosol Science, Vol. 32, pp. 1175-1200 (2001).
- Brodkey R. S., "**The phenomena of fluid motions"**. Addison-Wesley, p. 112 (1967).
- Bubnov V. A., **"Turbulent Isentropic Flows".** Journal of Engineering and Thermophysics, Vol. 71, p. 334-339 (1998).
- Carreau J. L., roger F., Loukarfi L., & Gbahoue L. **"Penetration of a horizontal gas jet submerged in a liquid"**. Raport Technique of CEA, DRNR/P/Nº 346 (1986).
- Chandrasekhar S., "**Hydrodynamic and Hydromagnetic Stability**". Oxford University Press (1981).
- Cheng N-S., "**Comparison of formulas for drag coefficient and settling velocity of spherical particles**". Powder Technology, Vol. 189, pp. 395-398 (2009).
- Cherdantsev A. V., Hann D. B., & Azzopardi B. J., **"Study of gas-sheared liquid film in horizontal rectangular duct using high-speed LIF technique: three-dimensional wavy structure and its relation to liquid entrainment"**. International Journal of Multiphase Flow, Vol. 67, pp. 52-64 (2014).
- Cherdantsev A. V., Hann D. B., Hewakandamby B. N., & Azzopardi B. J., **"Study of droplets deposited from the gas core onto a gas-sheared liquid film"**. International Journal of Multiphase Flow, Vol. 88, pp. 69-86 (2017).
- Chung H. S., & Murgatroyd W., "**Studies of the Mechanism of Roll Wave Formation on Thin Liquid Films**"**.** Symp. on Two-Phase Flow, Vol. 2, Paper A2, Exeter, UK (1965).
- Cieslinski J. T., & Mosdorf R., **"Gas bubble dynamics – experiment and fractal analysis"**. International Journal of Heat and Mass Transfer, Vol. 48, pp. 1808 (2005).
- Cioncolini A., & Thome J. R., "**Prediction of the entrained liquid fraction in vertical annular gas–liquid two-phase flow**". International Journal of Multiphase Flow, Vol. 36, pp. 293-302 (2010).
- Clement C.F., & Harrison R.G., **"Enhanced localized charging of radioactive aerosols"**. J. Aerosol Sci., Vol. 31, pp. 363-378 (2000).
- Cooper K. D., Hewitt, G. F., & Pinchin B., "**Photography of two-phase gas-liquid Flow**". Journal of Photographic Science, Vol. 12, pp. 269 (1964).

- Cousins L. B., Denton W. H., & Hewitt G. F., "**Liquid mass transfer in annular two-phase flow**". Symposium on Two Phase Flow, Exter, Engand (1965).
- Crowe C. T., **"Multiphase Flow Handbook (Mechanical Engineering)".** CRC Press, Taylor and Francis Group (2006).
- Dai Z., Wang B., & Qi L., **"Experimental study on hydrodynamic behaviors of high-speed gas jets in still water"**. Acta Mechanica Sinica Vol. 22 pp. 443–448 (2006).
- Dallman J. C., **"Investigation of separated flow model in annular gas–liquid two-phase flows"**. Ph.D. Thesis, University of Illinois, Urbana (1978).
- Dasgupta A., Chandraker D. K., Kshirasagar S., Raghavendra Reddy B., Rajalakshimi R., Nayak A. K., Walker S. P., & Hewitt G. G., **"Experimental investigation on dominant waves in upward air-water two-phase flow in churn and annular regime"**. Experimental Thermal and Fluid Science, Vol. 81, pp. 147-163 (2017).
- Davies C. N., **"Definitive Equations for the Fluid Resistance of Spheres"**. Proceedings of the Physical Society of London, Vol. 57, pp. 259-270 (1945).
- Davies C.N., **"Aerosol Science"**. Academic Press (1966).
- Dehbi A., Suckow D., & Güntay S., **"Aerosol Retention in Low-Subcooling Pools under Realistic Accident Conditions"**. Nuclear Engineering and Design 203, pp. 229-241 (2001).
- Dehbi A., Suckow D., & Lind T., **"Summary report on ARTIST Phase V tests for retention in the flooded bundle".** PSI, TM-42-08-18 ARTIST-75-08 (2008).
- DiNunno J. J., Anderson F. D., Baker R. E., & Waterfield R. L., "**Calculation of distance factors for power and test reactor sites"**. Atomic Energy Commission (1962).
- Epstein M., "**Theory of scrubbing of volatile fission product vapor containing gas jet in a water pool"**. ANS Winter Meeting November 11-16 1990, Washington DC, pp. 21-32 (1990).
- Escudero M., Marcos M. J., Swiderska-Kowalczyk M., Martin M., & López-Jiménez J., **"State of the art review on fission products aerosol pool scrubbing under severe accident conditions"**. Nuclear Science and Technology, European Commission Report, EUR 16241 EN (1995).
- Epstein M., **"Theory of Scrubbing of Volatile Fission Product Vapor Containing Gas Jet in a Water Pool".** ANS Winter Meeting, Washington DC, p. 21 (1990).
- Fernandes R. L. J., Jutte B. M., & Rodriguez M. G., "**Drag reduction in horizontal annular two-phase flow"**. International Journal of Multiphase Flow, Vol. 30, pp.1051-1069 (2004).
- Fernández Alonso D., Gonçalves J. A. S., Azzopardi B. J., & Coury J. R., "**Drop size measurements in Venturi scrubbers"**. Chemical Engineering Science, Vol. 56, pp.4901-4911 (2001).

- Flagan R. C., & Seinfeld J. H., **"Fundamentals of Air Pollution Engineering"**. Prentice Hall (1988).
- Flores A. G, Crowe K. E., & Griffith P., **"Gas-phase secondary flow in horizontal, stratified and annular two-phase flow"**. International Journal of Multiphase Flow, Vol. 21, No 2, pp. 207-221 (1995).
- Fore L. B. & Dukler A. E., **"The distribution of drop size and velocity in gas-liquid annular flow"**. Int. J. Multiphase Flow 21, pp. 137-149 (1995).
- Fore L. B, Ibrahim B. B., & Beus S. G., "**Visual measurements of droplets size in gas-liquid annular flow**". International Journal of Multiphase Flow, Vol. 28, pp. 1895-1910 (2002).
- Fukano T., & Furukawa T., "**Prediction of the Effects of Liquid Viscosity on Interfacial Shear Stress and Frictional Pressure Drop in Vertical Upward Gas-Liquid Annular Flow**". International Journal of Multiphase Flow, Vol. 24, No 4, pp. 587-603 (1998).
- Gamble R. E., Nguyen T. T., Shiralkar B. S., Peterson P. F., Greif R., & Tabata H., **"Pressure suppression pool mixing in passive advanced BWR plants"**. Nuclear Engineering and Design Vol. 204, pp. 321–336, (2001).
- Gelfand B. E., **"Droplet breakup phenomena in flows with velocity lag"**. Prog. Energ. Combust., Vol 22, pp. 201–265 (1996).
- Gjesing R., Hattel J., & Frisching U., **"Coupled atomization and spray modeling in the spray forming using openfoam**". Engineering Applications of Computational Fluid Mechanics, Vol. 3, No4, pp. 471-486 (2009).
- Gendarmes F., Boulaud D., & Renoux A., **"Electrical charging of radioactive aerosols - comparison of the Clement-Harrison model with new experiments"**. J. Aerosol Sc. Vol. 32, pp. 1437-1458 (2001).
- Gesselschaft für Reaktorsicherheit, **"German risk study nuclear power plants, Phase B a summary"**. Federal Minister of Research and Technology, GRS-74, Cologne, Federal Republic of Germany (1986).
- Gesselschaft für Reaktorsicherheit, **"The German risk study: summary"**. Federal Minister of Research and Technology, Cologne, Federal Republic of Germany (1979).
- Gormley P.G., & Kennedy M., **"Diffusion from a stream flowing through a cylindrical tube"**. Proc. Roy. Irish Academy, Vol. 52, pp. 163 (1949).
- Guildenbecher D. R., López-Rivera C. & Sojka P. E., "**Secondary atomization**". Experimental Fluids, Vol. 46, pp. 371-402 (2009).
- Gulawani S. S., Desphande S. S., Joshi J. B., Shah M.S., Prasad C. S. R., & Shukla D.S., "**Submerged gas jet into a liquid bath: A review**". Ind. Eng. Chem. Res., Vol. 46, No. 10 (2007).
- Güntay S., Dehbi A., Suckow D., & Birchley J., **"Accident management issues within the ARTIST project"**. NEA/CSNI/R (2001) 20, Nuclear Energy Agency (2001).

- Güntay S., Suchow D., Debhi A., & Kapulla R., **"ARTIST: Introduction and First Results".** Nuclear Engineering and Design, Vol. 231, pp. 109-120 (2004).
- Hall-Taylor N. S., Hewitt G. F., & Lacey P. M. C., "**The motion and frequency of large disturbance waves in annular two-phase flow of air-water mixtures**". Chemical Engineering Science, Vol. 18, pp. 537-552 (1963).
- Han H., Zhu Z., & Gabriel K., "**A study on the effect of gas flow rate on the wave characteristics in two-phase gas-liquid annular flow**". Nuclear Engineering and Design Nº 236, pp. 2580–2588 (2006).
- Hanratty T. J., & Engen M., "**Interaction between a turbulent air stream and a moving water surface**". AIChE Journal, Vol. 3 p. 299 (1957).
- Hanratty T. J., & Hersman A., "**Initiation of roll waves**". American Institute of Chemical Engineers Journal, Vol. 7 p. 488 (1961).
- Harby K., Chiva S., & Muñoz-Cobo J. L., **"An experimental investigation on the characteristics of submerged horizontal gas jets in liquid ambient"**. Experimental Thermal and Fluid Science, Vol. 53, pp. 26-39 (2014).
- Haste T., Payot F., & Bottomley P. D. W., **"Transport and deposition in the Phébus FP circuit"**. Annals of Nuclear Energy, Vol. 61, pp. 102-121 (2013).
- Henstock W. H., & Hanratty T. J., "**The interfacial drag and the height of the wall layer in annular flows**". AIChE Journal Vol.22 N.6, pp. 990-1000 (1976).
- Herranz L. E., & López C., **"ARI3SG: Aerosol Retention in the Secondary Side of a Steam Generator. Part I: Model essentials, verification and correlation".** Nuclear Engineering and Design, Approved Publication (2012).
- Herranz L. E., Fernández E., López C., & Berna C., **"Modeling Hydrodynamics of Submerged Gas Jets under Anticipated Conditions in Severe Nuclear Accidents"**. 8th International Conference on Multiphase Flow (ICMF 2013), Jeju, Korea (2013).
- Herranz L. E., Lind T., Dieschbourg K., Riera E., Morandi S., Rantanen P., Chebbi M., & Losch N., **"Technical Bases for Experimentation on Source Term Mitigation: The EU-PASSAM Project"**. The 10th International Topical Meeting on Nuclear Thermal-Hydraulics, Operation and Safety (NUTHOS-10), Okinawa, Japan (2014).
- Hewitt G. F., & Govan A. H., "**Phenomena and prediction in annular two-phase flow, advances in gas-liquid flows**". American Society of Mechanical Engineers, Winter Meeting, pp. 41-56 (1990).
- Hewitt G. F., & Hall-Taylor N. S., "**Annular Two-Phase Flow**". Pergamon Press, Oxford, pp. 136-139 (1970).
- Hewitt G. F., & Lovegrove P. C., "**Frequency and velocity measurements of disturbance waves in annular two-phase flow**". AKAEA Report, AERE-R4304 (1969).
- Hills J. H., "**The critical liquid flow rates for wave and droplet formation in annular gas–liquid flow"**. Exp. Heat Transfer Fluid Mech. Thermodyn. Ed. ETS 2, 1241–1247 (1997).

- Hinze J. O., "**Fundamentals of the Hydrodynamic Mechanism of Splitting in Dispersion Process**". AIChE Journal, Vol. 1, pp. 289-295 (1955).
- Hoefele E. O., "**Flow regimes of submerged gas jets**". PhD. Thesis, British Columbia University (1972).
- Hoefele E. O., & Brimacombe J. K., "**Flow Regimes in Submerged Gas Injection**". Metallurgical Transactions, Vol. 10B, pp. 631-648 (1979).
- Holowach M. J., Hochreiter L. E., & Cheung F. B., "**A model for droplet entrainment in heated annular flow**". International Journal of Heat and Fluid Flow, Vol. 23, pp. 807-822 (2002).
- Housiadas C., & Drossinos Y. **"Thermophetic deposition in tube flow"**. Aerosol Sci. Tech., Vol, 39, pp. 304-318 (2005).
- Hsiang L. P., & Faeth G. M., **"Near- Limit Drop Deformation and Secondary Breakup"**. International Journal of Multiphase Flow, Vol. 18, No 5, pp. 635-652 (1992).
- Hsiang L. P., & Faeth G. M., **"Drop deformation and breakup due to shock wave and steady disturbances"**. International Journal of Multiphase Flow, Vol. 21 No 4 pp. 545-560 (1995).
- Hughmark G. A., "**Film Thickness, Entrainment and Pressure Drop in Upward Annular and Dispersed Flow**". AIChE Journal, Vol. 19, pp. 1062-1065 (1973).
- IAEA-INES, "**INES the International Nuclear and Radiological Event Scale User's Manual 2008 Edition**". International Atomic Energy Agency (2013).
- IAEA-INSAG-10, "**Defence in Depth in Nuclear Safety INSAG-10**". Report by the International Nuclear Safety Advisory Group of the International Atomic Energy Agency (1996).
- Ishii M., & Grolmes M. A., "**Inception Criteria for Droplet Entrainment in Two-Phase Concurrent Film Flow**". AIChE Journal, Vol. 21 p. 308-318 (1975).
- Ishii M., & Kataoka I., "**Interfacial transfer in annular dispersed flow".** Argonne National Laboratoty, Conf.-820811-2, DE83-009571 (1983).
- Jacowitz L. A., & Brodkey R. S., "**An analysis of geometry and pressure drop for the horizontal annular two-phase flow of water and air in the entrance region of a pipe**". Chemical Engineering Science, Vol. 19, No. 4, pp. 261-274 (1964).
- Jacquemain D., **"Nuclear Power Reactor Core Melt Accidents"**, edp sciences, IRSN (2015).
- Jiao B., Qiu L., & Gan Z., "**Liquid Film Dryout Model for Predicting Critical Heat Flux in Annular Two-phase Flow**". Journal of Zheijang University SCIENCE A, Vol. 10, No3, pp. 398-417 (2009).
- Jimenez Varas G., **"Análisis integrado de seguridad de un accidente de SGTR en un reactor nuclear tipo PWR"**. PhD. Thesis Polytechnic University of Madrid (2012).

- Jung C. H., & Lee K. W., **"Filtration of fine particles by multiple liquid droplet and gas bubble systems"**. Aerosol Science and Technology, Vol. 29, pp. 389-401 (1998).
- Kataoka I., & Ishii M., "**Mechanism and correlation of droplet entrainment and deposition in annular two-phase flow**". NUREG/CR-2885, ANL-82-44 (1982).
- Kataoka I., & Ishii M., "**Entrainment and deposition rates of droplets in annular two-phase flow**". Conference ASME-JSME thermal engineering joint conference, Honolulu, HI, USA, Conference 830301—11, De83 009454 (1983).
- Kataoka I., Ishii M., & Nakayama A., "**Entrainment and deposition rates of droplets in annular two-phase flow**". International Journal of Heat and Mass Transfer, Vol. 43, pp. 1573-1589. (2000).
- Kim B. H., Peterson G. P., & Khim K. D., "**Analytical and experimental investigation of entrainment in capillary pumped wicking structures"**. Journal of Energy Resources Technology, Vol. 115, Decembre 1993, pp. 278-286. (1993).
- Kim H. T., Jung C. H., Oh S. N., & Lee K. W., "**Particle removal efficiency of gravitational wet scrubber considering diffusion, interception and impaction"**. Environmental Engineering Science, Vol. 18, No 2, pp. 125-136. (2001).
- Kissane M. P., **"On the nature of aerosols produced during a severe accident of a watercooled nuclear reactor"**. Nuclear. Engineering and. Design, Vol. 238, pp. 2792–2800 (2008).
- Kocamustafaogullari G., Smits S. R., & Razi J., "**Maximum and mean droplet sizes in annular two-phase flow**". International Journal of Heat and Mass Transfer, Vol. 37, pp. 955-965. (1994).
- Kolev N. I., "**Multiphase flow dynamics: thermal and mechanical interactions"**. Springer Science & Business Media, 3th Edition (2007).
- Krzeczkowski S., **"Measurement of liquid droplet disintegration mechanisms"**. International Journal of Multiphase Flow, Vol. 6 pp. 227-239 (1980).
- Lamb H., "**Hydrodynamics**". Cambridge University Press. 6th Edition. (1975).
- Laurinat J. E., "**Studies of the effects of pipe size on horizontal annular two-phase flows**". Ph.D. Thesis, University of Illinois, Urbana (1982).
- Leonard M. T:, Gauntt R. O., & Powers D. A., **"Accident Source Terms for Boiling Water Reactors with High Burnup Cores Calculated Using MELCOR 1.8.5"**. Sandia Report, SAND2007-7697 (2007).
- Levich V. G., **"Physicochemical hydrodynamics"**. Prentice-Hall, Englewood Cliffs N.J. (1962).
- Levy S., "**Two-Phase Flow in Complex Systems**". John Wiley & Sons INC. (1999).

- Liao Y., & Guentay S., **"Potential steam generator tube rupture in the presence of severe accident thermal challenge and tube flaws due to foreign object wear".** Nuclear Engineering and Design, Vol. 239, pp. 1128-1135 (2009).
- Lind T., & Suckow D., **"Report on the ARTIST II Phase V tests for the aerosol retention in the flooded bundle".** PSI, TM-42-10-02 ARTIST-84-09 (2010a).
- Lind T., Ammar Y., Dehbi A., & Güntay S., **"De-agglomeration mechanisms of TiO_2 aerosol agglomerates in PWR steam generator rupture conditions"**. Nuclear Engineering and Design, Vol. 240, pp. 2046-2053 (2010b).
- Lind T., Dehbi A., & Suckow D., **"Aerosol retention in the flooded steam generator bundle during SGTR".** Nuclear Engineering and Design, Vol. 241, pp. 357–365 (2011).
- Liu H., **"Science and engineering of droplets – Fundamentals and applications"**. Noyes Publications, Park Ridge, New Jersey, U.S.A. (2000).
- Lopes J. C. B., "**Droplet sizes, dynamics and deposition in vertical annular flow**". PhD. Thesis University of Houston (1984).
- Lopez C., & Herranz L. E., **"ARI3SG: Aerosol Retention in the Secondary Side of a Steam Generator. Part II: Model validation and uncertainty analysis".** Nuclear Engineering and Design, Approved Publication (2012).
- Lopez de Bertodano M. A., Assad A., & Beus S. G., "**Entrainment Rate for Droplets in the Ripple-Annular Regime for Small Vertical Tubes**". Bettis Atomic Power Laboratory, document DE-AC11-93PN38195 (1998).
- López-Jiménez J., Herranz L. E., Escudero M. J., Espigares M. M., Peyrés V., Polo J., Kortz Ch., Koch M. K., Brockmeier, Unger H., Dutton L. M. C., Smedley Ch., Trow W., Jones A. V., Bonanni E., Calvo M., & Alonso A., **"Pool scrubbing"**. Informes Técnicos Ciemat, N^{er} 805 (1996).
- Lopez C., & Herranz L. E., **"ARI3SG: Aerosol Retention in the Secondary Side of a Steam Generator. Part II: Model validation and uncertainty analysis".** Nuclear Engineering and Design, Vol. 248, pp. 282-292 (2012).
- Lopez de Bertodano M. A., Assad A., & Beus S.G., **"Experiments for entrainment rate of droplets in the annular regime".** International Journal of Multiphase Flow, Vol. 27, pp. 685-699 (2001).
- Loth E., "**Computational fluid dynamics of bubbles, drops and particles**". Draft Cambridge University Press (2010).
- Loth E., & Faeth G. M., **"Structure of underexpanded round air jets submerged in water"**, International Journal of Multiphase Flow , Vol.15, pp. 589–603 (1989).
- Loth E., & Faeth G. M., **"Structure of plane underexpanded air jets into water"**, AIChE Journal, Vol.36, No. 6, pp. 818–826 (1990).
- Loyalka S.K., **"Velocity slip coefficient and diffusion slip velocity for a multicomponent gas mixture"**. Physics of Fluids, Vol. 14, n° 12, pp. 2599-2604 (1971).

- Lozano O., Chiang C-P., & Llopis C., **"Development of a Vandellos II NPP Model using the TRACE Code: Application to an Actual Transient of Main Coolant Pumps Trip and Start-up"**. U.S. Nuclear Regulatory Commission, NUREG/IA-0243 (2011).
- MacDonald P. E., Shah V. N., Ward L. W., & Ellison P. G., **"Steam Generator Tube Failures"**. U. S. Nuclear regulatory Commission, NUREG/CR-6365 (1996).
- MacGillivray R., "**Gravity and Gas Density Effects on Annular Flow Average Film Thickness and Frictional Pressure Drop**". Ph.D. thesis, University of Saskatchewan, Saskatoon, Canada (2004).
- McCoy D. D., & Hanratty T. J., **"Rate of deposition of droplets in annular two-phase flow".** International Journal of Multiphase Flow, Vol. 3, No 4, pp. 319–331 (1977).
- Mantilla I., **"Mechanistic Modeling of Liquid Entrainment in Gas in Horizontal Pipes".** PhD. Thesis University of Tulsa (2008).
- Marshall W. R., "**Atomization and spray drying**". Chem. Engr. Prog. Monograph Series, No. 2, Vol. 50 (1954).
- Martin C. J., "**Annular Two Phase Flow**". Ph.D. thesis, Oxford University, U.K. (1983).
- Mugele R. A., & Evans H. D., **"Droplet size distribution in sprays"**. Ind. Enging Chem., Vol. 43, pp.1317-1324 (1951).
- Muñoz-Bueno R., Hontañón E., & Rucandio M.I., **"Deposition of fine aerosols in laminar tube flow at high temperature with large gas-to-wall temperature gradients"**. J. Aerosol Sci., Vol. 36(4), pp. 495-520 (2005).
- Nakazatomi M., & Sekoguchi K., **"Effect of pressure on entrainment flow rate in vertical upward gas-liquid annular two-phase flow. Part II: An assessment of published correlations of entrainment flow rate through high-pressure data and proposal of new correlations"**. Heat transfer-Japanese Research, Vol. 25(5), pp. 281-292 (1996).
- Newberry S., Donoghue J., Enris R., Lund R., Rubin A. & Yerokun J., **"Indian Point 2 Steam Generator Tube Failure Lessons-Learned Report"**. NRC technical report, TAC No. MA9163, ML013540068 (2000).
- Nikolaidis T., **"Water Ingestion Effects on Gas Turbine Engine Performance"**. PhD. Thesis University of Cranfield (2008).
- Ohba K., & Nagae K., "**Characteristics and behavior of the interfacial wave on the liquid film in a vertically upward air-water two-phase annular flow**". Nuclear Engineering and Design, Vol. 141, No. 1-2, pp. 17-25 (1993).
- Okawa T., Kitahara T., Yoshida K., Matsumoto T., & Kataoka I., "**New Entrainment rate Correlation in Annular Two-Phase Flow Applicable to Wide Range of Flow Condition**". International Journal of Heat and Mass Transfer, Vol. 45, pp. 87-98 (2002).

- Okawa T., Kotani A., Kataoka I., & Naito M., "**Prediction of Critical Heat Flux in Annular Flow Using a Film Flow Model**". Journal of Nuclear Science and Technology, Vol. 40, pp. 388-396. (2003).
- Omebere-Iyari N. K., & Azzopardi B. J., "**A study of flow pattern for gas/liquid flow in small diameter tubes**". Chemical Engineering Research and Design, Vol. 85, pp. 180-192 (2007).
- Owen D. G., & Hewitt G. F., "**An Improved Annular Two-Phase Flow Model**". Proceedings of the 3rd International Conference on Multiphase Flow, the Hague, the Netherlands (1987).
- Owczarski P. C., Scherck R. I., & Postma A. K., **"Technical Bases and User's Manual for the Prototype of a Suppression Pool Aerosol Removal Code (SPARC)"**, U. S. Nuclear Regulatory Commission, NUREG/CR-3317 PNL-4742 R1 (1985).
- Owczarski P. C., & Burk, K. W., **"SPARC-90: A Code for Calculating Fission Product Capture in Suppression Pools"**, U. S. Nuclear Regulatory Commission, NUREG/CR-5765 TI92 003256 (1991).
- Owen D. G., & Hewitt G. F., **"An improved annular two-phase flow model"**. Proceedings of the Third International Conference on Multiphase Flow, Hague, Netherlands (1987).
- Pak S. I., & Chang K. S., **"Performance estimation of a Venturi scrubber using a computational model for capturing dust particles with liquid spray"**. Journal of Hazardous Materials, B138, pp. 560-573 (2006).
- Pan L., & Hanratty T. J., "**Correlation of entrainment for annular flow in vertical pipes**". International Journal of Multiphase Flow, Vol. 32, pp. 363-384 (2002a).
- Pan L., & Hanratty T. J., "**Correlation of entrainment for annular flow in horizontal pipes**". International Journal of Multiphase Flow, Vol. 32, pp. 385-408 (2002b).
- Paras S. V., & Karabelas A. J., "**Properties of the Liquid Layer in Horizontal Annular Flow**". International Journal of Multiphase Flow, Vol. 17, No 4, pp. 439-454 (1991).
- Powers D. A., & Burson S. B., **"A simplified model of aerosol removal by containment sprays"**. NUREG/CR-5966 SAND92-2689 (1993).
- Ramsdale S., Friederichs H-G., & Güntay S., **"BUSCA JUN91: Reference Manual for the Calculation of Radionuclide Scrubbing in Water Pools".** ISBN 3923875665, GRS (1991).
- Patruno L. E., Marchioro P. A., Jenssen C. B., Marchetti J. M., Dorao C. A., Svendsen H .F., & Jakobsen H. A., "**Liquid Entrainment- droplet size distribution for a low surface tension mixture** ". Chemical Engineering Science, Vol. 65, No 18, pp. 5272-5284 (2010).
- Pilch M., & Erdman C. A., "**Use of break-up time data to predict the maximum size of stable fragment for acceleration induced breakup of a liquid drop**" *Int. J. Multiphase Flow*, Vol. 13, pp. 741–757(1987).

- Pontillon Y., Ducros G., & Malgouyres P.P., **"Behaviour of fission products under severe PWR accident conditions VERCORS experimental programme—Part 1: General description of the programme"**. Nuclear Engineering and Design, Vol. 240, p.p. 1843-1852 (2010a).
- Pontillon Y., & Ducros G., **"Behaviour of fission products under severe PWR accident conditions: The VERCORS experimental programme—Part 2: Release and transport of fission gases and volatile fission products"**. Nuclear Engineering and Design, Vol. 240, p.p. 1853-1866 (2010b).
- Pontillon Y., & Ducros G., **"Behaviour of fission products under severe PWR accident conditions. The VERCORS experimental programme—Part 3: Release of low-volatile fission products and actinides"**. Nuclear Engineering and Design, Vol. 240, p.p. 1867-1881 (2010c).
- Porcheron E., Lemaitre P., & Marchand D., **"Aerosol removal by emergency spray in PWR"**. Journal of Energy and Power Engineering, Vol. 5, pp. 600-611 (2011).
- Powers D. A, Leonard M. T., Gauntt R. O., Lee R. Y., & Salay M., **"Accident Source Terms for Light-Water Nuclear Power Plants Using High-Burnup or MOX Fuel"**. SANDIA Report, SAND2011-0128 (2011).
- Pozorsky J., & Minier J. P., "**On the Lagrangian turbulent dispersion models based on the Langevin equation**" *International Journal of Multiphase Flow, Vol. 24, pp. 913-945, (1998).*
- Rahman M. A., Heidrick T., & Fleck B. A., "**A critical review of advanced experimental techniques to measure two-phase gas/liquid flow**" *The Open Fuels & Energy Science Journal*, Vol. 2, pp. 54–70 (2009).
- Ramsdale S., Friederichs H-G., & Güntay S., **"BUSCA JUN91: Reference Manual for the Calculation of Radionuclide Scrubbing in Water Pools".** ISBN 3923875665, GRS (1991).
- Ranger A. A., & Nicholls J. A., **"The aerodynamic shattering of liquid drops"**. AIAA Jl 7, pp. 285-290 (1969).
- Ricou F. B., & Spalding D. B., **"Measurements of Entrainment by Axisymmetrical Turbulent Jets"**, Journal of Fluid Mechanics, Vol. 11, pp. 21-32 (1961).
- Roberts P. A., Azzopardi B. J., & Hibberd S., "**The Split of Horizontal Annular Flow at a T-Junction**" Journal of Chemical Engineering Science, Vol. 52, No. 20, pp. 3441–3453 (1997).
- Rodriguez J. M., "**Numerical Simulation of Two-Phase Annular Flow**". PhD. Thesis Rensselaer Polytechnic Institute of New York (2009).
- Roger F., Carreau J. L., Gbahoué L., Hobbes, P., Allou A., & Beauchamp F., "**Structure of strongly underexpanded gas jets submerged in liquids–Application to the wastage of tubes by aggressive jets**". Nuclear Engineering and Design, Vol. 273, pp. 119-130 (2014).
- Rudnick S. N., Koehler J. L. M., Martin K. P., Leith D., & Cooper D. W., "**Particle Collection Efficiency in a Venturi Scrubber: Comparison of**

Experiments with Theory". Environmental Science & Technology, Vol. 20, No. 3, pp. 237-242. (1986).

- Sawant P., Ishii M., & Mori M., "**Droplet Entrainment Correlation in Vertical Upward Co-current Annular Two-phase Flow**". Nuclear Engineering and Design, Vol. 238, pp. 1342-1352 (2008a).
- Sawant P., Ishii M., Hazuku T., Takamasa T., & Mori M., "**Properties of Disturbance Waves in Vertical Annular Two-phase Flow**". Nuclear Engineering and Design, Vol. 238, pp. 3528-3541 (2008b).
- Sawant P., Ishii M., & Mori M., "**Prediction of Amount of Entrained Droplets in Vertical Annular Two-phase Flow**". International Journal of Heat and Fluid Flow, Vol. 30, p. 715-728. (2009).
- Schadel S. A., "**Atomization and deposition rates in vertical annular two-phase Flow**". Ph.D. thesis, University of Illinois, Urbana-Champaign, Urbana, Illinois, U.S.A. (1988).
- Schmehl R., "**Tropfendeformation und nachzerfall bei der technischen gemischaufbereitung**". PhD. Thesis University of Karlsruhe (2003).
- Schubring D., & Shedd T. A., "**Wave behavior in horizontal annular air-water flow**". International Journal of Multiphase Flow, Vol. 34, pp. 636-646 (2008).
- Schubring D., & Shedd T. A., "**Critical friction factor modeling of horizontal annular base film thickness**". International Journal of Multiphase Flow, Vol. 35, pp. 389-397 (2009a).
- Schubring D., "**Behavior interrelationships in annular flow**". PhD. Thesis University of Wisconsin-Madison (2009b).
- Sekoguchi K., Takeishi M., & Ishimatsu, T., "**Interfacial structure in vertical upward annular flow**". Physico Chemical Hydrodynamics, Vol. 6, pp. 239-255 (1985).
- Setyawan A., Indarto, & Deendarlianto, **"Experimental investigation on disturbance wave velocity and frequency in air-water horizontal annular flow"**, Modern Applied Science, Vol. 8, No 4 (2014).
- Shi H-H., Wang B-Y., & Dai Z-Q., **"Research on the mechanics of underwater supersonic gas jets"**, Science China Press and Springer-Verlag Berlin Heidelberg, Physics, Mechanics and Astronomy, Vol. 53, No 3, pp. 527-535 (2010).
- Shirolkar J. S., Coimbra C. F. M., & Quieroz McQuay M., "**Fundamental aspects of modeling turbulent particle dispersion in dilute flows**". Prog. Energy Combustion Science, Vol. 22, pp. 363-399 (1996).
- Simmons M. J. H., & Hanratty T. J., "**Droplet size measurements in horizontal annular gas-liquid flow**". International Journal of Multiphase Flow, Vol. 27, pp. 861-883. (2001).
- Slinn W. G. N., "**Precipitation Scavenging in Atmospheric Sciences and Power Production"** 1979 Chap.11, Division of Biomedical Environmental Research, US Department of Energy. Washington D.C. (1983).

- Soffer L., Burson S. B., Ferrell C. M., Lee R. Y., & Ridgely J. N., "**Accident Source Terms for Light-Water Nuclear Power Plants"**. U. S. Nuclear Regulatory Commission, NUREG-1465 (1995).
- Someya S., Uchida M, Li Y., Ohshima H., & Okamoto K., **"Entrained droplets in underexpanded gas jet in water".** Journal of Visualization, DOI 10.1007/s12650-011-0089-7 (2011).
- Spore J. W., Elson J. S., Jolly-Woodruff S. J., Knight T. D., Lin J-C., Nelson R. A., Pasamehmetoglu K. O., Steinke R. G., Unal C., Mahaffy J. H., & Murray C., **"TRAC-M/FORTRAN 90 (Version 3.0) Theory Manual".** LA-UR-00-910 (2000).
- Stevanovic V., & Studovic M., "**A simple model for vertical annular and horizontal stratified two-phase flows with liquid entrainment and phase transitions: one-dimensional steady state conditions**". Nuclear Engineering and Design, Vol. 154, pp. 357-379. (1995).
- Talbot L., Cheng R.K., Schefer R.W., & Willis D. R.,**" Thermophoresis of particles in a heated boundary layer"**. J. Fluid Mech., Vol. 101, pp. 737-758 (1980).
- Tang J. N., Tseng C. C., Wang N. F., & Shyy W., "**Flow Structures of Gaseous Jets Injected into Water for Underwater Propulsion**". AIAA 2011-185, 49th AIAA Aerospace Meeting, 4-7 January 2011 Orlando, Florida, pp. 1-16. Copyright of American Institute of Aeronautics and Astronautics, (2011).
- Tatterson D. F., Dallman J. C., & Hanratty T. J., "**Drop sizes in annular gas-liquid flows**"**.** AIChE Journal. Vol. 23, pp. 68-76 (1977).
- Theerachaisupakij W., Matsusaka S., Akashi Y., & Masuda H., **"Reentrainment of deposited particles by drag and aerosol collision"**. Journal of Aerosol Science, Vol.34, pp. 261-274 (2003).
- US NRC, "**Primary System Fission Product Release and Transport – A state of the art report to the committee on the safety nuclear installations"**. U. S. Nuclear Regulatory Commission, NUREG/CR-6193, NEA/CSNI/R(94)2, ORNL/TM-12681 (1994).
- US NRC, "**Severe Accident Risks: An Assessment for Five U.S. Nuclear Power Plants"**. U. S. Nuclear Regulatory Commission, NUREG-1150 (1990).
- US NRC, "**Reassessment of the technical bases for estimating source terms"**. U. S. Nuclear Regulatory Commission, NUREG-0956 (1986).
- US NRC, "**Technical bases for estimating fission products behavior during LWR accidents"**. U. S. Nuclear Regulatory Commission, NUREG-0772 (1981).
- US NRC, "**The Reactor Safety Study: An Assessment of Accident Risk in U.S. Commercial Nuclear Power Plants"**. U. S. Nuclear Regulatory Commission Report, NUREG 75/014, WASH-1400 (1975).
- Utsuno H., & Kaminaga F., **"Prediction of liquid film dryout in two-phase annular-mist flow in a uniformly heated narrow tube development of analytical method under BWR conditions"** Journal of Nuclear Science and Technology, Vol. 35, No 9, pp. 643-653 (1998).

- Van Rossum J. J., "**Experimental investigation of horizontal liquid films**". Chemical Engineering Science, Vol. 11, p. 35 (1959).
- Van't Westende J. M. C., **"Droplets in annular-dispersed gas-liquid pipe-flows"**. PhD. Thesis University of Delft (2008).
- Wald A., **"An extension of Wilks' method for setting tolerance limits"**, Annals of Mathematical Statistics, vol. 14, nº 1, pp. 45-55 (1943).
- Wallis G. B., "**One-Dimensional Two-Phase Flow**". New York, McGraw-Hill, Inc, U.S.A. (1969).
- Wang X., Zhang L., & Moran M. D., "**Uncertainty assessment of current size-resolved parameterizations for below-cloud particle scavenging by rain**". Atmospheric Chemistry and Physics, Vol. 10, pp. 5685-5705. (2010).
- Wassel A. T., Mills A. F., & Bugby D. C., **"Analysis of radionuclide retention in water pools".** Nuclear Engineering and Design, Vol. 90(87) (1985).
- Wilks S. S., **"Determination of sample sizes for setting tolerance limits"**, Annals of Mathematical Statistics, vol. 12, nº 1, pp. 91-96 (1941).
- Weiland C. J., "**Characteristics of the high speed gas-liquid interface**". Thesis of faculty of the Virginia Polytechnic Institute and State University (2010).
- Weiland C., & Vlachos P. P., **"Round gas jets submerged in water".** International Journal of Multiphase Flow, Vol. 48, pp. 46-57 (2013).
- Wen H.Y., & Kasper G., **"On the kinetics of particle reentrainment from surfaces"**. Journal of Aerosol Science, Vol. 20(4), pp. 483-498 (1989).
- Wicks M., & Dukler A. E., **"In situ measurements of drop size distribution in two-phase flow: a new method for electrically conducting liquids"**. Third International Heat Transfer Conference, Chicago (1966).
- Wierzba A., **"Deformation and breakup of liquid drops in a gas stream at nearly critical Weber numbers"**. Experiments in Fluids, Vol. 9, pp. 59-64 (1990).
- Williams M. M. R., **"Nuclear Aerosol Behavior During Reactor Accidents"**. Progress in Nuclear Energy, Vol. 23, No 2, pp. 101-108 (1990).
- Williams L. R., Dykhno L. A., & Hanratty T. J., **"Droplet Flux Distributions and Entrainment in Horizontal Gas-Liquid Flows"**. International Journal in Multiphase Flow, Vol. 22, No 1, pp. 1-18 (1996).
- Woodmansee D. E., & Hanratty T. J., "**Mechanism for the removal of droplets from a liquid surface by a parallel air flow**". Chemical Engineering Science, Vol. 24, pp. 299-307 (1969).
- Yecko P., **"Viscous modes in two-phase mixing layers".** Physics of Fluid, Vol. 14, pp. 4115-4121 (2002).
- Yun G., Ishiwatari Y., Ikejiri S., & Oka Y., "**Numerical analysis of the onset of droplet entrainment in annular two-phase flow by hybrid method**". Annals of Nuclear Energy, Vol. 37, pp. 230-240 (2010).
- Zhang H-Q., & Sarica C., **"Low liquid loading gas/liquid pipe flow"**. Journal of Natural Science and Engineering, Vol. 3, pp. 413-422 (2011).

- Zhao H., & Zheng C., "**Stochastic Algorith and Numerical Simulation for Drop Scavenging of Aerosol**". Applied Mathematics and Mechanics, Vol. 27, No. 10, pp. 1321-1332. (2006).
- Zhao H., & Zheng C., **"Modeling of Gravitational Wet Scrubbers with Electrostatic Enhancement"** Chemical Engineering Technology, Vol. 31, No 12, pp. 1824-1837 (2008).
- Zhao X., "**Mechanistic-based models for slug flow in vertical pipes**". Thesis of Texas Tech University (2005).
- Zhivaikin L. Y., "**Liquid film thickness in film type units**". International Chemical Engineering, Vol. 2, No 3, p. 337 (1962).
- Zhu Z. F., "**A Study of the Interfacial Features of Gas-Liquid Annular Two-Phase Flow**". Ph.D. thesis, University of Saskatchewan, Saskatoon, Canada (2004).

Web Pages

- AREVA, information extracted from official page of AREVA UK: http://uk.areva.com/EN/home-668/how-does-a-pwr-work-description-and-explanation--areva-uk.html
- IAEA, official page of the International Atomic Energy Agency: https://www.iaea.org/
  International scale of significance of accidents involving ionizing radiation: http://www-ns.iaea.org/tech-areas/emergency/ines.asp
- NRC, information extracted from the official page of the Nuclear Regulatory Commission: http://www.nrc.gov/reactors/bwrs.html

Appendixes

APPENDIXES

Appendix I: The Droplet Size Distribution Functions

When droplets are suddenly exposed to a high speed gas stream the aerodynamic break-up is an important mechanism which determines the droplet size distribution function. In a first approach, the mean, maximum or Sauter diameters can be used to characterize the droplet sizes; that is, droplets have been considered by only one constant parameter. But, the next step is to consider a particle size discrete distribution function (Figure I-1). There are several size distribution functions frequently used in the literature, the most important distribution used to correlate particle sizes or droplet sizes measurements is the Log-Normal Distribution. But in fact, due to the existence of a critical value of droplet sizes, this distribution is usually truncated and the expression most widely used in the literature is the Upper Limit Log-Normal (ULLN) distribution function. Other possible distribution functions which appear in the literature are the Square-Root Normal, the Rosin-Rammler, the Nukiyama-Tanasawa, the Log-Hyperbolic, etc.

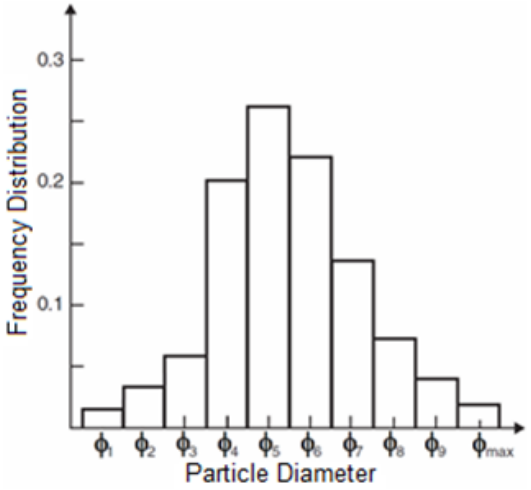

Figure I-1. Discrete frequency distribution of particle diameter.

A.1. Log-Normal Distribution

The log-normal mass frequency distribution is [Marshall, 1954]

$$f_m(\phi) = \frac{1}{\sqrt{2\pi}\phi\sigma_0}\exp\left[-\frac{1}{2}\left(\frac{\ln\phi - \ln\phi_{mM}}{\sigma_0}\right)^2\right] \qquad \textbf{Eqn. (I-1)}$$

where ϕ_{mM} is the mass median diameter. The geometric standard deviation can be found by plotting the cumulative distribution on log-probability coordinates, which yields a straight line with a positive slope. The value for σ_0 can be obtained from

$$\sigma_0 = \ln\frac{\phi_{84\%}}{\phi_M} \qquad \textbf{Eqn. (I-2)}$$

where $\phi_{84\%}$ is the diameter corresponding to the 84th percentile on the log-probability plot and ϕ_M is the median diameter (value at the 50% point). The value for σ_0 is the same for both the number and mass distributions.

A.2. Upper-Limit Log-Normal Distribution

Over the past few decades, a large number of experimental studies in annular flow have been carried out. In these works, different empirical expressions have been proposed for different parameters characterizing the droplet sizes distributions. The Upper Limit log-Normal distribution (ULLN) given by Mugele and Evans [Mugele, 1951] has been the most widely used for obtaining size distributions from the experimental measurements. The ULLN distribution function, defined in that way to describe droplet size distributions, has been also used in the description of atomizing jets and submerged jets.

An ULLN is a log-normal distribution truncated, i.e., it is designed to set a maximum particle diameter as the upper limit of the distribution. It can be written in the form:

$$f_v(\phi) = \frac{\lambda\phi_{\max}}{\sqrt{\pi}\phi(\phi_{\max} - \phi)}\exp\left(-\lambda^2 t^2\right) \qquad \textbf{Eqn. (I-3)}$$

where

$$t = \ln\left[\frac{b\cdot\phi}{\phi_{\max} - \phi}\right] \quad and \quad b = \frac{\phi_{\max} - \phi_{vm}}{\phi_{vm}} \qquad \textbf{Eqn. (I-4)}$$

being ϕ_{vm} the volume median diameter and λ the deviation around the mean. The distribution function is characterized by the parameters ϕ_{max}, ϕ_{vm} and λ. Typical values of the volume fraction distribution are presented in the works of Simmons and Hanratty [Simmons, 2001] (Table I-1), and Al-Sarkhi and Hanratty [Al-Sarkhi, 2002]. Both show values in the range of 3-10 for the quotient of ϕ_{max} divided by ϕ_{vm} and from 0.7 to 0.9 for the deviation around the mean, λ. For example, Figure I-2 displays the experimental droplet size distribution for several gas velocities maintaining constant the liquid velocity. This

figure shows that by increasing the gas velocity the distribution is shifted toward smaller droplet sizes, as well as also shows a gathering around the mean (decreasing of λ).

For a log-normal distribution, the Sauter mean diameter, ϕ_{32}, is related to the volume median diameter, ϕ_{vm}, by

$$\phi_{32} = \frac{\phi_{ym}}{\exp\left(\lambda^2/2\right)} \qquad \textbf{Eqn. (I-5)}$$

Table I-1. Summary of theoretical and experimental droplet size distribution parameters at the centerline [Simmons, 2001].

Experimental parameters						ULLN parameters				
U_g (m/s)	$\dot{m}_L$ (kg/m^{2}s)	Φ_{32} (μm)	Φ_{10} (μm)	Φ_{vm} (μm)	Φ_{90} (μm)	Φ_{vm} (μm)	φ_{max} (μm)	φ_{32} (μm)	λ	b
30	15.85	113.7	58.2	189.7	560.4	190.0	1400	115.6	0.67	6.4
30	22.88	111.3	57.7	185.4	534.5	188.0	1400	117.3	0.69	6.4
30	32.55	111.5	58.0	183.6	516.3	188.0	1350	117.9	0.69	6.2
30	41.20	112.0	58.4	183.8	510.8	188.0	1350	117.9	0.69	6.2
30	53.76	113.6	59.5	185.1	504.7	187.0	1350	120.4	0.71	6.2
30	61.54	114.5	60.3	186.6	503.6	187.0	1350	120.4	0.71	6.2
30	90.00	124.5	66.4	204.7	528.0	205.5	1350	136.0	0.73	5.6
30	122.00	134.0	71.5	221.9	557.1	222.0	1350	146.3	0.72	5.1
36	15.85	88.7	47.5	149.6	426.0	150.2	1500	97.9	0.73	9.0
36	22.88	90.0	48.6	151.4	419.9	151.5	1500	100.2	0.75	8.9
36	32.55	93.4	51.0	157.7	427.2	157.5	1500	105.3	0.75	8.5
36	41.20	96.9	53.1	164.1	438.2	163.9	1500	109.8	0.75	8.2
36	53.76	105.3	57.5	179.1	472.2	178.5	1450	119.6	0.75	7.1
36	61.54	108.9	59.4	184.6	482.6	184.1	1450	125.0	0.76	6.9
43	15.85	76.0	41.7	128.5	329.3	126.7	1500	88.2	0.80	10.8
43	22.88	79.0	43.3	133.6	333.4	133.6	1500	94.7	0.82	10.2
43	32.55	85.7	46.9	145.6	366.9	143.2	1500	101.8	0.82	9.5
43	41.20	91.4	50.1	157.1	397.2	157.1	1500	112.0	0.82	8.5
43	53.76	99.4	54.4	172.8	436.2	170.5	1500	119.8	0.80	7.8
43	61.54	102.9	56.3	178.9	452.3	180.6	1500	125.8	0.79	7.3
50	15.85	60.2	35.3	106.7	279.0	106.0	1700	75.2	0.83	15.0
50	22.88	65.2	37.9	114.3	288.1	117.0	1550	84.6	0.85	15.2
50	32.55	72.6	41.5	126.9	318.3	127.0	1550	91.3	0.84	11.2
50	41.20	79.0	44.7	138.8	352.0	139.0	1600	98.5	0.82	10.5
50	53.76	86.8	48.6	153.1	388.5	150.9	1400	103.5	0.78	8.3
50	61.54	92.5	51.5	163.0	415.0	163.0	1550	112.0	0.78	8.5

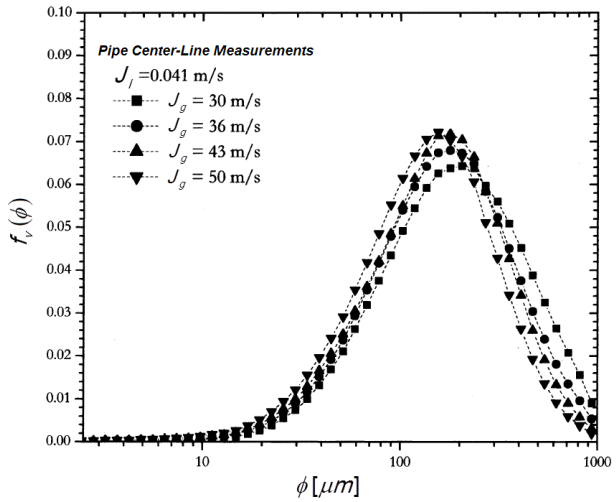

Figure I-2. Sample volume distribution obtained for annular flow at the center line at J_l = 0.041 m/s [Simmons, 2001].

Appendix II: SPARC90 and SPARC90-Jet Input and Output Files

This appendix shows two examples, an input and an output file, of the old SPARC90 code, added to the new output file provided by the new SPARC90-Jet version (which provides the above mentioned files and an additional results file).

Input file of SPARC90-Jet code

RCA2: RCA Experiments

1990,2,10

0.01,450.

2.00,2.00

2.00,2.00

0.,0.

58.6934,58.6934,

0.,0.

3.E-2,3.E-2

0.00,0.00

0.,0.

1.27E-5,2.01E-5,3.19E-5,5.05E-5,8.0E-5,

1.27E-4,2.01E-4,3.19E-4,5.05E-4,8.0E-4

0.0,0.0,

0.04,0.04,

0.29,0.29,

1.69,1.69,

6.37,6.37,

15.61,15.61,

24.92,24.92,

25.88,25.88,

17.5,17.5,

7.7,7.7,

0.,0.

0.00,0.00,

0.,0.

0.,0.

7.196,7.196,

0.,0.

0.,0.

0.,0.

120.,120.

2.68,2.68

120.,120.

2.3,2.3

1.,1.

2,0.666,1,0,10.,1,0.886,4,1,50.,0.,0.,50.,0,0

0.01,450.

20

Input file similar to the old SPARC90 version, it differs only in the introduction of a new possible vent choice, high injection velocity-jet discharge (third line from bottom, option 4).

Output file of SPARC90-Jet code

s p a r c 90

version = 1990

beginning execution . . .

PA13: POSEIDON II experiment

sparc code version = 1990

ndata= 2

nbins= 10

ti(i)= 0.10000E-01 450.00

rhoi(i)= 1.3000 1.3000

rhos(i)= 1.3000 1.3000

vhi(i)= 0.0000 0.0000

amws(i)= 150.90 150.90

solf(i)= 0.0000 0.0000

pmsdot(i)= 0.14900E-01 0.14900E-01

frcs(i)= 0.0000 0.0000

frrb(i)= 0.0000 0.0000

dpart(j)= 0.12700E-05 0.20100E-05 0.31900E-05 0.50500E-05 0.80000E-05 0.12700E-04 0.20100E-04 0.31900E-04 0.50500E-04 0.80000E-04

zmass(j,i)= 0.0000 0.0000

zmass(j,i)= 0.60000E-01 0.60000E-01

zmass(j,i)= 0.43000 0.43000

zmass(j,i)= 2.2550 2.2550

zmass(j,i)= 7.7350 7.7350

zmass(j,i)= 17.380 17.380

zmass(j,i)= 25.575 25.575

zmass(j,i)= 24.630 24.630

zmass(j,i)= 15.530 15.530

zmass(j,i)= 6.4100 6.4100

h2dot(i)= 0.0000 0.0000

h2odot(i)= 0.0000 0.0000

codot(i)= 0.0000 0.0000

co2dot(i)= 0.0000 0.0000

airdot(i)= 34.720 34.720

doti2(i)= 0.0000 0.0000

oridot(i)= 0.0000 0.0000

frpi(i)= 0.0000 0.0000

tgasin(i)= 270.00 270.00

pgasin(i)= 1.1000 1.1000

poolt(i)= 63.000 63.000

poolp(i)= 1.0000 1.0000

dmulti(i)= 1.0000 1.0000

kout= 2

vpool= 3.9300

klvn= 1

ngrow= 0

dx= 10.000

nvent= 1

dvent= 1.7720

mvent= 4

ntype= 1

subxt= 30.000

subdc= 0.0000

subhv= 0.0000

subsg= 30.000

mps= 0

jod= 0

tout(i)= 0.10000E-01 450.00

ncirc= 20

1 tout(1)= 0.01 minutes. materials leaving pool

particle bin number	particle diam dry (cm)	particle diam wet (cm)	grams per sec dry	grams per sec wet	number per sec	decon. factor df	rho	ammd
1	1.27E-06	1.2700E-06	0.0000E+00	0.0000E+00	0.0000E+00	3.2698E+00	1.30	1.4480E-06
2	2.01E-06	2.0100E-06	2.8060E-06	2.8060E-06	5.0764E+11	3.1861E+00	1.30	2.2918E-06
3	3.19E-06	3.1900E-06	2.0594E-05	2.0594E-05	9.3203E+11	3.1111E+00	1.30	3 .6372E-06
4	5.05E-06	5.0500E-06	1.1085E-04	1.1085E-04	1.2645E+12	3.0310E+00	1.30	5.7579E-06
5	8.00E-06	8.0000E-06	3.9273E-04	3.9273E-04	1.1269E+12	2.9347E+00	1.30	9.1214E-06
6	1.27E-05	1.2700E-05	9.1975E-04	9.1975E-04	6.5966E+11	2.8156E+00	1.30	1.4480E-05
7	2.01E-05	2.0100E-05	1.4234E-03	1.4234E-03	2.5751E+11	2.6772E+00	1.30	2.2918E-05
8	3.19E-05	3.1900E-05	1.4498E-03	1.4498E-03	6.5614E+10	2.5313E+00	1.30	3.6372E-05
9	5.05E-05	5.0500E-05	9.6356E-04	9.6356E-04	1.0992E+10	2.4015E+00	1.30	5.7579E-05
10	8.00E-05	8.0000E-05	4.1367E-04	4.1367E-04	1.1870E+09	2.3088E+00	1.30	9.1214E-05

1

1.3000E+00 dry particle density (gm/cm**3)

2.9411E-06 number median particle radius of dry particles (cm)

2.9411E-06 number median particle radius of wet particles(cm)

2.0091E+00 geometric standard deviation of dry particles

2.0091E+00 geometric standard deviation of wet particles

1.4901E-02 total grams/sec dry particles into pool

5.6971E-03 total grams/sec dry particles leaving pool

3.0718E-07 particle concentration upstream of vent exit (g/cm**3)

2.9679E+08 number concentration upstream of vent exit (1/cm**3)

3.6213E-07 particle concentration outside of vent exit (g/cm**3)

6.3000E+01 pool temperature (degrees celsius)

1.0000E+00 pressure above pool (atm)

1.0000E+02 relative humidity of gas leaving pool (percent)

4.8515E+04 total volumetric flow rate into pool (cc/s)

6.2246E+04 total volumetric flow rate out of pool (cc/s)

0.0000E+00 total flow rate of i2 into pool (gmoles/s)

0.0000E+00 flow rate of vapor i2 into pool (gmoles/s)

0.0000E+00 flow rate of particulate i2 into pool (gmoles/s)

0.0000E+00 total flow rate of i2 out of pool (gmoles/s)

0.0000E+00 flow rate of vapor i2 out of pool (gmoles/s)

0.0000E+00 flow rate of particulate i2 out of pool (gmoles/s)

0.0000E+00 half life of i2 vapor in primary system(sec)

0.0000E+00 pool particle concentration (g/liter)

0.0000E+00 total pool particulate mass (g)

0.0000E+00 pool iodine concentration (gmoles i2/l)

0.0000E+00 pool iodide concentration from particles (gmoles i2/l)

0.0000E+00 pool organic iodide concentration (gmoles/l)

0.0000E+00 total pool iodine as i2 (gmoles)

0.6918E-37 ph

0.1000E+01 decontamination factor by early condensation

0.2615E+01 overall particle decontamination factor

0.1000E+01 apparent i2 df

0.1000E+01 i2 overall decontamination factor

0.1000E+01 overall organic iodide df

1 tout(2)= 450.00 minutes. materials leaving pool

particle bin number	particle diam dry (cm)	particle diam wet (cm)	grams per sec dry	grams per sec wet	number per sec	decon. factor df	rho	ammd
1	1.27E-06	1.2700E-06	0.0000E+00	0.0000E+00	0.0000E+00	3.2698E+00	1.30	1.4480E-06
2	2.01E-06	2.0100E-06	2.8060E-06	2.8060E-06	5.0764E+11	3.1861E+00	1.30	2.2918E-06
3	3.19E-06	3.1900E-06	2.0594E-05	2.0594E-05	9.3203E+11	3.1111E+00	1.30	3 .6372E-06
4	5.05E-06	5.0500E-06	1.1085E-04	1.1085E-04	1.2645E+12	3.0310E+00	1.30	5.7579E-06
5	8.00E-06	8.0000E-06	3.9273E-04	3.9273E-04	1.1269E+12	2.9347E+00	1.30	9.1214E-06
6	1.27E-05	1.2700E-05	9.1975E-04	9.1975E-04	6.5966E+11	2.8156E+00	1.30	1.4480E-05
7	2.01E-05	2.0100E-05	1.4234E-03	1.4234E-03	2.5751E+11	2.6772E+00	1.30	2.2918E-05

8 3.19E-05 3.1900E-05 1.4498E-03 1.4498E-03 6.5614E+10 2.5313E+00 1.30 3.6372E-05

9 5.05E-05 5.0500E-05 9.6356E-04 9.6356E-04 1.0992E+10 2.4015E+00 1.30 5.7579E-05

10 8.00E-05 8.0000E-05 4.1367E-04 4.1367E-04 1.1870E+09 2.3088E+00 1.30 9.1214E-05

1

*1.3000E+00 dry particle density (gm/cm**3)*

2.9411E-06 number median particle radius of dry particles (cm)

2.9411E-06 number median particle radius of wet particles(cm)

2.0091E+00 geometric standard deviation of dry particles

2.0091E+00 geometric standard deviation of wet particles

1.4901E-02 total grams/sec dry particles into pool

5.6971E-03 total grams/sec dry particles leaving pool

*3.0718E-07 particle concentration upstream of vent exit (g/cm**3)*

*2.9679E+08 number concentration upstream of vent exit (1/cm**3)*

*3.6213E-07 particle concentration outside of vent exit (g/cm**3)*

6.3000E+01 pool temperature (degrees celsius)

1.0000E+00 pressure above pool (atm)

1.0000E+02 relative humidity of gas leaving pool (percent)

4.8515E+04 total volumetric flow rate into pool (cc/s)

6.2246E+04 total volumetric flow rate out of pool (cc/s)

0.0000E+00 total flow rate of i2 into pool (gmoles/s)

0.0000E+00 flow rate of vapor i2 into pool (gmoles/s)

0.0000E+00 flow rate of particulate i2 into pool (gmoles/s)

0.0000E+00 total flow rate of i2 out of pool (gmoles/s)

0.0000E+00 flow rate of vapor i2 out of pool (gmoles/s)

0.0000E+00 flow rate of particulate i2 out of pool (gmoles/s)

0.0000E+00 half life of i2 vapor in primary system(sec)

0.6323E-01 pool particle concentration (g/liter)

0.2485E+03 total pool particulate mass (g)

0.0000E+00 pool iodine concentration (gmoles i2/l)

0.0000E+00 pool iodide concentration from particles (gmoles i2/l)

0.0000E+00 pool organic iodide concentration (gmoles/l)

0.0000E+00 total pool iodine as i2 (gmoles)

0.6918E-37 ph

0.1000E+01 decontamination factor by early condensation

0.2615E+01 overall particle decontamination factor

0.1000E+01 apparent i2 df

0.1000E+01 i2 overall decontamination factor

0.1000E+01 overall organic iodide df

New Additional Output file of SPARC90-Jet code

RT-SC-01-02: LACE experiments

ZONA DE ROTURA

Presión de Estancamiento en la Rotura [Pa]= 327276.4

Presión Crítica

k=1.400 Pcrit [Pa]= 79074.0

Condiciones Subcríticas(P.estancamiento>P.crítica)

Velocidad Subcrítica [m/s]= 68.7

Termina de arrancan gotas en [cm] 3.370092

ENTRAINMENT INCEPTION VELOCITY

Vincp [m/s]=12.421

Valor de la Velocidad de Entrainment CONSTANTE para todo el jet gaseoso

PERFIL DE VELOCIDADES DEL JET GASEOSO SUMERGIDO

Zona de Establecimento del Jet

Velocidades Medias

Umedt-> Velocidad media total

Umedl-> Velocidad media zona de difusión

Celda= 1 Distancia [cm]= 0.0411 Ucelda[m/s]= 68.4216 UZonaDif.[m/s]= 59.1405

Celda= 2 Distancia [cm]= 0.1233 Ucelda[m/s]= 67.7123 UZonaDif.[m/s]= 50.4374

Celda= 3 Distancia [cm]= 0.2055 Ucelda[m/s]= 66.8090 UZonaDif.[m/s]= 51.3281

Celda= 4 Distancia [cm]= 0.2877 Ucelda[m/s]= 65.9226 UZonaDif.[m/s]= 51.3294

Celda= 5 Distancia [cm]= 0.3699 Ucelda[m/s]= 65.0498 UZonaDif.[m/s]= 51.1658

Celda= 6 Distancia [cm]= 0.4521 Ucelda[m/s]= 64.1868 UZonaDif.[m/s]= 50.9268

Celda= 7 Distancia [cm]= 0.5343 Ucelda[m/s]= 63.3296 UZonaDif.[m/s]= 50.6369

Celda= 8 Distancia [cm]= 0.6165 Ucelda[m/s]= 62.4740 UZonaDif.[m/s]= 50.3043

Celda= 9 Distancia [cm]= 0.6987 Ucelda[m/s]= 61.6157 UZonaDif.[m/s]= 49.9313

Celda= 10 Distancia [cm]= 0.7809 Ucelda[m/s]= 60.7500 UZonaDif.[m/s]= 49.5179

Celda= 11 Distancia [cm]= 0.8631 Ucelda[m/s]= 59.8725 UZonaDif.[m/s]= 49.0628
Celda= 12 Distancia [cm]= 0.9453 Ucelda[m/s]= 58.9784 UZonaDif.[m/s]= 48.5641
Celda= 13 Distancia [cm]= 1.0275 Ucelda[m/s]= 58.0631 UZonaDif.[m/s]= 48.0196
Celda= 14 Distancia [cm]= 1.1097 Ucelda[m/s]= 57.1220 UZonaDif.[m/s]= 47.4271
Celda= 15 Distancia [cm]= 1.1919 Ucelda[m/s]= 56.1504 UZonaDif.[m/s]= 46.7840
Celda= 16 Distancia [cm]= 1.2741 Ucelda[m/s]= 55.1439 UZonaDif.[m/s]= 46.0880
Celda= 17 Distancia [cm]= 1.3563 Ucelda[m/s]= 54.0982 UZonaDif.[m/s]= 45.3369
Celda= 18 Distancia [cm]= 1.4385 Ucelda[m/s]= 53.0093 UZonaDif.[m/s]= 44.5286
Celda= 19 Distancia [cm]= 1.5207 Ucelda[m/s]= 51.8732 UZonaDif.[m/s]= 43.6610
Celda= 20 Distancia [cm]= 1.6028 Ucelda[m/s]= 50.6865 UZonaDif.[m/s]= 42.7326
Celda= 21 Distancia [cm]= 1.6850 Ucelda[m/s]= 49.4460 UZonaDif.[m/s]= 41.7419
Celda= 22 Distancia [cm]= 1.7672 Ucelda[m/s]= 48.1490 UZonaDif.[m/s]= 40.6879
Celda= 23 Distancia [cm]= 1.8494 Ucelda[m/s]= 46.7933 UZonaDif.[m/s]= 39.5700
Celda= 24 Distancia [cm]= 1.9316 Ucelda[m/s]= 45.3772 UZonaDif.[m/s]= 38.3880
Celda= 25 Distancia [cm]= 2.0138 Ucelda[m/s]= 43.8998 UZonaDif.[m/s]= 37.1424
Celda= 26 Distancia [cm]= 2.0960 Ucelda[m/s]= 42.3608 UZonaDif.[m/s]= 35.8340
Celda= 27 Distancia [cm]= 2.1782 Ucelda[m/s]= 40.7606 UZonaDif.[m/s]= 34.4644
Celda= 28 Distancia [cm]= 2.2604 Ucelda[m/s]= 39.1006 UZonaDif.[m/s]= 33.0360
Celda= 29 Distancia [cm]= 2.3426 Ucelda[m/s]= 37.3830 UZonaDif.[m/s]= 31.5517
Celda= 30 Distancia [cm]= 2.4248 Ucelda[m/s]= 35.6108 UZonaDif.[m/s]= 30.0153
Celda= 31 Distancia [cm]= 2.5070 Ucelda[m/s]= 33.7880 UZonaDif.[m/s]= 28.4311
Celda= 32 Distancia [cm]= 2.5892 Ucelda[m/s]= 31.9196 UZonaDif.[m/s]= 26.8042
Celda= 33 Distancia [cm]= 2.6714 Ucelda[m/s]= 30.0110 UZonaDif.[m/s]= 25.1405
Celda= 34 Distancia [cm]= 2.7536 Ucelda[m/s]= 28.0689 UZonaDif.[m/s]= 23.4461
Celda= 35 Distancia [cm]= 2.8358 Ucelda[m/s]= 26.1003 UZonaDif.[m/s]= 21.7278
Celda= 36 Distancia [cm]= 2.9180 Ucelda[m/s]= 24.1126 UZonaDif.[m/s]= 19.9926
Celda= 37 Distancia [cm]= 3.0002 Ucelda[m/s]= 22.1137 UZonaDif.[m/s]= 18.2476
Celda= 38 Distancia [cm]= 3.0824 Ucelda[m/s]= 20.1117 UZonaDif.[m/s]= 16.5000
Celda= 39 Distancia [cm]= 3.1646 Ucelda[m/s]= 18.1142 UZonaDif.[m/s]= 14.7564
Celda= 40 Distancia [cm]= 3.2468 Ucelda[m/s]= 16.1290 UZonaDif.[m/s]= 13.0235
Celda= 41 Distancia [cm]= 3.3290 Ucelda[m/s]= 14.1630 UZonaDif.[m/s]= 11.3071

CARACTERÍSTICAS DE LAS GOTAS

Celda	*Dist.[cm]*	*Dgota[mm]*	*Vel.Gota[m/s]*	*Entr.[mg/s]*	*Got.Entr.[got./s]*	*Fr.Huecos*
1	*0.04110*	*1.42880*	*17.54*	*0.8320*	*0.6*	*0.999998987*
2	*0.12330*	*1.42111*	*17.41*	*2.1781*	*1.5*	*0.999996960*
3	*0.20549*	*1.42361*	*17.17*	*4.1977*	*2.9*	*0.999993443*
4	*0.28769*	*1.43096*	*16.95*	*6.8838*	*4.7*	*0.999988019*
5	*0.36989*	*1.43841*	*16.72*	*10.2337*	*6.9*	*0.999980450*
6	*0.45209*	*1.44603*	*16.51*	*14.2395*	*9.5*	*0.999970436*
7	*0.53428*	*1.45391*	*16.29*	*18.8908*	*12.3*	*0.999957681*
8	*0.61648*	*1.46215*	*16.07*	*24.1741*	*15.5*	*0.999941885*
9	*0.69868*	*1.47085*	*15.86*	*30.0726*	*19.0*	*0.999922812*
10	*0.78088*	*1.48016*	*15.64*	*36.5651*	*22.7*	*0.999900281*